Regulation of microglial surveillance and phagocytosis in health and disease

Pablo Izquierdo Garrudo

A thesis submitted to University College London

for the degree of Doctor of Philosophy

Department of Neuroscience, Physiology and Pharmacology

University College London

July 2021

Abstract

Microglia are the resident immune cells of the central nervous system. They survey the brain for redundant synapses, debris and dying cells, which they remove through phagocytosis. This thesis examines factors which regulate this microglial behaviour, in health and in Alzheimer's disease (AD).

Applying pharmacological manipulations to microglial uptake of fluorescent microbeads in rodent brain slices, I demonstrated that membrane potential, purinergic receptors and intracellular calcium regulated phagocytosis. Buffering intracellular Ca^{2+} inhibited bead phagocytosis, whereas removing external Ca^{2+} did not, suggesting that Ca^{2+} release from internal stores controls phagocytosis. I therefore characterised spontaneous and damage-evoked Ca^{2+} transients in microglia in brain slices.

A K^+ channel blocker that depolarises microglia inhibited bead uptake, and our lab has shown that microglial ramification is regulated by membrane voltage, set by the tonically-active plasma membrane K^+ channel THIK-1. I showed that THIK-1 is also required for phagocytosis of fluorescent microbeads. Using immunohistochemistry and electrophysiology, I found that mice lacking THIK-1 have an altered number of glutamatergic synapses, suggesting synapse development is regulated by THIK-1.

Surveillance and phagocytosis by microglia in AD were assessed using (i) a fluorescent form of amyloid beta (Aβ), (ii) *App*$^{NL\text{-}G\text{-}F}$ knock-in mice to mimic the disease, and (iii) knockouts for the AD-linked phagocytic receptor TREM2. I showed that, while astrocytes also contributed, microglia were the main Aβ phagocytes *in situ*. Lack of TREM2 increased surveillance in aged but not young mice, independently of THIK-1. In the AD mouse model, Aβ plaque coverage was unaffected by THIK-1 expression, but THIK-1 knockout mice exhibited a higher density of dendritic spines suggesting that Aβ-induced synapse loss depends on THIK-1. Microglia from fresh human biopsies confirmed that blocking THIK-1 has similar effects as in rodents, suggesting that manipulating THIK-1 could regulate microglial surveillance and phagocytosis in ageing humans.

Impact statement

In the UK around 850,000 people are living with dementia, at a cost to the health and social care systems of £35 billion per year. This burden is predicted to increase dramatically in the next 20 years. I carried out research on Alzheimer's disease, the most common form of dementia for which there is unfortunately no effective treatment to date. Specifically, I studied the role of microglia, the brain's resident immune cells. In early stages of Alzheimer's, microglia are thought to delay disease progression by preventing the accumulation of a toxic substance called Aβ through a process called phagocytosis, whereby they engulf and remove it. However, there is no consensus about whether microglial involvement in Alzheimer's disease is always beneficial, and these cells may become detrimental later in disease progression. My aim was to shed light on how microglial phagocytosis is controlled and understand what effect this could have on Aβ accumulation, which may help us to delay the disease in the future.

Looking at how microglia interact with their neighbouring cells can also be helpful to provide potential treatments. I have contributed to two important discoveries in this regard. First, my work in collaboration with researchers from Purdue University demonstrates that microglia are the main brain cells that take up Aβ in the rodent brain, although other cells also contribute. Secondly, Aβ is thought to kill nerve cells in the brain by triggering oxidative stress. As part of a wider study in our lab, I found that both microglia and another type of brain cell called pericytes respond to Aβ by producing reactive oxygen species. Our research has shown that these disrupt blood flow within the brain which can lead to dementia. By defining the underlying mechanism, we have been able to suggest new targets for early Alzheimer's therapy.

Some of these results have been disseminated to colleagues in conferences or published as pre-prints and peer-reviewed papers, and I have received the Jon Driver Prize in recognition of my work. In addition, I am profoundly interested in social and cultural issues, and in communicating science to non-scientists. I have spoken and written about my work and neuroscience more broadly in various settings, including on the fact-checking platform Metafact.io, and in 2017 I won the third prize at Famelab Spain for a piece about microglia and their various functions during brain development and in dementia.

Statement of candidate's contribution to this thesis

I, Pablo Izquierdo Garrudo, confirm that the work presented in this thesis is my own. Where data have been derived from other sources, I confirm that this has been indicated in the thesis. All figure production and writing were performed by me. Overall guidance was provided by my supervisor, David Attwell.

Signed (candidate)
Pablo Izquierdo Garrudo Date: 01/07/2021

Signed (supervisor)
David Attwell Date: 01/07/2021

Acknowledgements

It’s been quite a ride — but I have not been alone.

First and foremost, I need to thank David Attwell for welcoming me in his group and for being someone to look up to. I would have never been able to carry out this work without his guidance and support. Thanks for being there for me when things turned rough in or out of the lab, Dave — and of course for the constant reassurance that everything “will be fine”.

I am grateful to my lab friends for their constant support. To Lorena and Christian, for the pains au chocolat and for being great friends and mentors from the start line. To Win and Hiroko, for the lockdown picnics, the encouraging post-it notes and generally for being the best mates I could have dreamed of. To Tania, for the jokes, the vibes and the slightly blurry swimming sessions. To Thomas, for the continuous inspiration. To Ross, for going out of his way to help. To Felipe, Nils, Greg, Yoni, Lila, Grace and Anna, for really creating such a friendly atmosphere at work. You are all a great bunch. To Mike, Stuart and Bec for their hard work and their help with orders and animals. To my friends in the Ávila, Edwards, Smart and Ule labs, for encouraging me to carry on in research and for keeping in touch years after I walked out of their door. I would not have got here without standing on your shoulders.

I would like to extend my gratitude to Wellcome for funding this work, and to Patricia, Sarah and Alasdair from the 4-year PhD committee for giving me the opportunity to join this programme and for their support throughout these years.

I am extremely grateful to all my friends in London and elsewhere, especially to those that were there to try and keep me sane during a challenging final year. Alex, Ana, Aneliya, Anna, Annamaria, Berta, Bridget, Candela, Carlos, César, Dani, Daniela, Edu, Esther, Eva, Fer, Guille, Harsha, Irene B, Irene F, Irene S, Isa, Iván, Joel, Josep, Kaloyan, Kanya, Karina, Lorenzo, Magda, María, Marielle, Miguel, Oriol, Rodri, Roger, Sandra, Sara, Silvia, Vicky, Virgínia, Yajing, Zoe. I thank you all.

Finally, and most importantly, I want to thank Álvaro as well as my parents Asun and Pablo and my childhood and college friends for keeping me grounded from afar and for their love, understanding and support through the years. A vosotros, gracias.

Table of contents

List of figures

“Pero hay una voz, hay una voz dentro.

Y dice que no, dice que lo siento.

Dice que no se rinde, que hagan sus apuestas.

Que sigue el juego.”

Miss Caffeina, *Mira cómo vuelo* (2016)

1. Introduction

1.1 Microglia, the brain's immune cells

1.1.1 A brief history of microglial research

About half of the cells in the central nervous system (CNS) are not neurons but glia (from *γλία*, Greek for "glue"), which were originally conceived as mere static, connective structures. These include astrocytes (cells with a characteristic star-like structure and multiple branches that contact synapses and blood vessels), oligodendrocytes (cells which produce the lipid-rich myelin that ensheaths neuronal axons) and indeed microglia (Allen and Lyons, 2018).

Microglia were first described by Pío del Río-Hortega in 1919, who named them as such due to "the tiny size of their soma, which is considerably smaller than that of fibrous and protoplasmic astrocytes" (del Río-Hortega, 1919). The prevailing view in the field at the time was that put forward by his mentor Santiago Ramón y Cajal, whereby the central nervous system was composed of neurons, astrocytes and a "third element" of support cells. Hortega's superior staining technique, however, allowed him to identify microglia and oligodendrocytes, and to argue — much to Cajal's opposition — that the "third element" in fact consisted of these two different types of cells (Sierra et al., 2019). Hortega, whose seminal observation inaugurated what would later become the very dynamic field of microglial biology, hypothesised that microglia would act "as a voracious macrophage" and that they would "gather and degrade" neuronal processes and dying cells during development (del Río-Hortega, 1919). It was only decades later that the first evidence for the role of microglia in synaptic stripping would come (Blinzinger and Kreutzberg, 1968). Currently, they are known not only as the main professional phagocyte of the brain, but also to regulate neurogenesis, inflammation, control blood-brain barrier (BBB) permeability, vasculogenesis, myelination, and synapse monitoring and pruning (Prinz et al., 2019). Early studies mainly relied on microglial cultures (Giulian and Baker, 1986), where gene

expression is drastically changed and cells often fail to develop the complex process ramification and surveillance seen in microglia *in situ* (Bohlen et al., 2017). However, technical advances allowing the application of patch-clamping and imaging *in situ* and *in vivo* have unveiled unique aspects of microglial behaviour in recent years, including their dynamic, never-resting nature (Davalos et al., 2005; Nimmerjahn et al., 2005). New tools have also allowed development of microglia-containing organoid models (Ormel et al., 2018), studying the microglial genetic and epigenetic landscape in humans (Gosselin et al., 2017) and defining their disease-associated signatures (Keren-Shaul et al., 2017).

1.1.2 The resident immune cells of the central nervous system

Microglia alone account for 5 to 12% of brain cells, at a density varying between brain regions but particularly high in the hippocampus and substantia nigra (Lawson et al., 1990). With the exception of perivascular macrophages, microglia are the only immune cells that are present inside the CNS parenchyma physiologically. They derive from progenitors from the yolk sac that colonise the CNS through the vasculature before the closure of the BBB (around embryonic day 9 in mice and gestational week 4–5 in humans, thus preceding gliogenesis of astrocytes and oligodendrocytes; reviewed by Thion and Garel, 2017). The microglial population is kept stable by self-renewal throughout life, and indeed turns over several times during a lifetime in the rodent and human brain (Askew et al., 2017). Microglia progressively form a regular array throughout the brain and, as cells proliferate and migrate, they also ramify into more complex morphologies (Anderson et al., 2019).

Microglial processes are constantly moving to survey the brain, sense extracellular cues including signals of brain function (such as neurotransmitters and neuromodulators; Albertini et al., 2020), and extend to regions of damage in a directed manner (Davalos et al., 2005; Nimmerjahn et al., 2005). When processes arrive at such targets, they engulf and phagocytose invading organisms, cellular debris, dying cells or synapses, and participate in immune responses via release of reactive oxygen species (ROS, which damage pathogens), as well as cytokines and chemokines (which can alter neuronal and glial cell function).

Many of these functions are shaped by ion channels and cell surface receptors, as reviewed in Izquierdo et al. (2019) and summarised below. While mechanisms such as changes in gene expression operate on a timescale of hours, ion channels can change the cells' membrane voltage instantaneously, thus allowing microglial cells to rapidly adapt their behaviour in response to acute stimuli. Moreover, because of the very high membrane resistance of microglia, modulating the function of just a few ion channel molecules could suffice to alter their membrane potential and associated functions. In the following sections, I will explain how different aspects of microglial physiology are regulated, and then focus on their involvement in Alzheimer's Disease.

1.1.3 Control of microglial resting potential

Ion channels set the cell resting potential, which powers many other cellular processes (Figure 1.1). Microglia *in situ* exhibit a depolarised membrane potential (V_m) typically around -45 mV (Guneykaya et al., 2018; Madry et al., 2018; Wendt et al., 2017), although it ranges from -20 mV to -60 mV depending on species, brain region, sex and age (De Biase et al., 2017; Guneykaya et al., 2018; Schilling and Eder, 2015).

For microglia *in situ*, two-pore domain halothane-inhibited K^+ channel type 1 (THIK-1) K^+ channels maintain a negative V_m under physiological conditions (Madry et al., 2018). THIK-1 is not expressed by microglia in culture (Butovsky et al., 2014), where only Cl^- channels contribute to setting the resting V_m (Newell and Schlichter, 2005), showing how profoundly cultured microglia differ from their counterparts embedded in brain tissue.

Besides THIK-1, ion channel candidates for regulating the V_m of microglial cells include volume-regulated Cl^- channels or transient receptor potential (TRP) cation channels (Jiang et al., 2003; Kim et al., 2006; Newell and Schlichter, 2005), which have been documented in microglia *in situ* (Hines et al., 2009; Murana et al., 2017; Schilling and Eder, 2009; Zhang et al., 2014). Finally, voltage-gated, Ca^{2+}-gated and inwardly-rectifying K^+ channels may regulate microglial V_m. Although these are only weakly expressed by microglia *in situ* under healthy conditions, both $K_{ir}2.1$ and $K_v1.3$ are upregulated when microglia

become activated with age and in pathology (Avignone et al., 2015; Plescher et al., 2018; Schilling and Eder, 2015; Wendt et al., 2017).

1.1.4 Baseline process surveillance

Microglia are territorial cells and their ramified processes have non-overlapping territories when not responding to damage or disease (Jinno et al., 2007). In fact, microglia are more compact in species where they are more abundant (such as zebrafish or leech; Geirsdottir et al., 2019). However, processes are highly motile, continuously extending and retracting at ~2 µm/min which allows them to collectively survey the brain parenchyma every few hours (Davalos et al., 2005; Nimmerjahn et al., 2005).

Microglial ramification and surveillance depend on the resting potential, and hence on the tonic activity of THIK-1 channels (Madry et al., 2018). More ramified microglial cells exhibit a more hyperpolarised resting potential than less ramified cells (De Biase et al., 2017). Conversely, depolarisation of microglia, either by pharmacological blockade or genetic deletion of THIK-1 or by raising extracellular $[K^+]$, decreases microglial ramification and surveillance (Madry et al., 2018). Therefore, pathological rises of $[K^+]_o$, or downregulation of THIK-1 with ageing (Olah et al., 2018) or when microglia become activated in disease (Holtman et al., 2015; Krasemann et al., 2017), are expected to decrease microglial surveillance and events that depend on it. Although extracellular ATP and ADP can act via $P2Y_{12}$ receptors to potentiate THIK-1 activity, these channels are tonically active and maintenance of THIK-1-mediated surveillance is independent of purinergic signalling (Madry et al., 2018). Instead, the dominant effect of locally released ATP is to attract microglial processes towards the source (see section 1.1.5).

Microglial ramification and surveillance may also be modulated by cyclic AMP (cAMP). Under healthy conditions favouring microglial ramification and surveillance, [cAMP] is kept low via G_i-coupled receptor signalling (e.g. $P2Y_{12}$ or CX3CR1), whereas microglial activation is characterised by downregulation of G_i-coupled $P2Y_{12}$ receptors and upregulation of G_s-coupled adenosine A_{2A} receptors (Haynes et al., 2006; Orr et al., 2009).

Manipulations to raise [cAMP] reduce the ramification of large processes (Kalla et al., 2003; Pagani et al., 2015), although cAMP increases the growth of thin filopodia that extend from the main processes (Bernier et al., 2019).

Furthermore, microglial surveillance is promoted by tyrosine kinase receptors, which regulate microglial motility *in vitro* (Nolte et al., 1997), while microglial-specific deletion of the TAM tyrosine kinase subtypes Mer and Axl decreased microglial surveillance *in vivo* (Fourgeaud et al., 2016). Although the underlying mechanism remains elusive, tyrosine kinase receptors may affect two-pore domain K^+ channels, including THIK-1, which is more active upon tyrosine phosphorylation (Gierten et al., 2008). A summary of the ion channels and receptors controlling microglial surveillance is shown in Figure 1.1.

1.1.5 Targeted process motility to damaged areas

Microglia sense neuronal state and are the first line of defense in brain injury and pathologies. They rapidly send out processes to ensheath injured areas, thereby confining the damage (Davalos et al., 2005). This process, also known as chemotaxis, is regulated by ion channels and G protein-coupled receptors (GPCRs) and, unlike for surveillance, purinergic signalling plays an important role (Figure 1.2).

A rise of extracellular [ATP], caused by brain damage or neuronal hyperactivity, can be detected by receptors activated by ATP itself ($P2X_4$, $P2X_7$) or its byproducts ADP ($P2Y_{12}$) and adenosine (A_1, A_{2A}, A_3) generated by ectonucleotidase-mediated hydrolysis of ATP (Madry and Attwell, 2015). ADP is a high-affinity agonist of $P2Y_{12}$ receptors, the activation of which triggers chemotaxis (Haynes et al., 2006) and promotes interactions with the extracellular matrix by activating β-integrins, particularly at the bulbous endings of chemotactic processes (Ohsawa et al., 2010). Interestingly, while $P2Y_{12}$ activation triggers protrusion of large processes, it collapses filopodia (fine processes that allow fast sensing of the microenvironment), the formation of which is instead promoted by cAMP (Bernier et al., 2019).

Chemotaxis is also promoted by the TAM receptor tyrosine kinases Mer and Axl (Fourgeaud et al., 2016) and by the triggering receptor expressed on myeloid cells 2 (TREM2; Mazaheri et al., 2017). G_q-coupled 5-HT_{2B} serotonin receptors (Kolodziejczak et al., 2015) and G_i-coupled CX3CR1 fractalkine receptors (Pagani et al., 2015) can also attract microglial processes. Indeed, inhibiting G_i completely blocks chemotaxis (Merlini et al., 2021), while lack of $P2Y_{12}$ only delays it (Haynes et al., 2006), which suggests that other GPCRs contribute to G_i-mediated chemotaxis in the absence of $P2Y_{12}$. Although the serotonin-evoked chemotactic response resembles that evoked by ATP, deletion of 5-HT_{2B} receptors did not attenuate ATP-induced chemotaxis (Kolodziejczak et al., 2015), suggesting that the purinergic and serotonergic systems may operate independently. By contrast, noradrenaline inhibits injury- and ATP-triggered motility by activating G_s-coupled β_2 receptors (Gyoneva and Traynelis, 2013). Thus, while G_i- and G_q-coupled signalling promote process extension, G_s-coupled signalling mediates process retraction.

Of note, microglial chemotaxis to an ATP source depends on volume-sensitive Cl^- channels, which are activated during osmotic stress and membrane stretch (Hines et al., 2009), presumably because net water movement across the cell membrane, driven by ion fluxes, is needed for microglial processes to change shape as they move between cell structures. In brain slices, activation of microglial Cl^- channels requires a rise of $[Ca^{2+}]_i$ (Murana et al., 2017), as can be evoked via P2Y receptors (Eichhoff et al., 2011; Pozner et al., 2015). Cl^- channels may also mediate ATP release (Mitchell et al., 1998), thus establishing a feedforward loop to activate $P2Y_{12}$ receptors and Cl^- channel activity.

1.1.6 Regulation of phagocytosis

Phagocytosis is a finely controlled process that commences with microglial membrane wrapping around the substrate (Figure 1.3A) and by which microglia can phagocytose multiple targets, including bacteria, synapses and protein aggregates (Figure 1.3B). These cells even phagocytose newborn cells in developing (Cunningham et al., 2013) and juvenile (VanRyzin et al., 2019) animals, and in adults, where microglial

phagocytosis of apoptotic neuronal progenitors maintains neurogenesis (Diaz-Aparicio et al., 2020). On the other hand, decreased microglial phagocytosis of synapses is associated with delayed pruning in development (Paolicelli et al., 2011) and impaired connectivity between the hippocampus and the cortex in the adult brain (Zhan et al., 2014). Synapse engulfment by microglia is regulated by the complement system, which seems to predominate in the visual system (Schafer et al., 2012; Stevens et al., 2007) and the fractalkine receptor CX3CR1, which prevails in the cortex and hippocampus (Gunner et al., 2019; Paolicelli et al., 2011; Weinhard et al., 2018) — although even in these regions and despite contradictory reports (Welsh et al., 2020) complement may also contribute to the removal of weaker synapses in adults (Wang et al., 2020a) or in disease contexts (Hong et al., 2016a; Vasek et al., 2016).

Phagocytosis follows three conceptual stages: “find-me”, “eat-me” and “digest-me”. Released molecules such as ATP or CX3CL1 act as attractive “find-me” signals, while “eat-me” signals include phosphatidylserine (PtdSer), which becomes exposed on the surface of damaged membranes and allows recognition and removal of apoptotic cells (Scott-Hewitt et al., 2020) or synapses (Györffy et al., 2018). Microglial PtdSer-binding receptors include TREM2 and TAM receptors (Tyro3, Axl and Mer), and PtdSer can bind them directly or indirectly via opsonins (e.g. apolipoprotein E (APOE), complement C1q; Butler et al., 2021; Raiders et al., 2021). The function and regulation of TREM2 will be reviewed in section 1.2.4. “Eat-me” signals can also be soluble, like released UDP, which triggers phagocytosis by acting on microglial $P2Y_6$ receptors (Koizumi et al., 2007).

By contrast, “don’t-eat-me” signals prevent phagocytosis. These include CD47 on neuronal membranes, which binds signal-regulatory protein α (SIRPα) receptors on microglia such that CD47-tagged synapses are protected from removal during development (Lehrman et al., 2018). Sialylation (i.e., addition of a terminal sialic acid residue) to neuronal glycoproteins and lipids also inhibits phagocytosis, as it prevents the binding of complement opsonins and activates sialic acid-binding immunoglobulin-type lectin (Siglec) receptors on microglia, which inhibit phagocytosis (Puigdellívol et al., 2020). Additionally, because

phagocytosis relies on close-proximity interaction with membrane receptors, it can be impeded by physical barriers such as the glycocalyx surrounding the cell membrane (Imbert et al., 2021).

Following internalisation of the phagocytic cups, they transform into phagolysosomes which progressively fuse and acidify to degrade their contents and recycle their components ("digest-me"). The processing and digestion of phagocytosed material are less understood. However, it has been proposed that phagosomes deliver their cargo by fusing with a receiving compartment (or "gastrosome"), a unique vesicle type that, unlike phagosomes, is not transient but homeostatically maintains a certain size (Villani et al., 2019).

The phagocytic process depends on cytoskeletal rearrangements controlled by $[Ca^{2+}]_i$, which acts as a second messenger underlying responses to various stimuli (Melendez and Tay, 2008). While "resting" microglia rarely exhibit spontaneous Ca^{2+} transients *in vivo*, damage to nearby neurons rapidly raises their $[Ca^{2+}]_i$ (Pozner et al., 2015). Microglial $[Ca^{2+}]_i$ is also elevated in ageing (Del Moral et al., 2019), neurodegeneration (Brawek et al., 2014), inflammation (Riester et al., 2020) or in response to changes in neuronal activity (Umpierre et al., 2020). $[Ca^{2+}]_i$ rises are mainly via G_q-coupled UDP-mediated $P2Y_6$ receptor signalling (Eichhoff et al., 2011; Pozner et al., 2015), but ATP-evoked entry of extracellular Ca^{2+} via ionotropic $P2X_4$ and $P2X_7$ channels, as well as ADP-mediated activation of G_q-coupled $P2Y_1$ receptors, may also contribute (although the latter are rarely expressed by microglia; Umpierre and Wu, 2020).

$P2Y_6$ receptor activation raises $[Ca^{2+}]_i$ and triggers phagocytosis by G_q-mediated activation of phospholipase C (PLC), which generates 1,4,5-inositol-trisphosphate (IP_3) and downstream IP_3 receptor-dependent Ca^{2+} release from internal stores (Koizumi et al., 2007; Neher et al., 2014). $P2Y_6$ expression is upregulated upon damage, and contributes to phagocytic removal of debris by microglia (Wen et al., 2020). Release of intracellular Ca^{2+} may trigger subsequent capacitative Ca^{2+} influx through store-operated Ca^{2+} entry (SOCE). SOCE is mediated by the opening of Orai Ca^{2+} channels on the plasma membrane upon interaction with stromal interaction molecule (STIM), a Ca^{2+}-depletion sensor on the

endoplasmic reticulum (Prakriya et al., 2006). Both proteins are present in cultured microglia (Michaelis et al., 2015), and microglia have the highest mRNA expression of *Orai1* in the brain (Zhang et al., 2014). The latter is particularly enriched in podosomes, highly dynamic actin-rich subcellular microglial structures that interact with the extracellular matrix (Siddiqui et al., 2012). Knockdown of *Stim1* or *Orai1* prevents microglia from exhibiting UDP-evoked $[Ca^{2+}]_i$ elevations, and inhibits their phagocytic activity *in vitro* (Heo et al., 2015; Michaelis et al., 2015). Thus, SOCE may support $[Ca^{2+}]_i$ rises mediating $P2Y_6$-dependent phagocytosis, possibly by creating Ca^{2+} hotspots near phagosomes (as in neutrophils; Nunes et al., 2012).

Phagocytosis in immune cells is accompanied by a sustained hyperpolarisation (Kouri et al., 1980). This could serve to facilitate SOCE by maintaining sufficient driving force for Ca^{2+} entry, and may be mediated by the upregulation of $K_{ir}2.1$ or $K_v3.1$ K^+ channels (Franciosi et al., 2006). Interestingly, TREM2 deficiency leads to downregulation of various K^+ channels and impaired microglial phagocytosis (Wang et al., 2015; Zhao et al., 2018), suggesting that control of phagocytosis by TREM2 may be, at least in part, mediated by regulation of the membrane potential. Some of the ion channels and receptors that regulate phagocytosis by microglia are shown in Figure 1.3C.

1.1.7 Regulation of reactive oxygen species release

Production of superoxide by the NADPH oxidase (NOX) complex is required for phagocytes to efficiently destroy pathogens, in what is known as a “respiratory burst” of ROS generation (Thomas, 2017). ROS are produced upon exposure to disease-/pathogen-associated molecular patterns (DAMP/PAMPs; Della Bianca et al., 1999), mainly by NOX2 in microglia (Zhang et al., 2014). NOX2 is composed of two membrane catalytic subunits ($gp91^{phox}$ and $p22^{phox}$) and three regulatory cytosolic subunits ($p40^{phox}$, $p47^{phox}$ and $p67^{phox}$). NOX activity is regulated via the latter, which translocate to the membrane and assemble upon phosphorylation. Once the complex is assembled, the enzyme oxidises NADPH molecules to $NADP^+$ and H^+ and extrudes an electron across the cell membrane. This electron then reacts with oxygen to generate highly reactive superoxide ($O_2^{\cdot -}$) radicals which

contribute to bacterial lysis (Nayernia et al., 2014; Thomas, 2017). Additionally, different ROS species may act synergistically (e.g. $O_2^{\cdot -}$ and NO react to form highly reactive $ONOO^-$, which increases neuronal death *in vitro*; Mander and Brown, 2005). However, microglia also express antioxidants and enzymes like NAD(P)H-quinone oxidoreductase 1 (NQO1, also known as NAD(P)H dehydrogenase 1) or glutathione-S-transferases (GST), which function to limit oxidative stress and inflammation (Simpson and Oliver, 2020).

Electron pumping into the phagosome and H^+ release into the cytoplasm by NOX cause depolarisation and intracellular acidification, respectively. These would readily inhibit NOX activity (DeCoursey et al., 2003), so a charge compensation and H^+ removal mechanism may be required for sustained bacterial killing. H_v1 H^+ channels, which generate a hyperpolarising H^+ efflux when activated by the depolarisation accompanying electron extrusion, were shown to provide such a mechanism in blood immune cells (Femling et al., 2006). H_v1-deficient mice lacked voltage-gated H^+ currents in leukocytes and showed an impaired respiratory burst and decreased bacterial clearance (Ramsey et al., 2009). In the brain, microglia are the only cells expressing H_v1 channels at the mRNA (Zhang et al., 2014) and protein level (Okochi et al., 2009), although the significance of these currents is uncertain due to inter-species differences (De Simoni et al., 2008; Wu et al., 2012). In the absence of H_v1, other channels may contribute to charge compensation, such as small conductance Ca^{2+}-activated K^+ channels SK2/SK4, $K_v1.3$ K^+ or TRPV1 channels, which are involved in ROS production *in vitro* (Khanna et al., 2001; Schilling and Eder, 2011). A summary of the channels and enzymes regulating the generation of ROS is shown in Figure 1.3.

1.1.8 Regulation of activation state and cytokine release

It is now clear that the old binary view of microglial activation (i.e., into a pro-inflammatory M1 state or an anti-inflammatory M2 state) was overly simplified. Instead, microglia exist in a spectrum of activation states, with different stimuli shifting microglia toward particular protein expression profiles (Ransohoff, 2016). Microglial activation is

controlled by transcriptional switches induced by receptors such as TREM2 (Krasemann et al., 2017). For instance, microglia activated by amyloid beta (Aβ) upregulate immune response genes (Yin et al., 2017) and show altered purinergic signalling and K^+ currents (Wendt et al., 2017). Damaging effects of Aβ (Maezawa et al., 2018) and lipopolysaccharide (LPS; De Simoni et al., 2008) may also depend on $K_v1.3$ channels.

For inflammation to occur, K^+ efflux via THIK-1 and voltage-gated K^+ channels is required to trigger NLRP3 (NOD-like receptor family, pyrin domain containing 3) inflammasome-mediated release of pro-inflammatory cytokines by microglia. NLRP3 function develops in two stages: First, a priming signal (e.g. LPS or cytokines) is required for NFκB-mediated transcriptional upregulation of NLRP3 and IL-1β. Second, an activating signal triggers inflammasome assembly and activation, whereby caspase-1 cleaves interleukin precursors to be released from the cell (Man and Kanneganti, 2015). In this process, K^+ efflux, mobilization of $[Ca^{2+}]_i$ and decrease of [cAMP] have been identified as crucial checkpoints for NLRP3 assembly and activation in macrophages (Lee et al., 2012; Muñoz-Planillo et al., 2013). In LPS-primed microglia stimulated with ATP, activation of the $P2Y_{12}$-THIK-1 pathway was required for release of IL-1β *in situ* (Madry et al., 2018), consistent with a K^+ efflux-triggered mechanism. Depending on the cells' activation state, K_v channel activation may also provide the K^+ efflux needed for inflammasome activation (Di Lucente et al., 2018; Rangaraju et al., 2017). As THIK-1 channels are tonically active, they could act as an initial trigger for increased K^+ loss and inflammasome assembly, with upregulation of $K_v1.3$ following later.

Lastly, production of inflammatory mediators may require long-lasting elevations of $[Ca^{2+}]$, which occur *in vitro* in microglia and macrophages upon LPS treatment (Korvers et al., 2016). LPS induces microglial upregulation of $P2X_7$ channels (Choi et al., 2007), which mediate both K^+ efflux and Ca^{2+} entry when activated by high extracellular [ATP] and are involved in cytokine release *in vitro* (Choi et al., 2007; He et al., 2017). However, this may primarily be mediated by K^+ efflux, given that in macrophages K^+ efflux alone is sufficient to activate the NLRP3 inflammasome (Katsnelson et al., 2015). Finally, ATP release via gap

junctional hemichannels may contribute to inflammasome activation via $P2X_7$ (Parzych et al., 2017) and thus exacerbate inflammation. The ion channels and receptors regulating microglial cytokine release are shown in Figure 1.4.

1.2 Immune function in Alzheimer's Disease

1.2.1 The most common dementia

Alzheimer's Disease (AD) is the most common form of dementia, accounting for 60-70% of cases, often overlapping with Lewy-body disease, vascular dementia or frontotemporal dementia in older individuals (Alzheimer's Association, 2020). AD is a chronic neurodegenerative disorder that affects millions of people worldwide, but for which no effective disease-modifying therapies exist to date. More than 90% of cases have an onset above 65 years of age (late-onset AD, LOAD), while the remaining are early-onset AD (EOAD) cases, which typically also present a more rapid progression (Long and Holtzman, 2019).

In the AD brain, the two major hallmarks are extracellular deposition of Aβ plaques (also known as neuritic or senile plaques) and intracellular accumulation of neurofibrillary tangles in neurons, generated by aggregation of hyperphosphorylated microtubule-associated protein tau. Clinically measurable deficits, however, only emerge years or decades after these histopathological changes, when tissue damage is already profound (Harris et al., 2020). In a study with postmortem human brains, the levels of prion-like Aβ and tau conformers inversely correlated with age at death (i.e., they were higher in the subjects that died at a younger age; Aoyagi et al., 2019).

Although both Aβ and tau aggregate, spread and impair neuronal function in the brain, they also present clear differences. Tauopathy correlates better with cognitive decline than Aβ pathology does (Nelson et al., 2012), but accumulation of Aβ plaques precedes that of tau (Hanseeuw et al., 2019) and Aβ may act upstream in the pathogenic cascade. In fact,

Aβ dimers can induce hyperphosphorylation of tau (Jin et al., 2011), possibly by preventing inactivation of tau kinases like GSK3β (Hernández et al., 2010) or by activating the NLRP3 inflammasome (Halle et al., 2008), which can drive tauopathy (Ising et al., 2019). It has been proposed that, as Aβ load increases and Aβ-mediated tau hyperphosphorylation occurs, damage spreads leading to neurodegeneration and network disruption (Edwards, 2019).

However, Aβ also has direct toxic effects. For instance, because Aβ is highly hydrophobic, it can disrupt membranes (Flagmeier et al., 2020), perhaps by oligomers forming membrane pores (Ciudad et al., 2020). In fact, Aβ can pierce the cell membrane at synaptic sites (Capetillo-Zarate et al., 2011). Furthermore, Aβ-evoked constriction of capillary pericytes reduces cerebral blood flow (CBF), triggering a positive feedback loop whereby hypoxia may further increase Aβ production (Nortley et al., 2019). In turn, brain hypoperfusion can lead to tau hyperphosphorylation, either directly (Qiu et al., 2016) or by increasing levels of Aβ (Jin et al., 2011). CBF reduction can be caused by pericyte constriction of capillaries (Nortley et al., 2019) or neutrophil stalling (El Amki et al., 2020; which might be a consequence of the vasoconstriction). Of note, microglia also play a role in controlling CBF (Császár et al., 2021) and vascular integrity (Haruwaka et al., 2019), while vascular leakage promotes microglia-mediated synapse loss (Merlini et al., 2019).

Vascular dysfunction and neuroinflammation form part of the proposed “cellular phase” of AD, whereby the slow, progressive accumulation of classical histological markers (tau and Aβ) only manifests clinically once cellular homeostatic mechanisms have failed (De Strooper and Karran, 2016). This thesis will focus on how microglial function interacts with the amyloid component of AD (which can activate immune function alone; Matarin et al., 2015).

1.2.2 Processing of amyloid beta

Amyloid precursor protein (APP) is produced by neurons and is subject to alternate processing pathways. Once inserted into neuronal membranes, APP can be proteolytically cleaved by α-secretase and then γ-secretase (or by η-secretase followed by α- or β-

secretase), which does not generate Aβ. Alternatively, APP can be cleaved by β-secretase (BACE1) and then γ-secretase, which does generate Aβ that can be released to the extracellular space. Cleavage by γ-secretase via this route can occur at different residues of the C-terminal fragment generated by β-secretase, thus generating a range of Aβ peptides of which the most common contain 40 ($A\beta_{1-40}$) and 42 ($A\beta_{1-42}$) residues (Haass et al., 2012; O'Brien and Wong, 2011). These peptides (and particularly the more hydrophobic $A\beta_{1-42}$) are prone to aggregate into oligomers and fibrils and eventually deposit in the extracellular space, where they constitute the main component of senile plaques (Masters et al., 1985). As a result of this two-step process, the different pathways also generate additional fragments (soluble ectodomains APPsα, APPsβ, APPsη, p3, Aη-α, Aη-β or an intracellular C-terminal peptide), the precise functions of which remain unclear (Harris et al., 2020).

In some AD patients, mutations in enzymes involved in the processing of Aβ are responsible for dysregulated production of Aβ and thus disease development. These cases due to fully penetrant mutations in *APP* and presenilin 1 or 2 genes (*PSEN1/2*, which encode the catalytic subunits of γ-secretase), correspond to only around 1 in 100 patients. By contrast, these mutations are absent in the remaining, non-familial cases (although variants affecting APP processing are also associated with LOAD; Kunkle et al., 2019).

Even in non-familial cases, AD risk has a large genetic component: up to 80% of the lifetime risk of AD is genetic, while about a third is modifiable or environmental (Sierksma et al., 2020). Numerous genes exhibit differential expression in AD but, with very few exceptions, it remains unclear which are the core genes that directly affect disease when mutated and how AD risk variants affect cellular function. Adding to this complexity, risk variants often map within non-coding regulatory regions, such as enhancers (Podleśny-Drabiniok et al., 2020). A recent meta-analysis of Genome-Wide Association Studies (GWAS) identified as many as 75 risk loci. Some of these are in amyloid-processing pathways, including APP metabolism or cleavage (e.g. *ADAM10*), clearance (e.g. *APOE* or *CLU*) and microglial removal (e.g. *APOE*, *TREM2*, *PLCG2* or *CD33*; Bellenguez et al., 2020).

1.2.3 Genetics of Alzheimer's Disease: the role of microglia

Although Hortega was the first to identify and name microglia, Alois Alzheimer (1910) had already described accumulation of glial cells around amyloid plaques in the brain. Today, strong genetic evidence implicates microglia in the development and progression of AD. Genetic studies have linked numerous loci, single-nucleotide polymorphisms (SNPs) and variants in immune-related genes to AD risk (whether they increase it, like *TREM2*, or decrease it, like *PLCG2*), which highlights the importance of microglial responses for disease development and progression, and both GWAS and proteomic studies highlight the relevance of immune responses in AD (Johnson et al., 2020; Kunkle et al., 2019; Wightman et al., 2020). Specifically, pathway analysis approaches have linked a number of phagocytosis-related genes to LOAD risk. This includes genes involved in recognition of substrates (e.g. receptor genes like *TREM2*, *CR1* or *CD33*), engulfment (e.g. *PTK2B* or *ABI3*, which regulate cytoskeletal rearrangements and F-actin dynamics) and digestion (e.g. *BIN1* or *GRN*; Podleśny-Drabiniok et al., 2020). Furthermore, genetic data suggest that AD pathology arises from interactions between different pathways. AD risk genes are highly interconnected (Zhang et al., 2013) and considering the polygenic component of risk significantly improves prediction of LOAD and of conversion to LOAD from mild cognitive impairment (Chaudhury et al., 2019; Escott-Price et al., 2015).

The *APOE* ε4 allele is the most common among high-risk variants, and can increase AD risk by affecting Aβ seeding and accumulation through regulation of microglial responses, among other mechanisms. While the ε2 isoform is relatively protective and ε3 is viewed as neutral, carrying the ε4 allele markedly increases AD risk (Long and Holtzman, 2019; Sierksma et al., 2020). Indeed, ε4 increases the association of Aβ with synapses (Koffie et al., 2012) but reduces uptake of $A\beta_{1\text{-}42}$ by microglia (unlike ε2/3; Muth et al., 2019). *APOE4* knock-in also exacerbated atrophy of the entorhinal cortex and the hippocampus in AD model mice (Shi et al., 2017b). In turn, APOE signalling can be activated by a phenotypic

switch triggered by another major gene linked to AD risk, *TREM2*, which is a major driver of microglial response (Krasemann et al., 2017).

1.2.4 TREM2: a key regulatory hub

The TREM2 receptor contains an extracellular immunoglobulin-type ligand-sensing domain, which is connected to a transmembrane domain and a short cytosolic tail (Deczkowska et al., 2020). Its ligand-sensing domain can bind a number of anionic ligands, some of which are present physiologically (like low-density lipoprotein (LDL) or APOE, mentioned above), while others gain relevance in pathology (e.g. Aβ (Zhao et al., 2018), PtdSer, or LPS and nucleic acids from bacteria (Kober and Brett, 2017)).

TREM2 lacks intracellular motifs, but interacts with obligate co-receptors DNAX activation protein 10 or 12 (DAP10/12) for transduction via tyrosine-kinase Syk or phosphatidylinositol 3-kinase (PI3K), respectively, thus activating multiple downstream pathways (Deczkowska et al., 2020). Upon ligand binding, TREM2 promotes survival of immune cells (Ulland et al., 2017; Wang et al., 2015) possibly via colony-stimulating factor 1 receptor (CSF1R) signalling, expression of which is downregulated in *Trem2* knockdown microglia (Liu et al., 2020). It also promotes chemotaxis (Mazaheri et al., 2017) and phagocytosis (Filipello et al., 2018; Lee et al., 2018; Takahashi et al., 2005; Zhao et al., 2018), but counters inflammatory responses (Liu et al., 2020). Of note, soluble TREM2 resulting from receptor cleavage shows antagonistic effects, acting via NFκB to increase proinflammatory cytokines (Zhong et al., 2017). Soluble forms of TREM2 may also arise from alternative splicing (Kiianitsa et al., 2021).

In microglia from human AD patients, *TREM2* expression is upregulated (Jolly et al., 2019; Zhou et al., 2020). By contrast, rodent experiments show that Aβ seeding (Parhizkar et al., 2019) as well as accumulation of dead cells (Griciuc et al., 2019) increase in the absence of functional TREM2, as microglial clustering and phagocytosis are reduced. In agreement with a protective role for TREM2 in AD, several loss-of-function variants of TREM2 increase the risk of LOAD, including R62H and R47H, the latter being the most

common among AD-linked variants (Guerreiro et al., 2013; Jonsson et al., 2013). Microglia are less reactive in human carriers of the R47H or R62H variants (Zhou et al., 2020). In TREM2-R47H knock-in animals, where *Trem2* expression was reduced, microglial density and expression of lysosomal markers were also decreased (Liu et al., 2020). In line with reduced TREM2 activity, single-cell transcriptomics from AD patients revealed that R47H carriers presented enhanced inflammatory signatures (Sayed et al., 2020), and pro-inflammatory conditions may further suppress TREM2 expression, perhaps exacerbating the damage (Liu et al., 2020).

Mutations in signalling pathways downstream of TREM2 are also linked to disease. For instance, the co-receptor DAP12 has been identified as a key regulator in LOAD (Zhang et al., 2013) and loss-of-function variants of it cause Nasu-Hakola disease, a rare form of early-onset dementia (Paloneva et al., 2002). By contrast, a variant of PLCγ2, activated by TREM2 signalling, decreases the risk of AD by promoting protective TREM2-associated functions (Maguire et al., 2020; Takalo et al., 2020).

Overall, AD-linked variants of TREM2 are thought to increase risk by impairing its binding to ligands and thus its anti-inflammatory activity (Kober et al., 2016). Of note, TREM2 acts as a lipid sensor (Nugent et al., 2020; Wang et al., 2015) and the R47H mutation impairs binding of lipid ligands (Wang et al., 2015). In fact, defective lipid metabolism and handling is increasingly viewed as a driver of AD pathogenesis. In line with this notion, the detrimental effect of *APOE4* may be due to its poor lipidation, which compromises substrate recognition and phagocytosis (Hu et al., 2015). Cholesterol, when accumulated in lysosomes rather than delivered to neurons by apolipoproteins, promotes Aβ and tau pathology (Yup et al., 2021).

1.2.5 Evolution of microglial response in space and time

Together with the work studying dissociated microglia discussed in section 1.2.3, single-cell transcriptomics have been critical in allowing identification in rodents of unique microglial phenotypes which vary across space and time. Disease-associated microglia

(DAM) are characterised by upregulation of some genes (e.g. *Apoe* and *Trem2*, which act as response drivers; Krasemann et al., 2017) and downregulation of others (e.g. *P2ry12* or *Tmem119*, which preserve homeostasis; Keren-Shaul et al., 2017). Of note, DAM-equivalent clusters have not been identified in humans (Alsema et al., 2020), although some report significant changes between AD and non-AD microglia, and distinct microglial subpopulations have been detected (Mathys et al., 2019; Srinivasan et al., 2020).

Because the response to Aβ is highly localised, it is important to analyse changes *in situ* rather than in isolated cells: in the AD context, synapse levels change only in proximity to Aβ plaques (Koffie et al., 2009, 2012), where microglia suffer dramatic changes in gene expression (Chen et al., 2020), morphology and electrophysiological properties (Plescher et al., 2018; Wendt et al., 2017). By contrast, in regions distant from Aβ plaques, all the above remain largely unaffected. Additionally, spatial transcriptomics have revealed crosstalk between microglia, astrocytes and other cells and suggested multicellular coordination in the response to Aβ (Chen et al., 2020).

Importantly, the response of the cellular network builds up with exposure to Aβ, such that the levels of expression of different genes are more strongly correlated in regions with a higher Aβ burden (Chen et al., 2020). Microglial involvement in the disease may vary across disease stages. For instance, while these cells can cluster around Aβ plaques and contribute to removal of synapses, early changes in microglia might have a protective role, as anti-inflammatory protein markers are highly expressed in asymptomatic patients (Johnson et al., 2020). Therefore, a better knowledge of the mechanisms involved in key cellular processes, but also of their contribution at different disease stages, is required to improve prevention or treatment for AD, a complex multifactorial disease.

1.3 Aims of this thesis

1.3.1 To investigate the regulation of microglial process ramification and motility *in situ* in brain slices

Microglial morphology is crucial for their function. In particular, their ramified processes are essential for their continuous surveillance of the CNS. Whilst it has been shown that surveillance of microglial processes is regulated by THIK-1 channels, and that AD-linked TREM2 receptors control microglial responses in various contexts, it has never been tested whether these receptors control process motility or whether any functional interaction exists with THIK-1.

Experiments in this thesis investigate how microglial surveillance varies with age in acute living slices and whether it is affected by THIK-1 and TREM2. I also test whether the effect on surveillance of a short-term block of THIK-1 depends on whether TREM2 is expressed or not. For this and the following aims, I study microglial cells *in situ* in brain slices, where local cues and structures are relatively undisturbed. This work is described in Chapter 3.

1.3.2 To investigate a possible role for THIK-1 in controlling microglial phagocytosis

THIK-1 channels regulate a range of microglial behaviours, including their process movement and cytokine release upon stimulation with damage signals. However, their possible role in phagocytosis remains unexplored. Therefore, to examine a potential involvement of these channels in synaptic pruning, I first establish whether phagocytosis of labelled synthetic probes is affected by THIK-1 deficiency, and then examine synapse levels and function in THIK-1-deficient mice. To maximise clinical relevance, I also use living human brain slices from neurosurgery-derived brain tissue to study the effects of acute THIK-1 block on microglia and synapses. This work is described in Chapter 4.

1.3.3 To investigate microglial responses in *App*$^{NL-G-F}$ mice and the role of THIK-1

There is robust evidence indicating that microglial responses are associated with the development and progression of AD. I study microglial morphology and function in an animal model for AD, the *App*$^{NL-G-F}$ knock-in mouse. I also address whether microglial responses in this model are affected by THIK-1 expression.

Additionally, given that microglia do not work in isolation, I explore contributions of other glial cells to processes in which microglia take part. Specifically, I examine generation of ROS in microglia and pericytes upon exposure to Aβ oligomers, and phagocytosis of a fluorogenic Aβ probe in microglia and astrocytes. This work is described in Chapter 5.

1.3.4 To investigate the regulation of microglial Ca^{2+} signalling in health and disease

Ca^{2+} levels are commonly used as a proxy of cellular activity in neurons and astrocytes, but research on microglial Ca^{2+} signalling is relatively recent. As such, many questions remain as to how microglial $[Ca^{2+}]_i$ rises are controlled, whether they originate from extracellular influx or store-mediated release, and how Ca^{2+} signalling changes in disease states. Experiments in this thesis investigate microglial Ca^{2+} signalling in brain slices from healthy and Aβ-depositing mice that express a genetically-encoded Ca^{2+} indicator. I examine differences across cell compartments as well as possible effects of applying noradrenaline or of blocking THIK-1 channels or ROS production. This work is described in Chapter 6.

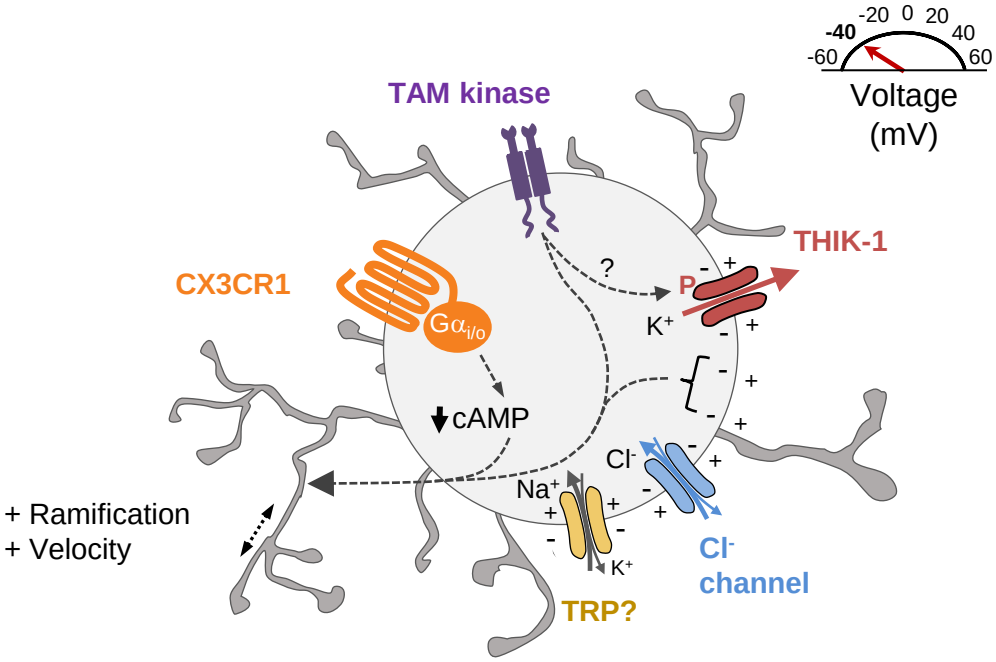

Figure 1.1. Regulation of microglial resting potential and surveillance.

A negative membrane potential (V_m) in "resting" microglia is maintained by tonically active THIK-1 K^+ channels, the activity of which is promoted by tyrosine kinase-mediated phosphorylation. Voltage-gated K^+ channels (K_v or K_{ir}) may contribute to a negative V_m in activated microglia. Cl^- channels and depolarising cation channels, such as the non-selective cation channels TRPV1 and TRPM7, may further regulate V_m and counteract a K^+ channel-evoked hyperpolarisation. A negative V_m, G_i-protein signalling-induced low [cAMP] (e.g. via CX3CR1) and tyrosine kinase activity promote microglial surveillance and ramification. Adapted from Izquierdo et al. (2019). Thin filopodia extending from the main processes, which also contribute to surveillance (Bernier et al., 2019) are not shown.

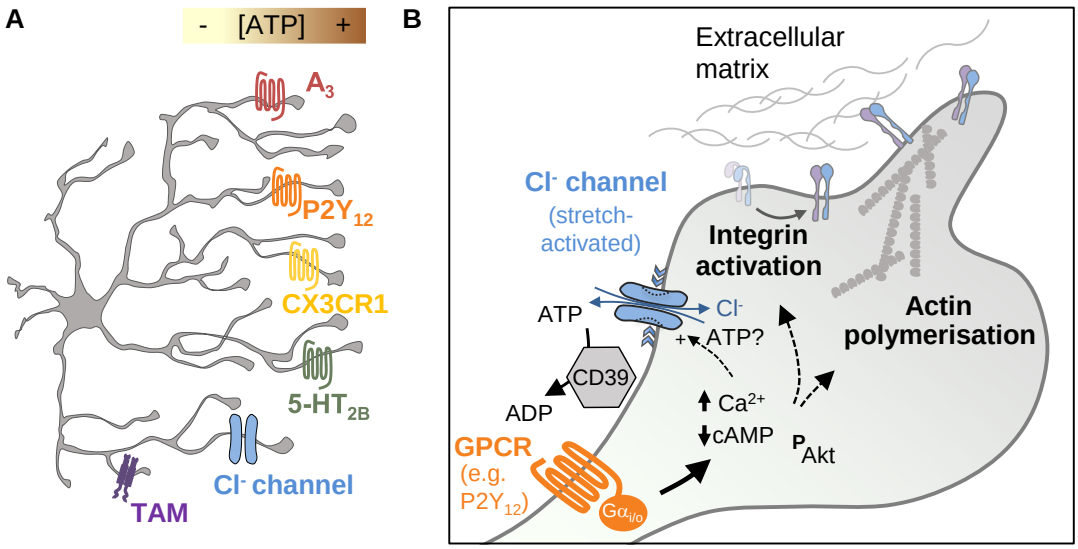

Figure 1.2. Regulation of targeted process movements.

(A) G protein-coupled receptor signalling mediated by adenosine A_3, $P2Y_{12}$, CX3CR1 and $5\text{-}HT_{2B}$ receptors, as well as TAM receptor tyrosine kinases, positively regulate targeted movements of microglial processes towards focal brain injury. Process outgrowth along an [ATP] gradient (shown at the top) mediated by $P2Y_{12}$ receptors is shown as an example. Ion channel activity via volume- and membrane stretch-activated Cl^- channels is also required to allow chemotaxis. **(B)** Close-up of a microglial growth cone as it extends to reach its target. Signalling cascades involving a decrease of [cAMP], phosphorylation of Akt kinase and a rise of $[Ca^{2+}]_i$ trigger the activation of integrin receptors, which promote interactions of microglial processes with the extracellular matrix. Cl^- channels may also release ATP to sustain local $P2Y_{12}$-receptor activation (by ADP generated by the ectonucleoside triphosphate diphosphohydrolase CD39) as a key driver of targeted motility. $P2Y_{12}$-mediated activation of THIK-1 is not needed for targeted process movements. Adapted from Izquierdo et al. (2019).

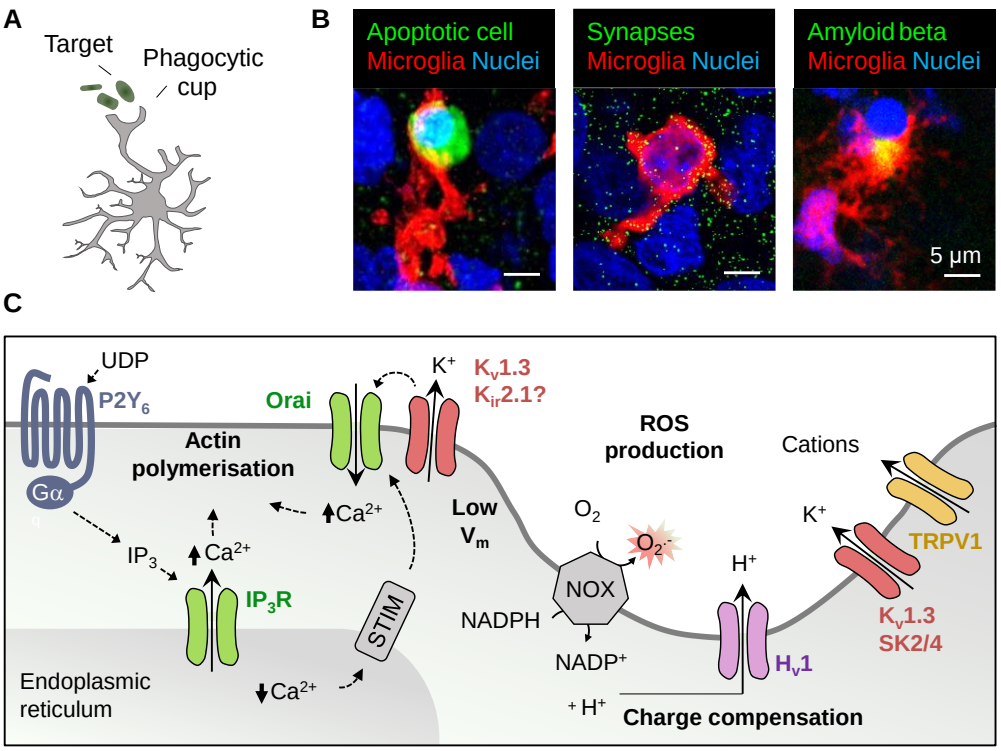

Figure 1.3. Regulation of phagocytosis and ROS production.

(A) Phagocytosis requires cytoskeletal rearrangements (e.g. for the formation of a phagocytic cup as cells engulf their targets). **(B)** Microglia (red) can phagocytose different cargos in health and disease contexts, including apoptotic cells, synapses and Aβ aggregates (immunolabelling for cleaved caspase 3 or Bassoon and $A\beta^{pH}$ fluorescence shown in green). **(C)** Phagocytosis requires a rise in $[Ca^{2+}]_i$, which is achieved mainly by $P2Y_6$ receptors evoking Ca^{2+} release from the endoplasmic reticulum via IP_3 receptor (IP_3R) channels. *In vitro* data suggest that capacitative Ca^{2+} entry might then also occur, whereby STIM on the endoplasmic reticulum senses store Ca^{2+} depletion and interacts with Orai channels triggering their opening and further entry of extracellular Ca^{2+}. $K_v1.3$ and $K_{ir}2.1$ may contribute by providing a large driving force for Ca^{2+} influx. A "respiratory burst" occurs during phagocytosis as NADPH oxidase (NOX) extrudes electrons across the cell membrane, which react with oxygen to form superoxide ($O_2^{\cdot-}$), a form of ROS. Sustained activation of NOX requires H^+ buffering, or H^+ release and charge compensation. H_v1 H^+ channels contribute to this in mice, with other candidates suggested by *in vitro* data including $K_v1.3$, SK2/4 and TRPV1 channels. Adapted from Izquierdo et al. (2019).

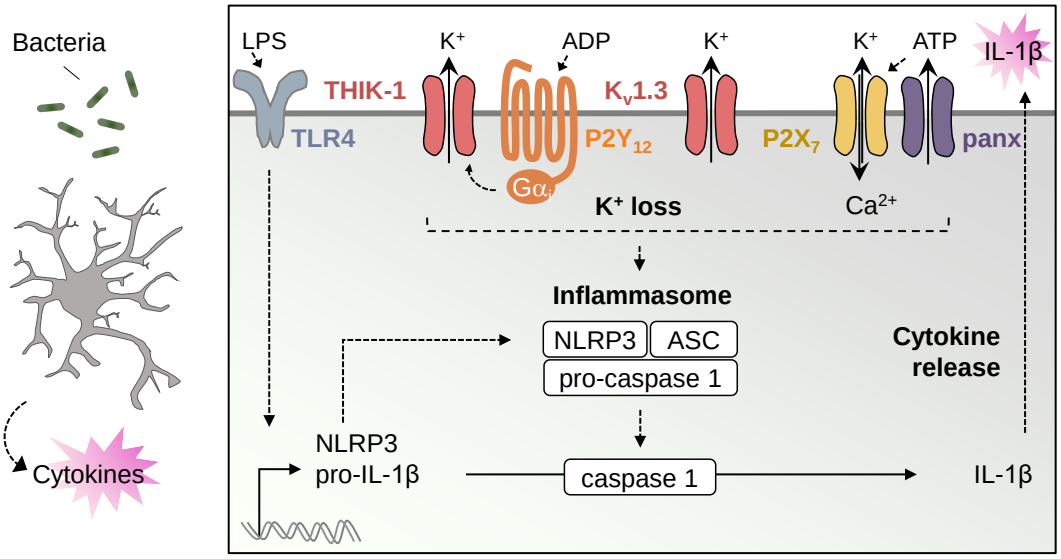

Figure 1.4. Regulation of inflammasome activation and cytokine release.

Priming of microglia (e.g. by lipopolysaccharide (LPS) on bacteria interacting with toll-like TLR4 receptors) triggers transcriptional upregulation of NLRP3. Assembly and activation of the NLRP3 inflammasome complex results in caspase 1 activation, which in turn can cleave interleukin precursors (e.g. pro-IL-1β, pro-IL-18) so that they are released from the cell as active mediators of inflammation. For inflammasome assembly to occur in microglia, K^+ loss is a crucial checkpoint. It can be achieved by activation of THIK-1 channels via ATP/ADP acting on $P2Y_{12}$ receptors, and via $K_v1.3$ channels which are upregulated in inflammation. $P2X_7$ cation channels have also been implicated, the gating of which may be promoted by ATP released via pannexin (panx) channels. Adapted from Izquierdo et al. (2019).

2. Methods

2.1 Introduction

In this Chapter, I will describe the basic resources and methods used for the experiments reported in this thesis, including specific details about experimental design and data analysis protocols.

2.2 Experimental models

2.2.1 Rodent procedures

All animal procedures were performed in accordance with the United Kingdom Animals (Scientific Procedures) Act 1986 and subject to local ethical review and procedures (Home Office License 70/8976). All rodents were born and housed in the central UCL Biological Services Unit, London. Mice were housed in individually ventilated cages (IVCs), while rats were kept in open shelf units. All rodents were maintained on a 12-hour/12-hour light/dark cycle, and food and water were available *ad libitum*. Because both environmental enrichment (Jung and Herms, 2014; Ziegler-Waldkirch et al., 2018) and circadian rhythms (Choudhury et al., 2020) can affect microglial behaviour, all cages had standardised cage enrichment (consisting of one cardboard tunnel and one chew stick per cage) and rodents were consistently sacrificed between 11 am and 3 pm. All animals were sacrificed by cervical dislocation followed by decapitation, except for experiments requiring perfusion-fixation (see section 2.4.2).

Sprague-Dawley rats were used for rat experiments. Where genetic manipulations were required for the study, mouse strains were used as described in the following sections (see sections 2.2.2–2.2.5). None of the genetic manipulations were lethal or led to gross abnormalities in the mice. All mouse strains were on a C57BL/6 background and age-

matched wildtype littermates were used as controls within each line. All mice were genotyped by polymerase chain reaction (PCR) amplification of genomic DNA extracted from ear clip biopsies and detection of amplified bands on 2% agarose gels.

2.2.2 THIK-1 knockout mice

The THIK-1 knockout (KO) line (Kcnk13-IN1-EM1-B6N) was generated by MRC Harwell as described in detail in Madry et al. (2018). Briefly, CRISPR/Cas9 was used to insert a single thymidine nucleotide into the wildtype DNA sequence for the gene encoding the THIK-1 channel protein, *Kcnk13* (Figure 2.1A). This leads to a frameshift and thus to a premature STOP codon after amino acid 68 in the open reading frame (Figure 2.1C), and also creates a restriction site for the enzyme *Taq*I (T^CGA), which can be employed as a genotyping strategy (Figure 2.1B).

While a mutant, truncated protein is still produced in the THIK-1 KO, it is of low complexity and will not form a transmembrane channel. To confirm this, I calculated hydrophobicity plots suggesting stretches of amino acids that could cross the hydrophobic lipid membrane based on the Kyte-Doolittle hydrophobicity score on a 13-residue window, using ExPASy ProtScale (https://web.expasy.org/protscale; Figure 2.1D). PSIPRED, MEMSAT-SVM (both on https://bioinf.cs.ucl.ac.uk/psipred) and Jpred4 (https://compbio.dundee.ac.uk/jpred4) were used to predict membrane helix and secondary structure of the WT and KO proteins. The THIK-1 WT protein could also be modelled by homology using ExPASy SWISS-MODEL (https://swissmodel.expasy.org) to confirm its homo-dimeric structure, similar to the resolved crystal structures of the human two-pore domain potassium ion channels K2P1 (TWIK-1, ID 3ukm.1) or TREK2 (K2P10.1, ID 4xdl.1). All these analyses confirmed a predicted truncated helix and coil structure for the THIK-1 KO protein, which is unable to form membrane-spanning domains and hence cannot form a functional channel (Figure 2.1E).

For studies on the *in vivo* effects of THIK-1 with regard to amyloid pathology, THIK-1 WT or KO animals were crossed to $App^{NL\text{-}G\text{-}F}$ animals (see section 2.2.4).

2.2.3 TREM2 knockout mice

Several TREM2 KO mouse lines have been created using different strategies. The strain used for the present study was originally generated in Marco Colonna's lab in Washington University in St Louis. Here, the targeting construct was designed to delete a portion of the transmembrane and intracellular domains of the receptor, encoded by exons 3 and 4 (Turnbull et al., 2006). This line does not show aberrant upregulation of *Treml1* (triggering receptor expressed on myeloid cells like 1), which is directly downstream of the 3' end of *Trem2* and has been found to be artifactually overexpressed in another commonly used TREM2 KO strain generated with a different targeting construct (Kang et al., 2018).

For two-photon imaging of fluorescently labelled microglia, TREM2 WT or KO animals were crossed to *Aif1*^{EGFP} transgenic animals originally generated in Shinichi Kohsaka's lab in Tokyo (Hirasawa et al., 2005). As a result, these mice express EGFP (enhanced green fluorescent protein) under the control of the *Aif1* promoter, which encodes the ionised calcium-binding adaptor molecule 1 (Iba1) and drives transgene expression in microglia/macrophages (Ito et al., 1998).

2.2.4 *App*$^{NL-G-F}$ knock-in mice

To study plaque coverage and microglial internalisation of Aβ in the presence and absence of THIK-1, THIK-1 KO were crossed with *App*$^{NL-G-F}$ knock-in mice developed by Takaomi Saido's group in Japan.

While traditional transgenic models overexpress *App* and thus overproduce non-Aβ APP fragments, knock-in lines avoid such artefacts (Joel et al., 2018). In the *App*$^{NL-G-F}$ mouse, the APP sequence harbours a humanised Aβ region and three pathogenic mutations (Swedish, Iberian and Arctic). The Swedish mutation (KM670/671NL) raises the overall levels of $Aβ_{1-40}$ and $Aβ_{1-42}$, the Iberian/Beyreuther mutation (I716F) increases the ratio of $Aβ_{1-42}$ to $Aβ_{1-40}$, and the Arctic mutation (E693G, located in the Aβ region) accelerates aggregation of Aβ by facilitating its oligomerisation and reducing its proteolytic degradation (Saito et al., 2014).

Similar to other Aβ-based models, neurofibrillary tangles and neurodegeneration are not detected in *App*$^{NL-G-F}$ mice (Saito et al., 2014). In terms of behaviour, homozygotes display some impairment in spatial memory at 6 months of age as measured by the Y-maze test (Saito et al., 2014) but their phenotype is otherwise mild (Latif-Hernandez et al., 2019). However, they do present consistent amyloidosis with Aβ plaques developing from as early as 2 months (Saito et al., 2014) which makes this model suitable to study the initial stages of AD-related pathology. Aβ plaques were stained by immunolabelling (see section 2.8.1). For testing thioflavin-S staining, slices were submerged in 0.01% thioflavin-S (Sigma T1892) made in 50% ethanol, for 15 min and differentiated in 50% ethanol for 1 min.

2.2.5 *Cx3cr1*^{CreER} x GCaMP5g-IRES-tdTomato transgenic mice

For calcium imaging experiments, I used mice where microglia and macrophages expressed GCaMP5g (Figure 2.2A). For this, floxed GCaMP5g-IRES-tdTomato mice were crossed with tamoxifen-inducible *Cx3cr1*^{CreER} mice, both of which lines will be described below. GCaMP5g is a genetically encoded calcium indicator engineered by fusion of the circularly permutated green fluorescent protein (cpGFP), the calcium-binding protein calmodulin (CaM), and the M13 peptide. Upon binding of intracellular calcium to CaM, GCaMP5g undergoes a conformational change that increases its fluorescence at certain excitation wavelengths (Figure 2.2C; Baird et al., 1999).

The GCaMP5g-IRES-tdTomato reporter mouse strain is a Cre recombinase-inducible system developed in the group of Petr Tvrdik in Utah (Gee et al., 2014). These mice express GCaMP5g and separately a red fluorescent protein tag (tdTomato) in a bicistronic fashion, which aids identification of positive cells with low intracellular calcium levels, such as microglia. They are expressed under the control of the CAG promoter, but expression of GCaMP5g and tdTomato only occurs after Cre-mediated excision of a floxed STOP cassette, which would otherwise lead to a premature termination of transcription. Thus, by crossing these animals with mice expressing an inducible form of Cre driven by a cell type-specific promoter, we can control which cells express the reporter and make them do so in

an inducible manner, thereby avoiding potential effects of buffering calcium levels during development (Tsien et al., 1996).

For this study, these mice were crossed to a *Cx3cr1*^{CreER} mouse line developed by Steffen Jung's lab in Israel (Yona et al., 2013), where tamoxifen-inducible CreER (Cre recombinase fused to an estrogen receptor ligand-binding domain) is expressed under the control of the largely microglia/macrophage-specific fraktalkine receptor *Cx3cr1* promoter (it is also expressed in oligodendrocyte precursor cells more weakly; Zhang et al., 2014).

In the experimental *Cx3cr1*^{CreER} x GCaMP5g-IRES-tdTomato mice, which were heterozygotes for *Cx3cr1*^{CreER}, Cre recombination was induced by oral gavage of tamoxifen (120 µg/g body weight) to the adults for four consecutive days (Figure 2.2B). Tamoxifen (Sigma T5648) was prepared by dissolving it at 15 mg/ml in corn oil and incubated on a rotator overnight at room temperature. Upon tamoxifen administration, Cre-mediated recombination results in the deletion of the loxP-flanked STOP sequence and thus expression of GCaMP5g and tdTomato only where Cre is expressed (i.e., *Cx3cr1*$^{+}$ microglia, macrophages and oligodendrocyte precursor cells). Imaging was performed at least 21 days after the first tamoxifen dose.

For experiments analysing calcium levels in *App*$^{NL-G-F}$ microglia, I crossed the *Cx3cr1*^{CreER} x GCaMP5g-IRES-tdTomato mice with the *App*$^{NL-G-F}$ strain described in section 2.2.4 to generate experimental animals that were heterozygotes for *Cx3cr1*^{CreER} and either wildtype or homozygotes for *App*$^{NL-G-F}$.

2.2.6 Human biopsy tissue from neurosurgical operations

Human tissue data were obtained for this study while investigating a possible role for microglia in regulating pericyte-mediated control of cerebral blood flow by altering the number of functional synapses. Samples were kindly provided by the neurosurgeon Huma Sethi (National Hospital for Neurology and Neurosurgery, Queen Square, London) and sliced by Chanawee Hirunpattarasilp from our lab. Healthy cortical tissue overlying the tumour was taken from subjects aged 29–74 undergoing glioma resection. Ethical approval

was obtained (REC number 15/NW/0568, IRAS ID 180727 (v3.0), as approved on 9-10-2018 for extension and amendment to include cells interacting with pericytes) and all patients gave informed written consent for the removed tissue, which would otherwise have been discarded, being used for research. Only the patients' sex, age and the clinical indication for their surgery were given to us by the surgeon, with all other details remaining confidential. All tissue handling and storage were in accordance with the Human Tissue Act (2004).

2.3 Solutions and pharmacology

2.3.1 Slicing solutions

All solutions were prepared using ultrapure de-ionised water (ddH_2O; Milli-Q, Millipore) and were oxygenated with 95% O_2/5% CO_2 prior to use.

For experiments on animals younger than P12, brains were sliced in a bicarbonate-based slicing solution containing (in mM): 124 NaCl, 2.5 KCl, 26 $NaHCO_3$, 1 NaH_2PO_4, 10 glucose, 1 $CaCl_2$, 2 $MgCl_2$ and 1 kynurenic acid (to block receptors mediating effects of glutamate released during the slicing). Osmolarity was adjusted to ~295 mOsM and pH was set to 7.4 when bubbled with 5% CO_2.

For the remaining experiments, two solutions were prepared for brain slicing, and the period thereafter when slices were stored before use:

(1) A N-Methyl-D-glucamine (NMDG)-based slicing solution containing (in mM): 93 NMDG (replacing NaCl, to lower the cation entry evoked by slicing and reduce cell swelling), 2.5 KCl, 20 HEPES, 30 $NaHCO_3$, 1.2 NaH_2PO_4, 25 glucose, 0.5 $CaCl_2$ (lower than normal to reduce Ca^{2+} influx), 10 $MgCl_2$, 5 sodium ascorbate (as an antioxidant), 2.4 sodium pyruvate (as an energy source) and 1 kynurenic acid. Osmolarity was adjusted to ~300 mOsM, and pH was set to 7.4 with HCl.

(2) A storage solution containing (in mM): 92 NaCl, 2.5 KCl, 20 HEPES, 30 $NaHCO_3$, 1.2 NaH_2PO_4, 25 glucose, 2 $CaCl_2$, 1 $MgCl_2$, 5 sodium ascorbate, 2.4 sodium

pyruvate and 1 kynurenic acid. Osmolarity was adjusted to ~300 mOsm, and pH was set to 7.4 with NaOH.

2.3.2 Artificial cerebrospinal fluid

Rodent and human brain slices were incubated or superfused with a solution mimicking the cerebrospinal fluid (artificial cerebrospinal fluid, aCSF). Two solutions were used for the different experiments, as indicated in the Results chapters:

(1) A bicarbonate-based aCSF when constant bubbling with CO_2 was possible, which contained (in mM): 124 NaCl, 2.5 KCl, 26 $NaHCO_3$, 1 NaH_2PO_4, 10 glucose, 2 $CaCl_2$ and 1 $MgCl_2$. Osmolarity was adjusted to ~295 mOsM and the solution had a pH of 7.4 when bubbled with 20% O_2/5% CO_2/75% N_2.

(2) Alternatively, a HEPES-based aCSF solution was used, which contained (in mM): 140 NaCl, 2.5 KCl, 10 HEPES, 1 NaH_2PO_4, 10 glucose, 2 $CaCl_2$ and 1 MgCl. Osmolarity was adjusted to ~295 mOsM and pH was set to 7.4 with NaOH. This was oxygenated with 20% O_2/5% CO_2/75% N_2.

For slice incubation experiments, slices were placed in small chambers or a cell culture incubator and incubated in aCSF supplemented with drugs as indicated (see the next section for details). During live imaging experiments, aCSF was delivered to the imaging chamber via a peristaltic pump at 2–4 ml/min and passed through a heating block encasing the perfusion inlet. Flow rate and heating intensity were manually adjusted to reach a temperature of 33–34°C at the imaging chamber. In these experiments, brain slices were secured in the imaging chamber by placing them beneath a custom-made platinum U-shaped harp glued to parallel nylon strands.

2.3.3 Pharmacological agents

For various experiments, brain slices were incubated or superfused with aCSF in the presence or absence of the following pharmacological agents, as indicated: 50 µM BAPTA-AM (to buffer intracellular Ca^{2+}, Merck A1076), 50 µM bupivacaine (a two-pore

domain K^+ channel and voltage-gated Na^+ channel blocker, Sigma B5274), 1 µM charybdotoxin (a Ca^{2+}-activated K^+ channel blocker, Anorspec 28244), 10 µM cytochalasin D (an actin polymerisation inhibitor, Sigma 22144), 10 µM MRS2578 (a $P2Y_6$ receptor blocker, Cayman CAY19704), 15 µM noradrenaline (Sigma A7257), 150 units/ml superoxide dismutase (SOD1, a ROS scavenger, Sigma S7571), 25 or 50 µM tetrapentylamonium (TPA, a two-pore domain K^+ channel and voltage-gated K^+ channel blocker, Sigma 258962) or 500 nM tetrodotoxin citrate (TTX, to block voltage-gated Na^+ channels, Abcam ab120055).

2.3.4 Amyloid beta preparation

For ROS imaging experiments, Aβ oligomers were prepared as described by Nortley et al. (2019). Briefly, synthetic $Aβ_{1-42}$ (Bachem H-7442) was resuspended at a nominal 5 mM in DMSO on the day before experiments, bath-sonicated for 10 min and vortexed for 30 s. Aβ was diluted to a nominal 100 µM with phosphate buffered saline buffer (PBS, pH 7.4, ThermoFisher BR0014G), vortexed for 15 s and incubated at 4°C for 24 h, which we have shown results predominantly in Aβ oligomer formation (Nortley et al., 2019). The Aβ peptide concentration in the PBS stocks was determined for each batch using a Pierce BCA protein assay kit (ThermoFisher 232227), and nominal concentrations were corrected accordingly. Immediately before use, Aβ preparations were centrifuged at 14,000 g for 10 min at 4°C to remove fibrils and the supernatants (containing soluble Aβ) were diluted to 72 nM in aCSF.

For confirmation of Aβ preparations, peptide samples (3.7 µg) were loaded onto discontinuous acrylamide gels (4% stacking gel, 12% separating gel) along with Novex Sharp pre-stained molecular weight markers (ThermoFisher 57318) and electrophoretically separated at 150 V. Gels were stained for total protein using a SilverXpress Silver Staining kit (Invitrogen LC6100) according to the manufacturer's protocol.

I have also used a human $Aβ_{1-42}$ analogue ($Aβ^{pH}$) developed and kindly provided by our collaborators from Gaurav Chopra's group in Purdue University. $Aβ^{pH}$ (molecular weight 5355 g/mol) is conjugated to Protonex Green dye (PTXG) and exhibits green fluorescence

upon internalisation into the acidic phagosomes of cells but is non-fluorescent at physiological pH, unlike traditional non-pH dependent fluorophore conjugates of Aβ, thus allowing us to image $A\beta^{pH}$ uptake into glial lysosomes *in situ* and *in vivo* (Prakash et al., 2021).

To prepare $A\beta^{pH}$, a stock solution was made dissolving the solid powder at 50 µM in HEPES-based aCSF. The vial was vortexed thoroughly, bath-sonicated for 10 s and incubated at 37°C in the dark for 24 h to initiate aggregation. It was then either immediately used for experiments or stored at -20°C for future experiments. During this process, vials were always wrapped in foil.

2.4 Brain tissue preparation

2.4.1 Acute slice preparation for *in situ* experiments

Rodents for *in situ* experiments were killed by cervical dislocation and decapitation. After quickly removing the skull and extracting the brain with a spatula into a Petri dish, the cerebellum was removed. Both brain hemispheres were dorsally cut at an angle as previously described (Bischofberger et al., 2006), before fixing the cut surface to the vibratome specimen holder with liquid glue (Loctite 1620715). 250 µm hippocampal slices were then prepared on a Leica VT1200S vibratome. For human samples, donor tissue (typically ~1 cm^3) was glued to the vibratome specimen holder, and 300 µm slices were made on a dedicated Leica VT1000S vibratome.

For experiments on neonatal rodents under P12 (all rat experiments), slicing was done in bicarbonate-based slicing solution at 4°C, and slices were immediately transferred to bicarbonate-based slicing solution at room temperature until use.

For experiments on rodents older than P12 and on human tissue, slicing was done in NMDG-containing slicing solution at 4°C. Heat recovery followed whereby slices were

immediately transferred to warmed (35°C) slicing solution for 20 min, and then to storage solution at room temperature until use.

2.4.2 Perfusion-fixation and fixed slice preparation

For preparing fixed brain samples for immunohistochemistry, mice were deeply anaesthetised with an overdose of pentobarbital sodium (Euthatal, 200 µg/g body weight) injected intraperitoneally. The toe pinch reflex response was used to determine depth of anaesthesia. Once responses were lost, surgery was performed (Gage et al., 2012) and mice were transcardially perfused with PBS, followed by 4% paraformaldehyde (PFA, pH 7.4). Whole brains were then removed and post-fixed in PFA for 24 hours at 4°C before transferring to PBS containing 0.03% sodium azide for storage at 4°C. Subsequently, 50 to 70 µm sagittal slices were prepared on a Leica VT1200S vibratome.

2.5 Slice incubation experiments

2.5.1 Acute treatment with channel blockers

Brain slices from human or rat were incubated in aCSF supplemented with drugs as indicated. Slices were placed in small chambers and incubated at 35°C for 40 min prior to fixation in 4% PFA for 1 hour (human) or 45 min (rodent) at room temperature, and immunostained and imaged followed as described below (see section 2.8).

2.5.2 Phagocytosis of synthetic probes

Hippocampal brain slices were allowed to recover at room temperature for 2.5 hours so that the microglia would activate and become more phagocytic (Krabbe et al., 2012, 2013; Kurpius et al., 2006). They were then transferred to 24-well plates and incubated with 3 µm serum coated, FITC-labelled resin microbeads (Sigma 72439; $1.7x10^7$ microbeads per well in aCSF) for 1.5 hours in a cell culture incubator at 35°C (or at 4ºC, as a negative control). Microbead suspensions were supplemented with drugs as indicated (see details in

section 2.3.3). In addition, 30 min prior to applying the microbead suspension (i.e., during the last 30 min of the recovery period), slices were pre-incubated with the drugs at the same concentration as that contained in the microbead suspension. For high $[K^+]_o$, aCSF containing 120 mM KCl (replacing 117.5 mM NaCl with KCl) was used.

For brain slice experiments with $A\beta^{pH}$, sagittal hippocampal slices made from P12 rats were allowed to recover for 2.5 hours at room temperature before being transferred to 24-well plates and incubated with 5 µM $A\beta^{pH}$ in HEPES-based aCSF for 1.5 hours at 35°C.

In both cases, following incubation, slices were rinsed in cold PBS, fixed in 4% PFA for 45 min at room temperature and immunostained and imaged as described below (see section 2.8).

2.5.3 Imaging of reactive oxygen species

Cortical brain slices were incubated with dihydroethidium, which upon $O_2\cdot^-$-specific oxidation to ethidium binds to the DNA and RNA of $O_2\cdot^-$-producing cells (Wu et al., 2012). Cortical slices (250 µm thick) from P21 rats were incubated in aCSF or in aCSF containing $A\beta_{1\text{-}42}$ (72 nM) or $A\beta_{1\text{-}42}$ + SOD1 (150 units/ml) at 34ºC. Dihydroethidium (DHE, Cayman 104821) was made up at 5 mg/ml in anhydrous DMSO and added to all solutions at a final concentration of 8 µM immediately before use, to avoid auto-oxidation of the dye. To limit the intracellular accumulation of oxidised product over time, slices were not pre-incubated with DHE. After 40 min, the slices were quickly rinsed in PBS, mounted and immediately imaged using a confocal microscope. To define the identity of ROS-producing cells, slices were fixed in 4% PFA for 20 min and immunostained for NG2 and Iba1. Alexa 488-isolectin B_4 (ThermoFisher I21411, 10 µg/ml) was also added with the secondary antibodies to label blood vessels. Isolectin B_4 binds to α-D-galactose residues in the basement membrane generated by pericytes and endothelial cells, and thus outlines pericytes (Mishra et al., 2014).

For glutathione imaging, cortical brain slices were incubated with $A\beta$ and fixed as described above, then incubated with 10 mM N-ethylmaleimide (NEM) for 4 h at 4ºC and

washed thoroughly with PBS. The sections were then immunolabelled with a GSH-NEM antibody which is specific to this adduct and does not react with oxidised glutathione or glutathione linked to proteins (see antibody details in section 2.8.1), thereby allowing quantification of reduced glutathione after reaction with NEM (Won et al., 2015).

2.6 Electrophysiology

Slices were individually transferred to the recording chamber and perfused at 3-5 ml/min with aCSF, which was maintained at 32–34ºC. Pyramidal neurons in the CA1 region of the dorsal hippocampus were selected visually using an Olympus 60×/0.9 water-immersion objective in combination with differential interference contrast (DIC) optics. Cells were recorded in the whole-cell voltage-clamp configuration with glass patch-pipettes (resistance in the bath solution 2–4 MΩ). Junction potentials (-10 mV) were corrected for. Recorded signals were sampled and digitized at 20 kHz, filtered at 4 kHz, and then further filtered offline at 2 kHz for analysis and data presentation. During the entire course of recording, access resistance was monitored by periodically applying a -5mV voltage pulse. Cells were excluded from analysis if the access resistance changed by more than 20% during the course of an experiment.

To study excitatory synapses, pipettes were filled with internal solution containing (in mM): 132.3 K-gluconate, 7.7 KCl, 4 NaCl, 0.5 $CaCl_2$, 10 HEPES, 5 EGTA, 4 MgATP, and 0.5 Na_2GTP (pH 7.2–7.3). The calculated reversal potential for Cl^- (E_{Cl}) with these solutions was ~-62mV, and a holding potential (V_h) of ~-65mV was used. To isolate single vesicular events, 500 nM TTX was applied, and the frequency and amplitude of EPSCs in TTX were monitored. To assess whole cell glutamate receptor-mediated currents, cells were whole-cell voltage-clamped at -40mV and recorded in the presence of the $GABA_AR$ antagonist GABAzine (10 µM, Tocris 1262). N-methyl-D-aspartic acid (NMDA, 10 µM; Tocris 0114) or kainic acid (Tocris, 1 µM; Tocris 0222) were bath-applied sequentially (ensuring that holding current returned to the original control level before subsequent drug application after 10–15

min), and the resulting change in current was measured. Peak shifts in holding current induced by each drug were reported as the appropriate glutamate receptor-mediated current.

The frequencies and amplitudes of spontaneous and miniature EPSCs (sEPSCs and mEPSCs, respectively) were measured using automatic detection of these events with Mini Analysis 6.0.7 (Synaptosoft) software followed by inspection of individual events for analysis. For assessment of synaptic current frequencies, events during the 180 s immediately before TTX application (defined as the baseline period) were compared to mean frequencies observed from 100 s after TTX application onset (over 180 s). The change of mean current induced by NMDA and kainic acid was calculated by defining the mean current in 20 s segments for control solution and at the peak of the NMDA and kainic acid applications by making histograms of all data points, and then fitting a Gaussian distribution to each histogram to define the mean current (using Clampfit 10.4, Molecular Devices).

2.7 Dendritic staining and imaging

2.7.1 Golgi-Cox staining technique

Dendritic spines were visualised using an adapted version of the Golgi-Cox staining technique. This procedure, initially described by Camilo Golgi in 1879 but still widely used (Welsh et al., 2020), allows visualisation of neuronal morphology by sparsely labelling cells. The staining protocol was adapted from Zaqout and Kaindl (2016) and Zhong et al. (2019). Briefly, brains were first impregnated and washed, slices were made and staining was developed (Figure 2.3A).

To prepare the impregnation solution, 25 ml of 5% $K_2Cr_2O_7$ (w/v in ddH_2O) were first mixed with 25 ml of 5% $HgCl_2$ (w/v in ddH_2O). Then, 20 ml of 5% K_2CrO_4 (w/v in ddH_2O) and finally 50 ml ddH_2O were added to the mixture. The solution was then kept for at least 3 days before use to allow formation of dark precipitates, and 5 ml were taken from the upper clear

part into individual polystyrene bijou tubes (one per brain). Once animals were killed and their brain was quickly removed, hemisected and rinsed in ddH_2O, brain hemispheres were immersed in impregnation solution at room temperature for 10–12 days in the dark. Brains were then transferred to 1% (w/v) polyvinylpyrrolidone (Acros Organics 227480250) in 0.1 M PBS for 4°C for 5–7 days to reduce background staining. After the first 24 h, this solution was replaced by fresh solution to remove traces of the impregnation reagents. Brains were then sliced on their sagittal axis at 100 µm using a dedicated vibratome. Slices were directly transferred onto slides previously coated with 2% (w/v) gelatin from porcine skin (Sigma G2500). After each slice was loaded on the slide, excess solution was removed with filter paper and a PBS-soaked piece of paper was gently pressed on the slide to remove any air bubbles that could remain between the slice and the slide, thus increasing adherence. Slides were then allowed to dry for 2–3 days in the dark.

For developing, the slides were incubated in the following sequence of solutions using histological staining jars and racks (Simport Scientific M900-12):

- ddH_2O twice for 5 min each
- 50% ethanol (v/v in ddH_2O) for 5 min
- 20% ammonia solution (v/v in ddH_2O) for 10 min
- ddH_2O twice for 5 min each
- 5% sodium thiosulfate (w/v in ddH_2O) for 10 min
- ddH_2O twice for 1 min each
- 50, 75, 90, 95 and 100% ethanol (v/v in ddH_2O) for 5 min each
- 100% xylene for 10 min

For mounting, the dehydrated slides were taken out of xylene one by one, Permount mounting media (Fisher Chemical 15820100) was applied to them dropwise and a coverslip was gently placed on top. Slices were not allowed to dry out at any point before coverslipping, as this would result in tissue cracking. Samples were stored at room temperature in the dark until imaging.

All solution preparation, tissue impregnation and developing steps were carried out under a chemical fume-hood, mercury-containing solutions were disposed of separately and all solutions were stored at room temperature in the dark.

2.7.2 Bright-field imaging and spine analysis

Sections were imaged using a Zeiss AxioScan.Z1 slide scanner and a Plan-Apochromat 40×/0.95 Corr M27 objective (NA 0.95). 49.2 µm stacks were acquired at 1.2 µm step size, where focus depth was set automatically for each slice and exposure time was set at 200 µs.

Following acquisition, dendritic segments of CA1 pyramidal neurons were selected as regions of interest (Figure 2.3B). Only segments that fit the following criteria were used: (i) non-primary apical dendrites, (ii) longer than 30 µm, (iii) at least 100 µm away from the soma, and (iv) absence of highly clustered stained cells that would prevent identification of the cell to which the segment of interest belonged.

Spine numbers were counted in each dendritic segment (Figure 2.3C) and averaged over the segment's length to obtain the spine density per µm. At least 7–18 dendritic segments were analysed per animal, each from a different neuron. Selection of dendritic segments and spine counts were done with the researcher blind to genotype, and only spines with a clear protrusion and attachment to the dendritic shaft were counted (this was aided by scrolling through the *z*-stack).

2.8 Conventional fluorescence imaging

2.8.1 Immunohistochemistry

Free-floating slices were stained for fluorescence imaging as follows. Slices were permeabilised and blocked in a solution containing 10% normal horse serum and 0.02% Triton X-100 in PBS (hereafter, blocking solution) in 24-well plates, followed by incubation with primary antibodies in blocking buffer for 12 hours at 4°C with agitation (mouse anti-

amyloid beta (1:500, IBL 27725), rabbit anti-amyloid precursor protein (1:500, Abcam ab32136), mouse anti-Bassoon (1:300, Novus NB120-13249), mouse anti-beta-actin (1:5,000, Proteintech 66009), rabbit anti-cleaved caspase 3 (1:250, Abcam ab2302), rat anti-CD68 (1:250, BioRad MCA1957), chicken anti-GFAP (1:500, Abcam ab4674), mouse anti-glutathione:N-ethylmaleimide (1:500, Millipore MAB3194), rabbit anti-Homer1 (1:300, Synaptic Systems 160002), goat anti-Iba1 (1:500, Abcam ab5076), rabbit anti-Iba1 (1:500, Synaptic Systems 234003) or mouse anti-vGluT1 (1:300, Abcam ab134283)).

The following day, the antibody solution was removed. Following four 10 min washes in PBS, Alexa-conjugated secondary antibodies (Invitrogen) diluted 1:1,000 in blocking buffer were applied for 4 hours at room temperature with agitation. After three new washes in PBS (10 min each), slices were incubated with 4′,6-diamidino-2-phenylindole (DAPI, Invitrogen D1306, diluted 1:50,000 in PBS) for 30 min to visualise nuclei and rinsed in PBS. Slices were then mounted on SuperFrost Plus slides (Fisher 10149870) using fluorescence mounting medium (Dako S3023). Samples were stored at 4°C in the dark until imaging.

2.8.2 Confocal and widefield imaging

In confocal microscopy, a pinhole is placed in front of the detector, which physically blocks out-of-focus signal from reaching the detector. This increases signal-to-noise ratio, even though much of the sample is illuminated by the conically-shaped excitation light beam. This is particularly relevant for studying phagocytosis, as it enables more accurate detection (subject to the resolution limit) of where in the depth axis (*z*) a particle is, and so whether or not a given particle has been engulfed by a cell, for instance. Here, three-dimensional *z*-stacks were obtained using a Zeiss LSM700 confocal microscope with a Plan-Apochromat 20×/0.8 or a Plan-Apochromat 63×/1.4 Oil DIC M27 objective, and the specific settings for each experiment will be described in the next section. Pinhole size was always set at 1 Airy unit (AU) to block collection of out-of-focus signal, thus increasing signal-to-noise ratio and allowing me to more accurately study target engulfment.

For assessment of overall Aβ plaque load and microgliosis across different brain regions, sections were imaged using a Zeiss AxioScan.Z1 slide scanner and a Plan-Apochromat 20×/0.8 M27 objective. In contrast to most of the data presented in this thesis, which was acquired by confocal or two-photon imaging, this is a widefield imaging system where the entire focal volume is illuminated and all emitted signal is collected across the slices' depth. For these experiments, channels were set as follows (wavelengths and wavelength ranges in nm; exc. = excitation; em. = emission):

Channel 1 (used for CD68; beam splitter 498) filter exc. 453–485, filter em. 507–546.

Channel 2 (used for Iba1; beam splitter 568) filter exc. 540–546, filter em. 587–640.

Channel 3 (used for Aβ; beam splitter 660), filter exc. 630–650, filter em. 670–710.

Channel 4 (used for DAPI; beam splitter 395), filter exc. 330–375, filter em. 430–470.

2.8.3 Image acquisition and analysis

For microbead phagocytosis analysis, confocal stacks were obtained at 2 µm z-step intervals using a Zeiss LSM700 microscope with a Plan-Apochromat 20×/0.8 objective. To assess phagocytosis, the percentage of phagocytic microglia (i.e., $Iba1^+$ cells which had internalised >1 $FITC^+$ microbeads) was calculated. All imaging and analyses were done with the researcher blind to genotype and treatment.

For synapse analysis, brain slices were imaged (102 µm x 102 µm) at 3–6 µm from the slice surface using a Zeiss LSM700 microscope with a Plan-Apochromat 63×/1.4 objective. Three confocal images from the CA1 *stratum radiatum* region (at 1.5 µm intervals) were taken per brain slice, and 5 brain slices were taken per animal. Images were analysed individually and then averaged across stacks and brain slices to obtain animal means. After background subtraction (with a 10-pixel rolling ball average), marker areas were quantified using a custom-based intensity threshold protocol with ImageJ-FIJI, and the Analyze Particles function was used to quantify puncta number and areas. For thresholding, sample images were first manually thresholded for each channel blinded to condition and genotype, and a suitable range above threshold was established which was then kept constant

throughout (Bassoon: 15-255; Homer1: 30-255; images were 8-bit). Size exclusion (>1.2 μm^2, <0.05 μm^2) was applied to exclude any objects unlikely to represent synaptic puncta. Synapses were defined by the presence of overlapping presynaptic and postsynaptic puncta (McLeod et al., 2017). Presynaptic colocalization with microglia was analysed as the total area of Bassoon puncta within the Iba1-stained cell area after thresholding. For human synapse analysis, images were processed by super-resolution radial fluctuation (SRRF) analysis (Gustafsson et al., 2016) to improve resolution prior to thresholding and quantification. All imaging and analysis were done with the researcher blind to genotype or treatment.

For cell density analysis, brain slices were imaged (640 µm x 640 µm) using a Zeiss LSM700 microscope with a Plan-Apochromat 20×/0.8 objective. Cell density and spatial distribution were analysed as in Davis et al. (2017). Briefly, cell counts were performed to obtain cell density as well as the average nearest-neighbour distance between cells (NND) and their regularity index. The latter is the ratio of the mean NND to the standard deviation of the NND for the whole population of cells and describes how regular is the spacing of microglia. One maximum-projected z-stack (3 µm depth) from the CA1 *stratum radiatum* region was analysed per slice, and 5 slices were averaged per animal.

For Sholl analysis, confocal stacks (at 0.34 µm z-step intervals) of Iba1-stained microglia were obtained from the CA1 *stratum radiatum* using a Zeiss LSM700 microscope with a Plan-Apochromat 63×/1.4 objective, encompassing the whole thickness of the brain slice (Figure 2.4A). Three-dimensional cell reconstructions were performed using the automatic cell tracing tool Neuron Tracing v2.0 on Vaa3D (vaa3d.org), manually adjusting the background threshold for each image to obtain the best possible reconstruction (i.e., a compromise between picking up all real processes and no background; Figure 2.4B). After the reconstructions were manually checked for obvious errors against the raw images, they were analysed using custom-written MATLAB software described in Madry et al. (2018) and available from https://github.com/AttwellLab/Microglia, which is based on the method described by Sholl (1953). Briefly, a series of concentric spheres were drawn at 5 µm

intervals from the centre of the cell (established by the analyst; the soma was assumed to have a 5 µm radius to avoid mis-assigning Iba1 signal differences within the soma as representing processes). A profile of branching points was generated across the Sholl spheres (i.e., based on distance from the microglial cell soma), to assess cell ramification and overall process architecture (Figure 2.4C). For each condition, analysis was performed using the cell as the statistical unit as most variance occurred between cells rather than slices or animals. All imaging and analysis were done with the researcher blind to genotype and condition.

For analysis of superoxide levels**,** a single image stack was acquired at the middle of each slice and the fluorescence intensity of the maximum intensity projections was measured using ImageJ-FIJI. In maximum intensity projections of *z*-stacks, regions of interest (ROIs) were then drawn around the nuclei of pericytes (defined as NG2-expressing cells on isolectin B_4-labelled capillaries) and Iba1-expressing immune cells (microglia and perivascular macrophages), and the DHE signal within each ROI was measured in ImageJ-FIJI. For each *z*-stack, a mean intensity per pericyte or Iba1-labelled cell, and the total intensity per population of pericytes or Iba1-labelled cells, were calculated, and analysis was performed using the *z*-stack as the statistical unit. All imaging and analysis were done with the researcher blind to treatment.

For analysis of glutathione levels**,** ROIs were drawn around the somata of NG2- and isolectin B_4-labelled pericytes and Iba1-expressing immune cells as above, and the total fluorescence signal for GSH-NEM was quantified for each cell and averaged over cells. All imaging and analysis were done with the researcher blind to treatment.

For analysis of phagocytosis of Aβ^{pH} by glial cells, imaging was done using a Zeiss LSM700 confocal microscope and a 20x objective, where 10 µm image stacks (1 µm *z*-step interval) were acquired. For analysis, the percentage of Aβ^{pH} signal within microglial or astroglial cells was calculated by binarising the microglia or astrocyte channel, creating a mask to define microglial or astrocytic location, and multiplying it by the raw Aβ^{pH} signal. The

fluorescence intensity of $A\beta^{pH}$ colocalising with either cell type mask was then expressed as a percentage of the total $A\beta^{pH}$ signal across the field.

For analysis of Aβ plaque coverage and microgliosis in App^{NL-G-F} mice, the process was as follows. Firstly, channels for CD68, Iba1 and Aβ were split. After background subtraction (using a 10-pixel rolling ball average for CD68 and Iba1 and an 80-pixel rolling ball average for Aβ), all channels were manually thresholded with the researcher blind to genotype. For each brain region selected, a percentage area of plaque coverage was then calculated. Separately, a mask was created for microglia at plaques (created as $Iba1^+$ 'AND' $A\beta^+$) and another for microglia away from plaques (created as $Iba1^+$ 'AND NOT' $A\beta^+$) by using the image operators on ImageJ-FIJI. These masks were then transposed to the binarised CD68 channel, thus allowing calculation of a percentage area coverage of CD68 within microglia located at Aβ plaques and away from Aβ plaques.

2.9 Two-photon imaging

2.9.1 Principles of two-photon imaging

Two-photon fluorescence imaging relies on the excitation of a fluorophore not by a single photon but by simultaneous absorption of two photons. In comparison to single-photon excitation, the two photons can now carry half the energy, and hence their wavelength doubles, falling into the near-infrared spectrum. For instance, the simultaneous absorption of two long wavelength photons (each ~860–960 nm) is equivalent to that of a single blue photon (~488 nm), and both would excite EGFP without altering its emission spectrum. Near-infrared radiation is less absorbed by biological specimens. Moreover, the scattering of light drastically depends on its wavelength (Rayleigh scattering~1/wavelength^4). According to this formula and going back to the EGFP example, a 488 nm beam would scatter about 7 times more than an 860 nm beam. Thus, longer wavelengths penetrate more with less scattering, and allow imaging deeper into the tissue (Tauer, 2002).

In confocal imaging, the use of a pinhole allows for optical sectioning of the imaged sample. By contrast, in two-photon imaging, optical sectioning comes intrinsically from the fact that excitation of the sample is restricted to fluorophores in the very small volume (the objective's focal point) where the intensity is high enough for there to be a significant probability of 2 photons being absorbed nearly simultaneously. Outside of this volume two-photon absorption is negligible and so no fluorescence is generated, which limits out-of-focus signal and avoids the need for a pinhole. The highly localised two-photon excitation, added to the reduced energy of the photons result in less photo-bleaching and photo-toxicity compared to conventional single-photon fluorescence imaging techniques, and facilitate live imaging of the tissue over time.

These features explain the great potential of two-photon microscopy for dynamic, live imaging *in situ* and even for intra-vital imaging in small animals. Because photons have a two-fold longer wavelength in two-photon microscopy, however, image resolution is compromised using this technique (from Abbe's law, which predicts that the resolution limit is approximately equal to the wavelength). In addition, the two photons must hit the fluorophore within ~1 femtosecond of each other to be absorbed, which requires a laser that is able to generate fast pulses of high peak power (Benninger and Piston, 2013).

2.9.2 Imaging of microglial surveillance

For two-photon imaging of microglial motility, microglia (located 70-110 μm below the slice surface) were imaged at 32–34ºC while superfused with oxygenated HEPES-buffered aCSF. Stacks were acquired every 60 s at 2 μm depth intervals using Zeiss LSM710 and LSM780 microscopes with a water immersion W Plan-Apochromat 20×/1.0 DIC M27 objective, equipped with a Spectraphysics Mai Tai DeepSee eHP Ti:Sapphire infrared laser (Spectra-Physics) tuned to 920 nm (to excite EGFP) at 6–12% of its maximum power (the mean laser power under the objective did not exceed 35 mW).

The resulting movies need pre-processing to remove noise and correct for random drifts of the field of view that occur during imaging, particularly those caused by poor placing

of the harp used to secure the slices in the imaging chamber and/or by flow rate or temperature fluctuations. After the acquired *xyzt*-stacks were despeckled and background subtracted, they were registered in 3D along both the *z* and *t* axes using PoorMan3Dreg. Stacks were then maximum intensity projected onto the *z* axis. Registration was repeated on the *xyt*-stacks using MultiStackReg (Figure 2.5A). This process resulted in movies with the somata stationary, allowing reliable assessment of process movements. Cells of interest were manually selected by drawing a ROI around them (including all their cell processes) to perform surveillance analysis on individual cells. Extracted cells were binarised by manually selecting a signal threshold, and the resulting movies were used for analysis of pixels surveyed and generation of subsequent data (initial slope of a graph of pixels surveyed against time, cumulative surveillance and surveillance index) employing custom-written MATLAB software described in Madry et al. (2018), available from https://github.com/AttwellLab/Microglia (Figure 2.5B). All analyses were performed with the researcher blind to genotype and condition.

2.9.3 Calcium imaging

Microglial Ca^{2+} imaging experiments were done with slices from *Cx3cr1*^{CreER} x GCaMP5g-IRES-tdTomato or *Cx3cr1*^{CreER} x GCaMP5g-IRES-tdTomato x *App*$^{NL-G-F}$ transgenic mice that had been orally dosed with tamoxifen at least 21 days prior to imaging to induce GCaMP5g and tdTomato expression (see section 2.2.5).

Imaging was performed using the same setup as described above for microglial surveillance. However, microglial Ca^{2+} transients are rare and can be brief (Eichhoff et al., 2011; Pozner et al., 2015). Thus, to increase the acquisition rate and aid their detection, single scans were acquired at a high speed (1 µs pixel dwell time) of an area of 106 µm x 106 µm (pixel size 0.21 µm; overall frame acquisition time 25 ms). The laser was tuned to 920 nm to allow acquisition of both GCaMP5g and tdTomato signals. Prior to imaging, a *z*-stack (1 µm step intervals) was first taken to confirm the morphology of the imaged cells as visualised by tdTomato expression. Then, single plane images were

acquired every second for 5 min (300 frames) to minimize bleaching, with drugs added to the circulating aCSF 10 min prior to recording where indicated.

To examine lesion-evoked $[Ca^{2+}]_i$ rises, a 20 s baseline was recorded in aCSF with or without drugs, after which a laser injury was performed in an area where no microglial cells were present (which mimics ATP release to the extracellular milieu by injured neurons; Davalos et al., 2005) and a further 5 min of images (300 frames) were recorded. For the injury, a small (6 µm radius) circular ROI was drawn, which was bleached in a single scan (177.3 µs pixel dwell time) with the laser tuned to 920 nm (to avoid time lag due to changing wavelengths) at 80% of its maximum power.

For analysis, all movies from the same field of view were concatenated and registered using the MultiStackReg and TemplateMatching tools in ImageJ-FIJI. No further image processing was done. ROIs were then drawn around microglial somata and processes and ΔF/F was calculated as $(F_t – F_o)/ F_o$, where F_t is the fluorescence intensity of the ROI at each timepoint and F_o is the fluorescence averaged over the baseline.

For spontaneous Ca^{2+} analysis, I used custom-written MATLAB code adapted from Krasnow et al. (2018) which is available from https://github.com/AttwellLab/MyelinCalcium. For each ROI, I generated a locally time-smoothened baseline using a baseline fit with the piecewise cubic Hemite interpolating polynomial in MATLAB, with a smoothing time of 100 frames. Then, Ca^{2+} transients were defined using a detection threshold set to 2.25 x the standard deviation of the first 100 points in the trace that had $\Delta F/F < 0.1$ (to exclude contributions of Ca^{2+} transients to the baseline). Transients were then further confirmed with a minimal area threshold ($\int \Delta F/F \, dt > 0.15$; i.e., they were excluded if this condition was not satisfied) and manually checked to exclude false positives, e.g. resulting from increased background signal. Finally, Ca^{2+} transient rates per 300 s were calculated and used for statistical analysis, using the cell as the statistical unit.

For lesion-evoked Ca^{2+} analysis, ΔF/F was calculated using the fluorescence intensity of the ROI averaged over the 20 s preceding the laser lesion as a baseline. Values of ΔF/F at the peak following the lesion were compared across experiments for statistical

analysis, using the cell as the statistical unit. For producing representative images of the GCaMP peak signal, a multicolour (Fire) lookup table was applied to microglial images in ImageJ-FIJI to help distinguish different intensity values.

2.10 Western blotting

2.10.1 Protein extraction

Brain hemispheres were quickly dissected and hippocampi from each animal were placed in separate 1.5 ml tubes that were immediately moved to dry ice. To extract proteins and break down membranes, lysates were prepared by submerging freshly dissected samples in radioimmunoprecipitation assay (RIPA) lysis buffer (2 ml per brain hemisphere) containing 50 mM Tris pH 7.5, 1 mM ethylene diamine tetraacetic acid (EDTA), 2 mM ethylene glycol tetraacetic acid (EGTA), 150 mM NaCl, 1% NP-40, 0.5% sodium deoxycholate, 0.1% sodium dodecyl sulfate (SDS) and one tablet of protease inhibitor cocktail (Roche 11836153001) per 10 ml of buffer. Each sample was manually homogenised on ice using disposable pestles, centrifuged for 30 min at 12,000 rpm at 4°C and the supernatant was transferred to a new tube for storage at -20°C.

2.10.2 Electrophoresis and immunoblotting

The protein concentration of the samples was determined prior to Western blotting using a Pierce BCA protein assay kit (ThermoFisher 232227) and 40 µg of each sample were loaded onto discontinuous acrylamide gels (4% stacking gel, 12% separating gel) and resolved by sodium dodecyl sulfate polyacrylamide gel electrophoresis (SDS-PAGE) at 120 V. Samples were diluted in sample buffer (62.5 mM Tris-HCl, pH 6.8, 2% SDS, 25% glycerol, 0.01% bromophenol blue, 5% β-mercaptoethanol), heated to 90°C for 5 min for denaturing proteins and spinned at 12,000 rpm prior to loading. A pre-stained molecular weight ladder was used for band identification (ThermoFisher LC5800). Proteins were then

transferred to a 0.45 µm nitrocellulose membrane (GE 10600002) by wet electro-transfer in 25 mM Tris-HCl, pH 8.3, 192 mM glycine, 20% methanol for 1 h at 30 V.

Following transfer, membranes were transiently stained by immersion in Ponceau solution (Sigma P7170) to visualise bands and trim membranes. Membranes were then incubated in blocking solution containing 0.1% Tween-20 and 4% powder milk (w/v) in PBS for 1 h at room temperature. Immunoblotting followed in sealed plastic film bags (see antibodies in 2.8.1) overnight at 4°C. After three 10 min washes in blocking solution, the membranes were incubated for 1 h at room temperature in horseradish peroxidase (HRP)-conjugated secondary antibodies raised in goat (ThermoFisher) diluted 1:10,000 in blocking solution. Following three 10 min washes in 0.1% Tween-20 in PBS, signal was detected upon reaction with enhanced chemiluminescent HRP substrate (Millipore WBLUR0500) with an ImageQuant LAS 4000 camera.

2.10.3 Densitometric analysis

To quantify protein bands on Western blots, boxes were placed on each lane using the Gels tool in ImageJ-FIJI and the intensity profile of each was obtained. For each lane profile plot, a straight line was drawn across the base of the peak to define the band (thereby subtracting background signal) and the area under the curve was calculated. Values were then normalised by dividing by the loading control (a protein with an assumed constant level of expression, e.g. β-actin) and then by the average of the WT values.

2.11 Statistics

Data will be presented as mean ± standard error of the mean (s.e.m.) throughout this thesis. Details of the statistical tests used in each set of experiments will be described in the corresponding Results chapters. Data normality was assessed using the D'Agostino-Pearson test. Statistical significance was assessed using unpaired two-tailed Student's t-tests (for normally distributed data), Mann-Whitney tests (for non-normally distributed data)

or one- or two-way analysis of variance (ANOVA) for multiple comparisons. Two-tailed Wilcoxon matched-pairs signed rank tests were used for paired analysis. When multiple comparisons were tested, p-values were corrected using post-hoc tests as indicated. Corrected p-values were considered significant if they were less than 0.05. All statistical analysis was performed in Microsoft Excel 2016, GraphPad Prism 7 and Sigmaplot 11.

A

AAGGTCGGCAGAGCACATCCTCCCCGGGGCGTG
GGCACAAGTCCGCGGGCAGCAACCCTCGCGGAG
CTGTCCTCCAGTGCCATGGCTGGCCGCGGTTGC
GGCTGCAGCCCCGGCCACCTGAA**T**CGAGGACAA
CGCGCGCTTCCTGCTGCTCGCTGGGCTCATCCT
GCTCTACCTGCTGGGCGGCGCCGCAGTCTTCTC
CGCGCTGGAGCTAGCGCAGGAGTTGCAGGCCAA
GCAGCGCTGGGAAGAGCGCCTGGCCAACTTCAG
CCGGGGCCACAACCTGAGCCGTGAAGAGCTGCG
AGGTTTCCTCCGCCACTACGAGGAAGCCACCAG

B

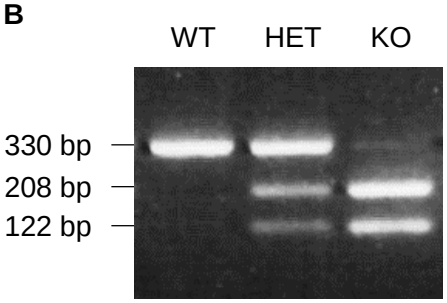

C **WT (405 residues):**

MAGRGCGCSPGHLNEDNARFLLLAGLILLYLLG
GAAVFSALELAQELQAKQRWEERLANFSRGHNL
SREELRGFLRHYEEATRAGIRMDSVRPRWDFTG
AFYFVGTVVSTIGFGMTTPATTGGKIFLIFYGL
IGCASTILFFNLFLERLITVIACVMRSCHQQQL
RRRGAVTQDNMKAPEKGEADSLTGWKPSVYYVM
LILCLASVAISCGASALYTTMEGWSYFDSVYFC
FVAFSTIGFGDLVSSQNAQYESQGLYRFFNFFL
ILMGVCCIYSLFNVISILIKQTVNWILRKLDSG
CFPPCQRGLLRSRRNVVMPGNIRNRCNISIETD
GVMESDTDGRRLSGEMISMKDTNKVSLAILQKQ
LSEMANGGPHQNSASSRDDEFSGGVGAFAVMNN
RLAETSGDR

KO (68 residues):

MAGRGCGCSPGHLNRGQRALPAARWAHPALPAG
RRRSLLRAGASAGVAGQAALGRAPGQLQPGPQP
EP

D

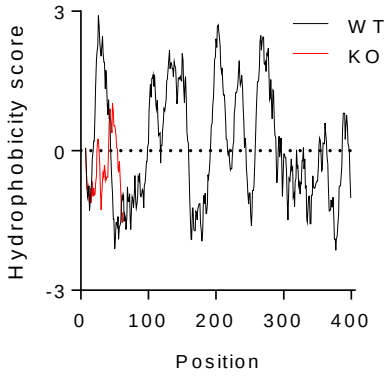

E

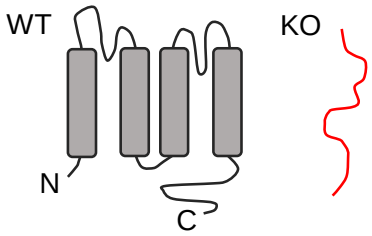

Figure 2.1. Generation of THIK-1 KO (Kcnk13-IN1-EM1-B6N) mice.

(A) Fragment of the knockout (KO) DNA sequence delimited by PCR primer-binding regions (underlined) showing the single T insertion (red), which results in the generation of a restriction site for *Taq*I (T^CGA, shown in bold) and a premature STOP codon (blue). **(B)** Agarose gel showing bands generated for wildtype (WT), THIK-1 heterozygote (HET) and homozygote KO, following PCR amplification and digestion with *Taq*I. **(C)** Amino acid sequence of the encoded WT and KO proteins. In red, KO residues that differ from the WT as a result of the frameshift caused by the T insertion. **(D)** Hydrophobicity plot for each protein showing the Kyte-Doolittle score on a 13-residue window, calculated on https://web.expasy.org/protscale. **(E)** Predicted protein structures for WT (left) and KO (right, lacking transmembrane domains).

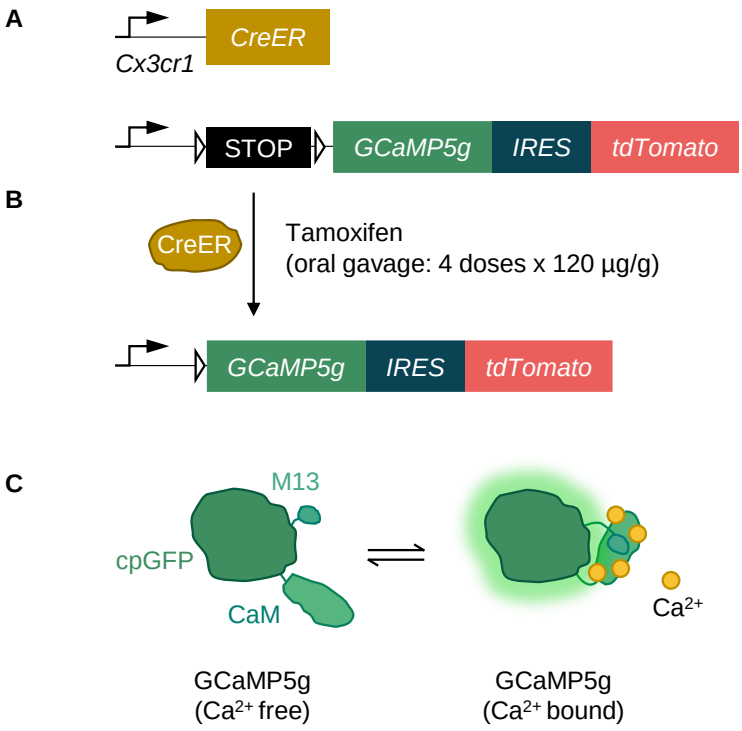

Figure 2.2. *Cx3cr1*^{CreER} x GCaMP5g-IRES-tdTomato transgenic mice.

(A) Mice generated for calcium imaging experiments, where microglia and macrophages express GCaMP5g, were generated by crossing *Cx3cr1*^{CreER} mice with floxed GCaMP5g-IRES-tdTomato mice. **(B)** Tamoxifen administration results in the activation of the CreER recombinase, which is only present in *Cx3cr1*-expressing cells (microglia, macrophages and more weakly oligodendrocyte precursor cells). After Cre-mediated cleavage of the floxed STOP cassette, GCaMP5g and tdTomato are expressed in these cells. **(C)** GCaMP5g is a fusion protein composed of circularly permutated green fluorescent protein (cpGFP), the calcium-binding protein calmodulin (CaM), and the M13 peptide. Rises of intracellular Ca^{2+} concentration are detected by an increase in fluorescence emission.

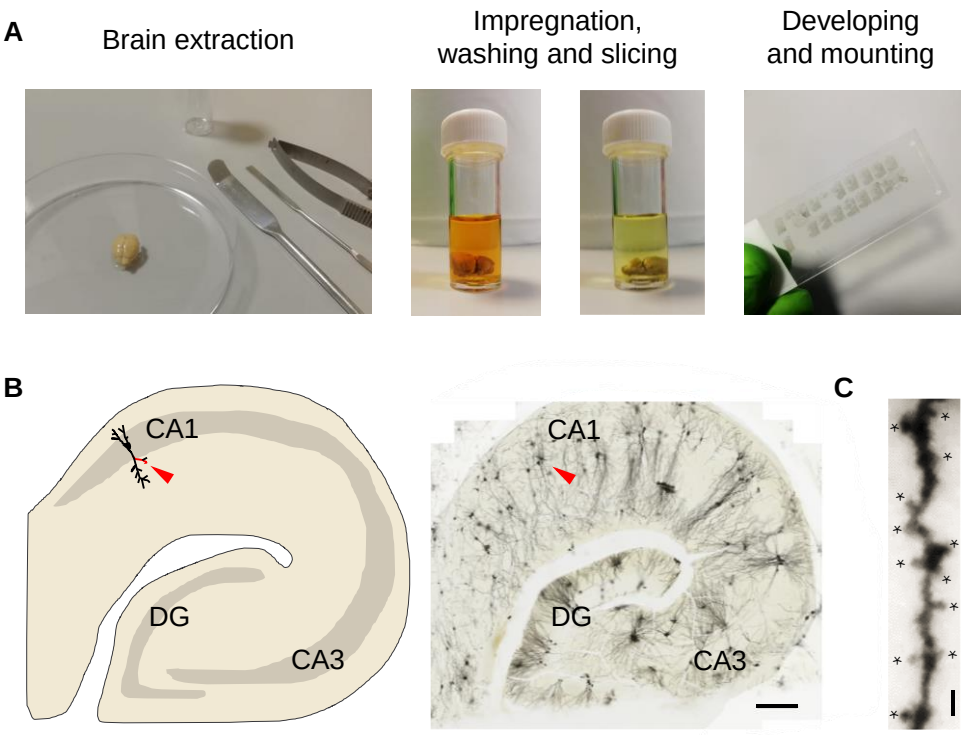

Figure 2.3. Golgi-Cox staining technique.

(A) Main stages of the staining procedure, involving brain extraction, impregnation (10-12 days), washing (a further 5-7 days), brain slicing and a final developing and mounting step. **(B)** Schematic illustration (left) and representative image (right) of a Golgi-Cox stained hippocampal slice. Dentate gyrus (DG), CA3 and CA1, and a CA1 pyramidal neuron are indicated. Red arrowhead: a secondary apical dendrite that would be valid for analysis. Scale bar: 200 µm. **(C)** Representative image of a Golgi-Cox stained dendritic segment, with spines indicated by stars. Scale bar: 2 µm.

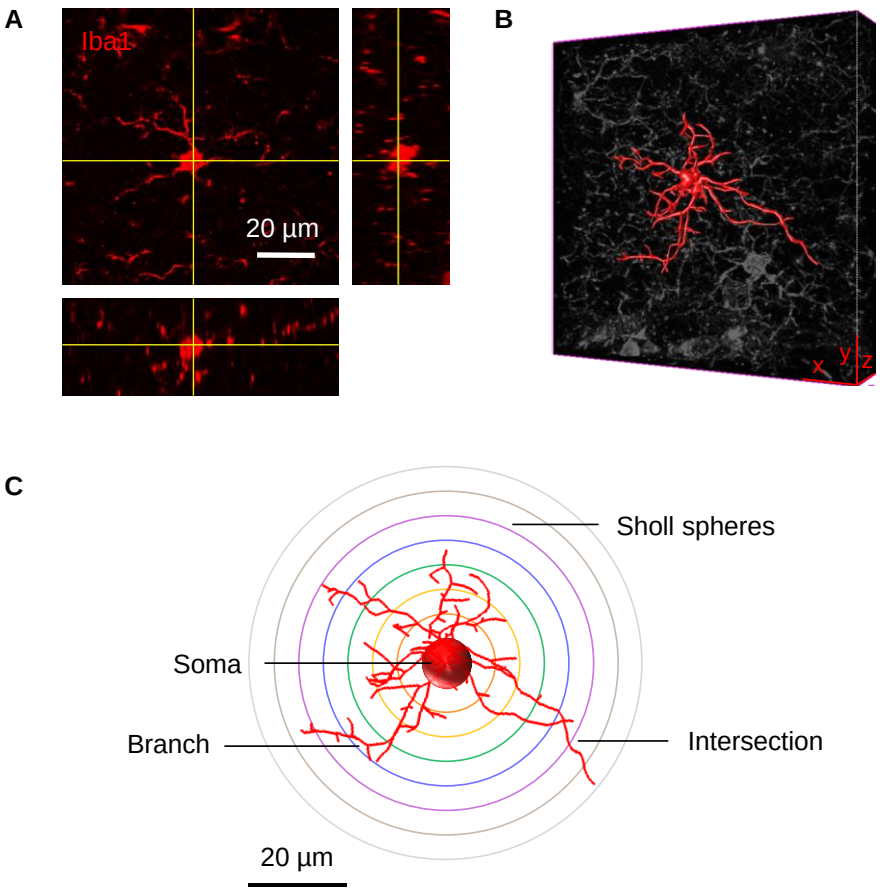

Figure 2.4. Sholl analysis of microglia.

(A) Microglia were labelled with Iba1 and imaged on a confocal microscope to obtain *z*-stacks. Orthogonal projections at the level of the crosshairs show the estimated centre (soma) of the cell. **(B)** Vaa3D tracing tools were used to generate three-dimensional reconstructions of each cell. These were used to calculate total process length per microglial cell. **(C)** Running a Sholl-based MATLAB script on the reconstructions, where concentric spheres were drawn at 5 µm intervals from the cell soma, microglial process branches and sphere intersections were traced for each Sholl radius.

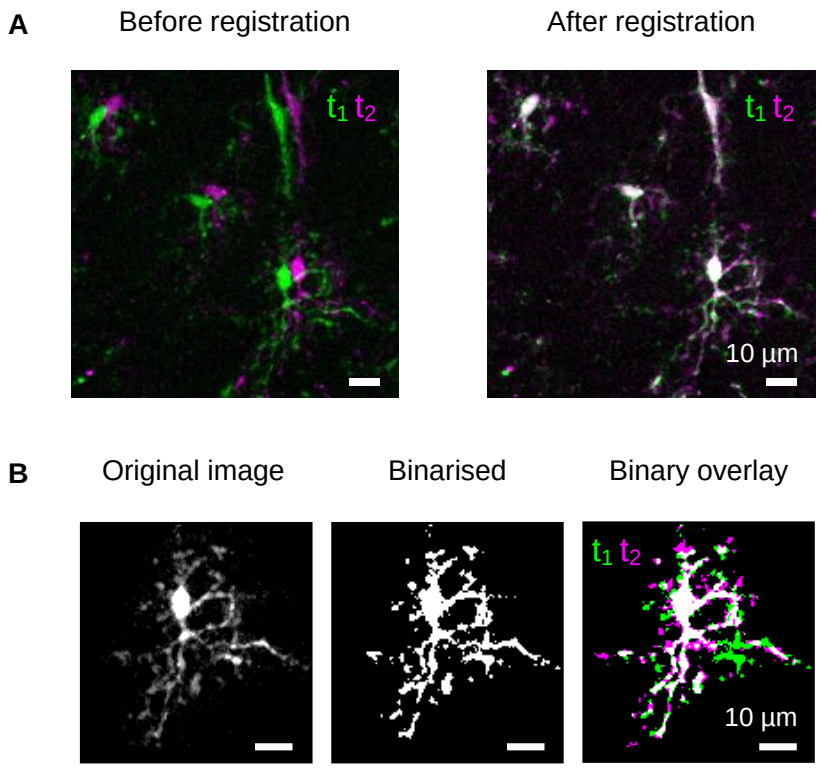

Figure 2.5. Analysis of microglial surveillance.

(A) Movies were pre-processed to remove noise and correct for random drifts of the field of view that occur during imaging. After the acquired *xyzt*-stacks were despeckled and background subtracted, 3D registration along both the *z* and *t* axes followed using PoorMan3DReg. Stacks were then maximum intensity projected onto the *z* axis. Registration was repeated on the *xyt*-stacks using MultiStackReg. This process keeps the somata in a fixed position in the image and allows reliable assessment of process movements. **(B)** Cells of interest are manually selected and binarised, which allows analysis of pixels surveyed and generation of subsequent data (initial slope of the graph of total number of pixels surveyed versus time, cumulative surveillance, and surveillance index) using MATLAB. On the representative cell shown, green pixels correspond to process retractions while magenta pixels correspond to process extensions, between two times t_1 and t_2, while white indicates no change.

3. Regulation of microglial morphology and surveillance

3.1 Introduction

Because microglial morphology is known to reflect the cells' functional state, morphological changes are widely used to assess their function. These cells transit reversibly through a range of patterns from more ramified to more amoeboid-like shapes. More ramified microglia are typically considered less reactive, and present long and fine processes stemming from small somata. By contrast, activated microglia are often ovoid and less ramified, presenting large cell bodies but only a few short, thick extensions if any at all (Karperien et al., 2013).

A number of strategies have examined somatic features to assess microglial morphology, with activated microglia thought to exhibit larger and more irregular somata (Davis et al., 2017). Others use the ratio of soma to cell size (Hovens et al., 2014), the number of process endpoints (Morrison and Filosa, 2013) or the number of crossings of the cells on a grid superimposed on an image of them (Zanier et al., 2015), which provides an estimate for process coverage. Here, the imaged cells were reconstructed in 3D and their process length and ramification were analysed.

Historically, fully ramified microglia have been characterised as "resting". However, microglia are never truly resting, and these cells are instead actively engaged as vigilant sentinels. By extending and retracting their processes in all directions, microglia constantly scan their surroundings (Nimmerjahn et al., 2005). Microglial motility underpins their other functions; e.g. it is a crucial first step presumably required for the subsequent detection of pathogens or damage signals, towards which the cells exhibit directed motility (Madry and Attwell, 2015). While metabotropic $P2Y_{12}$ receptors are required for chemotaxis (Haynes et al., 2006), baseline surveillance operates independently of chemotaxis and is controlled by membrane voltage, the resting value of which (around -40 mV) is regulated by the two-pore domain K^+ channel THIK-1 (Madry et al., 2018). THIK-1 is the main K^+ channel expressed by

microglia *in situ*, and also promotes ramification of their processes (Madry et al., 2018). Here, as a prelude to further work in the thesis, I reproduced previous results that block of THIK-1 reduces microglial ramification in rodents, and then tested whether such an effect could be replicated in human microglia.

Another factor regulating microglial function is the TREM2 receptor, which has received great interest in the last few years. Microglial TREM2 receptors promote microglial phagocytosis (Lee et al., 2018; Takahashi et al., 2005; Wang et al., 2015; Zhao et al., 2018) and certain mutations in TREM2 increase the risk for AD (see section 1.2.4). In addition, TREM2 receptors also modulate microglial K^+ channels and membrane potential and so, like THIK-1, might regulate morphology and surveillance. Because various K^+ channels are reportedly downregulated in TREM2-deficient microglia (Ulland et al., 2017; Wang et al., 2015) and microglia from TREM2 KO are more depolarised (Zhao et al., 2018), it is conceivable that TREM2's role in phagocytosis arises, at least in part, from its modulation of microglial K^+ channels and membrane potential. This would be consistent with the idea that immune cells hyperpolarise when undertaking phagocytosis (Kouri et al., 1980). Considering the functional interaction between TREM2 and K^+ channels, I studied whether surveillance and morphology of microglia, controlled by THIK-1, are affected by TREM2 KO. In addition, I analysed microglial surveillance at various ages (from 1 to 10 months) and examined whether it was altered in TREM2 KO mice. Finally, I also examined how surveillance in TREM2 deficient mice was affected by THIK-1 inhibition.

In this chapter, as for the experiments presented throughout this thesis, microglia were studied *in situ* in acute brain slices or in slices from perfusion-fixed brains. This is because cultured microglia, which lack cues from their local and systemic environment, change their gene expression profile within minutes of being in culture (Bennett et al., 2018; Gosselin et al., 2017), and most isolation protocols use enzymatic dissociation of brain tissue, which further activates microglia (Marsh et al., 2020).

3.2 Microglial process length does not correlate with soma measures in physiological conditions

While the importance of microglial morphology is widely recognised and its quantitative analysis is used to infer microglial functional states (Karperien et al., 2013), no gold-standard for such interpretations exists to date. Here, three criteria were used for an initial evaluation of microglial morphology: soma area, soma circularity (calculated as $4\pi(\text{area}/\text{perimeter}^2)$) and total process length. To establish whether any correlation existed between them, brain slices from 7 wildtype mice were stained for the myeloid cell marker ionised calcium-binding adapter molecule 1 (Iba1), 124 microglia from the CA1 *stratum radiatum* in the hippocampus were imaged and all three variables were measured in each of them. This marker and brain region were used throughout the present study, unless otherwise indicated. For the analysis of process morphology, a method based on Sholl analysis was used as explained in detail in section 2.8.3. To test whether any morphological differences arose between young and adult mice, this analysis used cells from P30 and P100 animals.

Cells from both age groups showed a similar soma size (44.8 ± 1.2 µm at P30 and 47.2 ± 1.0 µm at P100, p=0.08), soma circularity (0.75 ± 0.01 at P30 and 0.71 ± 0.01 at P100, p=0.13) and process length (645 ± 32 µm at P30 and 683 ± 28 µm at P100, p=0.7; Figure 3.1).

The results contrasted with prior work implying an association between larger and less rounded soma (Davis et al., 2017), although there was a trend for such a correlation (but without reaching statistical significance, p=0.07; Figure 3.1A) when combining results from both ages (as no significant differences were detected between them). Of note, neither soma size (p=0.17; Figure 3.1B) nor soma circularity (p=0.16; Figure 3.1C) correlated with process length (although I cannot rule out a more significant correlation when microglial properties change in pathology). Given that brain surveillance by microglia is carried out by their processes, subsequent analysis of microglial morphology was done, not by focusing on

the soma, but by measuring the length and ramification of the processes to obtain a more reliable estimate of their surveillance capacity.

3.3 THIK-1 regulates microglial morphology in rodents and humans

Microglia from THIK-1 KO mice are less ramified (Madry et al., 2018). I confirmed that, in agreement with that previous report which used both pharmacology and genetic deletion to examine the effects of decreasing THIK-1 function, short-term block of THIK-1 with 50 µM tetrapentylammonium (TPA) resulted in deramification of microglia in acute brain slices from P12 rats. Because microglial processes at all branch orders, and not just first-branch processes, are motile (Nimmerjahn et al., 2005), the total process length was quantified for each cell and ramification was analysed throughout the process tree at increasing distances from the soma (as in Figure 2.4). Incubation with 50 µM TPA for 40 min significantly reduced microglial process length (by 32%, p=0.01) and ramification (p=0.004), as revealed by three-dimensional Sholl analysis (Figure 3.2).

Next, I tested whether THIK-1 also affects microglial morphology in human brain slices. Human microglia are morphologically similar to those in rodents (Geirsdottir et al., 2019) and they express THIK-1 at the RNA level (Galatro et al., 2017; Zhang et al., 2016). Having confirmed that impairment of THIK-1 leads to microglial deramification in rodents, I inhibited THIK-1 pharmacologically in living brain slices from adult human donors obtained from neurosurgery (since KO experiments are not possible) to test whether it could recapitulate the deramification observed in rodents. Acute block of THIK-1 channels by incubation with 50 µM TPA for 40 min significantly reduced microglial process length (by 33%, $p=10^{-9}$) and ramification ($p=10^{-4}$; Figure 3.3A-D). Block of THIK-1 with 50 µM bupivacaine, used for confirmation, also reduced the total process length (by 32%, p=0.01) and ramification (p=0.02; Figure 3.3E-H). Both TPA and bupivacaine also block ion channels other than THIK-1 (voltage-gated K^+ channels and voltage-gated Na^+ channels, respectively), but the fact that they have the same effect on microglial morphology suggests

that it is their effect on the two-pore domain channel THIK-1 that generates the change of morphology seen. Thus, block of THIK-1 function in microglia in living human slices can be achieved with short-term pharmacological treatment and has similar effects as in rodents.

3.4 TREM2 regulates microglial morphology and surveillance

TREM2 has been suggested to affect microglial numbers, activation and morphology in development (Filipello et al., 2018). I analysed the morphology of microglia from P30 perfusion-fixed TREM2 WT and KO mice, and observed a 17% increase in total process length ($p=0.03$) and ramification ($p=10^{-4}$) in the KO (Figure 3.4). Thus, unlike THIK-1, TREM2 seems to decrease microglial ramification.

To understand whether TREM2 (like THIK-1) plays a role in modulating microglial surveillance, I employed live two-photon imaging of EGFP-expressing microglia in acute brain slices from mice that expressed or lacked TREM2, and analysed surveillance on the single cell level (see details in section 2.9.2). For these experiments, I included older animals, as microglial motile responses are thought to be reduced by ageing (Damani et al., 2011) and TREM2 may function to support surveillance as dementia- or age-related changes occur (Poliani et al., 2015). Thus, I used mice at ages ranging from P30 to P300 to investigate whether ageing had any effect on surveillance, and whether any potential effects of TREM2 were age-dependent.

To calculate a surveillance index, the numbers of process extensions and retractions per minute (both of which are similarly fast; Nimmerjahn et al., 2005) were quantified over the duration of each recording by counting pixels that appear and disappear between consecutive frames of the binarised, maximum intensity-projected cells (Figure 3.5A). Two-way ANOVA analysis revealed an overall effect of age on surveillance, whereby microglia from older animals exhibited higher surveillance (Figure 3.5B-C). Surveillance was similar between microglia expressing and lacking TREM2 at P30 ($p= 0.89$) and P100 ($p=0.25$), but at P300 surveillance was 31% higher for TREM2 KO microglia ($p=10^{-3}$;

Figure 3.5B). Similarly, the initial slope of surveillance of the maximum intensity-projected cells over the first 2 min of imaging was similar between genotypes at P30 (p=0.22) and P100 (p=0.16), but 19% higher in the absence of TREM2 at P300 (p=0.04; Figure 3.5C). Consequently, the cumulative area surveyed after 10 min was increased by 26% in KO compared to WT at P300 ($p=7x10^{-4}$) but it was not different between genotypes at P30 (p=0.3) or P100 (p=0.11; Figure 3.5D). In summary, age increases surveillance, and TREM2 decreases it but only in old animals.

3.5 THIK-1-mediated control of surveillance is independent of TREM2

Finally, as THIK-1 and TREM2 have opposing actions on morphology and surveillance, I investigated whether their effects interact by superfusing brain slices from WT and TREM2 KO mice with 50 µM TPA for 20 min after imaging cells in unsupplemented aCSF for 20 min (Figure 3.6A). As expected, treatment with TPA resulted in deramification and decreased surveillance in microglia (Figure 3.6B). Of note, blocking THIK-1 reduced surveillance of both TREM2 WT and KO microglia, and did so in all three age groups studied (Figure 3.6C-E).

When calculating the percentage of baseline surveillance remaining when THIK-1 was blocked, the reduction of surveillance by TPA was stronger in younger animals (p=0.005 for the overall effect of age) but similar between TREM2 WT and KO mice (p=0.63 for the overall effect of genotype; Figure 3.7). This suggests that the role of THIK-1 in promoting surveillance is not dependent on expression of TREM2 but does depend on age.

3.6 Discussion

The work presented in this Chapter addressed the role of THIK-1 channels and TREM2 receptors in regulating microglial morphology and surveillance. The length and branching of the processes were analysed, rather than soma measures, which were found

not to correlate with microglial process length under physiological conditions. Acute THIK-1 block reduced microglial ramification *in situ* in brain slices from both rodents (as described previously by Madry et al., 2018) and humans. However, although TREM2 KO is reported to depolarise microglia, mimicking THIK-1 KO in this regard, TREM2 KO had the opposite effect to THIK-1 KO (i.e., it increased microglial ramification). Surveillance increased with age, and TREM2 KO also increased microglial surveillance but only in old (P300) mice. Finally, block of THIK-1, was more effective in decreasing microglial surveillance in younger animals but its effect was similar on microglia from TREM2 WT and KO mice.

Because no universal standard exists to classify microglia based on their morphology, comparisons across studies are difficult, particularly as the definitions used and variables measured differ. Here, I showed that the size and shape of somata are not related to those of processes (Figure 3.1), at least when considering variability in the physiological situation. Thus, I focused on the morphology of microglial processes as these are the elements that carry out surveillance of the brain parenchyma. The semi-automatic 3D reconstruction method used here (described in section 2.8.3) minimises manual input, thus increasing analysis speed and avoiding rater bias. However, it remains unclear which morphological features are more informative of microglial function. Several groups have proposed using a composite index to circumvent this issue (while minimising rater bias and avoiding loss of statistical power from correcting for multiple comparisons). After extracting morphology descriptors from the images (e.g. process length, perimeter, sphericity, soma area, number of end nodes or of segments per branch) and identifying which measures discriminate best between conditions, a composite morphological index can be obtained by running a principal component analysis on those descriptors (Clarke et al., 2021; Heindl et al., 2018). Such an approach may be more informative in future work.

I have shown that inhibiting THIK-1 rapidly affects microglial morphology in living brain slices from not only rats (Figure 3.2) but also humans (Figure 3.3), suggesting that it could potentially have clinical use. Various gaseous anaesthetics can be used to modulate THIK-1 *in vivo* (Madry et al., 2018). However, they could have multiple, opposing effects. For

instance, by blocking THIK-1, isoflurane decreases microglial process motility (Madry et al., 2018). On the other hand, however, neuronal hypoactivity (which such anaesthetics will induce) increases process extension (Liu et al., 2019; Umpierre et al., 2020). Thus, gaseous anaesthetics could lead to either a net decrease (Nebeling et al., 2019) or increase of surveillance *in vivo* (Liu et al., 2019; Stowell et al., 2019).

TREM2 mediates synapse remodelling in the hippocampus during development (Filipello et al., 2018), and may sense damaged synapses and contribute to their elimination in AD (Gratuze et al., 2020). Here, I examined a potential role for TREM2 in regulating process ramification and surveillance, which I expected to be required for such functions. There is controversy in this field: in one previous study, TREM2 KO led to hyperramification of microglial processes already at P18-20 (Filipello et al., 2018), which is consistent with the data presented here (at P30, Figure 3.4). By contrast, others found that changes of microglial morphology by TREM2 KO were only detectable in old mice (e.g. at 12 but not 6 months of age; Poliani et al., 2015).

An increase in ramification might be expected to increase surveillance (Madry et al., 2018), but TREM2 KO was found to increase surveillance only in old mice, and to have no effect in younger mice (Figure 3.5). The effect on surveillance in old mice is consistent with TREM2-mediated signalling leading to cytoskeletal rearrangements (Phillips et al., 2018), but the lack of a change of surveillance at young ages means that this is unable to explain the effect of TREM2 in mediating synapse remodelling during development (Filipello et al., 2018).

The finding that TREM2 deficiency alters surveillance only in old mice (Figure 3.5) is in agreement with the notion of effects of TREM2 being age-dependent (Linnartz-Gerlach et al., 2019). This has been shown before for process chemotaxis toward injury sites (which was impaired by TREM2 deficiency in 9-14 month-old mice but not in 3-5 month-old mice; Sayed et al., 2018). However, in contrast with my data, surveillance did not differ in either age group in that study. As their results were obtained by imaging the brain through cranial windows, rather than in brain slices as here, this may suggest that the effects of TREM2

deficiency depend on microglia being activated to some extent — which is likely to be the case in slices (Kurpius et al., 2006) and particularly in older animals (Del Moral et al., 2019). This would reconcile these findings with the fact that TREM2 dysfunction becomes more relevant during ageing and in disease.

The data presented here suggest that THIK-1 and TREM2 have opposing actions on microglial ramification and surveillance: THIK-1 increasing them (Figure 3.2–3.3,3.6) and TREM2 decreasing them in older mice (Figures 3.4–3.5). In agreement with these proteins having antagonistic effects, THIK-1 promotes activation of the NLRP3 inflammasome (Madry et al., 2018) while TREM2 restrains inflammation (Liu et al., 2020).

Reduction of microglial surveillance by THIK-1 block was not affected by TREM2 genotype, however, suggesting that TREM2 and THIK-1 mediated regulation of surveillance are independent (Figure 3.7). I considered whether TREM2 has its effect by modulating THIK-1 and these data would be consistent with TREM2 suppressing THIK-1, since TREM2 KO would then increase THIK-1 activity and hyperpolarise the cell, increasing ramification (Madry et al., 2018). Indeed, TREM2 reportedly controls expression of other K^+ channels and the membrane potential of microglia (Zhao et al., 2018). However, Zhao et al. (2018) found that TREM2 KO led to microglial depolarisation rather than hyperpolarisation. Further, the effect of TREM2 KO on membrane voltage was prevented when blocking K_v/K_{ir} channels (Zhao et al., 2018). Additional experiments are required to clarify whether any interaction exists between THIK-1 and TREM2, e.g. by testing whether THIK-1 expression or currents are altered in TREM2 KO animals.

Of note, my data indicate an increase of microglial motility with age (from P30 to P300; Figure 3.5). Little is known about how microglial baseline surveillance changes during life, but an *in vivo* study of cortical microglia reported a small but statistically significant decrease in microglial process motility in older mice (Hefendehl et al., 2014). There could be at least two reasons for such a discrepancy: first, a regional difference between cortex and hippocampus; second, the fact that I imaged microglia *ex vivo* (as discussed above). In line with this, some suggest that studies on brain slices, where long-range neuronal connections

are lacking, may alter microglial motility (Umpierre and Wu, 2020). Thus, future experiments will seek to reproduce (or refute) the presented results *in vivo*.

Interestingly, while microglial surveillance increases with age, the effect of THIK-1 block is smaller in older animals (Figure 3.7). This is in line with the reported downregulation of this channel with age (Hickman et al., 2013) and suggests that other K^+ channels might gain importance in promoting surveillance by maintaining the resting potential at old ages as THIK-1 expression declines. Future work should examine not just potential upregulation of other microglial channels in aged animals, but also whether compensation mechanisms arise in the absence of THIK-1 in the KO microglia.

The precise mechanisms controlling microglial surveillance are unknown, but they are likely to converge onto cytoskeletal dynamics. Inhibiting G_i signalling, which makes F-actin less compartmentalised, reduces process length, branching and surveillance of microglia (Merlini et al., 2021). Similarly, microglia expressing a mutant RhoA, a master regulator of actin dynamics, were less ramified (Socodato et al., 2020).

In terms of THIK-1 function specifically, it is also unclear how membrane voltage is linked to microglial ramification. Of note, acute optogenetic depolarisation of microglia using channelrhodopsin did not affect their morphology and decreased their surveillance only slightly (Laprell et al., 2021). Yet, pharmacological block of THIK-1, which also depolarises these cells, reduced both within minutes (Madry et al., 2018). Thus, this discrepancy is unlikely to reflect differential effects of short-term versus chronic depolarisation. Instead, it may be due to channelrhodopsin expression being restricted to somata and thus not affecting the membrane voltage of processes. Alternatively, it is possible that it is a change of $[K]_i$ and not membrane potential *per se* that regulates cytoskeletal changes (as THIK-1 block will raise $[K]_i$ but optogenetic depolarization will lower it). In agreement with this, it is a fall in $[K]_i$ that triggers inflammasome activation (Muñoz-Planillo et al., 2013).

This study has assessed the contribution of THIK-1 and TREM2 to the motility of microglial processes. Of note, microglial motility is complex and there are stark regional and compartmental differences in its regulation. For instance, isoflurane (which blocks THIK-1)

reduces the process motility of hippocampal (Madry et al., 2018) but not cortical microglia (Liu et al., 2019). On the other hand, cerebellar microglia are less ramified and they survey less (possibly because their expression of THIK-1 (*Kcnk13*) is lower than that in cortical/hippocampal microglia; Pan et al., 2020), but present a characteristic somatic motility, which their cortical counterparts lack (Stowell et al., 2018). This suggests that movement of processes and somata are regulated by different mechanisms and THIK-1 is unlikely to promote the latter. Similarly, it is worth noting that nanoscale sensing by filopodia, transient thin, hair-like structures located at the process tips, is not regulated by THIK-1 (Bernier et al., 2019). Moreover, processes extend rapidly upon activation of $P2Y_{12}$ (which decreases [cAMP]) but filopodia retract (Bernier et al., 2019). Together, these data suggest that the motility of the various cellular compartments is controlled by different mechanisms, and thus all conclusions here are restricted to the motility of large microglial processes.

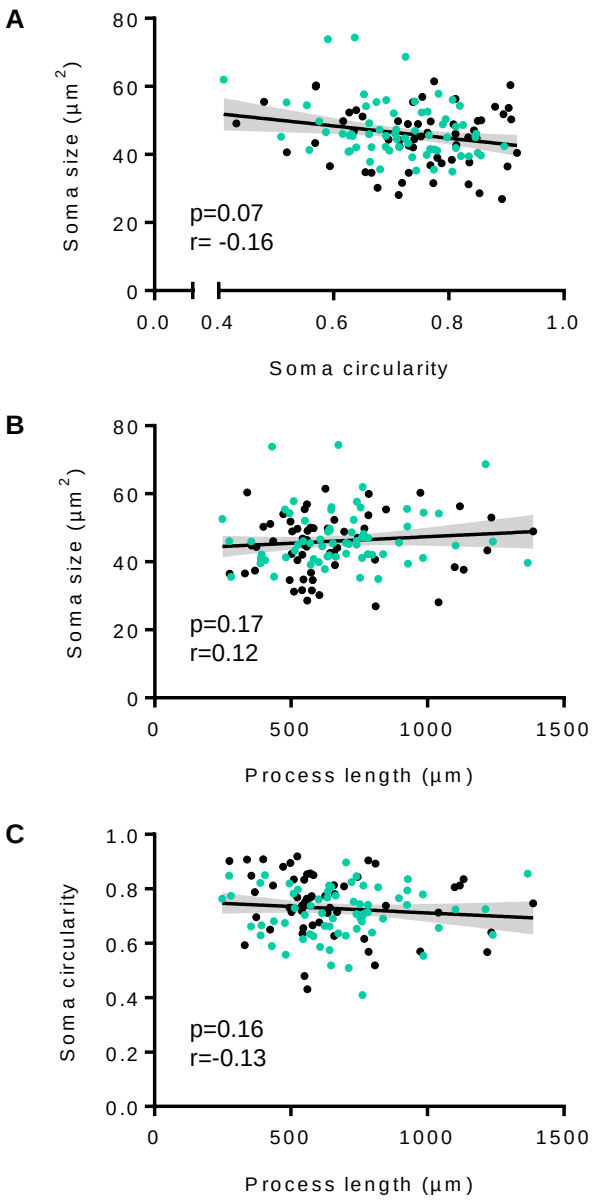

Figure 3.1. Microglial process length, soma size and roundness are not correlated in physiological conditions.

(A-C) Paired analysis of somatic and process measures of 124 hippocampal CA1 microglial cells from 7 wildtype mice at age P30 (black circles) or P100 (turquoise circles), showing no difference in morphology between age groups (see numbers in the main text) and a lack of correlation between (A) soma circularity and size, (B) soma size and process length and (C) soma circularity and process length. Error bands show 95% confidence bands of the best-fit linear regression for both age groups combined. Statistical significance was tested with Spearman's correlation.

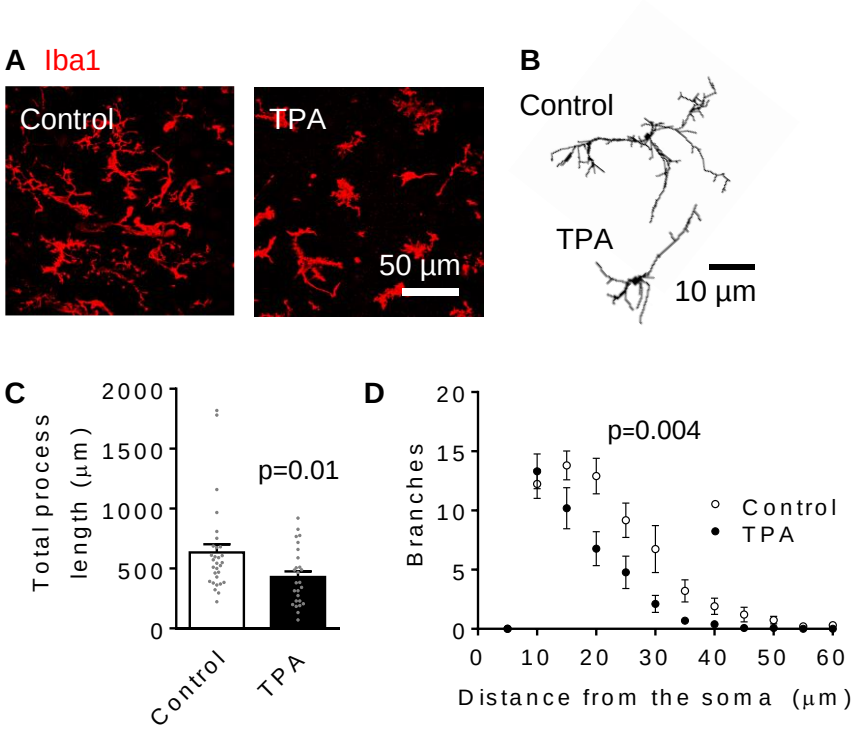

Figure 3.2. Block of THIK-1 deramified microglia in rat brain slices.

(A) Representative confocal images from rat hippocampal slices showing the effect of 50 µM TPA treatment (40 mins) on microglial morphology (Iba1, red), which decreased microglial ramification. **(B)** Representative 3D-reconstructed microglia. **(C-D)** Morphological analysis of microglia from control (30 cells from 2 animals) and TPA-treated microglia (26 cells from 2 animals), showing Sholl analysis-derived (C) total process length and (D) number of process branches at distances (in 5 µm increments) from the cell soma. Data shown as mean ± s.e.m. Statistical significance was tested with a Mann-Whitney test (C) or two-way ANOVA followed by Sidak's post-hoc tests for individual comparisons (D), using the cell as the statistical unit.

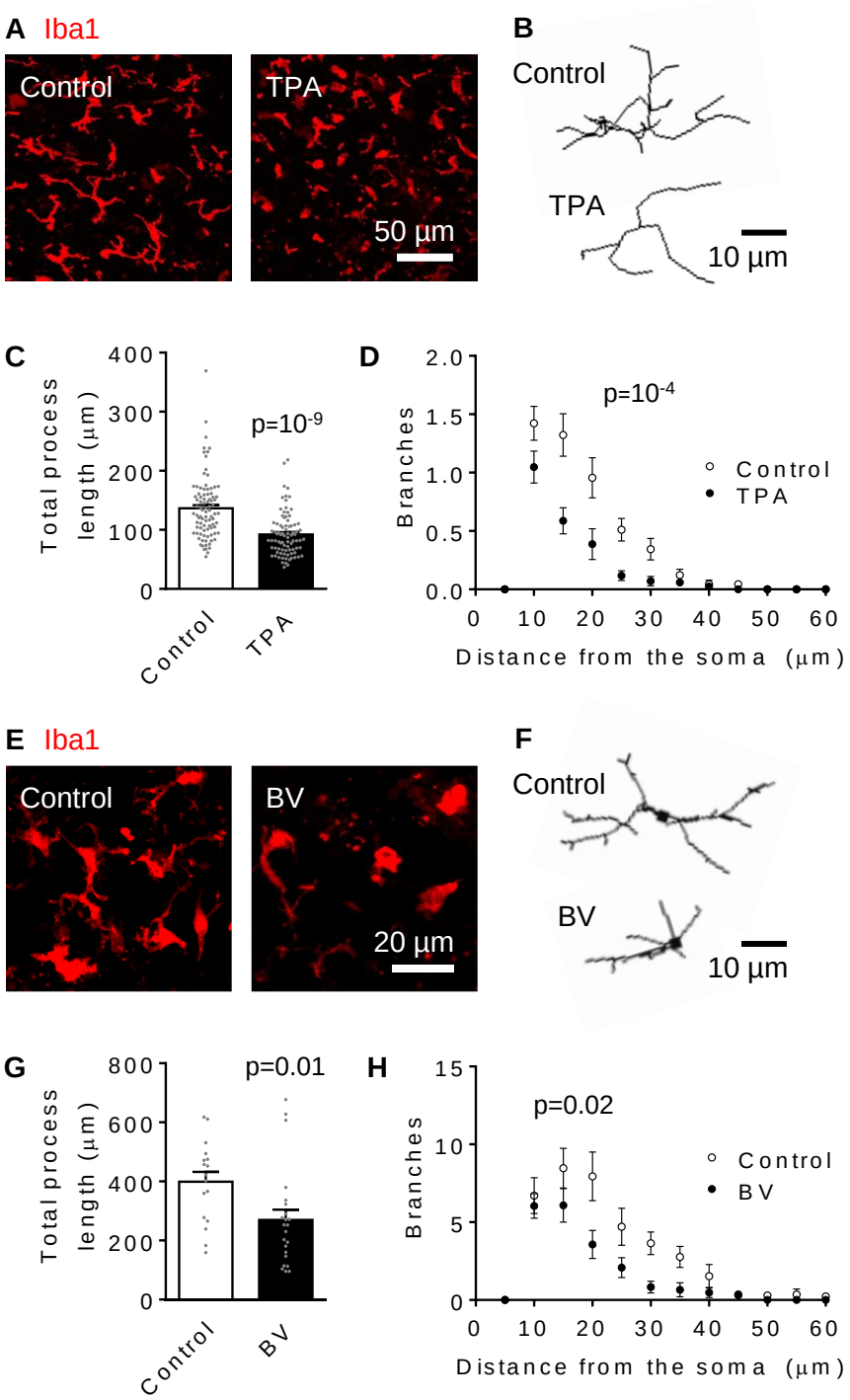

Figure 3.3. Block of THIK-1 deramified microglia in human brain slices.

(A) Representative confocal images from human cerebral cortical slices showing the effect of 50 µM TPA treatment (40 mins) on microglial morphology (Iba1, red), which decreased microglial ramification. **(B)** Representative 3D-reconstructed microglia. **(C-D)** Morphological analysis of microglia from control (90 cells from 3 human subjects) and TPA-treated

microglia (85 cells from 3 human subjects), showing Sholl analysis-derived (*C*) total process length and (*D*) number of process branches at distances (in 5 µm increments) from the cell soma. **(E-H)** As (A-D) but showing the effect of 50 µM bupivacaine treatment by comparing control (17 cells from one human subject) and bupivacaine-treated microglia (23 cells from one human subject). Data shown as mean ± s.e.m. Statistical significance was tested with Mann-Whitney tests (C, G) or two-way ANOVA followed by Sidak's post-hoc tests for individual comparisons (D, H), using the cell as the statistical unit.

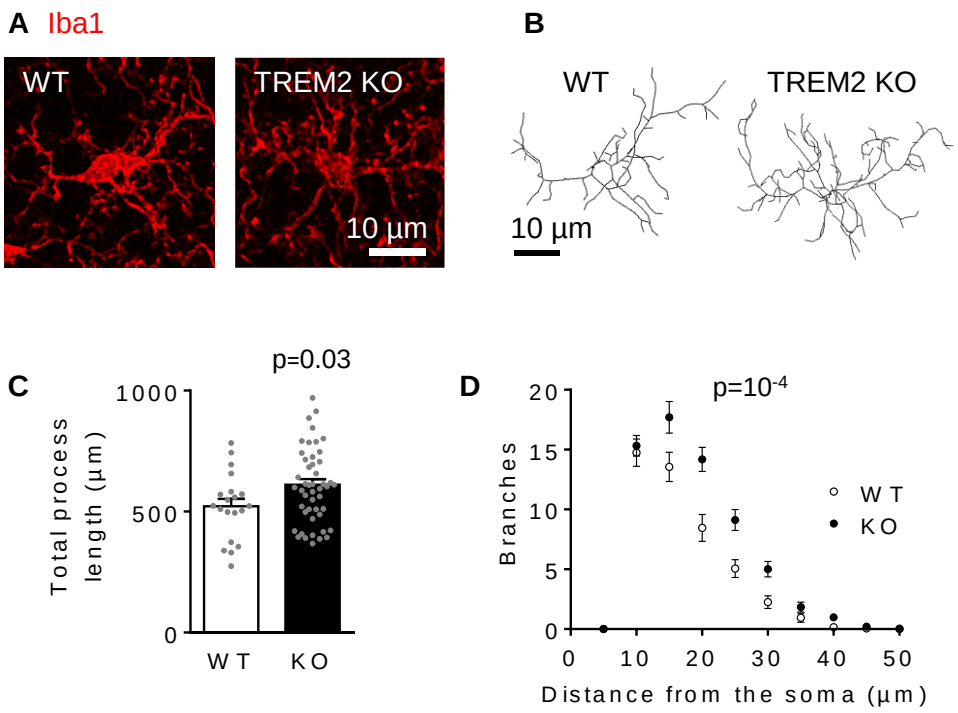

Figure 3.4. TREM2 knockout increased microglial ramification.

(A) Representative confocal images from P30 hippocampal microglia (Iba1, red) from wildtype (WT) and TREM2 knockout (KO) mice showing increased microglial ramification in the latter. **(B)** Representative 3D-reconstructed microglia. **(C-D)** Morphological analysis of microglia from WT (20 cells from one animal) and KO microglia (49 cells from 2 animals), showing Sholl analysis-derived (*C*) total process length and (*D*) number of process branches at distances (in 5 µm increments) from the cell soma. Data shown as mean ± s.e.m. Statistical significance was tested with unpaired two-tailed Student's t-test (C) or two-way ANOVA followed by Sidak's post-hoc tests for individual comparisons (D), using the cell as the statistical unit.

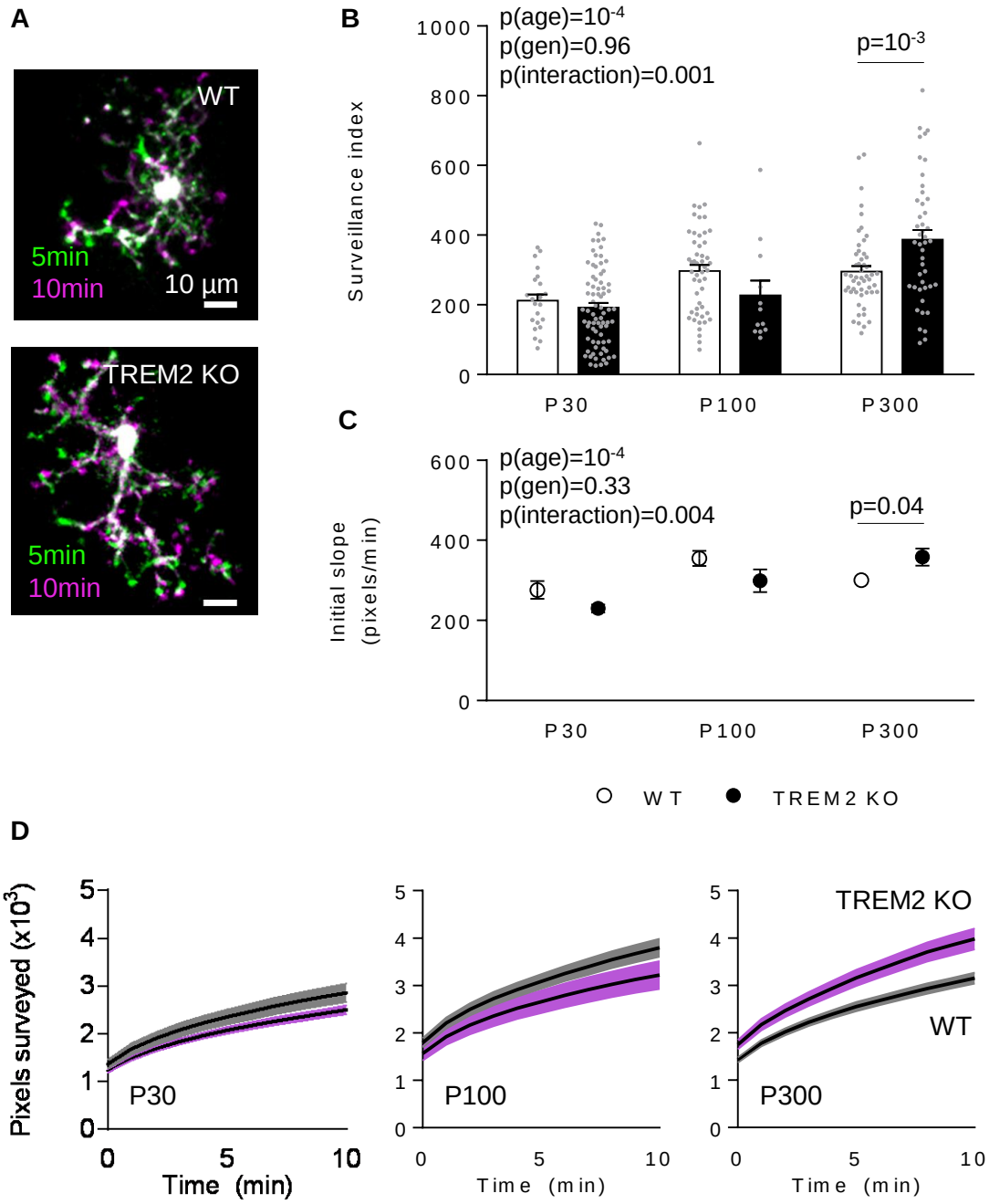

Figure 3.5. TREM2 knockout increased microglial surveillance in old mice.

(A) Representative two-photon images of EGFP-expressing microglia in slices from P300 wildtype (WT) and TREM2 knockout (KO) mice, showing an overlay of images taken 5 min apart to visualise process extensions (purple) and retractions (green) during this time interval. **(B)** Quantification of the surveillance index of microglia from WT or KO mice at age P30 (n=22 cells from 2 WT and 76 cells from 2 KO animals), P100 (50 cells from 3 WT

animals and 12 cells from 2 KO animals) and P300 (52 cells from 4 WT animals and 45 cells from 4 KO animals), showing that surveillance increased with age and that TREM2 deficiency increased surveillance only in P300 mice. Three significance values are given on the graph: p(age) assesses whether differences between ages achieve statistical significance; p(gen) assesses whether differences between genotype (with or without TREM2) achieve statistical significance; p(interaction) assesses whether differences between ages interact statistically significantly with differences due to genotype. **(C)** Initial slope of pixels surveyed in maximum-intensity projections of images of microglia from WT and TREM2 KO mice of each age group (measured in the first 2 min of recording, to avoid confounding by pixel overlap in the maximum-intensity projections). **(D)** Time course of the pixels surveyed per cell over 10 min (cumulative surveillance). Data shown as mean ± s.e.m. Statistical significance was tested with two-way ANOVA followed by Sidak's post-hoc tests for individual comparisons, using the cell as the statistical unit.

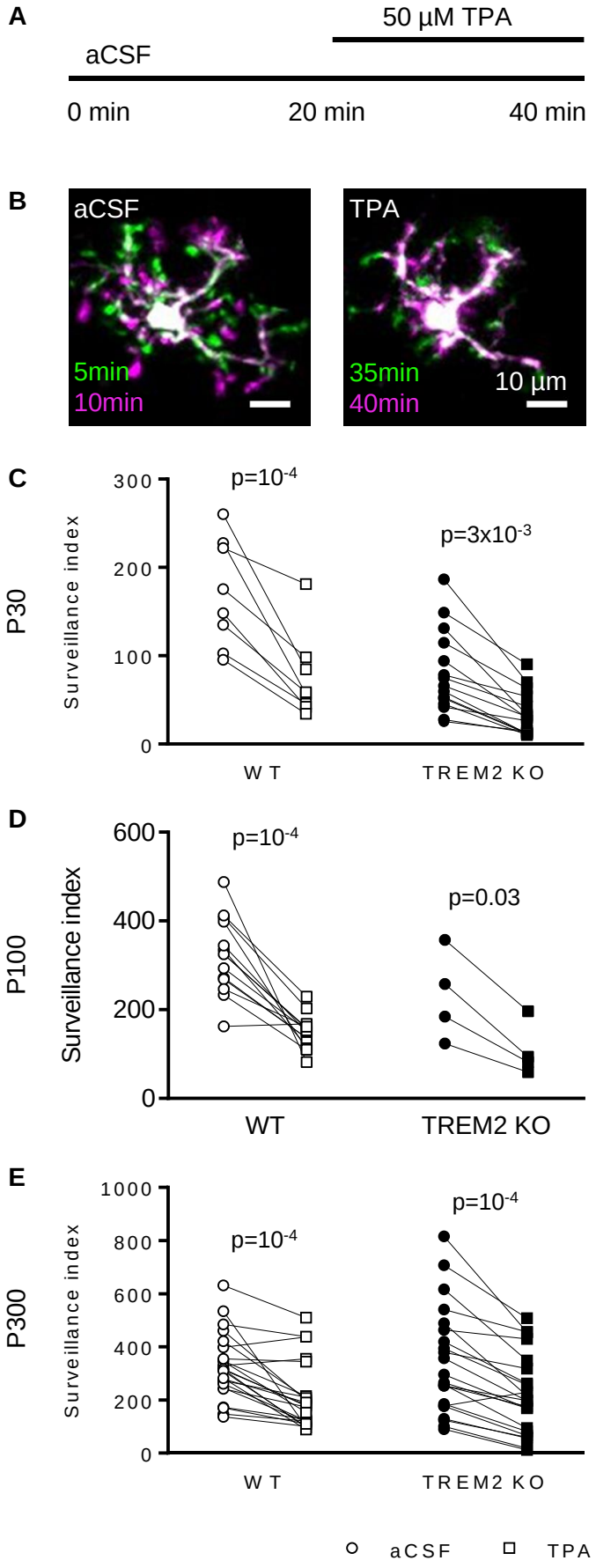
A
50 µM TPA
aCSF
0 min
20 min
40 min
B
aCSF
5min
10min
TPA
35min
40min
10 µm
C
P30
Surveillance index
300
200
100
0
p=10-4
p=3x10-3
WT
TREM2 KO
D
P100
Surveillance index
600
400
200
0
p=10-4
p=0.03
WT
TREM2 KO
E
P300
Surveillance index
1000
800
600
400
200
0
p=10-4
p=10-4
WT
TREM2 KO
aCSF
TPA

Figure 3.6. Block of THIK-1 reduced surveillance in TREM2 knockouts.

(A) Schematic of the experiment, showing superfusion of brain slices with 50 µM TPA for 20 min following 20 min of baseline recording in unsupplemented aCSF. **(B)** Representative two-photon images of EGFP-expressing microglia in a wildtype slice, before (left) and after (right) TPA treatment, showing an overlay of images taken 5 min apart to visualise process extensions (purple) and retractions (green) during each time interval. **(C-E)** Surveillance index before (circles) and after (squares) TPA treatment in wildtype (WT) and TREM2 knockout (KO) microglia from (C) P30, (D) P100 and (E) P300 animals, showing a decrease of surveillance by TPA in all groups (n=8 WT and 15 KO cells for P30, 14 WT and 4 KO cells for P100, 22 WT and 24 KO cells for P300). Data shown as mean ± s.e.m. Statistical significance was tested with two-way ANOVA followed by Sidak's post-hoc tests for individual comparisons, using the cell as the statistical unit.

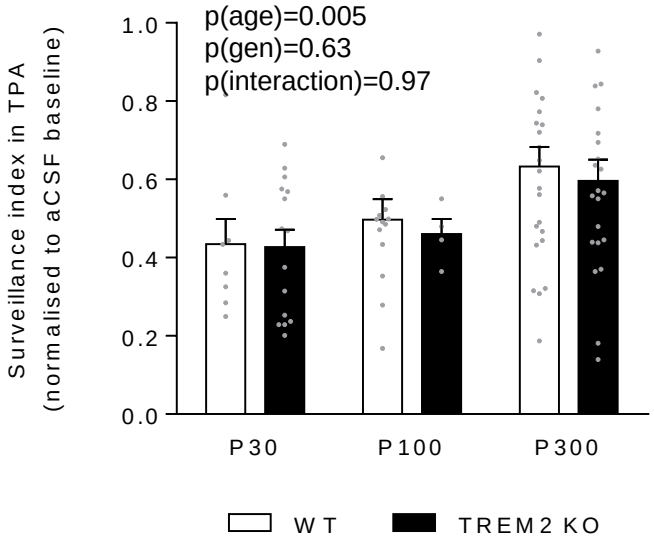

Figure 3.7. Reduction of surveillance by THIK-1 block was stronger in younger animals and occurred independently of TREM2 expression.

Fraction of baseline surveillance remaining after treatment with 50 μM TPA for 20 min, showing a more drastic reduction of surveillance by TPA at younger ages, and that this effect was not different between wildtype (WT) and TREM2 knockout (KO) microglia in any of the age groups analysed (n=8 WT and 15 KO cells for P30, 14 WT and 4 KO cells for P100, 24 WT and 22 KO cells for P300). Data shown as mean ± s.e.m. Statistical significance was tested with two-way ANOVA followed by Sidak's post-hoc tests for individual comparisons, using the cell as the statistical unit. Three significance values are given on the graph: p(age) assesses whether differences between ages achieve statistical significance; p(gen) assesses whether differences between genotype (with or without TREM2) achieve statistical significance; p(interaction) assesses whether differences between ages interact statistically significantly with differences due to genotype.

4. Regulation of microglial phagocytosis

4.1 Introduction

Microglia can internalise and degrade targets that they have previously detected and contacted. This process, referred to as phagocytosis, occurs throughout life in both physiological and pathological conditions. Microglia can phagocytose both dead and viable cells (Brown and Neher, 2014), myelin sheaths (Hughes and Appel, 2020) and amyloid debris (Lee et al., 2018).

However, microglia are more than mere cleaners of the brain parenchyma. These cells are key for normal brain development (Hong et al., 2016b) and their processes interact with various neuronal compartments. While microglial contacts at non-synaptic regions regulate dendrite branching and axonal pathfinding during development as well as neuronal excitability, contacts at synaptic sites control synapse formation, strength, plasticity and elimination (Badimon et al., 2020; Cserép et al., 2020a; Pfeiffer et al., 2016). Microglia-synapse contacts can lead to formation of dendritic spines as well as new filopodia in spine heads (Miyamoto et al., 2016; Weinhard et al., 2018). On the other hand, microglia-mediated circuit pruning also occurs as redundant or less active synapses are removed (Paolicelli et al., 2011; Schafer et al., 2012). Synapse phagocytosis is controlled by a fine balance between "eat-me" and "don't-eat-me" signals, which respectively promote removal (e.g. C1q or C3/CD11b; Wilton et al., 2019) or protect synapses from pruning (e.g. CD47; Lehrman et al., 2018). A number of signalling pathways are involved in microglia-mediated removal of synapses during development, including complement factors in the visual system (Stevens et al., 2007) or the fractalkine receptor (Basilico et al., 2019; Paolicelli et al., 2011) and TREM2 (Filipello et al., 2018) in the hippocampus.

Microglial THIK-1 K^+ channels maintain ramification of microglial processes and their surveillance of the brain (Madry et al., 2018), so I investigated whether they also promote the elimination of synapses during development by phagocytosis (or “nibbling”, termed

trogocytosis; Weinhard et al., 2018). As immune cells have been shown to hyperpolarise when phagocytosing targets (Kouri et al., 1980), the hyperpolarisation maintained by microglial THIK-1 channels might also promote phagocytosis directly. Regulation of phagocytosis by membrane potential could also explain why phagocytosis is impaired in TREM2 KO mice where microglia are depolarised (Zhao et al., 2018). Finally, because developmental mechanisms are thought to be reactivated during ageing and disease (Dejanovic et al., 2018; Hong et al., 2016a; Vasek et al., 2016; Werneburg et al., 2020; Wu et al., 2019), understanding the mechanisms controlling microglial phagocytosis may suggest therapeutic aproaches for the mature brain. Therefore, I also examined the role of THIK-1 in adult human microglia to see whether its modulation could affect synapse number.

4.2 Microglial phagocytosis is regulated by K^+ channels

Ion channels and receptors controlling microglial motility might be involved in phagocytosis. These include $P2Y_{12}$ receptors that regulate ATP-evoked microglial chemotaxis to an injury site (Haynes et al., 2006) and THIK-1 K^+ channels which regulate microglial morphology and surveillance (Madry et al., 2018). It was previously reported that $P2Y_{12}$ receptors regulate phagocytosis (Blume et al., 2020; Diaz-Aparicio et al., 2020), but the role of microglial K^+ channels is still unknown. Therefore, I first tested whether blocking THIK-1 (the dominant K^+ channel expressed in “resting” microglia) affects microglial phagocytosis *in situ* in brain slices from P12 rats. Following a recovery period of a few hours after brain slicing, which allows some microglial activation to occur (Kurpius et al., 2006), fluorophore-labelled resin microbeads were applied (Krabbe et al., 2012, 2013) onto rat hippocampal slices in the presence or absence of pharmacological blockers (Figure 4.1A). Beads were coated with serum prior to their addition to the brain slices to further boost microglial phagocytosis (Bohlen et al., 2017).

Microglia engulf and phagocytose their substrates thanks to membrane protrusions and phagocytic cups, the formation of which relies upon cytoskeletal rearrangements (Mao

and Finnemann, 2015). Indeed, microglia were seen to form phagocytic cups and engulf microbeads *in situ* (Figure 4.1B-C). As negative control experiments, I incubated the brain slices at 4ºC, or in the presence of the actin inhibitor cytochalasin D, both of which disrupt cytoskeletal dynamics (Albert et al., 1998). I found that both conditions potently blocked phagocytosis (by 90% and 87%, respectively; $p=10^{-4}$ compared to control for both; Figure 4.2). MRS2578, a blocker of the $P2Y_6$ receptor which is known to regulate microglial phagocytosis (Koizumi et al., 2007; Wen et al., 2020) also reduced the fraction of microglia that were phagocytic (by 31%, $p=10^{-3}$; Figure 4.2).

Potassium efflux across the microglial membrane via THIK-1 was previously found to control NLRP3 activation (Madry et al., 2018; Muñoz-Planillo et al., 2013). I found that elevating the extracellular K^+ concentration ($[K^+]_o$) to prevent such efflux and depolarise the cells reduced the fraction of microglia that were phagocytic by 29% ($p=10^{-3}$; Figure 4.3). This was done in the presence of tetrodotoxin (TTX) to block voltage-gated Na^+ channels and thus action potential-evoked synaptic transmitter release from neurons (TTX had no effect by itself: p=0.9; Figure 4.3). To determine how the raised $[K^+]_o$ altered phagocytosis, I applied blockers of different K^+ channel types. Blocking Ca^{2+}-activated K^+ channels with charybdotoxin had no significant effect (p=0.7), but both the K^+ channel blockers bupivacaine and tetrapentylammonium (TPA) reduced phagocytosis by a third (p=0.01 and 10^{-4}, respectively, for treatment with 50 µM of each drug compared to control; Figure 4.3). Since bupivacaine blocks both two-pore domain channels and voltage-gated Na^+ channels while TPA blocks both two-pore domain channels and voltage-gated K^+ channels (Lotshaw, 2007; Piechotta et al., 2011), these data are consistent with K^+ efflux via THIK-1 (or downstream changes in microglial membrane voltage, V_m) regulating phagocytosis.

Because the pharmacology of these drugs is not entirely specific for THIK-1, I also used a THIK-1 KO mouse line, where I found that deletion of THIK-1 had a similar inhibitory effect on microglial phagocytosis: the fraction of phagocytic microglia was reduced by 59% in THIK-1 KO mice compared to WT littermates ($p=2x10^{-4}$; Figure 4.4).

4.3 THIK-1 regulates microglial phagocytosis of synapses

Deficits in microglial phagocytosis could result in impaired pruning of synapses during development (Schafer et al., 2013), so we tested the effects of THIK-1 KO on hippocampal synapse numbers. Using P17-P19 mice, when synapse pruning in the hippocampus is near its peak (Paolicelli et al., 2011; Weinhard et al., 2018), I assessed the labelling of presynaptic (Bassoon) and postsynaptic glutamatergic (Homer1) markers in the *stratum radiatum* of the CA1 hippocampal region by immunohistochemistry (McLeod et al., 2017). A colocalisation of both markers was taken to indicate an excitatory synapse (Figure 4.5A). In the THIK-1 KO, while no postsynaptic change was detected ($p=0.9$), the fraction of the imaged area labelled by the presynaptic marker approximately doubled compared to that in WT littermates ($p=0.02$). As a result, the derived total synaptic area (defined as overlap of Bassoon and Homer1 labelling) was 57% higher in KO mice ($p=0.03$; Figure 4.5D). The increase in colocalisation was produced by a 67% increase in the number ($p=0.03$; Figure 4.5E), but not the size ($p=0.8$; Figure 4.5H), of presynaptic terminals, with no change in the number or size of postsynaptic terminals ($p=0.2$; Figure 4.5F,I).

In addition, I used Western blots to quantify the amount of Homer1 protein present in RIPA-soluble protein lysates from the hippocampus of P17 WT and THIK-1 KO mice, which confirmed no change in the KO ($p=0.3$; Figure 4.6). Lastly, I used Golgi-Cox staining to study whether THIK-1 deletion altered dendritic spine density of hippocampal CA1 neurons in these mice. The results again confirmed no effect of THIK-1 deletion on postsynaptic elements at P17 ($p=0.7$; Figure 4.7).

To demonstrate that the increase in presynaptic terminal number in the KO was caused by a reduction of phagocytosis, I next assessed the presence of Bassoon puncta inside Iba1-labelled microglia (Figure 4.8A). In THIK-1 KO mice, Bassoon colocalisation with microglia was significantly reduced (Figure 4.8B). Taken together, these data suggest that THIK-1 regulates the number of glutamatergic synapses by promoting microglial uptake of presynaptic material.

4.4 THIK-1 regulates excitatory synaptic transmission

To further confirm that THIK-1 regulates removal of functional excitatory synapses, I collaborated with Hiroko Shiina from our lab, who performed whole-cell voltage-clamp recording of CA1 pyramidal neurons from P17-19 mice (Figure 4.9). The sEPSC frequency was enhanced in pyramidal neurons from THIK-1 KO compared to WT mice ($p=0.004$), with no amplitude alteration ($p=0.1$; Figure 4.9A-C). Since this increase in the KO could be due either to a higher number of excitatory synapses or to higher activity (or an increased vesicle release probability) of presynaptic neurons, we bath-applied TTX to block action potential-mediated neurotransmitter release. Consistent with immunolabelling results showing more synapses in the KO (Figure 4.5), the mEPSC frequency approximately doubled in THIK-1 KO pyramidal neurons compared to in WT cells ($p=0.006$), without a change in the mean amplitude of the mEPSCs ($p=0.4$; Figure 4.9A,D-E).

We tested postsynaptic effects of THIK-1 deficiency electrophysiologically (Figure 4.9F-G) by bath-applying the glutamate receptor agonists NMDA (to activate NMDA receptors, 10 µM; Figure 4.9F) and kainic acid (to activate AMPA/KA receptors, 1 µM; Figure 4.9G). Consistent with immunolabelling, Western blot and Golgi-Cox staining experiments showing no effect on postsynaptic terminals (Figures 4.5–4.9), electrophysiological experiments revealed no significant differences between the THIK-1 KO and WT in their NMDA- and kainate-induced macroscopic currents ($p=0.5$ and 0.7, respectively; Figure 4.9F-G). Thus, THIK-1 deficiency selectively enhances the number of excitatory presynaptic release sites without affecting: (i) the postsynaptic glutamate receptor density (as assessed from the spontaneous and miniature EPSC amplitudes), (ii) the number of postsynaptic terminals (assessed either immunohistochemically or by counting dendritic spines), or (iii) the total (synaptic plus extrasynaptic) glutamate receptor number (assessed from the response to NMDA and kainate).

The effect of THIK-1 deletion on synapse levels did not result from an altered number of microglia, as overall microglial density and distribution in the hippocampal and cortical

areas analysed were all similar in WT and THIK-1 KO mice (Figure 4.10). Altogether, our data suggest that THIK-1 deficiency leads to an increase in the number of functional excitatory synapses, which is due to THIK-1 regulating microglial internalisation of excitatory presynaptic terminals, presumably via its effect on the microglial membrane potential.

4.5 Block of THIK-1 affects synapse density in human brain slices

Finally, to assess the relevance of my findings to understanding the human brain, I again used live human cortical slices obtained from neurosurgically-resected tissue to study acute effects of THIK-1 block. Having confirmed that impairment of THIK-1 leads to microglial deramification both in rodents (Figure 3.2) and in live human microglia *in situ* (Figure 3.3), here I studied whether pharmacological inhibition of THIK-1 could recapitulate in human brain slices the effect on synapses seen in rodents, where deletion of THIK-1 increased the number of excitatory synapses (Figure 4.5). Perhaps surprisingly (see Discussion) given the brief period of block (40 min treatment), the fractional area of the image that was labelled for the vesicular glutamate transporter 1 (vGluT1), an excitatory presynaptic marker, was increased by 25% in the TPA-treated slices ($p=2x10^{-4}$; Figure 4.11A-B). I obtained similar effects on microglial ramification and synapse number when treating slices with bupivacaine ($p=0.003$; Figure 4.11C-D). Bupivacaine and TPA have different targets but both block two-pore K^+ channels (see above), consistent with THIK-1 mediating the effects seen (although the possibility that these drugs share another, unreported target cannot be excluded). Taken together, these data suggest that THIK-1 channels control synapse levels not only in rodents but also in the adult human brain.

4.6 Discussion

The work presented in this Chapter addressed the role of THIK-1 in controlling microglial phagocytosis and identified effects of its pharmacological block or genetic deletion

on synapse numbers and function. First, using pharmacological blockers and THIK-1 KO mice, I found that lack of THIK-1 activity reduced microglial phagocytosis. Second, I investigated possible effects on synapse pruning in the hippocampus. Postnatal (P17-19) mice lacking THIK-1 expression had an increased number of glutamatergic synapses, which was due to impaired removal of presynaptic terminals by THIK-1 KO microglia. Third, in microglia in living human brain slices, blocking THIK-1 rapidly increased synaptic density.

Microglia are not merely passive support cells. Instead, they continuously survey the brain parenchyma and control neuronal function. THIK-1 channels, the main K^+ channels in "resting" microglia, regulate their ramification, surveillance and cytokine release (Madry et al., 2018). Here, using pharmacology and THIK-1 knockout mice, I demonstrated that microglial phagocytosis is also controlled by THIK-1 (Figures 4.3–4.4). Furthermore, both immunohistochemistry and electrophysiology showed that the number of hippocampal excitatory synapses is increased in THIK-1 KO mice (Figures 4.5, 4.9).

The requirement of THIK-1 for phagocytosis may in part be due to its role in enhancing microglial ramification and surveillance, which will increase the probability of a microglial cell encountering a target to phagocytose. However, the tonically active THIK-1 channel may also promote phagocytosis by keeping microglia hyperpolarised (Madry et al., 2018), since a hyperpolarised membrane voltage is associated with phagocytosis in macrophages (Kouri et al., 1980). A depolarised membrane potential is also seen in TREM2 KO microglia, in which phagocytosis is reduced (Zhao et al., 2018).

This study indicates that THIK-1-mediated promotion of synapse loss is mainly via a presynaptic effect (Figures 4.5–4.9). While others have reported internalisation of postsynaptic materials as well (Paolicelli et al., 2011; Sipe et al., 2016; Wang et al., 2020a), there is now evidence that microglial phagocytosis preferentially targets presynaptic compartments both in health (Lee et al., 2021a; Schafer et al., 2012; Weinhard et al., 2018) and disease (Gunner et al., 2019; Vasek et al., 2016; Werneburg et al., 2020). This might be partly due to "eat-me" tags (such as C1q; Györffy et al., 2018; or PtdSer; Scott-Hewitt et al., 2020) being preferentially located on presynaptic sites.

Adult rodent (Wang et al., 2020a) and human (Tzioras et al., 2019) microglia continue to internalise synapses into adulthood, after the normal developmental period is over, which might be detrimental if excessive (Salter and Stevens, 2017). In adult mice, memories persist better when microglia are depleted (Wang et al., 2020a). In live brain slices from adult human donors, I found that even short-term application of THIK-1 blockers increased the amount of presynaptic vGluT1 puncta (Figure 4.11), which suggests a fast removal (and presumably replacement) of synapses. Work on hippocampal slices has shown that individual presynaptic internalisation events are rapid (frequently shorter than 3 minutes; Weinhard et al., 2018). However, turnover of synapses is generally low *in vivo*, taking from hours to months (Grutzendler et al., 2002; Majewska et al., 2006; Trachtenberg et al., 2002), which contrasts with my data (Figure 4.11) that suggest rapid replacement in acute brain slices. Synapse turnover may be much faster *ex vivo* due to microglia being partly activated and neurons being damaged by the slicing procedure (Fiala et al., 2003). Indeed, slicing leads to a loss of spines and synaptic responses (Eguchi et al., 2020). This parallels the acceleration of synapse loss reported in traumatic brain injury in humans, although that occurs over days (Jamjoom et al., 2021). Despite these differences with the *in vivo* situation, my results suggest a role of microglial THIK-1 in regulating human synapse turnover.

Synapse loss is a strong indicator of cognitive decline (DeKosky et al., 1996; Long and Holtzman, 2019; Terry et al., 1991). Synaptic deficits precede amyloid deposition in animal models of dementia (Cummings et al., 2015) and microglial phagocytosis of synaptic material is increased in AD patients (Tzioras et al., 2019). Ablation of microglia rescues synaptic loss and reduces memory impairment in mouse models of dementia (Spangenberg et al., 2016). Thus, manipulating microglia-synapse interactions may provide clinical benefit for cognitive impairment. Specifically, being able to block microglial phagocytosis in a time-controlled manner could help protect synapses from removal. It would be interesting to test whether short-term block of THIK-1 *in vivo* (e.g. using THIK-1-blocking anaesthetics such as isoflurane or sevoflurane) results in an increase in synapse number, and the magnitude and duration of any such effect in normal ageing, brain injury and dementia models. Microglial

responses (and especially phagocytosis) are crucial for the development and progression of dementia (Podleśny-Drabiniok et al., 2020). Since amyloid-targeting therapies have all failed, possibly because therapeutic interventions are given too late (Long and Holtzman, 2019), it would be advantageous to devise therapeutic agents that control phagocytosis to prevent synapse loss early on. The potential involvement of THIK-1 in regulating microglial responses in a model of amyloid pathology will be examined in detail in the next Chapter.

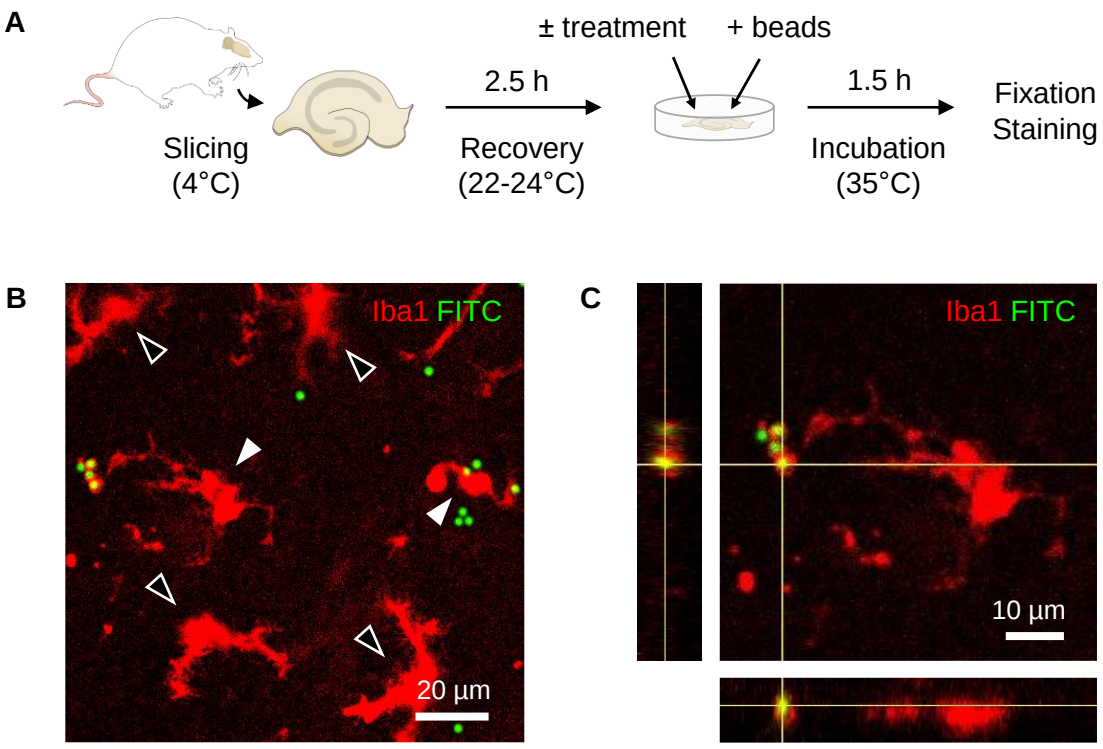

Figure 4.1. Microglia phagocytosed fluorophore-labelled microbeads *in situ.*

(A) Diagram of the phagocytosis assay. **(B)** Representative maximum intensity projection of a confocal z-stack of microglia (Iba1, red) in acute hippocampal rat slices incubated with 3 µm microbeads (FITC, green). Black arrowheads indicate non-phagocytic cells, white arrowheads indicate phagocytic cells. Some microbeads remain outside microglia. **(C)** Close-up of the phagocytic microglial cell at the left of panel (A). Orthogonal projections at the level of the crosshairs show engulfment of the fluorescent microbeads inside a phagocytic cup.

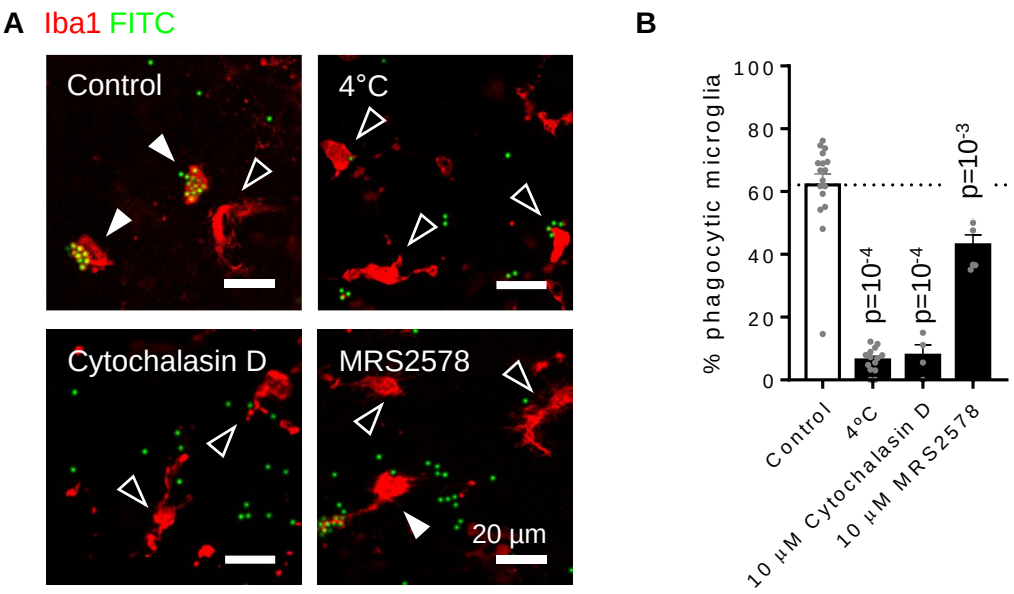

Figure 4.2. Pharmacological inhibition of microglial phagocytosis *in situ*.

(A) Representative single plane images of microglia (Iba1, red) in acute hippocampal rat slices incubated with 3 µm microbeads (FITC, green), at 35°C (control, 10 µM cytochalasin D or 10 µM MRS2578 (a $P2Y_6$ blocker)) or 4°C. Black arrowheads indicate non-phagocytic cells, white arrowheads indicate phagocytic cells. **(B)** Percentage of microglia that phagocytosed microbeads in each condition, showing a reduction by exposure to cold (4°C), cytoskeletal disruption (cytochalasin D) or block of $P2Y_6$ receptors (MRS2578) (control: n=17 slices from 4 animals; 4°C: n=14 slices from 4 animals; cytochalasin D: n=4 slices from one animal; MRS2578: n=6 slices from 3 animals). Data shown as mean ± s.e.m. P-values compare with control and statistical significance was tested with one-way ANOVA followed by Dunn's multiple comparison tests using brain slices as the statistical unit.

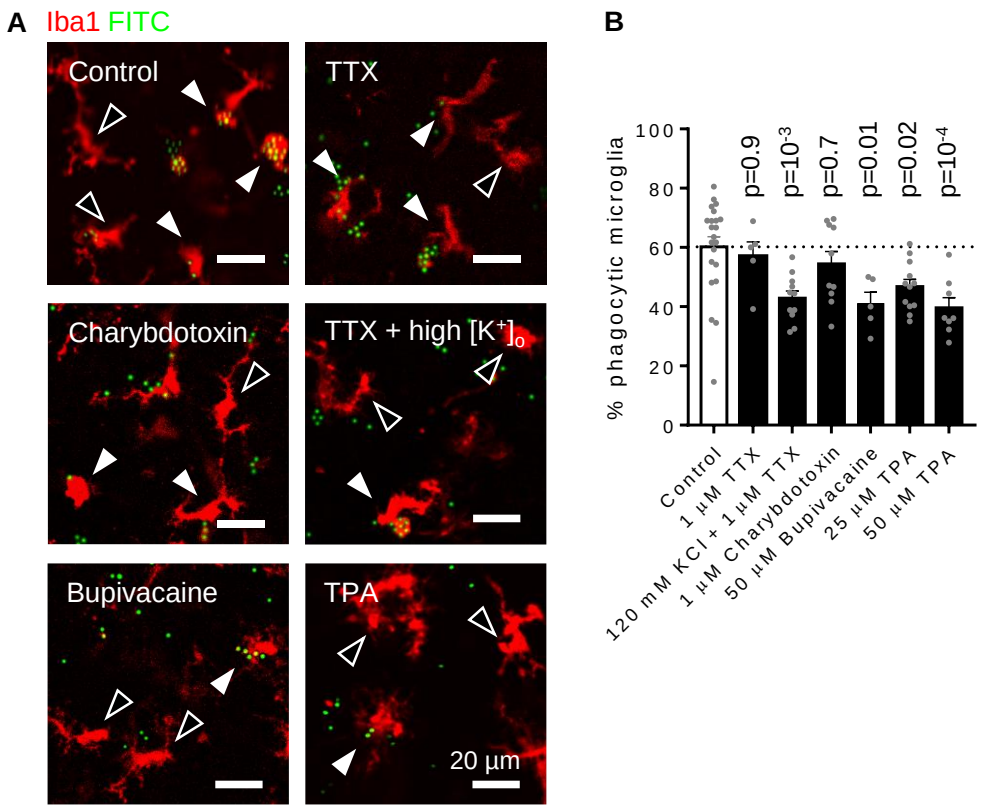

Figure 4.3. Two-pore domain K^+ channels control microglial phagocytosis *in situ*.

(A) Representative single plane images of microglia (Iba1, red) in acute hippocampal rat slices incubated with 3 µm microbeads (FITC, green), either untreated (control) or treated with 1 µM tetrodotoxin (TTX), 1 µM TTX + 120 mM KCl (high $[K^+]_o$), 1 µM charybdotoxin, 50 µM bupivacaine or 50 µM tetrapentylammonium (TPA). Black arrowheads indicate non-phagocytic cells, white arrowheads indicate phagocytic cells. Some microbeads remain outside microglia. **(B)** Percentage of microglia that phagocytosed microbeads in each condition, showing a reduction by high $[K^+]_o$ and two-pore K^+ channel block (bupivacaine, TPA) but not by calcium-activated K^+ channel block (charybdotoxin) (control: n=22 slices from 6 animals; TTX: n=5 slices from 2 animals; TTX + 120 mM KCl: n=11 slices from 4 animals; charybdotoxin: n=10 slices from 4 animals; bupivacaine: n=5 slices from 2 animals; 25 µM TPA: n=12 slices from 3 animals; 50 µM TPA: n=8 slices from 3 animals). Data shown as mean ± s.e.m. P-values compare with control and statistical significance was tested with one-way ANOVA followed by Dunn's multiple comparison tests using brain slices as the statistical unit.

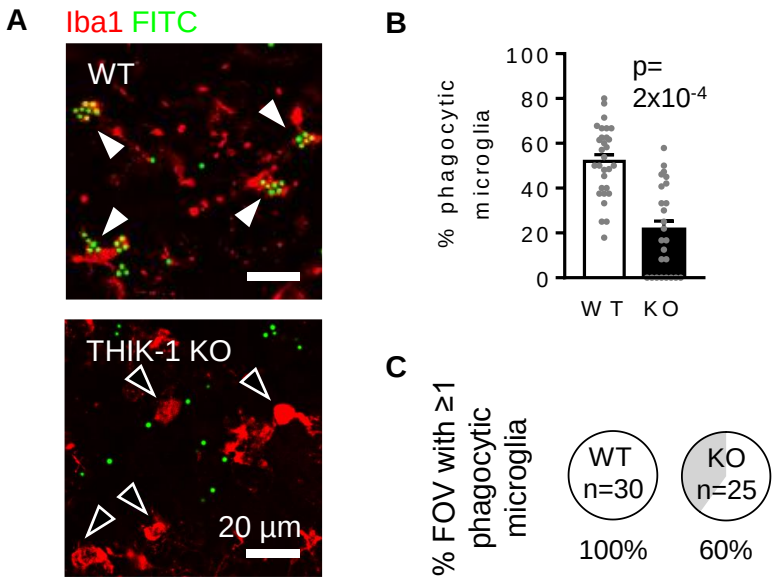

Figure 4.4. THIK-1 K^+ channels control microglial phagocytosis *in situ.*

(A) Representative single plane images of microglia (Iba1, red) in acute hippocampal slices from wildtype (WT) and THIK-1 knockout (KO) mice incubated with 3 µm microbeads (FITC, green). **(B)** Percentage of microglia that phagocytosed microbeads in each genotype, showing a reduction in the KO. Data shown as mean ± s.e.m. **(C)** Doughnut charts showing that only 60% of the analysed fields of view (FOV) contained phagocytic microglia in the KO, while all did in the WT (significantly different by Chi-squared test: p=0.0005). The number of total microglia per FOV was not different (WT: 15.0 ± 1.8, KO: 12.3 ± 2.1; p=0.34) between genotypes. Statistical significance was tested with Mann-Whitney tests using brain slices as the statistical unit.

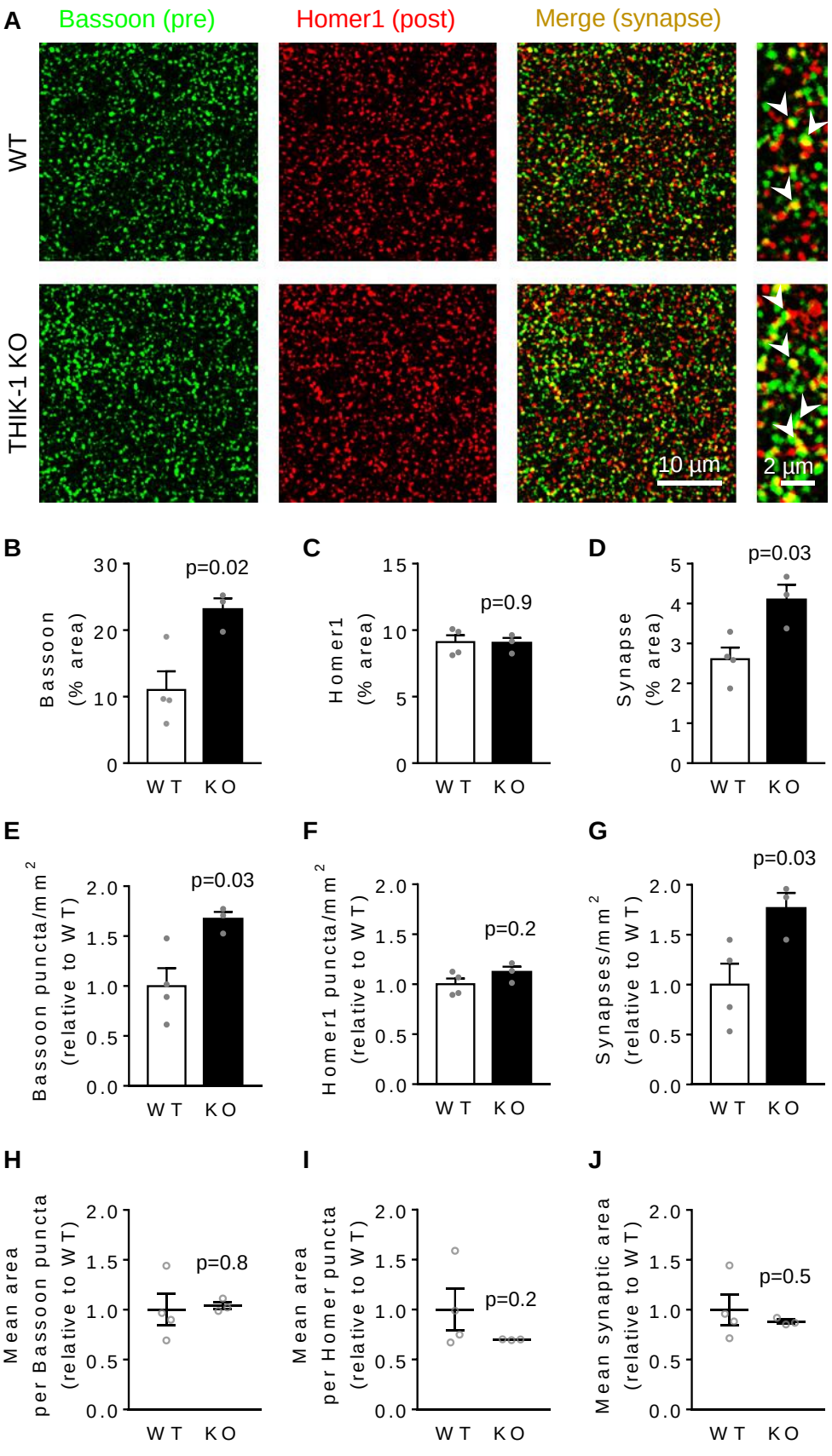
A
Bassoon (pre)
Homer1 (post)
Merge (synapse)
WT
THIK-1 KO
10 µm
2 µm
B
Bassoon (% area)
p=0.02
C
Homer1 (% area)
p=0.9
D
Synapse (% area)
p=0.03
E
Bassoon puncta/mm2 (relative to WT)
p=0.03
F
Homer1 puncta/mm2 (relative to WT)
p=0.2
G
Synapses/mm2 (relative to WT)
p=0.03
H
Mean area per Bassoon puncta (relative to WT)
p=0.8
I
Mean area per Homer puncta (relative to WT)
p=0.2
J
Mean synaptic area (relative to WT)
p=0.5
WT
KO

Figure 4.5. THIK-1 deletion increased synapse number in the developing hippocampus.

(A) Representative confocal images from the CA1 *stratum radiatum* of wildtype (WT) or THIK-1 knockout (KO) mice at P17-P19, showing the presynaptic marker Bassoon (green) and the excitatory postsynaptic marker Homer1 (red). The merged image and expanded views on the right show colocalised puncta (yellow). **(B-D)** Quantification of the area covered by (B) Bassoon, (C) Homer1 and (D) colocalised puncta, showing an increased fraction of the imaged area labeled for synapses in KO mice. **(E-G)** Quantification of the numbers of (E) Bassoon, (F) Homer and (G) synaptic puncta per mm^2, showing increased numbers of presynaptic puncta and synapses in KO mice. Average numbers in WT mice were 53 puncta/100 μm^2 for Bassoon, 42 puncta/100 μm^2 for Homer1 and 26 synapses/100 μm^2. **(H-J)** Quantification of (H) Bassoon, (I) Homer and (J) overlapping puncta size, showing no changes in synaptic terminal size in KO mice (WT: n=4 animals; KO: n=3 animals; 3 confocal stacks from 5 brain slices averaged per animal). Data shown as mean ± s.e.m. Statistical significance was tested with Mann-Whitney tests using animals as the statistical unit.

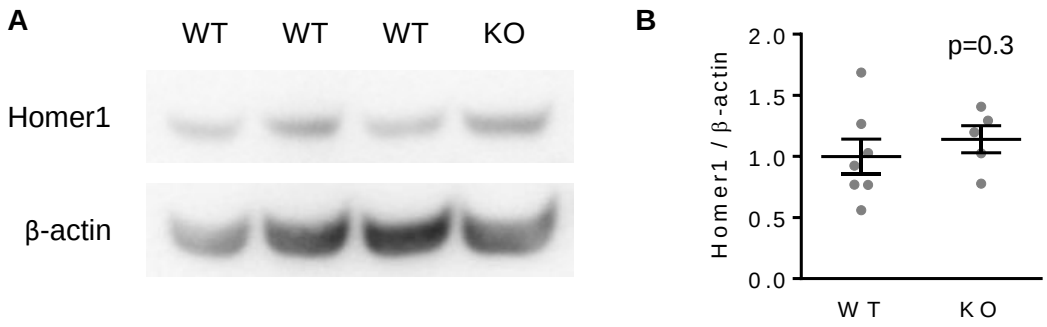

Figure 4.6. THIK-1 deletion did not affect Homer1 protein levels in the developing hippocampus.

(A) Representative Western blot of RIPA-soluble lysates from hippocampi of P17 mice expressing (WT) or not expressing (KO) THIK-1 channels. **(B)** Densitometric analysis of blot signals normalised by β-actin expression, showing no changes in levels of Homer1 protein in the hippocampus of THIK-1 KO mice (WT: n=7 animals; KO: n=5 animals). Data shown as mean ± s.e.m. Statistical significance was tested with a Mann-Whitney test using animals as the statistical unit.

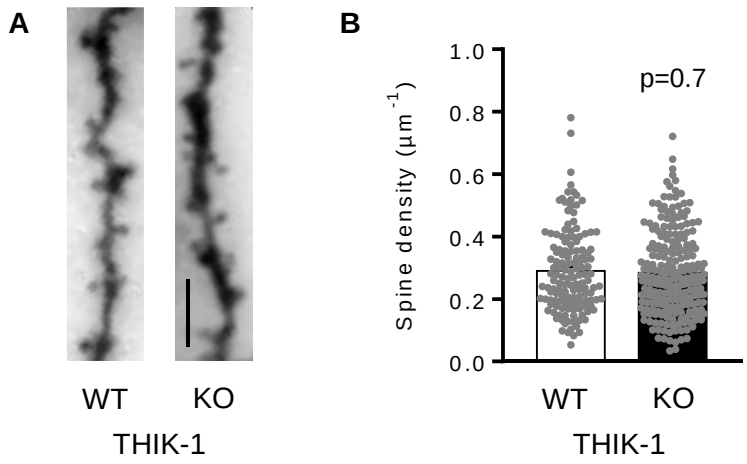

Figure 4.7. THIK-1 deletion did not affect spine density in the developing hippocampus.

(A) Representative images of Golgi-Cox-stained non-primary apical CA1 dendritic segments from P17 mice that were either wildtype (WT) or knockout (KO) for THIK-1. Scale bar: 5 µm. **(B)** Quantification of spine density in the analysed dendritic segments, showing no difference between WT and KO mice (n=138 dendrites from 4 WT mice and 219 dendrites from 5 KO mice). Data shown as mean ± s.e.m. Statistical significance was tested with a Mann-Whitney test using dendrites as the statistical unit.

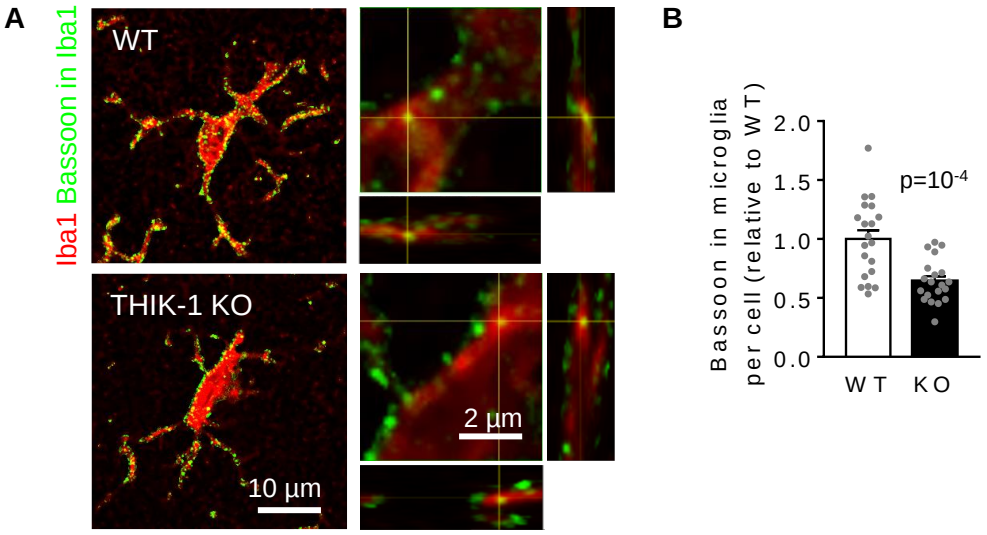

Figure 4.8. THIK-1 deletion decreased microglial phagocytosis of presynaptic material in the developing hippocampus.

(A) Representative confocal images showing Bassoon puncta (green) located within microglia (Iba1, red). On the right, close-up of microglial processes with orthogonal projections at the level of the crosshairs showing Bassoon puncta within microglia. **(B)** Quantification of the area of Bassoon puncta colocalising with each microglial cell, showing a decrease in KO microglia (WT: n=20 cells from 4 animals; KO: n=20 cells from 3 animals). Data shown as mean ± s.e.m. Statistical significance was tested with an unpaired two-tailed Student's t-test using cells as the statistical unit.

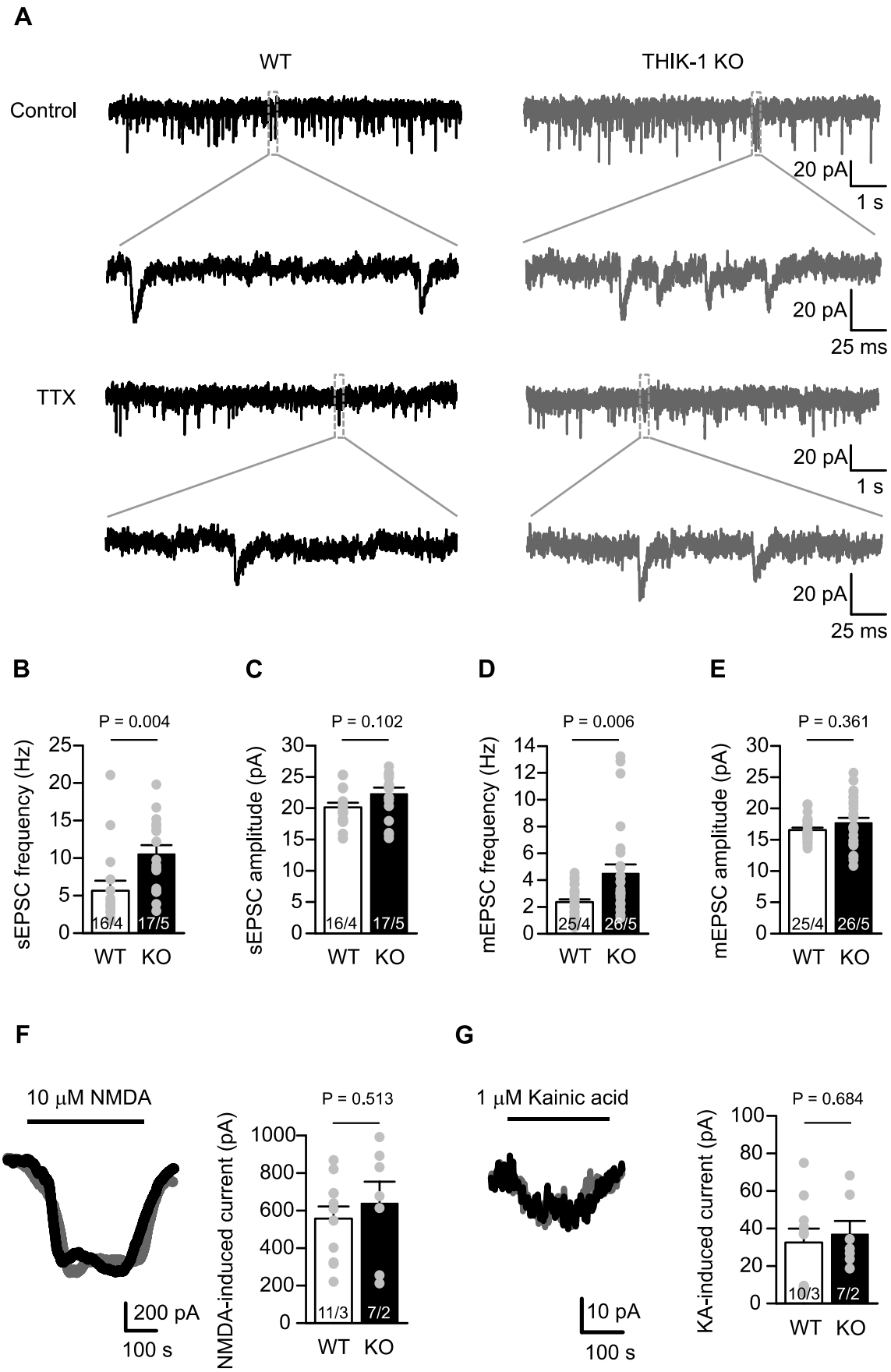
A
WT
THIK-1 KO
Control
TTX
20 pA
1 s
20 pA
25 ms
20 pA
1 s
20 pA
25 ms
B
P = 0.004
sEPSC frequency (Hz)
16/4
17/5
WT
KO
C
P = 0.102
sEPSC amplitude (pA)
16/4
17/5
WT
KO
D
P = 0.006
mEPSC frequency (Hz)
25/4
26/5
WT
KO
E
P = 0.361
mEPSC amplitude (pA)
25/4
26/5
WT
KO
F
10 μM NMDA
200 pA
100 s
P = 0.513
NMDA-induced current (pA)
11/3
7/2
WT
KO
G
1 μM Kainic acid
10 pA
100 s
P = 0.684
KA-induced current (pA)
10/3
7/2
WT
KO

Figure 4.9. THIK-1 deletion increased excitatory synaptic transmission in the developing hippocampus.

(A) Representative current traces from whole-cell voltage-clamped CA1 pyramidal neurons (V_h = -65 mV, E_{Cl} = -62mV) in WT (black, left) and THIK-1 KO (grey, right) hippocampal slices. The top two rows show spontaneous EPSCs (sEPSCs), i.e., including both miniature EPSCs (mEPSCs) and those evoked by spontaneous action potentials. The bottom two rows show mEPSCs in 500 nM TTX. The second and fourth row traces expand the indicated areas in the first and third rows. **(B-C)** Bar graphs showing sEPSC (B) frequency and (C) amplitude, comparing WT and THIK-1 KO. Grey circles overlaid show raw values in individual cells. Numbers on bars are of cells/animals, and s.e.m. values use cells as the statistical unit. **(D-E)** As for C-D but showing mEPSC (D) frequency and (E) amplitude, comparing WT and THIK-1 KO in 500 nM TTX. **(F)** Representative traces of whole-cell currents (V_h = -40 mV, E_{Cl} = -62 mV) from WT (black) and THIK-1 KO (red) hippocampal CA1 pyramidal cells, and bar graph of mean current induced by 10 µM NMDA bath application to WT and THIK-1 KO cells. **(G)** As for (F) but applying 1 µM kainic acid. Data shown as mean ± s.e.m. Statistical significance was tested with Mann-Whitney tests (B, D, E) and unpaired two-tailed Student's t-tests (C, F, G) using cells as the statistical unit.

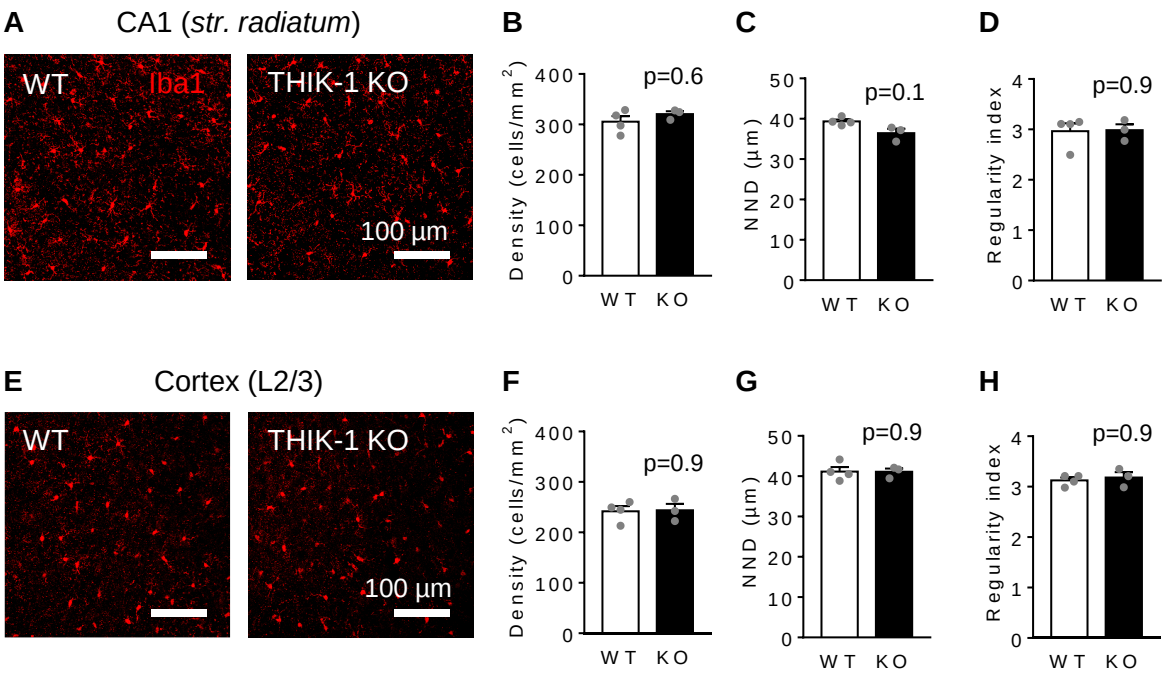

Figure 4.10. Microglial density and spatial distribution were not changed in the hippocampus or cortex of THIK-1 knockout mice.

(A) Representative maximum intensity projection of confocal z-stacks showing hippocampal microglia from the CA1 *stratum radiatum* area (Iba1, red) in wildtype (WT) and THIK-1 knockout (KO) mice. **(B-D)** Quantification of (B) microglial density, (C) average nearest-neighbour distance (NND) and (D) regularity index, showing no differences between genotypes. **(E-H)** As (A-D) but for microglia from cortical layer 2/3 (WT: n=4 animals; KO: n=3 animals; 5 slices averaged per animal). Data shown as mean ± s.e.m. Statistical significance was tested with Mann-Whitney tests using animals as the statistical unit.

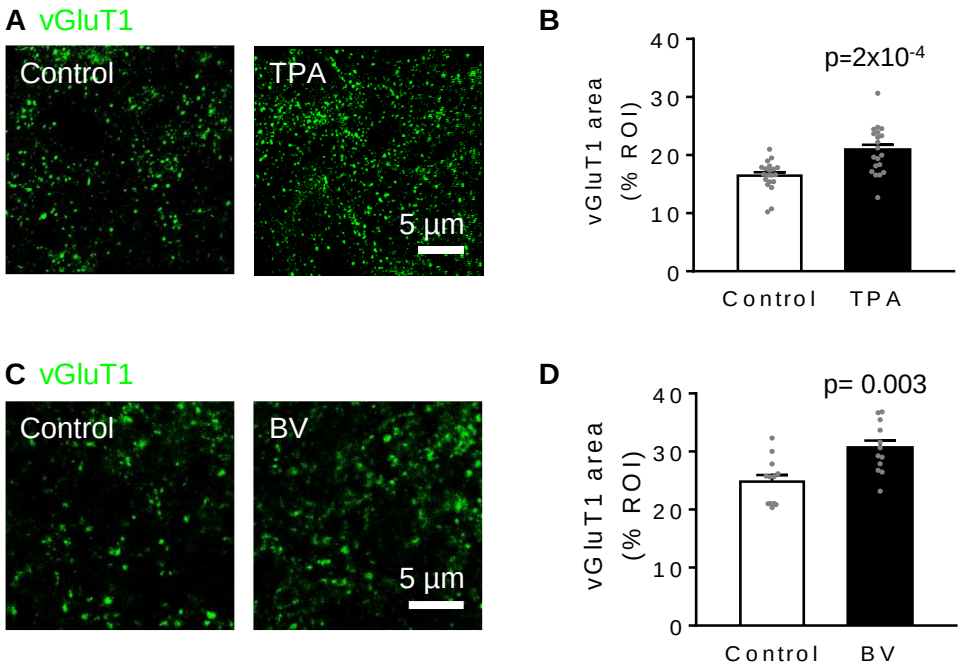

Figure 4.11. Block of THIK-1 increased presynaptic density in human brain slices.

(A) Representative SRRF-confocal images of human slices incubated in the absence or presence of TPA (which blocks THIK-1), showing vGluT1 puncta (green). **(B)** Quantification of the area covered by vGluT1, showing an increase in TPA-treated slices compared to controls (20 slices from 2 human subjects per condition). **(C)** As (A) but for slices incubated in the absence or presence of bupivacaine (which also blocks THIK-1). **(D)** As (B) but showing an increase in bupivacaine-treated slices compared to controls (12 per condition from one human subject). Data shown as mean ± s.e.m. Statistical significance was tested with unpaired two-tailed Student's tests using brain slices as the statistical unit.

5. Regulation of microglial responses to Aβ

5.1 Introduction

This chapter examines three key responses of microglia to the Aβ generated in Alzheimer's disease (AD): reactive oxygen species (ROS) generation, morphological changes and phagocytosis of Aβ.

The main toxic Aβ species generated excessively in AD is $A\beta_{1-42}$, a small ~4.5 kDa peptide produced by the cleavage of the amyloid precursor protein (APP) on neuronal membranes by β- and γ-secretases (O'Brien and Wong, 2011). Aβ oligomers have multiple downstream actions, including generating hyperexcitability of neurons by preventing glutamate uptake (Zott et al., 2019), disassembly of synaptic sites (Purro et al., 2012), and hyperphosphorylation of the cytoskeletal protein tau (Jin et al., 2011) which leads to synaptic dysfunction and cognitive decline (Polydoro et al., 2009). Following on from previous work (e.g. Suo et al., 1998), recent findings in our group demonstrated that Aβ also causes pericyte-mediated constriction of brain capillaries during AD, which leads to reduced cerebral blood flow via a mechanism involving ROS (Nortley et al., 2019). Oxidative stress has been linked to AD (Tönnies and Trushina, 2017) and, in cortical brain autopsies from AD patients, pathology correlated with expression of the regulatory subunits of the superoxide-producing NADPH oxidase (NOX; Shimohama et al., 2000). Here, I added to pharmacological studies on blood flow performed by Ross Nortley and Chanawee Hirunpattarasilp by directly testing whether acute exposure to Aβ increases ROS levels in brain slices, and which cells generate the ROS (which I suspected would include microglia; Della Bianca et al., 1999).

While therapeutic strategies for AD have primarily focused on targeting antibodies to Aβ or the enzymes that generate it (Anderson et al., 2017), intrinsic removal of Aβ remains poorly understood. Phagocytosis by glial cells is essential to regulate brain function during health and disease (Raiders et al., 2021). In early AD, as Aβ starts to accumulate, glial phagocytosis of Aβ (as well as Aβ clearance across endothelial cells into the blood or lymph;

Rasmussen et al., 2018) is thought to limit its deposition (Long and Holtzman, 2019). Impaired phagocytic function of glial cells during later stages of AD might contribute to worsened disease outcome (Krabbe et al., 2013; Wendt et al., 2017), but the underlying mechanisms are largely unknown.

Although microglia are generally considered the professional phagocytes of the CNS, astrocytes are also competent phagocytic cells with important roles during both health and disease (Basak et al., 2012; Chung et al., 2013). In phagocytic cells, phagosomes mature by fusing with lysosomes to form highly acidic phagolysosomes and mobilising the phagocytosed material for enzymatic degradation. The pH of phagosomal organelles during this maturation process is progressively reduced to ~5.5-4.5 (Canton, 2014). To understand how Aβ pathology builds up during the disease, a better understanding of Aβ degradation is required, including the identification of how different cells and receptors contribute to its clearance. Here, to study Aβ phagocytosis by glial cells, I replaced the microbeads in the slice assay (see Chapter 4, Figure 4.1) by the fluorescent Aβ derivative $A\beta^{pH}$, kindly provided by collaborators from Purdue University. This reporter becomes fluorescent at acid pH values, and hence upon internalisation into lysosomes, as these provide an acidic environment.

Aβ oligomers are ultimately deposited as extracellular plaques in AD brain, where the balance between clearance and deposition determines the progression of amyloid pathology (Long and Holtzman, 2019). Given the role of THIK-1 in regulating phagocytosis (Chapter 4.2), I tested whether THIK-1 affects phagocytosis *in vivo* in animals depositing Aβ by crossing THIK-1 KO with $App^{NL\text{-}G\text{-}F}$ mice. I quantified Aβ plaque load in the brain of these mice at 4 months of age, and assessed synaptic changes as well as lysosomal load in their microglia as a proxy for phagocytic function, both in the presence or absence of THIK-1 expression.

5.2 Microglia and pericytes release ROS in response to Aβ

In AD, combined production of Aβ oligomers and tau dysfunction are known to cause neuronal damage and synaptic loss, which result in cognitive impairment (Long and Holtzman, 2019). However, epidemiological data show that vascular factors are important contributors to AD risk, and biomarker research has shown that the first change in AD is a decrease of cerebral blood flow (Iturria-Medina et al., 2016). In a study from our group to which I contributed, pericytes were seen to constrict capillaries both in *App*$^{NL-G-F}$ mice and in human AD patients with cognitive decline that were depositing Aβ. Furthermore, pericyte constriction of human capillaries increased with Aβ burden (Nortley et al., 2019).

Crucially, Aβ-evoked vasoconstriction was found to require ROS. In rat cortical slices, the constriction was blocked by inhibiting all NOX isoforms with diphenyleneiodonium or by scavenging with SOD1 the superoxide generated when Aβ activates NOX (Nortley et al., 2019). These results suggested the involvement of NOX-mediated ROS generation in the Aβ-evoked capillary constriction. Thus, I aimed to quantify changes in oxidative stress induced by Aβ exposure and to identify its source.

Oligomers are the molecular species believed to be responsible for the toxic effects of Aβ (Klein et al., 2001; Koffie et al., 2009). Here, Aβ was oligomerised (as per the protocol in section 2.3.4) and silver staining of SDS-PAGE gels was used to assess the degree of aggregation. The predominant species produced, other than monomers, had a molecular weight of 2 to 4 times that of monomers (Figure 5.1A). For the experiments in this section, I applied soluble $A\beta_{1-42}$ at 72 nM (oligomeric plus monomeric, calculated from the monomeric molecular weight), which is comparable to the soluble Aβ concentrations found in the post mortem brains of AD patients (Roberts et al., 2017).

To assess changes in oxidative stress in response to Aβ, I employed imaging of the ROS sensor dihydroethidium in brain slices, which generates fluorescence when oxidised dihydroethidium intercalates into DNA (Figure 5.1B). Dihydroethidium has been widely used

to image ROS production by immune cells, both in our group (De Simoni et al., 2008) and by others (Park et al., 2017; Wu et al., 2012).

Exposure to Aβ oligomers for 40 minutes evoked a two-fold increase of ROS generation in the brain slices, as assessed by dihydroethidium fluorescence (Figure 5.1C-D). Adding superoxide dismutase (SOD1) abolished the Aβ-evoked ROS production (Figure 5.1C-D), confirming that the signal was generated by superoxide or a species derived from it (Gutteridge, 1985).

Next, I assessed which cell type generated ROS in response to Aβ. Previous work had suggested that ROS can be generated in response to Aβ by microglia (Della Bianca et al., 1999) or perivascular macrophages (Park et al., 2017), both of which label for Iba1. However, the cells showing the brightest oxidised dihydroethidium fluorescence were located on capillaries, had the morphology of pericytes, and labelled for NG2 but not Iba1 (Figure 5.2A), implying that they are pericytes. I quantified the ROS signal generated in regions of interest placed over the nuclei of Iba1-labelled immune cells or NG2-expressing cells on capillaries (pericytes), in 6 slices not exposed to Aβ (containing a total of 238 Iba1-labelled cells and 128 pericytes) and 8 slices exposed to Aβ (containing 270 Iba1-labelled cells and 171 pericytes). Aβ significantly increased ROS production in immune Iba1-expressing cells by a factor of 1.8 ($p=0.05$) and in pericytes by a factor of 7.3 ($p=0.001$). Taking into account the different numbers and basal ROS production of each cell type revealed that Aβ-evoked 6.4-fold more total ROS generation by pericytes than by immune cells (Figure 5.2B), at least for these experiments investigating acute application of Aβ.

To confirm that both pericytes and microglia generate ROS in response to Aβ, in brain slices I fluorescently imaged the level of reduced glutathione (GSH), which is consumed as it scavenges ROS (GSH and dihydroethidium signals are inversely correlated; Won et al., 2015). Aβ (72 nM applied for 40 mins) reduced the GSH level in microglia by 55% and in pericytes by 20% ($p=10^{-4}$ and $p=0.006$, respectively; Figure 5.3). These changes cannot be converted to ROS synthesis rates because they will be affected by each cell

type's GSH level and regeneration rate by glutathione reductase, both of which differ between cell types (Rojo et al., 2014).

Given the importance of microglial phagocytosis in AD (Podleśny-Drabiniok et al., 2020) and having established that Aβ induces oxidative stress in microglia as well as pericytes, I tested whether blocking ROS production would affect microglial phagocytosis *in situ*. Using the microbead phagocytosis assay, I found that incubation of the brain slices with SOD1 (150 U/ml) for 1.5 hours significantly reduced the fraction of phagocytic microglia by 19% (from 60.3 ± 4.6% to 48.9 ± 3.1%; p=0.04; Figure 5.4), implying that ROS production contributes to phagocytosis. Therefore, Aβ-induced generation of ROS in microglia may initially be an adaptative response to increase their phagocytosis of Aβ, although it leads to detrimental effects in AD including the described reduction of cerebral blood flow (Nortley et al., 2019).

5.3 Microglia and astrocytes phagocytose Aβ peptides *in situ*

Next, I studied phagocytosis specifically of Aβ. Common tools to study Aβ phagocytosis include Aβ conjugates with non-pH sensitive fluorescent reporters, such as FITC (Jones et al., 2013) or Cy5 (Park et al., 2017). However, non-pH-dependent dyes contribute to a noisy background that hinders the clear visualisation of phagocytic cells and make it difficult to clearly differentiate between membrane-adherent and internalised particles.

I collaborated with Gaurav Chopra's lab at Purdue University, who had developed and characterised a novel pH-sensitive fluorogenic Aβ reporter, $A\beta^{pH}$, which I used in proof-of-principle experiments to investigate Aβ phagocytosis by glial cells *in situ*. $A\beta^{pH}$ was synthesised by linking a synthetic human $A\beta_{1-42}$ peptide to the pH-sensitive Protonex Green dye (PTXG), which allows intracellular tracking of the probe. $A\beta^{pH}$ aggregation is similar to that of non-conjugated Aβ as demonstrated by atomic force microscopy *in vitro* (Prakash et al., 2021).

While other pH-sensitive commercial dyes exist and have been conjugated with Aβ (e.g. pHrodo; Haney et al., 2018), our collaborators' research showed that this PTXG-conjugate outperforms pHrodo. $Aβ^{pH}$ exhibits lower background uptake by cells, more sustained fluorescence over time and a more acidic pKa of 5.2–5.9. Thus, $Aβ^{pH}$ exhibits increased green fluorescence in the pH range found within acidic lysosomal organelles (pH of 4.5–5.5), but not at the extracellular and cytoplasmic physiological pH values of 7.4 and 7.1, respectively, and is therefore better suited for mechanistic studies (Prakash et al., 2021).

To assess phagocytic uptake of $Aβ^{pH}$ in the hippocampus, I applied 5 μM $Aβ^{pH}$ (for 1.5 hours at 35°C) to live rat hippocampal slices. $Aβ^{pH}$ fluorescence was detected in the $Aβ^{pH}$-exposed slices (Figure 5.5). As expected, blocking phagocytosis with cytochalasin D or incubating the slices at 4°C (see Chapter 4, Figure 4.2) greatly reduced the mean $Aβ^{pH}$ fluorescence detected. Specifically, cytochalasin D reduced signal intensity by 57% ($p=0.04$) and cold temperature reduced it by 98% ($p=0.01$; Figure 5.5).

To assess which cells were acting as phagocytes, $Aβ^{pH}$-exposed brain slices were also stained for glial cell-specific markers. Microglia phagocytosed $Aβ^{pH}$ as seen by the localisation of $Aβ^{pH}$ within the Iba1-positive cells (Figure 5.6A). However, green fluorescence signal was seen both within Iba1-positive cells and outside these cells, presumably reflecting phagocytic uptake of $Aβ^{pH}$ by cells other than microglia, such as astrocytes. Indeed, staining for GFAP demonstrated internalisation of $Aβ^{pH}$ within astrocytes (Figure 5.6B). Summing over cells, approximately 60% of the internalised $Aβ^{pH}$ was phagocytosed by microglia and 40% by astrocytes (Figure 5.6C). Thus, in hippocampal brain slices, these data suggest that the contribution of microglia to the clearance of acutely applied $Aβ^{pH}$ is more prominent than that of astrocytes.

5.4 Microglial phagocytosis of Aβ is not affected by THIK-1

Glial cell responses to Aβ depend critically on disease stage and on their precise microenvironment, which determines their cellular state and gene expression profile (Chen et al., 2020). Because acute exposure to Aβ (as in the previous two sections) cannot mimic the slow increase that occurs over time *in vivo*, I next studied microglial responses to Aβ in a mouse model of AD, the *App*$^{NL-G-F}$ knock-in, where amyloid pathology develops gradually over months. For the interpretation of the labelling described below, it is important to know that the *App*$^{NL-G-F}$ knock-in generates Aβ with the human sequence (see section 2.2.4).

There are several ways to detect endogenous Aβ plaques in fixed brain tissue. Thioflavin staining (Figure 5.7A, left) labelled compact, dense plaque cores as expected from previous work (Bacskai et al., 2001; Clayton et al., 2021). Immunolabelling for APP (Figure 5.7A, centre) was also consistent with previous reports that APP accumulates both in neuronal somata and in dystrophic neurites around Aβ plaques (Chidlow et al., 2017; Jordà-Siquier et al., 2020), as does BACE1 (Sadleir et al., 2016). By contrast, an antibody against the N-terminus of human Aβ (clone 82E1) allowed specific detection of Aβ plaques generated by the *App*$^{NL-G-F}$ knock-in with minimal background labelling elsewhere (Figure 5.7A, right), and so was used throughout this study. Of note, this antibody reacts with both soluble and fibrillar Aβ, but does not cross react with rodent-endogenous Aβ nor with holo-APP (Horikoshi et al., 2004; Saito et al., 2014).

Amyloid burden increased progressively in *App*$^{NL-G-F}$ mice. While no plaques were detected in the cortex by Aβ immunolabelling at 1 month of age, some were already present at 2.5 months, followed by robust deposition at 4 months and at 11 months (Figure 5.7B). This progression with age was consistent with previous reports from this model (Chen et al., 2020; Saito et al., 2014). For reliable assessment of amyloid pathology (i.e., avoiding individual variability at onset but also ceiling effects), 4-month-old mice were used throughout this study; 3 to 6 months is a common age range used across studies with this model (Aikawa et al., 2019; Clayton et al., 2021; Nortley et al., 2019). At that age, Aβ

plaques can be detected across the brain in perfusion-fixed slices from *App*$^{NL-G-F}$ mice (Figure 5.7C). In the cortex, one of the brain regions with a higher amyloid burden, 5.9% ± 0.6% of the area was covered by Aβ plaques (significantly higher than in WT mice, p=0.04, where coverage was not significantly different from zero, p=0.33; Figure 5.7D).

Next, I characterised morphological changes in microglia in *App*$^{NL-G-F}$ mice by Sholl analysis of cells from perfusion-fixed brains. While microglia were highly ramified in WT mice, their ramification and size were reduced in *App*$^{NL-G-F}$ mice, particularly in microglia located at Aβ plaques (Figure 5.8A). The total process length per cell was reduced more closer to Aβ plaques. While the total process length was 682.3 ± 31.5 µm in WT microglia, it was reduced by 13.4% (to 590.7 ± 29.6 µm) in *App*$^{NL-G-F}$ microglia distant from Aβ plaques (not significantly different from WT, p=0.07) and by 64.3% (to 243.7 ± 12.6 µm) in *App*$^{NL-G-F}$ microglia at Aβ plaques ($p=10^{-4}$; Figure 5.8B). Similarly, process ramification was reduced more closer to Aβ plaques, with *App*$^{NL-G-F}$ microglia showing less branched processes and less branches near the soma compared with WT. Among these cells, microglia at Aβ plaques again showed more drastic changes compared with plaque-distant cells ($p=10^{-4}$; Figure 5.8C). Thus, the microglial morphological response to Aβ depends considerably on the cells' local environment and it is the cells which are presumably most exposed to Aβ that exhibit the most dramatic morphological changes, while those further away display an intermediate phenotype more similar to WT microglia.

A well-established behaviour of microglia exposed to Aβ accumulation *in vivo* is their clustering and upregulation of CD68-positive lysosomes around Aβ plaques (Medawar et al., 2019; Parhizkar et al., 2019). In our *App*$^{NL-G-F}$ model, this was already obvious at 4 months of age (Figure 5.9A) when, as discussed above, widespread plaque deposition occurs. In plaque-proximal microglia, engulfment of Aβ inside CD68-positive lysosomes could be confirmed by confocal imaging (Figure 5.9B).

Having established that THIK-1 regulates phagocytosis (Chapter 4), I studied whether deletion of THIK-1 would alter Aβ clearance by these activated microglia. For this, I crossed *App*$^{NL-G-F}$ mice with the THIK-1 KO line and measured the fraction of the microglial

area that was covered by CD68 in the absence or presence of THIK-1 expression. The percentage area coverage of CD68 (also known as scavenger receptor class D member 1, or lysosomal-associated membrane protein 4, LAMP4) is regularly used as an indicator of phagocytic activity (Ayata et al., 2018; Filipello et al., 2018; Guillot-Sestier et al., 2015; Liu et al., 2020; Medawar et al., 2019), so I hypothesised that CD68 coverage would be lower in the THIK-1 KO mice. Both in cortical and hippocampal microglia, CD68 coverage was approximately two-fold larger in cells at Aβ plaques than in cells away from plaques ($p=10^{-4}$), highlighting the key role of phagocytosis in the microglial response to Aβ. However, THIK-1 deletion did not alter lysosomal coverage in either of these two subgroups, either in the cortex (Figure 5.10A-B) or in the hippocampus (Figure 5.10C-D).

To confirm that microglial phagocytosis of Aβ was not affected by THIK-1 expression, I assessed Aβ plaque levels in different brain regions: layer 2/3 of the cortex and the CA1 region of the dorsal hippocampus (which show robust plaque deposition), and the molecular layer of the cerebellum and dorsal striatum (which show little plaque deposition; Figure 5.11A). The fraction of the area covered by Aβ plaques was not affected by deletion of THIK-1 in any of these regions, arguing against a role of THIK-1 in regulating microglial phagocytosis of Aβ in 4-month-old *App*$^{NL-G-F}$ mice.

Finally, I assessed synaptic changes in *App*$^{NL-G-F}$ mice. Synapse removal by microglia occurs in development (Paolicelli et al., 2011; Schafer et al., 2012), during when I had already established that it is controlled by THIK-1 (see Chapter 4.3). However, synapse loss is also known to occur in AD, where it correlates strongly with cognitive decline (Terry et al., 1991). Therefore, I used Golgi-Cox staining to study whether THIK-1 deletion altered dendritic spines in *App*$^{NL-G-F}$ mice, together with BSc student Grace Gillis who helped with the analysis under my supervision.

The spine density in dendrites from CA1 hippocampal neurons was not altered by THIK-1 deletion in adult mice in the absence of Aβ pathology (referred to here as "*App* wildtype", p=0.37; Figure 5.12A-B). This is consistent with data from young mice showing that THIK-1 does not induce postsynaptic changes in the healthy brain (see Chapter 4.3,

Figures 4.5–4.7). By contrast, in *App*$^{NL-G-F}$ mice, spine density in CA1 neurons was increased by 12% when THIK-1 was deleted (p=0.02; Figure 5.12C-D). This would be consistent with microglia reactivating their synapse removal activity upon Aβ-induced activation (but with more focus on postsynaptic spines; see Discussion below), which may not be as effective in the absence of THIK-1.

5.5 Discussion

The work presented in this Chapter addressed the role of Aβ in regulating microglial ROS generation, phagocytosis and morphology, and revealed contributions of other cell types to ROS generation and phagocytosis. First, I identified both pericytes and microglia as key sources of Aβ-induced oxidative stress. Second, incubating brain slices with a fluorescent Aβ probe, I found that microglia may outperform astrocytes in phagocytosing Aβ. Finally, I studied microglial response to Aβ produced endogenously *in vivo*. In the *App*$^{NL-G-F}$ mouse model (where microglia located at Aβ plaques suffer profound morphological and functional changes), I found that deletion of THIK-1 did not affect phagocytosis of Aβ, but it did modestly increase spine density in CA1 neurons, suggesting that blocking THIK-1 in Aβ-activated microglia may help reduce synapse loss early in AD.

As part of my collaboration in a study led by Ross Nortley in our group, I studied oxidative stress induced by Aβ oligomers in the rat brain and identified which cells contribute to it, i.e., pericytes and microglia. I showed that Aβ induces ROS production (Figure 5.2) and depletes reduced glutathione (an antioxidant) in both microglia and pericytes (Figure 5.3), consistent with both of these cell types generating ROS.

I had expected that, in response to Aβ, the main generator of ROS would be microglia or macrophages (Della Bianca et al., 1999; Park et al., 2017), but at least for the acute application of Aβ that I studied this was not the case. Iba1-expressing microglia and macrophages do increase ROS generation when exposed to Aβ (Figure 5.2B), and production of ROS might help microglia phagocytose more efficiently, as lowering ROS level

with SOD1 reduced phagocytosis *in situ* in a microbead assay (Figure 5.4). However, the significant rise of ROS generation in microglia was dwarfed by the far greater rise generated by pericytes (Figure 5.2B). This unexpected dominance of pericytes upon acute exposure to Aβ is similar to what has been reported in a peripheral inflammation context, where these cells might act as first responders to peripheral immune challenge (Duan et al., 2018).

Although it cannot be ruled out that microglia might take up dihydroethidium less well than pericytes or that the microglial contribution to ROS generation may exceed that of pericytes in the chronic scenario where Aβ accumulates slowly in AD, the leading role of pericytes described here is also consistent with pharmacological data: a blocker of NOX2 (expressed in microglia; Zhang et al., 2014) reduced the Aβ-evoked vasoconstriction by 45%, while a blocker of NOX4 (expressed in pericytes; Kuroda et al., 2014) completely abolished it (Nortley et al., 2019). Thus, NOX4 in pericytes seems to be the main generator of the ROS involved in the constriction of capillaries after Aβ exposure, at least in the short term.

For these experiments, I used the marker Iba1 to label immune cells as both microglia and macrophages express this protein (Zhang et al., 2014). However, it will also be interesting to establish the relative contribution of microglia and macrophages to Aβ-evoked ROS generation, which will likely depend on Aβ levels in the parenchyma *versus* the bloodstream. Differentiating the contribution of these two cell types would be possible by using microglia-specific markers such as TMEM119 (Ruan et al., 2020) or HEXB (Masuda et al., 2020a), or markers of border-associated macrophages such as CXCL4 (McKinsey et al., 2020). Given my results that THIK-1 (see Chapter 4.3, Figure 4.4) and ROS (Figure 5.4) both promote phagocytosis, future work should also examine possible links between K^+ flux, membrane potential and oxidative stress, by assessing ROS levels in Aβ-exposed slices incubated with THIK-1 blockers, or in microglia from *App*$^{NL\text{-}G\text{-}F}$ mice expressing or not expressing THIK-1. Both K^+ flux (Muñoz-Planillo et al., 2013) (mediated by THIK-1 in microglia; Madry et al., 2018) and ROS (Cruz et al., 2007) contribute to NLRP3 inflammasome activation, although they might act independently (Groß et al., 2016). Finally,

these experiments raise the question of whether previous work may have wrongly attributed ROS generation by pericytes to immune cells (Park et al., 2017). Thus, it will be important to ensure that immune cell depletion (e.g. by administration of clodronate liposomes) does not alter the pericyte population.

As a proof-of-concept to study phagocytosis of Aβ in brain slices, I imaged glial uptake of Aβ by using the $A\beta^{pH}$ probe, which exhibits green fluorescence upon internalisation into acidic (e.g. lysosomal) organelles of cells. The results confirmed that $A\beta^{pH}$ can be used to visualise phagocytosis in live cells without the use of any Aβ-specific antibodies (Figure 5.5). Of note, the probe was internalised by both astrocytes and microglia in rat hippocampal slices (Figure 5.6), which is in line with recent evidence demonstrating that astrocytes are able to phagocytose synapses (Lee et al., 2021a) and cellular debris (Morizawa et al., 2017).

I found that microglia phagocytose more $A\beta^{pH}$ than astrocytes (approximately 60% and 40% of the $A\beta^{pH}$, respectively). The apparent dominance of microglia in phagocytosing $A\beta^{pH}$ was in agreement with experiments performed by our collaborators in several different biological model systems including cell lines (human HMC3 cells, and mouse BV2 and N9 cells), primary cultures and *in vivo* in the cortex and the retina. Topical application onto the mouse somatosensory cortex through a cranial window rendered comparable results (70% and 25% of signal within microglia and astrocytes, respectively; Prakash et al., 2021). Following stereotaxic injection of $A\beta^{pH}$ into the mouse somatosensory cortex *in vivo*, the contribution of astrocytes to uptake was already minor at an early time (24 hours post injection), and further decreased later (72 hours). Furthermore, microglia in retinal tissues engulfed $A\beta^{pH}$ but no signal was detected in astrocytes (Prakash et al., 2021).

However, conclusions about the contribution of microglia *versus* astrocytes should be cautious. It is not clear whether their endosomal/lysosomal function is comparable, and the degradation rate of engulfed material may differ between both cell types (Lööv et al., 2015; Magnus et al., 2002). Because detection will depend critically on how rapidly the internalised probe is destroyed by lysosomes, this could affect the detected relative contribution.

Taken together, these data identify both microglia and astrocytes as responsible for Aβ phagocytosis in the brain, and confirm that $Aβ^{pH}$ can be used to investigate the mechanisms mediating Aβ phagocytosis. Having a tool to assess Aβ uptake and clearance *in vivo* (including in real-time in live mice; Prakash et al., 2021) could contribute significantly to understanding the onset of AD. Future work could use $Aβ^{pH}$ in e.g. Tmem119-tdTomato (Ruan et al., 2020), in which the internalised Aβ will show green fluorescence within red microglial cells, thus allowing monitoring of Aβ uptake in real time without the need for antibodies or fixed tissue staining downstream of the Aβ treatment.

Finally, I switched to $App^{NL\text{-}G\text{-}F}$ mice to analyse microglial responses to long-term accumulation of Aβ. In this model, I showed that not all microglia are affected to a similar extent by Aβ exposure. Instead, proximity to Aβ plaques controls microglial behaviour and cells located at plaques show the most dramatic changes.

It is known that microglia can readily change their shape and motility upon sensing local function or damage related signals (Umpierre and Wu, 2020). Clustering of microglia around Aβ plaques has been reported previously in $App^{NL\text{-}G\text{-}F}$ (Chen et al., 2020; Saito et al., 2014) and indeed in other models (Condello et al., 2015; Medawar et al., 2019; Parhizkar et al., 2019). By separating cells into separate groups based on their proximity to Aβ plaques, I found that both microglial morphology (Figure 5.8) and their phagocytic capacity (Figure 5.10) are tightly controlled by the presumed level of Aβ exposure, whereby large differences exist between plaque-proximal and plaque-distant cells and the latter represent an intermediate phenotype closer to that of WT microglia. This finding is consistent with studies on other amyloid-based AD models. In TgCRND8 and 5XFAD transgenic mice, changes of microglial ramification and electrophysiology depend upon their proximity to Aβ plaques (Plescher et al., 2018; Wendt et al., 2017), and ultrastructural analysis of microglia from APP/PSEN1 transgenic mice revealed similar differences in soma size and phagocytosis (El Hajj et al., 2019).

In plaque-associated microglia, lysosomal function (as assessed by the percentage area labelled for CD68) was increased (Figure 5.10), suggesting that they attempted to

remove Aβ, which could be detected inside their lysosomes (Figure 5.9). Indeed, fibrillar material and a larger number of lysosomes can be detected in processes from plaque-associated microglia by electron microscopy (El Hajj et al., 2019). However, some argue that this might merely reflect their increased activation, and that the main role of these cells in AD is to remove synapses upon being triggered by Aβ, rather than removing Aβ itself (Spangenberg et al., 2016). In agreement with this, while THIK-1 controls phagocytosis (see Chapter 4.3), its deletion in *App*$^{NL\text{-}G\text{-}F}$ mice did not affect Aβ burden (Figure 5.11). Despite microglial sensitivity to their proximity to Aβ plaques, previous work suggests that plaque load is largely independent of microglia (Grathwohl et al., 2009; Olmos-Alonso et al., 2016; Spangenberg et al., 2016), arguing against a primary role for microglial phagocytosis in plaque removal.

By contrast, THIK-1 deletion modestly increased the spine density of CA1 neurons in *App*$^{NL\text{-}G\text{-}F}$ mice (Figure 5.12). This was not the case in WT mice and is thus consistent with microglia resuming their engulfment of synapses when activated by Aβ, and with THIK-1 being involved in such activity (as in development; see Chapter 4.3, Figure 4.8). These results are in agreement with ultrastructural analysis revealing increased encircling of spines by microglial processes in APP/PSEN1 transgenic mice (El Hajj et al., 2019). Further, depletion of microglia increased spine density in 5XFAD mice (Spangenberg et al., 2016).

Effects of Aβ on postsynaptic sites are not entirely surprising. As discussed in Chapter 4, synaptic pruning in the healthy brain is thought to occur mainly at presynaptic rather than postsynaptic sites (Schafer et al., 2012; Weinhard et al., 2018). In postmortem brain samples from AD patients, microglia contained more presynaptic material than in control brains (Tzioras et al., 2019). However, postsynaptic function might also be compromised in the context of AD (Rajendran and Paolicelli, 2018). Removal of postsynaptic material by microglia in AD may reflect differential targeting of “eat-me” signals. Remarkably, C1q is barely detectable in postsynaptic fractions of healthy brains (Dejanovic et al., 2018), where it predominantly associates with the presynapse (Györffy et al., 2018). By contrast, C1q levels increased in postsynaptic fractions of brains from AD patients and from tau-

P301S mice (Dejanovic et al., 2018). In the latter, C1q mainly bound to postsynaptic sites. Indeed, the increase in synapse tagging with C1q seen in these mice, which correlated with more microglial engulfment, was mainly driven by increased postsynaptic binding (Dejanovic et al., 2018). This suggests that, while microglia may use common mechanisms to target synapses in development and disease (Hong et al., 2016b), these remain context-dependent.

Of note, not all spines are equivalent in terms of microglial pruning. For instance, turnover in the mouse hippocampus depends on spine size (Pfeiffer et al., 2018). The increase in spine density induced by microglial ablation was accompanied by a reduction in mean spine head volume in cortical (Ma et al., 2020) and olfactory bulb neurons (Wallace et al., 2020). In fact, microglial depletion led to a relative increase in the number of filopodia and long thin spines and a concomitant reduction in the number of mushroom and stubby spines (Ma et al., 2020). Consistent with this, microglial pruning is thought to mainly target immature long thin spines (indeed, only these increased in number in MHC-II KO mice, where microglial phagocytosis was blocked; Pasciuto et al., 2020). Thus, future work should examine the effects of THIK-1 expression on specific spine types. By measuring spine length, and head and neck volume, spines can be classified according to certain thresholds (Risher et al., 2014) or using unbiased cluster analysis (Pfeiffer et al., 2018). However, this would require fluorescent labelling of dendrites by either genetic expression of a neuronal reporter (e.g. *Thy1*^{GFP}; Ma et al., 2020) or by DiOlistic labelling of brain slices (Pasciuto et al., 2020). While Golgi-Cox staining allows inexpensive and fast imaging and does not require specialised equipment or transgenic lines, thinner protrusions or spines above or below the dendritic shaft cannot be reliably counted in bright-field images, which might contribute to values of spine density often being lower in studies using Golgi-Cox staining (~4 spines per 10 µm, similar to my results; e.g. Afroz et al., 2016; Welsh et al., 2020) compared to studies using fluorescence (>10 spines per 10 µm; e.g. Pfeiffer et al., 2018; Ye et al., 2019). Moreover, spine density is typically higher in studies with cultured cells (e.g. Chang et al., 2015; Ferreras et al., 2017; Filipello et al., 2018) and spine morphology is

affected by fixation (Tamada et al., 2020), highlighting that minimal tissue disruption is required to accurately study these sensitive elements.

Lastly, synapse loss also depends heavily on proximity to Aβ plaques. In APP/PSEN1 transgenic mice, spine turnover was higher than in wildtype controls in dendrites near plaques, but unaffected elsewhere (Liebscher et al., 2014). In a different APP/PSEN1 line (Koffie et al., 2009) and in AD patients (Koffie et al., 2012), levels of the postsynaptic marker PSD95 were most reduced at plaque cores, but recovered to wildtype levels as close as 50 µm from the plaques. Thus, it will be crucial to analyse spine counts (and how phagocytosis of synapses is affected by THIK-1) away from and near to Aβ plaques, where any effects might be more drastic.

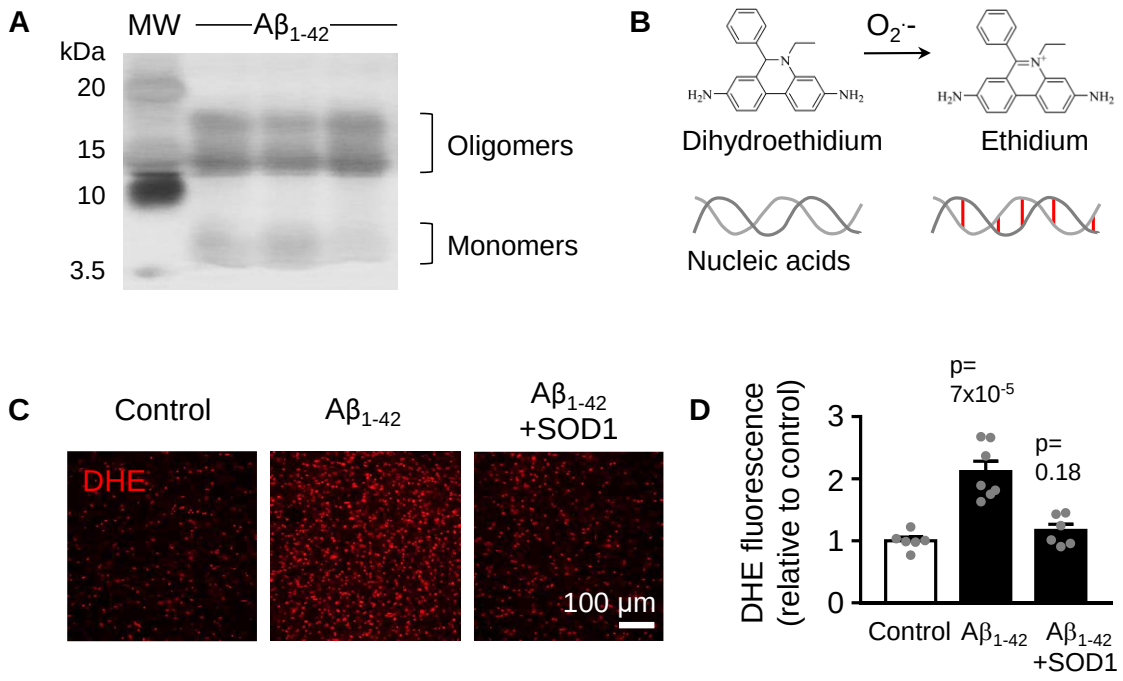

Figure 5.1. Aβ increased ROS levels in brain slices.

(A) Silver staining of an SDS-PAGE gel for $A\beta_{1-42}$ peptides showing formation of oligomers in the preparations used. **(B)** Schematic showing the ROS-mediated oxidation of dihydroethidium dye (DHE) to ethidium (and 2-hydroxyethidium, not shown), which can intercalate into cellular nucleic acids and allow assessment of ROS level by fluorescence. **(C)** Representative images of DHE-loaded rat cortical slices incubated in control aCSF or aCSF containing $A\beta_{1-42}$ (72 nM) or $A\beta_{1-42}$ + SOD1 (150 units/ml) for 40 min, showing that Aβ increases ROS level (red), and that this is inhibited by SOD1. **(D)** Fluorescence (normalised to value in control) of slices incubated in aCSF (n=6), $A\beta_{1-42}$ (n=7) or $A\beta_{1-42}$ + SOD1 (n=6). Data shown as mean ± s.e.m. Statistical significance was tested with one-way ANOVA followed by Dunn's post-hoc tests using brain slices as the statistical unit.

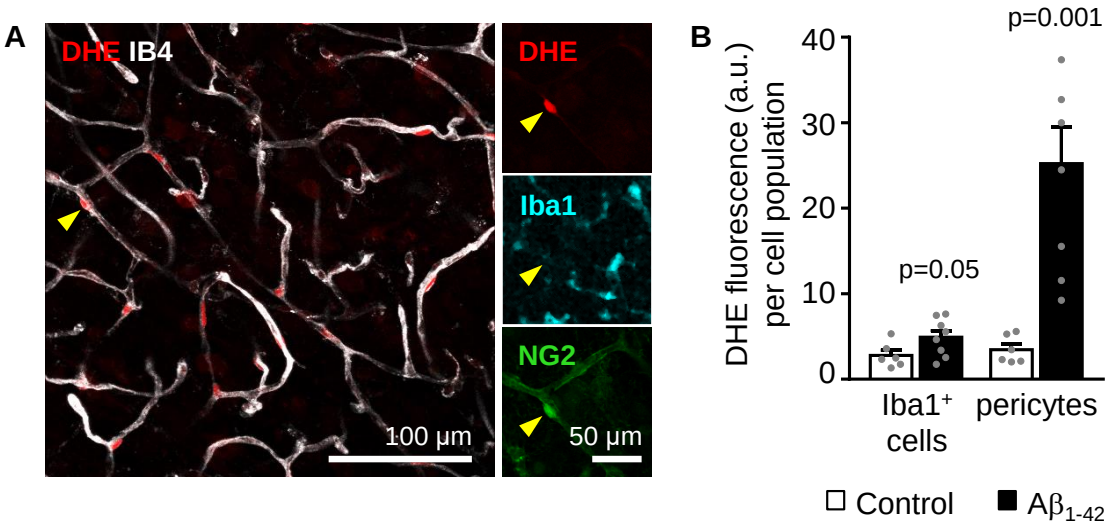

Figure 5.2. Aβ evoked ROS generation in microglia and pericytes.

(A) Left: Image of a cortical slice showing that the brightest dihydroethidium (DHE, red) signal was detected in cells located on isolectin IB_4 (IB_4)-labelled blood vessels (yellow arrowhead). Right insets: Immunolabelling shows that these cells colocalise with NG2 (green), but not with Iba1 (cyan), implying that they are pericytes rather than microglia or perivascular macrophages. **(B)** Soma DHE fluorescence (arbitrary units, a.u.) from the population of pericytes, or of Iba1-labelled cells, after 40 mins in the absence (n=6 slices) or in the presence of $A\beta_{1\text{-}42}$ (8 slices; fluorescence was averaged across 3 image stacks for each slice). Data shown as mean ± s.e.m. Statistical significance was tested with Mann-Whitney tests using brain slices as the statistical unit.

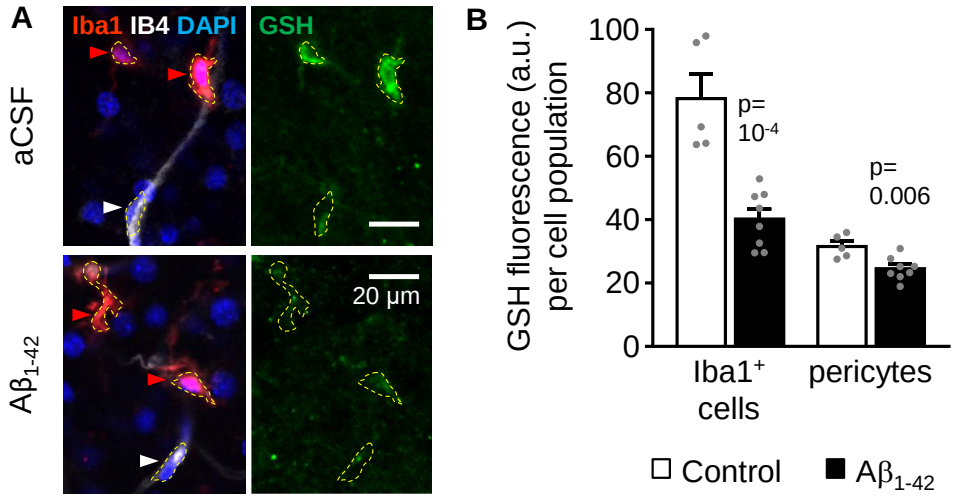

Figure 5.3. Aβ depleted reduced glutathione in microglia and pericytes.

(A) Representative images of microglia (red arrowheads) and pericytes (white arrowheads) labelled for GSH (green, right panels) in rat neocortical slices. Top panels: control conditions, when microglia show a higher level of GSH than pericytes (note that the pericyte nucleus does not label for GSH). Bottom panels: in the presence of 72 nM $A\beta_{1-42}$, which lowers the GSH level in both pericytes and microglia. Yellow dashed lines indicate measurement ROIs. **(B)** Quantification of GSH level for the population of pericytes and microglia averaged across 3 images from each slice (control: n=5 slices; $A\beta_{1-42}$: n=8 slices). Data shown as mean ± s.e.m. Statistical significance was tested with Mann-Whitney tests using brain slices as the statistical unit.

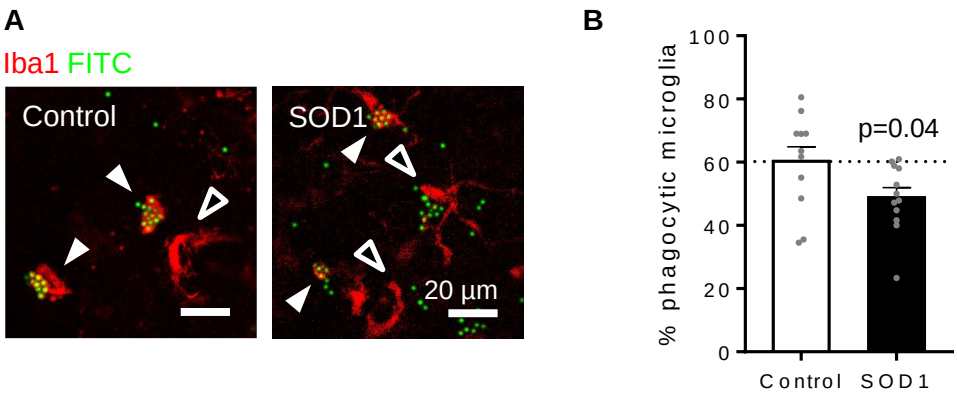

Figure 5.4. Scavenging ROS reduced microglial phagocytosis.

(A) Representative single plane images of microglia (Iba1, red) in acute hippocampal rat slices incubated with 3 µm microbeads (FITC, green), in aCSF in the absence (control) or presence of 150 U/ml superoxide dismutase (SOD1). **(B)** Percentage of microglia that phagocytosed microbeads in each condition, showing a reduction by SOD1 (control: n=11 slices from 3 animals; SOD1: n=12 slices from 3 animals). Data shown as mean ± s.e.m. Statistical significance was tested with a Mann-Whitney test using brain slices as the statistical unit.

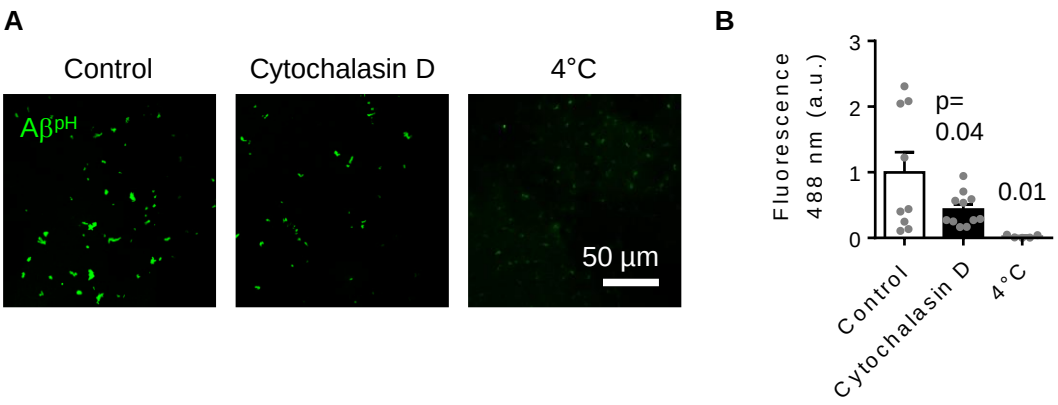

Figure 5.5. Aβ^{pH} signal was reduced by blocking phagocytosis in rat hippocampal slices.

(A) Representative images of fluorescence detected at 488 nm (green) in slices incubated with Aβ^{pH} in the absence (control) or presence of 10 µM cytochalasin D, or incubated at 4°C. **(B)** Quantification of mean fluorescence at 488 nm in each condition, showing a sharp reduction by cytochalasin D (n=11 slices from 2 animals) and cold temperature (n=5 slices from one animal) compared to control (n=9 slices from 2 animals). Data shown as mean ± s.e.m. Statistical significance was tested with one-way ANOVA followed by Dunn's multiple comparison tests.

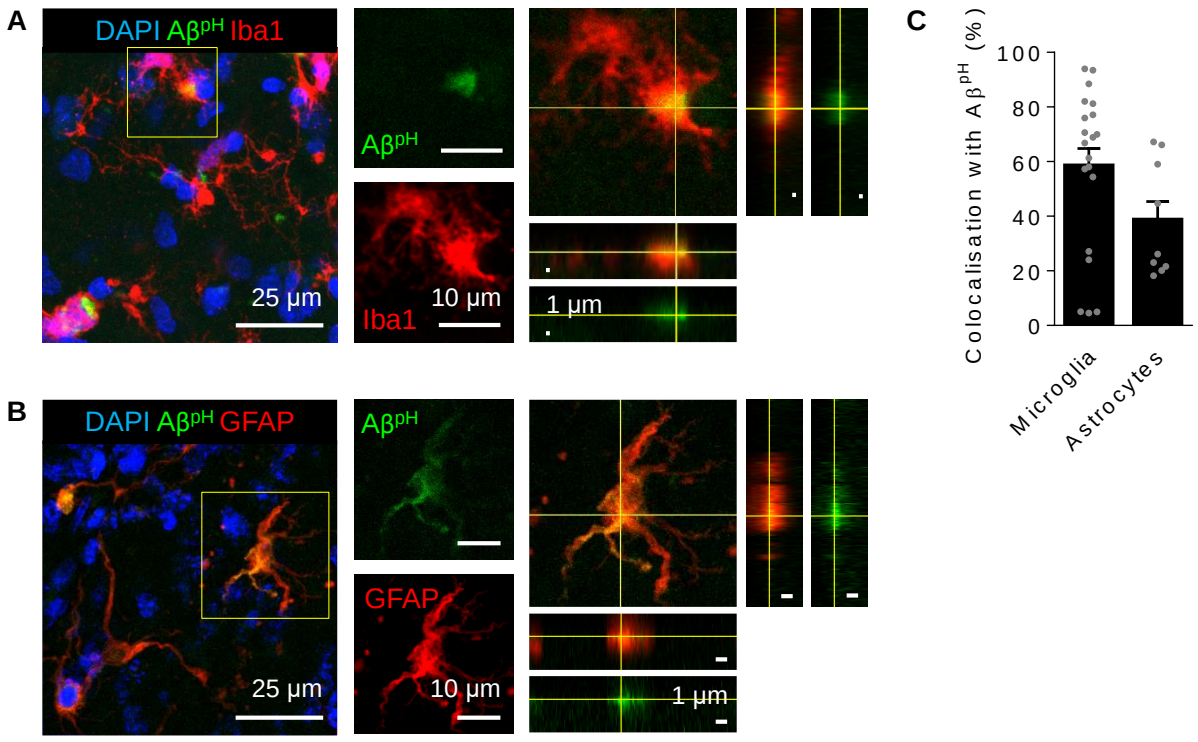

Figure 5.6. Aβ^{pH} was phagocytosed by both microglia and astrocytes *in situ* in rat hippocampal slices.

(A) Representative 2D maximum intensity projection of a confocal *z*-stack showing microglia (red) phagocytosing Aβ^{pH} (green). A close-up of the indicated cell (yellow square) is shown on the right. Orthogonal projections at the level of the crosshairs show internalisation of Aβ^{pH} within the microglial cell. **(B)** As (A), but showing astrocytes phagocytosing Aβ^{pH}. **(C)** Quantification of Aβ^{pH} colocalised with microglia and astrocytes, as defined by Iba1 and GFAP staining, respectively. Data shown as mean ± s.e.m., collected from n=20 and 8 slices for microglia and astrocytes respectively, from 3 animals.

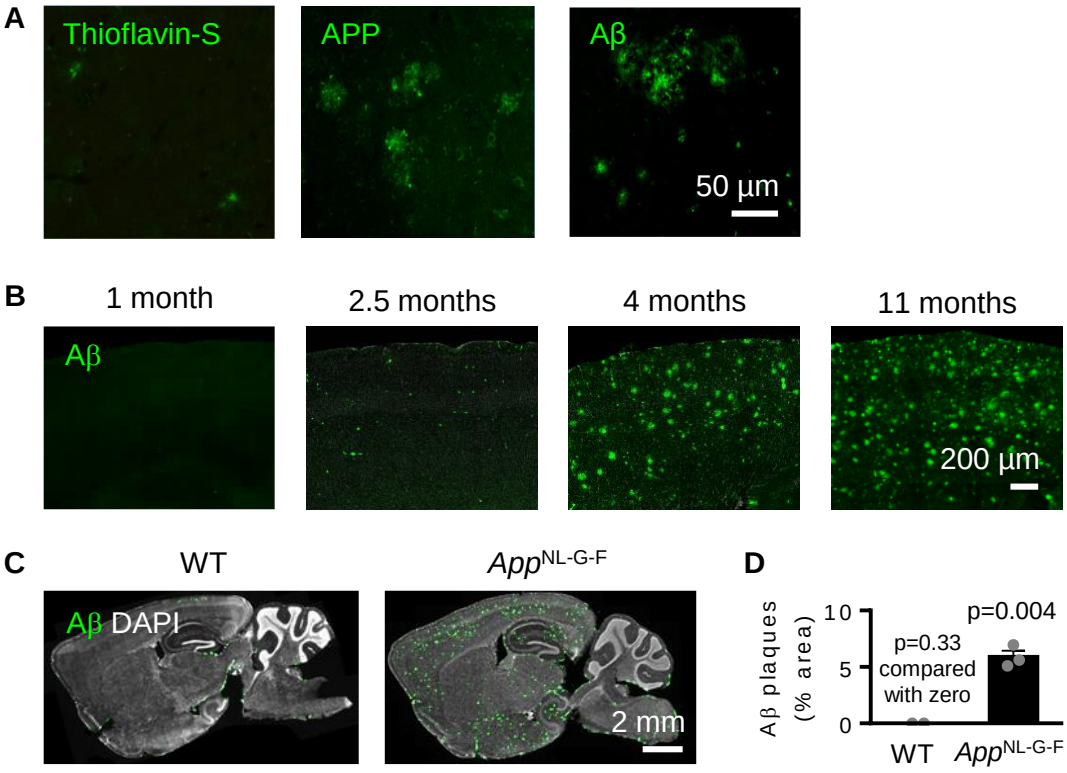

Figure 5.7. Development of Aβ pathology in *App*$^{NL-G-F}$ mice.

(A) Representative images of Aβ staining by thioflavin or by immunolabelling for amyloid precursor protein (APP, which accumulates in damaged neurites around plaques) or human Aβ generated by the *App*$^{NL-G-F}$ knock-in. **(B)** Representative cortical images from *App*$^{NL-G-F}$ mice, showing the progressive deposition of Aβ plaques with age. **(C)** Representative whole-section sagittal brain slices from WT and *App*$^{NL-G-F}$ mice at 4 months of age, showing robust deposition of Aβ plaques (green) in different brain areas (but not in the striatum or the cerebellum) in *App*$^{NL-G-F}$ mice. Nuclei are labelled with DAPI (white) for reference. **(D)** Quantification of the cortical area covered by Aβ plaques in 3 *App*$^{NL-G-F}$ mice compared with 2 WT mice. Data shown as mean ± s.e.m. Statistical significance was tested with Mann-Whitney test using animals as the statistical unit.

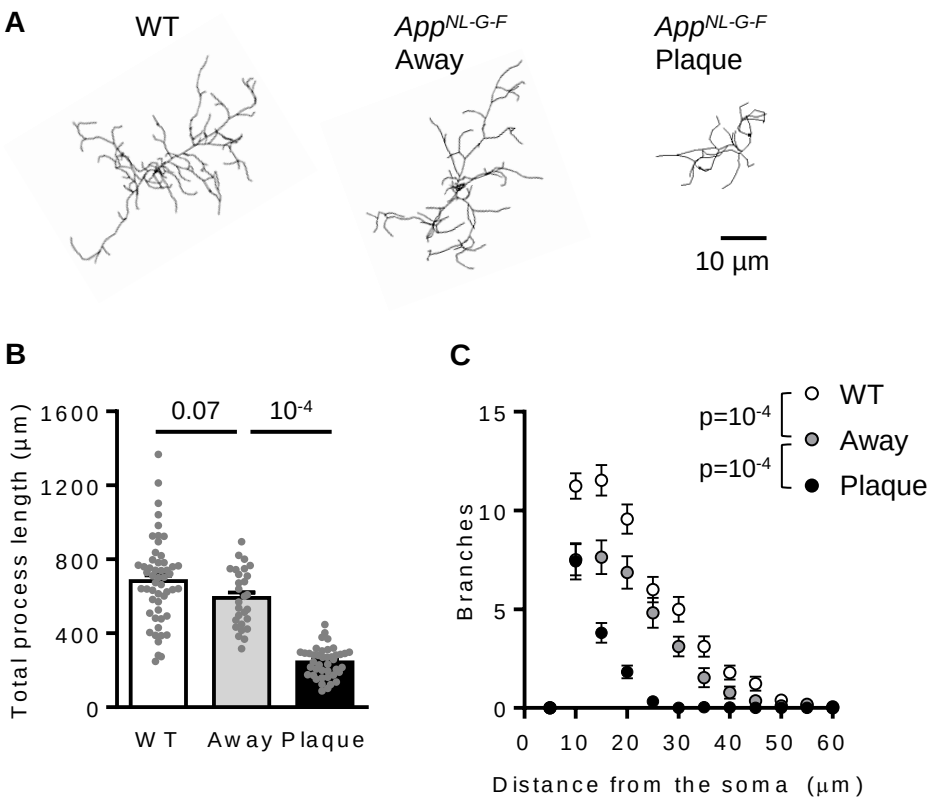

Figure 5.8. Morphological analysis of microglia in *App*$^{NL-G-F}$ mice.

(A) Representative 3D-reconstructed WT microglia, and *App*$^{NL-G-F}$ microglia away from and at Aβ plaque in 4-month-old mice**. (B-C)** Sholl analysis-derived (B) total process length and (C) number of process branches at distances (in 5 µm increments) from the cell soma, showing a sharp deramification of microglia at plaques (e.g. a 58.7% shorter process tree compared to microglia away from plaques or 64.3% shorter compared with WT; n=53 WT cells, 28 *App*$^{NL-G-F}$ cells away from plaques and 42 cells at plaques from 3 mice). Data shown as mean ± s.e.m. Statistical significance was tested with one-way ANOVA followed by Dunn's (B) or two-way ANOVA followed by Sidak's post-hoc tests for individual comparisons (C) using cells as the statistical unit.

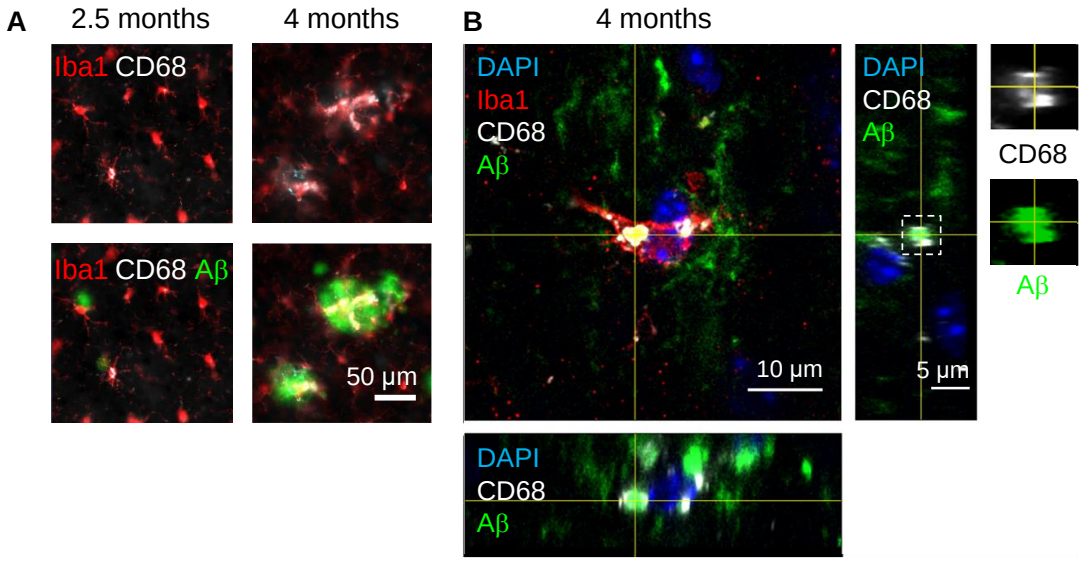

Figure 5.9. Phagocytosis of Aβ by microglia in *App*$^{NL\text{-}G\text{-}F}$ mice.

(A) Representative images of hippocampal microglia (Iba1, red) in *App*$^{NL\text{-}G\text{-}F}$ mice at 2.5 (left) and 4 months of age (right). At 4 months, when large Aβ plaques (green) have already developed, microglia show increased expression of the lysosomal marker CD68 (white) as they cluster around them. **(B)** Microglial cell phagocytosing Aβ in a 4-month-old *App*$^{NL\text{-}G\text{-}F}$ mouse. Orthogonal projections at the level of the crosshairs show internalisation of Aβ by the microglial cell. Right panels show a closeup of the indicated area (white dashed square) to highlight the presence of Aβ within the CD68-positive lysosome.

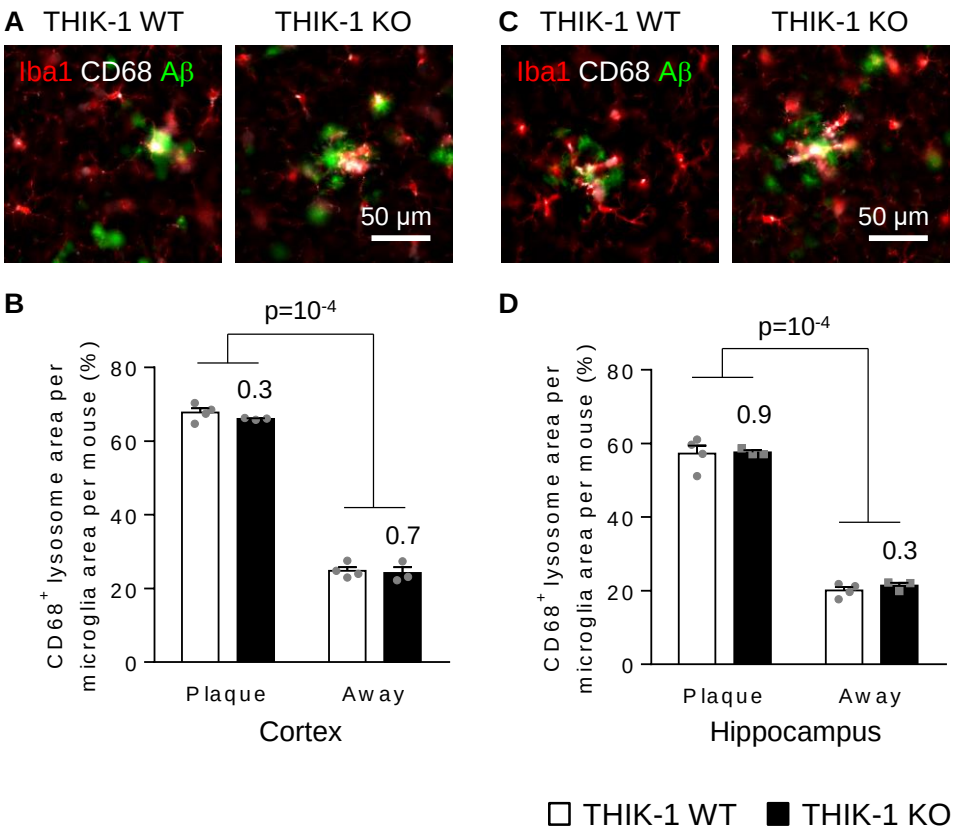

Figure 5.10. CD68 level was increased in *App*$^{NL-G-F}$ microglia at Aβ plaques, independently of THIK-1 expression.

(A) Representative images of cortical microglia (Iba1, red) in 4-month-old *App*$^{NL-G-F}$ mice that were wildtype (WT) or knockout (KO) for THIK-1, showing expression of CD68 (white) in cells associated with Aβ (green). **(B)** Quantification of the fraction of the microglia area covered by CD68 in the cortex of 4 THIK-1 WT and 3 THIK-1 KO brains, showing a sharp increase in plaque microglia compared to cells away from plaques, but no difference between the WT and the KO. **(C)** As (A), but for hippocampal microglia. **(D)** As (B), but for hippocampal microglia. Data shown as mean ± s.e.m. Statistical significance was tested with two-way ANOVA followed by Sidak's post-hoc tests using animals as the statistical unit.

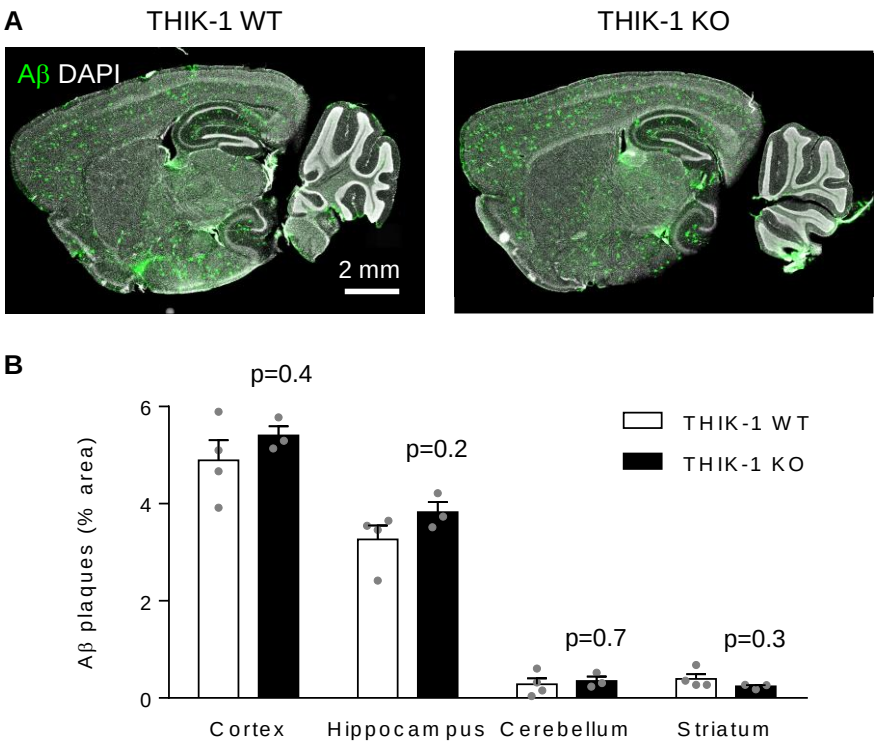

Figure 5.11. THIK-1 deletion did not alter Aβ plaque level in *App*$^{NL-G-F}$ brains.

(A) Representative whole-section sagittal brain slices from 4-month-old *App*$^{NL-G-F}$ mice that were wildtype (WT) or knockout (KO) for THIK-1 showing Aβ plaques (green). Nuclei were labelled with DAPI (white) for reference. Green areas at the edge of tissue regions are artefacts resulting from the automated scanner for the image acquisition changing focus, and were excluded from the analysis. **(B)** Quantification of the area covered by Aβ plaques in the cortex (layer 2/3), dorsal hippocampus (CA1), cerebellum (molecular layer) and dorsal striatum of 4 WT and 3 KO mice, showing no difference between WT and KO in any of these regions. Data shown as mean ± s.e.m. Statistical significance was tested with Mann-Whitney tests using animals as the statistical unit.

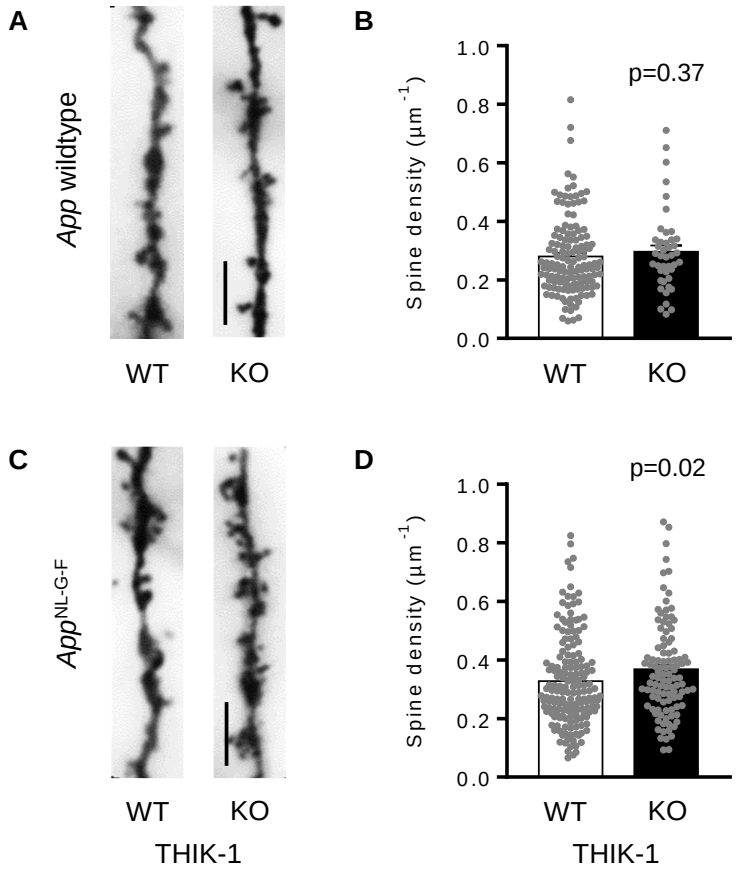

Figure 5.12. THIK-1 deletion slightly increased hippocampal spine density in *App*$^{NL-G-F}$ mice.

(A) Representative images of Golgi-Cox-stained non-primary apical CA1 dendritic segments from 4-month-old mice that were either wildtype (WT) or knockout (KO) for THIK-1, both lacking the *App*$^{NL-G-F}$ knock-in. Scale bar: 5 µm. **(B)** Quantification of spine density in the analysed dendritic segments, showing no difference between WT and KO mice (n=135 dendrites from 3 WT mice and 43 dendrites from one KO mouse). **(C)** As in (A), but for *App*$^{NL-G-F}$ knock-in mice that were either WT or KO for THIK-1. **(D)** As (B), but for *App*$^{NL-G-F}$ mice, showing a small but significant increase in spine density in THIK-1 KO mice compared with THIK-1 WT mice (n=166 dendrites from 8 WT mice and 105 dendrites from 4 KO mice). Data shown as mean ± s.e.m. Statistical significance was tested with Mann-Whitney tests using dendrites as the statistical unit.

6. Regulation of microglial Ca^{2+} signalling

6.1 Introduction

The contribution of Ca^{2+} as a second messenger regulating microglial functions, and its source, have been controversial. However, actin polymerisation and the subsequent cytoskeletal rearrangements involved in phagocytosis are finely controlled by Ca^{2+}, and rises in $[Ca^{2+}]_i$ have been reported before and during phagocytic events (Melendez and Tay, 2008; Nunes and Demaurex, 2010). For instance, microglial interaction with myelin sheaths (which will later be phagocytosed) elevates their $[Ca^{2+}]_i$ in zebrafish (Hughes and Appel, 2020). Further, the Ca^{2+} chelator BAPTA reduced formation of phagocytic cups in cultured phagocytes, similarly to the effect of the actin inhibitor cytochalasin D (Gronski et al., 2009). Here, I aimed to understand the contribution of extracellular *versus* endoplasmic reticulum-released Ca^{2+} to rises in $[Ca^{2+}]_i$ underlying phagocytosis. For this, I used the microbead-based assay presented in previous chapters.

Phagocytic cells exhibit periodic spontaneous Ca^{2+} transients as well as stimulus-evoked $[Ca^{2+}]_i$ rises (Brawek and Garaschuk, 2013). *In vitro* studies have identified a number of ligands evoking Ca^{2+} responses in microglia, including pathology-related substances such as LPS and Aβ (Brawek and Garaschuk, 2013). However, these studies were on neonatal microglia which become amoeboid under culture conditions, raising questions about the relevance of *in vitro* approaches. Here, I took advantage of a genetically-encoded Ca^{2+} indicator (GECI), GCaMP5g, to visualise changes in $[Ca^{2+}]_i$, as the GCaMP fluorescence increases upon binding Ca^{2+}. While all indicators have an intrinsic buffering effect (because they bind Ca^{2+} ions; McMahon and Jackson, 2018), GECIs avoid cell-specificity issues and cell dialysis seen with organic Ca^{2+}-sensitive indicators. Further, they allow investigation of Ca^{2+} dynamics in processes, whereas Ca^{2+}-sensitive dyes label mainly somata (Reeves et al., 2011). For these reasons, GECI-expressing mouse strains are increasingly used for

imaging Ca^{2+} in microglia. Here, basal and evoked Ca^{2+} signals were examined in GCaMP-expressing WT and *App*$^{NL-G-F}$ mice.

6.2 Intracellular Ca^{2+} is required for microglial phagocytosis

Following interaction with target ligands, microglia form phagocytic cups: a process which depends on fine cytoskeletal rearrangements controlled by Ca^{2+} levels (Melendez and Tay, 2008). Preliminary data from our lab, obtained from hippocampal microglia filled with the Ca^{2+} indicator Fluo-4, showed that local Ca^{2+} transients occur in microglial processes which are carrying out phagocytosis (Christian Madry, unpublished). Thus, I aimed to establish whether intracellular or extracellular Ca^{2+} were required for microglial phagocytosis of fluorescently-tagged microbeads in acute hippocampal slices from rat brains. Removal of external calcium ($[CaCl_2]_o$=0) did not significantly affect phagocytosis of the beads (p=0.23). However, buffering of intracellular calcium with 50 µM BAPTA-AM (a membrane-permeable ester form of BAPTA, which has its ester groups removed by intracellular esterases after it enters the cell) reduced phagocytic rate by 74.6% ($p=10^{-3}$; Figure 6.1). These results indicate that Ca^{2+} is involved in microglial phagocytosis in intact (i.e., non-patch-clamped) microglia in brain slices, and suggest that phagocytosis relies upon $[Ca^{2+}]_i$ rises originating from internal store release rather than membrane influx into microglia from the extracellular milieu.

6.3 Block of THIK-1 channels prevents Ca^{2+} signalling in microglia

To study the dynamics of Ca^{2+} signalling in microglia, I used a CreER-loxP system, which enables conditional targeting of transgenes by using cell type-specific promoters. Here, I took advantage of the fractalkine receptor *Cx3cr1* promoter to drive expression of CreER and thus expression of the GECI GCaMP5g (and the reporter tdTomato) in immune cells. Cre recombinase has been fused to a ligand-binding domain of the estrogen receptor

(CreER), which allows temporal control of the gene expression upon dosage with tamoxifen. Although estrogen receptor activation by tamoxifen may affect metabolism (Wallen et al., 2001), gavage administration (120 µg tamoxifen/g body weight) for four consecutive days was not toxic and did not alter the weight of the treated animals, which was monitored daily (Figure 6.2A).

Two problems may arise from the use of the Cre-loxP system. First, some leakiness (i.e., a certain level of excision of the loxP sites and expression of the fluorescent reporter without administration of tamoxifen) has been reported in conditional lines including *Cx3cr1*^{Cre} (Van Hove et al., 2020). This could be due to long lived cell types allowing more time for residual CreER-mediated recombination, and/or the fact that the relatively short length of the loxP-flanked STOP cassette is sensitive to recombination by small amounts of CreER (Van Hove et al., 2020). However, in the current study no leaky expression of GCaMP5g or tdTomato were seen in slices from uninduced animals (Figure 6.2B).

Another drawback of Cre-loxP systems is the potential for unspecific expression, i.e., expression in unwanted cell types (Stifter and Greter, 2020). While this is a considerable issue for experiments working with isolated cells (which are likely to change their transcriptome and may also lose identifiable features that they would normally have *in situ;* Bohlen et al., 2017), it is less of a concern when imaging cells *in situ* as in the current study. Of note, however, *Cx3cr1*^{CreER} mice target gene expression to microglia but also other immune cells, including macrophages residing in the meninges and perivascular spaces. Therefore, I used the tdTomato and transmitted light signals to select cells that did not lie on vessels, so as to focus on parenchymal microglia and avoid macrophages. Ca^{2+} responses were calculated (and are shown throughout) as ΔF/F, which represents the change in fluorescence intensity (F) at a certain time relative to that at baseline (see 2.9.3 for details) and allows for a more reliable comparison across experiments, as changes in indicator expression or in fluorescence excitation intensity/detection efficiency are cancelled out (Semyanov et al., 2020).

First, I studied basal Ca^{2+} activity in these mice (using a threshold value to exclude background noise, see 2.9.3). Microglial somata showed a low frequency of spontaneous Ca^{2+} transients (0.6 ± 0.1 per 300 s; Figure 6.3). I investigated whether blocking THIK-1 channels would result in reduced Ca^{2+} activity in microglia, which may provide a mechanism for THIK-1-mediated regulation of microglial phagocytosis. When blocking THIK-1 channels with 50 µM bupivacaine or 50 µM TPA, the rate decreased to 0.2 ± 0.1 per 300 s (p=0.04) and 0 per 300 s (p=0.03), respectively (Figure 6.3). As these drugs both block THIK-1 but have other different targets (see Chapter 4), I am assuming that their common effect is mediated by THIK-1 block, although an alternative, unknown common target for both of these drugs cannot be excluded.

To study evoked Ca^{2+} responses in microglia, focal laser lesions were used as a well-established proxy to trigger a response of microglia to injury, similar to focal ATP application mimicking neuronal disruption (Davalos et al., 2005; Haynes et al., 2006; Madry et al., 2018). Focal lesions provoke neuronal damage, which acutely increases microglial $[Ca^{2+}]_i$ with a low latency (0–5 seconds; Eichhoff et al., 2011). Such a Ca^{2+} rise is due to the activation of G_q-coupled purinergic receptors, which activate intracellular IP_3-mediated Ca^{2+} release via activation of PLC (Eichhoff et al., 2011). This is a very local response and cells away from the lesion do not send out processes or increase their Ca^{2+} transient rates, so I analysed cells at ~30 µm from the lesion site.

First, I confirmed that lesions induced a robust, rapid (latency ~1 s) Ca^{2+} rise (Figure 6.2C). Following the $[Ca^{2+}]_i$ peak, damage led to process outgrowth from nearby microglia toward the lesion site (as described by Davalos et al., 2005; Madry et al., 2018). A raised level of Ca^{2+} was detected in the growing processes (Figure 6.2C), suggesting that microglial Ca^{2+} is not only required for the formation of phagocytic cups but is also involved in process motility. This is consistent with reports that the start of process movements correlates with Ca^{2+} activity (Umpierre et al., 2020) and that their chemotaxis towards a laser ablation site is delayed by a Ca^{2+} chelator (Pozner et al., 2015).

While laser lesions induced consistent Ca^{2+} responses in untreated microglial somata, exposure to 50 µM bupivacaine reduced the peak response amplitude by 52% ($p=0.03$). When treated with 50 µM TPA, the response was abolished (100%; $p=10^{-4}$; Figure 6.4). Added to the data above, this suggests that block of THIK-1 channels prevents Ca^{2+} activity in microglia. Interestingly, bupivacaine greatly reduced both spontaneous and evoked Ca^{2+} activity while TPA effectively abolished both. A stronger effect of TPA might indicate a contribution of both two-pore domain and voltage-gated K^+ channels, as the latter are blocked by TPA but not bupivacaine. Potential mechanistic explanations will be discussed in section 6.5.

6.4 Microglial Ca^{2+} activity is increased by proximity to Aβ plaques

Various stimuli trigger Ca^{2+} activity in microglia. Combs et al. (1999) were the first to describe, in a primary culture system, that Aβ exposure increases $[Ca^{2+}]_i$ in microglia by promoting Ca^{2+} release from internal stores. It must be noted that Ca^{2+} responses of microglia have already been described in AD model mice by Olga Garaschuk's group, who showed that Ca^{2+} activity increases in activated microglia near plaques and identified its dependence upon purinergic signalling (Brawek et al., 2014). However, they used a dye indicator, OGB-1, which they electroporated into microglial cells. Organic Ca^{2+} indicators are toxic to cells because they can inhibit the Na^+,K^+-ATPase, which alters their membrane potential, causes swelling and disrupts their metabolism (Smith et al., 2018). By contrast, GECIs like the one expressed in our mice are not expected to cause toxicity (Smith et al., 2018) and allow study of undisturbed microglia (although all Ca^{2+} indicators will buffer $[Ca^{2+}]_i$ to some extent).

In the light of previous work suggesting stark morphological and functional differences between microglia near to and away from Aβ plaques (Brawek et al., 2014; Plescher et al., 2018; Wendt et al., 2017), I analysed them separately in imaging of *App*$^{NL-G-F}$ mice, using a distance of >50 µm from the nearest plaque edge (identified as described

below) as the defining criterion for plaque-distant microglia. A number of stains have been developed to label Aβ plaques in living brain tissue, including thioflavin-S (Bacskai et al., 2001) and methoxy-XO4 (Klunk et al., 2002). However, issues may arise from insufficient penetration into slices, labelling of only some Aβ plaque types or non-selective binding to β-sheet motifs of other proteins (Eichhoff et al., 2008; Tejera and Heneka, 2019; Yuan and Grutzendler, 2016). Thus, in this study I relied on two intrinsic cues for identification of Aβ plaques (and thus of microglia at and away from them). First, I used the fact that Aβ plaques are intrinsically fluorescent at both green and red emission wavelengths when two-photon illuminated at 920 nm. Plaques were visible in non-tamoxifen-treated *App*$^{NL\text{-}G\text{-}F}$ animals (Figure 6.5) and not in WT mice (as shown in Figure 6.2B; note that in the remaining of this Chapter, WT refers to *Cx3cr1*^{CreER} x GCaMP5g-IRES-tdTomato mice, i.e., not expressing *App*$^{NL\text{-}G\text{-}F}$). Second, the characteristic clustering of tdTomato-expressing microglia at Aβ plaques (as shown in Chapter 5, Figure 5.9) was also used for confirmation (Figure 6.5).

In microglial somata, the frequency of Ca^{2+} transients was higher closer to Aβ plaques (Figure 6.6A-B). While WT microglia showed 0.4 ± 0.1 transients per 300 s, in *App*$^{NL\text{-}G\text{-}F}$, microglia away from Aβ plaques showed 1.3 ± 0.2 transients per 300 s (p=0.1 compared with WT) and microglia at Aβ plaques showed 2.2 ± 0.3 transients per 300 s ($p=10^{-4}$ compared with WT). However, this effect was not seen in the microglial processes, where the transient rate remained stable regardless of *App*$^{NL\text{-}G\text{-}F}$ expression (Figure 6.6C-D). In these regions, 2.7 ± 0.6 transients per 300 s were detected in WT microglia, compared to 2.9 ± 0.4 transients per 300 s in *App*$^{NL\text{-}G\text{-}F}$ microglia away from Aβ plaques (p=0.9) and 2.6 ± 0.2 transients per 300 s in those at Aβ plaques (p=0.9).

Because of the different behaviour of somata and processes, I did a paired analysis for a subset of cells from each group from which I had calculated transient rates in both regions (Figure 6.6E). Within a given cell, processes display higher basal Ca^{2+} activity than do somata in WT mice (3.5-fold; p=0.04). This remains true for *App*$^{NL\text{-}G\text{-}F}$ microglia away from Aβ plaques (1.9-fold; p=0.02). However, plaque microglia present a similar transient rate in processes and somata (p=0.6). In summary, these data suggest that somatic regions are

more sensitive to Aβ exposure, which increases their spontaneous Ca^{2+} activity to levels comparable to those seen in processes. By contrast, process Ca^{2+} transients are more frequent and are unaffected by Aβ exposure.

Next, I aimed to characterise whether and how Aβ affected lesion-evoked Ca^{2+} responses in microglia. As before, laser injury triggered a robust, rapid peak of $[Ca^{2+}]_i$ in WT microglial somata. However, such a response was impaired in the *App*$^{NL-G-F}$ mice (Figure 6.7). In *App*$^{NL-G-F}$ microglia away from plaques, peak Ca^{2+} response was reduced by 29% ($p=0.03$), and for those at plaques peak Ca^{2+} response dropped by 78% ($p=10^{-4}$). Together, these data suggest that, while Aβ increases spontaneous Ca^{2+} activity in microglial somata, it renders them less able to mount lesion-evoked responses. In both cases, microglia away from Aβ plaques presented an intermediate phenotype between those at plaques and their WT counterparts.

Finally, I investigated two AD-relevant factors that may modulate Ca^{2+} responses in *App*$^{NL-G-F}$ microglia: amine transmission and oxidative stress. Noradrenergic (locus coeruleus) neurodegeneration is characteristic of AD, and depletion of noradrenaline transmission exacerbates pathology in mouse models (Heneka et al., 2006). Noradrenaline enhances microglial phagocytosis (Heneka et al., 2010) and controls their surveillance and response to injury (Liu et al., 2019; Stowell et al., 2019). Therefore, I studied whether bath application of noradrenaline would alter the Ca^{2+} activity of microglia.

On the other hand, oxidative stress is exacerbated in AD (Praticò and Sung, 2004). In mice, I have shown that exposure to Aβ evokes ROS in microglia (Chapter 5, Figure 5.2) as they become more phagocytic (Chapter 5, Figure 5.10). *In vitro*, there is a cross-talk between Ca^{2+} and ROS levels, whereby a rise of one drives an increase of the other, and ROS have been described to trigger endoplasmic reticulum Ca^{2+} release in culture systems (Görlach et al., 2015; Yan et al., 2006). However, evidence from cells *in situ* is lacking. Superoxide dismutase 1 (SOD1, 150 U/ml) scavenges reactive superoxide generated when Aβ activates NADPH oxidase (Nortley et al., 2019) and is able to inhibit ROS generation

induced by Aβ (Chapter 5, Figure 5.1). Thus, I studied whether using SOD1 to alter ROS levels in *App*$^{NL-G-F}$ microglia would impact their Ca^{2+} responses.

In *App*$^{NL-G-F}$ microglia, spontaneous Ca^{2+} activity was not affected by bath application of either noradrenaline or SOD1 (Figure 6.8). For microglia away from Aβ plaques (Figure 6.8A-B), 1.3 ± 0.2 transients per 300 s were detected in untreated cells, 0.8 ± 0.4 transients per 300 s were detected in noradrenaline-treated cells (p=0.2) and 1.7 ± 0.9 per 300 s in SOD1-treated cells (p=0.9). For microglia at Aβ plaques (Figure 6.8C-D), 2.2 ± 0.3 transients per 300 s were detected in untreated cells, 1.5 ± 0.4 transients per 300 s were detected in noradrenaline-treated cells (p=0.4) and 2.4 ± 0.5 per 300 s in SOD1-treated cells (p=0.9).

Noradrenaline did not affect lesion-evoked Ca^{2+} responses either: the peak Ca^{2+} response was not statistically significantly different in noradrenaline-treated microglia from that of control cells, regardless of whether the cell was distant from (p=0.1; Figure 6.9) or located at an Aβ plaque (p=0.3; Figure 6.10).

Similarly, plaque-located microglia treated with SOD1 did not exhibit statistically different Ca^{2+} responses compared to control cells (p=0.9; Figure 6.10). However, in microglia away from Aβ plaques, SOD1 treatment seemed to prevent lesion-evoked Ca^{2+} rises (these cells showed a 99% lower peak Ca^{2+} response than control cells; p=0.03; Figure 6.9). This suggests that ROS could mediate evoked Ca^{2+} signals in microglia, but in a manner depending on Aβ levels, assuming these to be higher nearer plaques.

6.5 Discussion

The work presented in this Chapter addressed the role of Ca^{2+} in microglial phagocytosis and identified factors that regulate Ca^{2+} dynamics in these cells. First, by using a microbead-based assay and pharmacology, Ca^{2+} release from intracellular stores was identified as important for phagocytosis. Second, using GCaMP reporter mice, THIK-1 channel block was found to inhibit Ca^{2+} signalling in these cells both under baseline

conditions and upon lesioning. Further, in mice crossed with the AD model *App*$^{NL-G-F}$, proximity to Aβ plaques was found to increase the Ca^{2+} activity of microglial somata, which are less active than processes in the absence of amyloid pathology.

Microglial Ca^{2+} dynamics are key for phagocytosis. In cultured phagocytes, chelating or removing extracellular Ca^{2+}, or depleting Ca^{2+} stores with thapsigargin (which blocks Ca^{2+} pumping into the endoplasmic reticulum) all reduced uptake of apoptotic cells (Gronski et al., 2009). This suggests that both sources of Ca^{2+} are likely to play a role in phagocytosis, at least *in vitro*, and supports the view that entry of extracellular Ca^{2+} helps replenish depleted stores.

However, this might change *in situ*, where intracellular Ca^{2+} seems to play a larger role. The microbead assay data presented here suggests that intracellular store-mediated Ca^{2+} release, rather than extracellular entry, is responsible for the increases in $[Ca^{2+}]_i$ required for phagocytosis (Figure 6.1). This is consistent with previous reports showing that chelating intracellular Ca^{2+} with BAPTA-AM reduced Ca^{2+} activity of microglia (Pozner et al., 2015) and depleting intracellular Ca^{2+} stores with thapsigargin blocked damage-induced Ca^{2+} transients (Eichhoff et al., 2011). The requirement for internal calcium for phagocytosis is also in line with the fact that $P2Y_6$, a well-known receptor mediating phagocytosis, triggers IP_3-dependent Ca^{2+} release from internal stores (Koizumi et al., 2007). In AD model mice, Ca^{2+} activity also relies on purinergic signalling and intracellular release of Ca^{2+} as both the P2 receptor antagonist pyridoxalphosphate-6-azophenyl-2′,4′-disulfonic acid (PPADS) and cyclopiazonic acid (which blocks endoplasmic reticulum Ca^{2+}-ATPases) abolished basal transients *in vivo* (Brawek et al., 2014). Of note, however, off-target effects of BAPTA-AM cannot be ruled out (Brawek and Garaschuk, 2013) and indeed preliminary data from our lab suggest that THIK-1 currents are reduced in presence of BAPTA-AM (Christian Madry, unpublished). Further, topically applied BAPTA-AM reduced the process movement speed of LPS-primed microglia *in vivo* (Pozner et al., 2015), which would be consistent with an effect on THIK-1. Because blocking THIK-1 inhibits phagocytosis (see Chapter 4.2, Figure 4.4), BAPTA-AM could be reducing phagocytic rate, at least in part, by acting on THIK-1. Thus,

future work should seek to better dissect the contributions of K^+ and Ca^{2+}, and specifically understand whether the effects of THIK-1 blockers and Ca^{2+} chelators on phagocytosis are additive, synergistic or independent, as well as whether BAPTA-AM reduces phagocytosis in THIK-1 KO microglia.

In contrast to data from *in vitro* preparations, microglia *in situ* present spontaneous Ca^{2+} transients much less frequently (Brawek et al., 2014; Eichhoff et al., 2011; Pozner et al., 2015; Umpierre et al., 2020). Compared to other cells (like neurons or astrocytes, where ~100% or ~80% of the population respectively show basal Ca^{2+} activity; Eichhoff et al., 2011), basal Ca^{2+} activity is rare in microglia *in situ*. While early *in vitro* work seemed to suggest that Ca^{2+} signalling was widespread in these cells, *in vivo* experiments on dye-electroporated microglia showed only ~20% of them displayed transients over 15 minutes (Eichhoff et al., 2011), and a later study using GECI-expressing microglia found only ~4% of cells were active over 20 min (Pozner et al., 2015). This suggests that activation of microglia (which is arguably higher in electroporated *versus* intact GECI-expressing cells, and even higher in culture) enhances their Ca^{2+} responses.

The average basal Ca^{2+} activity rate for untreated microglia in this study was 0.13 transients/min (Figure 6.3), which is similar to previous work (e.g. 0.17 transients/min *in vivo* in adult mice; Brawek et al., 2014). Comparing figures across studies would be inappropriate, however, as no estimate is fully correct. For instance, most studies (including the present one) image single focal planes rather than *z*-stacks. While 3D imaging would provide additional information, single-plane imaging is widely deemed more reliable: *z*-stack scanning impedes detection of rapid events (because it reduces scanning speed). In addition, signal from deeper frames would not be comparable (in intensity) to that from more superficial frames within a stack (Semyanov et al., 2020). However, single-plane scanning does mean that some events fail to be detected, particularly in out-of-focus processes, which could be relevant particularly considering the higher Ca^{2+} activity of processes (Figure 6.6E). Thus, an absolute estimate of Ca^{2+} transient rates in microglia cannot easily be accurately established.

On the other hand, as mentioned, different experimental conditions might artifactually increase Ca^{2+} activity in setups that provoke microglial activation. Tissue heating, which can also alter glial Ca^{2+} signals (Schmidt and Oheim, 2020), was reduced in this study by limiting the laser intensity and imaging in short sessions. However, other factors will inevitably modify microglial behaviour, particularly in slice work. Brain slicing not only damages microglia and induces their activation, but also disrupts long-range neuronal connections (decreasing neuronal activity: Umpierre et al., 2020). Both could contribute to artifactually increasing Ca^{2+} activity, compared to *in vivo*. Even *in vivo*, acute window protocols lead to higher process Ca^{2+} activity than chronic windows (Umpierre et al., 2020), which is thought to reflect microglial activation following craniotomy (Xu et al., 2007). Therefore, for a better estimate of microglial Ca^{2+} activity under physiological conditions, future work should preferably use chronic window *in vivo* imaging of GECI reporter mice.

This work, suggesting a higher rate of Ca^{2+} transients in microglial processes *versus* in somata (Figure 6.6E), adds to previous studies suggesting that glial Ca^{2+} is finely regulated across the cell (Semyanov et al., 2020). Again, differences in Ca^{2+} activity between cell compartments might also differ *ex vivo* versus *in vivo*. For example, astrocytic Ca^{2+} fluctuations are larger in cell microdomains in brain slices, but differences narrow *in vivo* (Srinivasan et al., 2015). This may suggest that cell processes are more sensitive to damage (e.g. from slicing), highlighting their functional relevance, which could explain the increased basal rate of Ca^{2+} activity that I detected in microglial processes compared to somata when imaging cells in brain slices.

Block of THIK-1 channels prevented Ca^{2+} activity in microglia. Because the main route for extracellular Ca^{2+} entry into microglia is via ligand-gated Ca^{2+}-permeable receptors, hyperpolarisation is thought to control Ca^{2+} response coupling in microglia (Laprell et al., 2021). This could explain how blocking THIK-1 channels, which depolarises the microglial membrane voltage (Madry et al., 2018), reduces Ca^{2+} rises. However, it would not be consistent with most Ca^{2+} coming from intracellular stores, as the plasma membrane voltage will not affect the driving force for IP_3-mediated store release. Only if THIK-1 channels were

also present in intracellular membranes (e.g. those forming the endoplasmic reticulum), would the voltage of these internal compartments become more negative relative to the cytoplasm when blocking THIK-1 and would that decrease the driving force for Ca^{2+} release. Nevertheless, it is not known whether THIK-1 channels are also expressed on the internal membranes of microglia, and the scant evidence available to date indicates that THIK-1 channels are targeted to the outer rather than internal membranes in transfected MDCK and HeLa cells (Chatelain et al., 2013; Renigunta et al., 2014).

Alternatively, TPA and bupivacaine could be blocking Ca^{2+} activity by acting on other two-pore domain K^+ channels expressed by microglia, such as THIK-2 (*Kcnk12*) or TWIK-2 (*Kcnk6*), which transcriptome data suggest are present in the cell (Zhang et al., 2014). TWIK-2 is not inhibited by bupivacaine (Chavez et al., 1999), which in this study also reduced microglial Ca^{2+} activity, so it is unlikely to be the target. However, THIK-2 is trafficked to the endoplasmic membrane in transfected cells (Chatelain et al., 2013; Renigunta et al., 2014), so blocking it could conceivably reduce Ca^{2+} release from intracellular stores and explain the observed reduction in Ca^{2+} activity. To confirm this, it will be important to: (i) establish which two-pore domain K^+ channels are expressed in internal membranes in microglia, and (ii) dissect the precise contribution of each channel to regulating microglial Ca^{2+} activity, e.g. by crossing the *Cx3cr1*^{CreER} x GCaMP5g-IRES-tdTomato mice to our THIK-1 KO strain and repeating the performed experiments as a first approximation.

Perhaps surprisingly, isoflurane reportedly increases microglial Ca^{2+} activity *in vivo* (Umpierre et al., 2020). Although isoflurane blocks THIK-1 currents (Madry et al., 2018) and would thus be expected to decrease Ca^{2+} activity according to the data presented here, additional effects could arise *in vivo* with isoflurane decreasing noradrenaline release, increasing cerebral blood flow and affecting neuronal activity (Umpierre et al., 2020). The bimodal response of microglia to neuronal activity shows that they can sense any deviation from homeostatic activity, but the receptors underlying this remain unclear. While the raised $[Ca^{2+}]_i$ when neuronal activity is enhanced is likely due to purinergic signalling (Eichhoff et

al., 2011), the receptors mediating Ca^{2+} signals when neuronal activity is decreased remain to be identified.

During AD, intracellular Ca^{2+} signals are profoundly dysregulated, but robust evidence from undisturbed microglia and a precise understanding of the underlying mechanisms are lacking (Brawek and Garaschuk, 2014). Contrary to previous work where basal transient rate was found to be unchanged in AD model mice (Brawek et al., 2014), I found an increase in microglia close to Aβ plaques (Figure 6.6). Importantly, my data suggest that proximity to plaques increases spontaneous Ca^{2+} transient rate specifically in microglial somata, while processes are not affected. This could be due to processes already being activated upon brain slicing, as discussed, which might override the effect of Aβ such that they exhibit increased basal Ca^{2+} activity regardless of Aβ exposure. Similarly, it is possible that microglial activation caused by Ca^{2+}-sensitive dye electroporation in Brawek et al. (2014) masked the effects of Aβ on microglial somata, which the present study did detect.

Overall, my data suggest that basal Ca^{2+} activity changes near Aβ plaques, around which the Aβ concentration is presumably the highest, such that spontaneous activity is raised by proximity to plaques (Figure 6.6) but evoked responses are reduced (Figure 6.7). In Brawek et al. (2014), microglia away from plaques presented a non-activated morphology, which is consistent with the Aβ concentration being lower away from plaques, and with Aβ effects being dose-dependent. Of note, the size of the detected spontaneous transients did vary between microglia near and away from plaques in that study, suggesting that the level of Aβ exposure or proximity to plaques might affect the magnitude of Ca^{2+} responses. Specifically, the size of Ca^{2+} transients was reduced by a third in plaque-proximal microglia, compared to ramified cells away from plaques (Brawek et al., 2014). If Aβ-activated microglia are unable to mount large responses, that might explain why these cells show impaired responses to ATP application or laser injury, even though they manage to exhibit a baseline of smaller periodic transients when not responding to injury. In line with this, chemotaxis towards ATP was impaired in activated, Aβ plaque-proximal microglia (Brawek

et al., 2014), suggesting that Ca^{2+} rises evoked by injury might be reduced in these cells, although they did not examine this.

Two substances related to AD pathogenesis were investigated here as potential factors regulating microglial Ca^{2+} activity: noradrenaline and ROS.

Noradrenaline controls microglial surveillance and interaction with spines (Liu et al., 2019; Stowell et al., 2019). It also stimulates Aβ phagocytosis by microglia *in vitro*, while its depletion *in vivo* (which occurs in AD patients) increased $Aβ_{1-42}$ levels in the brain of AD model mice (Heneka et al., 2010). This effect on phagocytosis may conceivably arise from noradrenaline acting on microglial $α_1$ receptors (but see below) and thus raising $[Ca^{2+}]_i$ by G_q-mediated signalling and enhancing phagocytosis. Given the importance of microglial phagocytosis of both synaptic elements and Aβ in AD, a process in which Ca^{2+} plays a key role, I studied whether noradrenaline application would affect microglial Ca^{2+} activity in GCaMP-expressing *App*$^{NL-G-F}$ mice, either basally or upon lesioning.

In unstimulated microglia, noradrenaline acts on the predominantly expressed $β_2$ receptors (Gyoneva and Traynelis, 2013), which are G_s-coupled, so simplistically no Ca^{2+} change would be expected. Expression of $α_1$ receptors is negligible in unstimulated microglia (Zhang et al., 2014). By contrast, microglial activation by LPS leads to a switch towards expression of $α_{2A}$ receptors (Gyoneva and Traynelis, 2013). Similarly, their activation by Aβ may induce expression of G_q-coupled $α_1$ receptors and thus increase $[Ca^{2+}]_i$. However, no effect of noradrenaline was found in *App*$^{NL-G-F}$ mice (Figures 6.8–10), suggesting that, in our model, Aβ-activated microglia, like non-stimulated microglia (Gyoneva and Traynelis, 2013; Zhang et al., 2014), do not express G_q-coupled $α_1$ receptors and thus exposure to noradrenaline does not affect $[Ca^{2+}]_i$. More studies will need to be done analysing whether noradrenaline triggers changes of microglial $[Ca^{2+}]_i$ *in vivo*, and if so through which receptors.

Finally, I hypothesised that the effect of Aβ plaque proximity increasing the Ca^{2+} activity of microglia (Figure 6.6) could be mediated by ROS. This would be consistent with my data suggesting that Aβ oligomers induce ROS production in microglia (Chapter 5,

Figure 5.2), and with reports that ROS trigger Ca^{2+} release from internal stores in isolated cells (Görlach et al., 2015; Yan et al., 2006). Modulation of Ca^{2+} release by ROS-mediated oxidation of the IP_3 receptor may provide a mechanism (Bánsághi et al., 2014). If Aβ-evoked changes in microglial Ca^{2+} activity were mediated by ROS, SOD1 could prevent them by lowering ROS in microglia and thus rescue responses to WT levels. However, in microglia at Aβ plaques, no effect of SOD1 was found (Figure 6.10). This may be due to a number of reasons, including: (i) the fact that evoked responses of plaque microglia are already very small in control conditions, (ii) a poorer penetration of SOD1 (a relatively large, 32 kDa homodimer) into plaque areas, or (iii) Aβ levels being too high at plaques for SOD1 to achieve superoxide elimination effectively.

On the other hand, I found that the effect of superoxide elimination with SOD1 affected evoked Ca^{2+} response on *App*$^{NL-G-F}$ microglia away from Aβ plaques. Contrary to what was expected, SOD1 exacerbated the loss of evoked Ca^{2+} responses in these cells (Figure 6.9). Overall, these data suggest that oxidative stress may contribute to Ca^{2+} responses in *App*$^{NL-G-F}$ microglia away from Aβ plaques, but that the role of ROS is likely more complex and possibly involves other species including H_2O_2 (the levels of which are increased as superoxide is removed by SOD1). For instance, H_2O_2 is damaging and triggers inflammatory responses in macrophages (Kim et al., 2008). To better understand the contributions of ROS species, future work should test the direct effect of H_2O_2 and of inhibiting NADPH oxidase with diphenyleneiodonium (DPI; Nortley et al., 2019) on microglial Ca^{2+} responses.

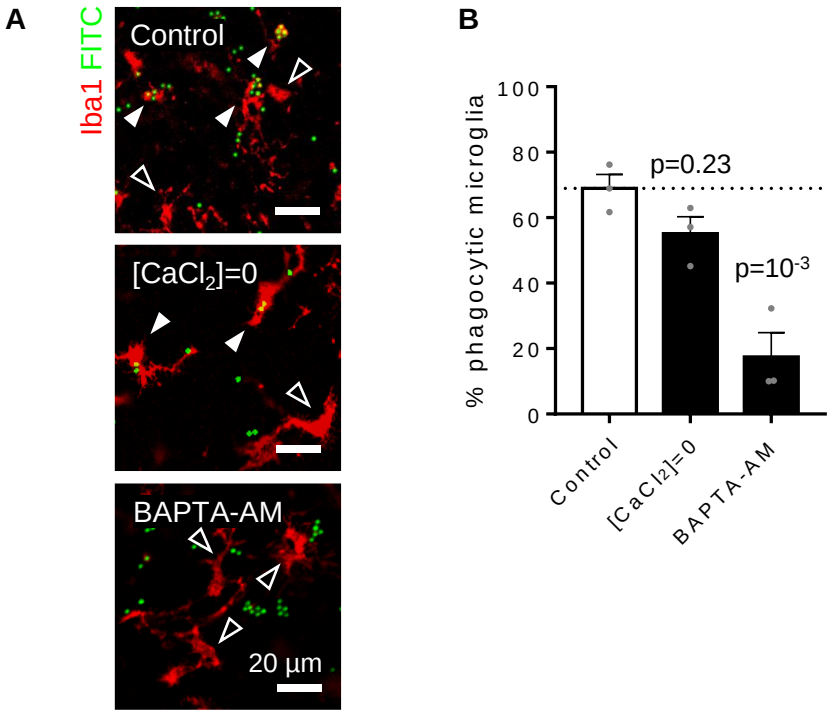

Figure 6.1. Ca^{2+} was required for microglial phagocytosis.

(A) Representative single plane images of microglia (Iba1, red) in acute hippocampal rat slices incubated with 3 µm microbeads (FITC, green), in aCSF with 2 mM $CaCl_2$ (control), no external $CaCl_2$ ([$CaCl_2$]=0) or 50 µM BAPTA-AM with 2 mM $CaCl_2$. **(B)** Percentage of microglia that phagocytosed microbeads in each condition, showing a significant reduction by chelating intracellular Ca^{2+} with BAPTA-AM (3 slices from 2 animals per condition). Data shown as mean ± s.e.m. Statistical significance was tested with one-way ANOVA followed by Dunn's multiple comparison tests.

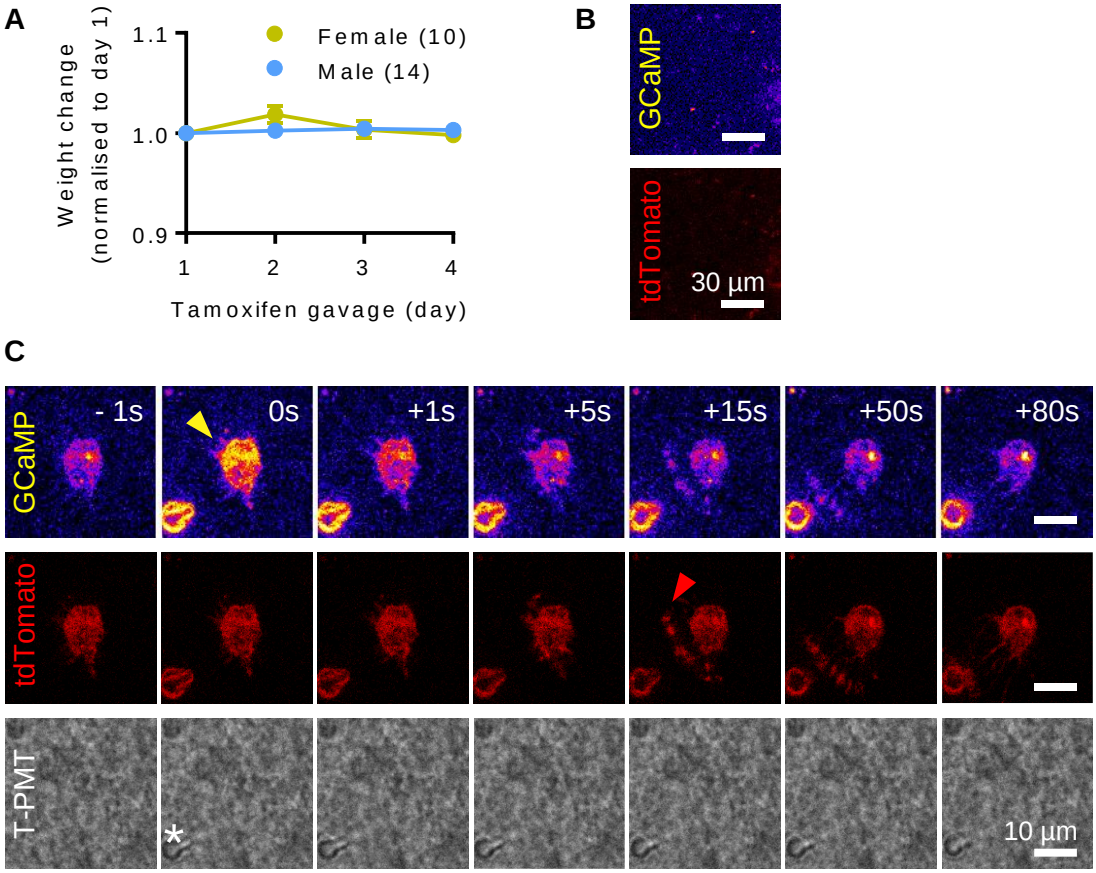

Figure 6.2. Microglia expressed fluorescent reporters and responded to laser damage. **(A)** Tamoxifen administration did not provoke weight change in the treated animals (mean ± s.e.m. shown). **(B)** Non tamoxifen-induced microglia presented very low leak expression of GCaMP (yellow) and tdTomato (red). Images were taken with the same excitation and emission settings as panel (C). **(C)** Tamoxifen-induced microglia expressed GCaMP and tdTomato. When exposed to an acute laser injury (star in the transmitted light channel, T-PMT), tdTomato-labelled microglia responded very rapidly (less than 1 s) with a transient rise of their intracellular calcium level, as detected by GCaMP (yellow arrowhead). Subsequently, they sent out processes that converged at the injury site on a slower timescale (red arrowhead). Times shown indicate seconds before or after the laser ablation.

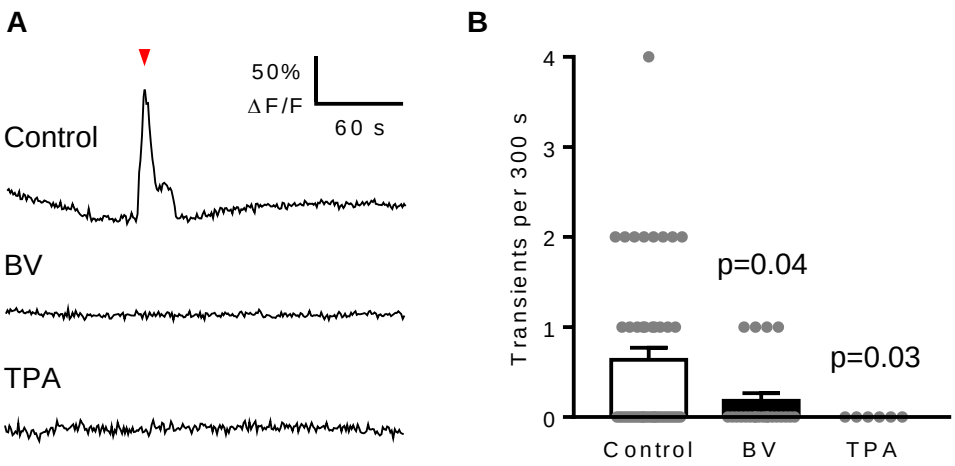

Figure 6.3. Spontaneous microglial Ca^{2+} activity was reduced by THIK-1 channel block.

(A) Representative traces showing rare spontaneous Ca^{2+} transients (red arrowhead) in control microglial somata as measured by GCaMP fluorescence changes (ΔF/F), which are abolished in the presence of 50 µM bupivacaine (BV) or 50 µM tetrapentylammonium (TPA). **(B)** Quantification of spontaneous Ca^{2+} transient frequency, showing a significant reduction by BV (n=22 from 4 mice; p=0.04) and TPA (n=6 from 3 mice; p=0.03) compared to control somata (n=47 from 8 mice). Data shown as mean ± s.e.m. Statistical significance was tested with one-way ANOVA followed by Dunn's multiple comparison tests.

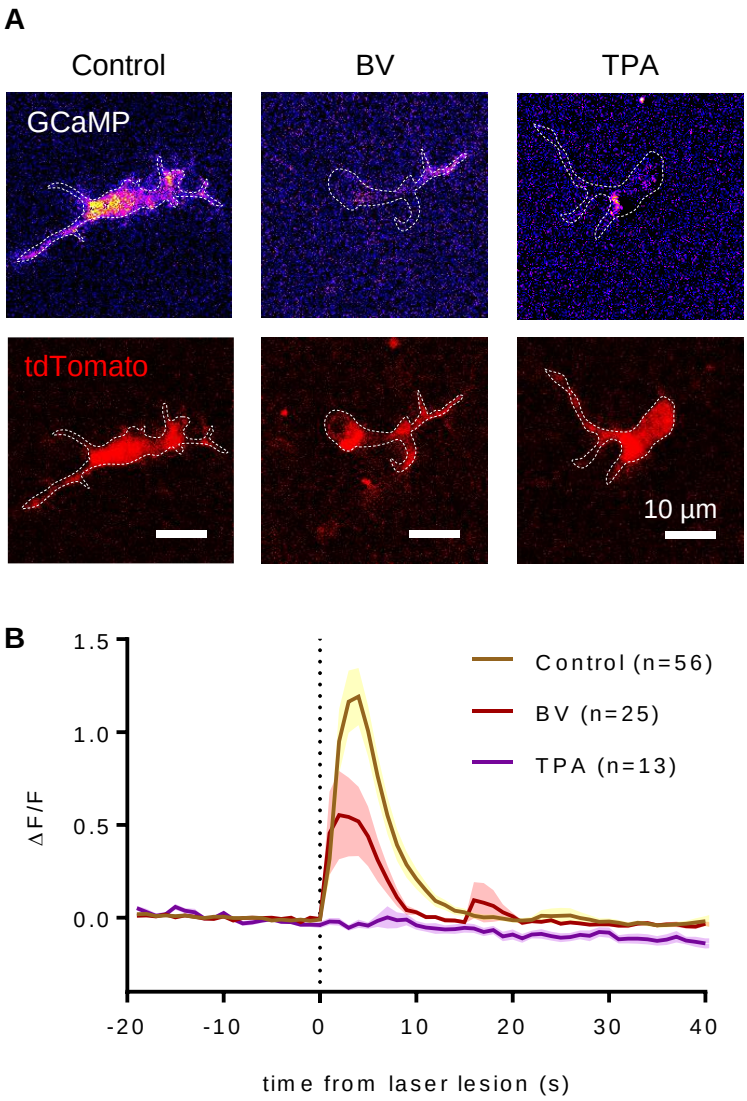

Figure 6.4. Lesion-induced microglial Ca^{2+} rises were reduced by THIK-1 channel block.

(A) Representative microglial cell (tdTomato, red) incubated in control aCSF (control), 50 µM bupivacaine (BV) or 50 µM tetrapentylammonium (TPA). Laser lesion-evoked Ca^{2+} rises are measured by GCaMP fluorescence changes (ΔF/F shown at peak). **(B)** Quantification of somatic $[Ca^{2+}]_i$ levels over time (ΔF/F) showing their increase upon laser lesion (vertical dashed line). Both BV (n=25 from 4 mice; p=0.03) and TPA (n=13 from 3 mice; $p=10^{-4}$) significantly reduced the lesion-induced $[Ca^{2+}]_i$ rise compared to control microglia (n=56 from 8 mice). Data shown as mean ± s.e.m. Statistical significance was tested with one-way ANOVA followed by Dunn's multiple comparison tests.

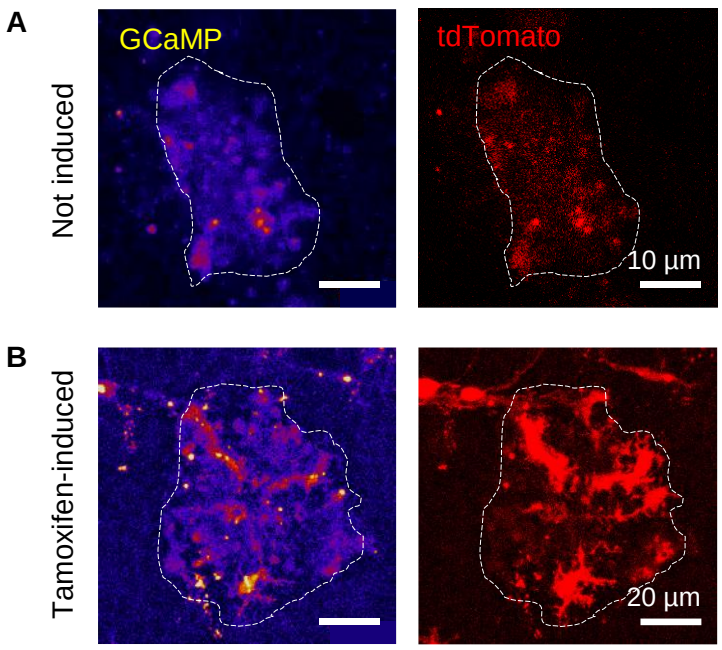

Figure 6.5. Identification of Aβ plaques.

(A) Non tamoxifen-induced *App*$^{NL-G-F}$ animals presented low leak fluorescence both from GCaMP (yellow) and tdTomato (red). However, Aβ plaques are autofluorescent at 920 nm, which allowed their identification. **(B)** In tamoxifen-induced animals, autofluorescence of Aβ plaques remained. Additionally, microglia expressed TdTomato and GCaMP as intended, which allowed further confirmation of plaques by checking for microglial clustering.

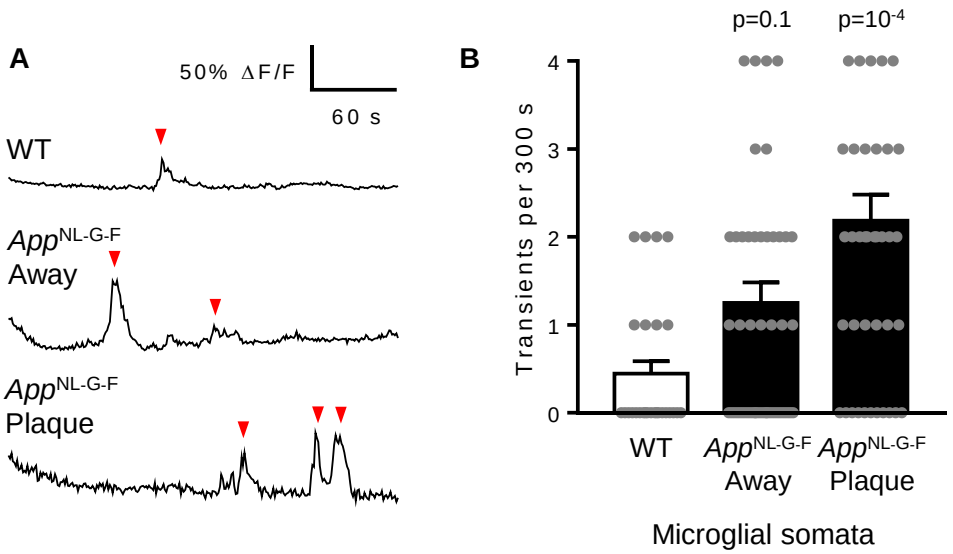
A
50% ΔF/F
60 s
WT
AppNL-G-F
Away
AppNL-G-F
Plaque
B
p=0.1
p=10-4
Transients per 300 s
0
1
2
3
4
WT
AppNL-G-F
Away
AppNL-G-F
Plaque
Microglial somata

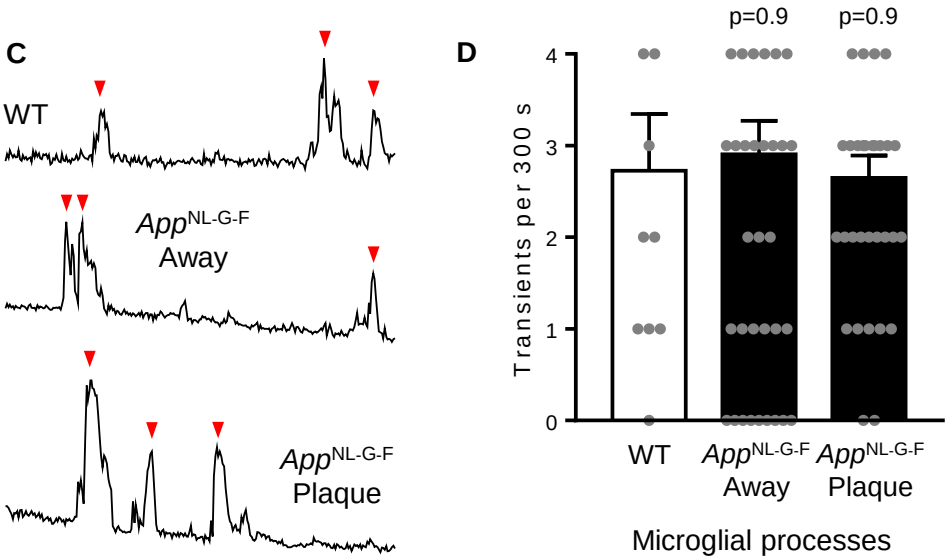
C
WT
AppNL-G-F
Away
AppNL-G-F
Plaque
D
p=0.9
p=0.9
Transients per 300 s
0
1
2
3
4
WT
AppNL-G-F
Away
AppNL-G-F
Plaque
Microglial processes

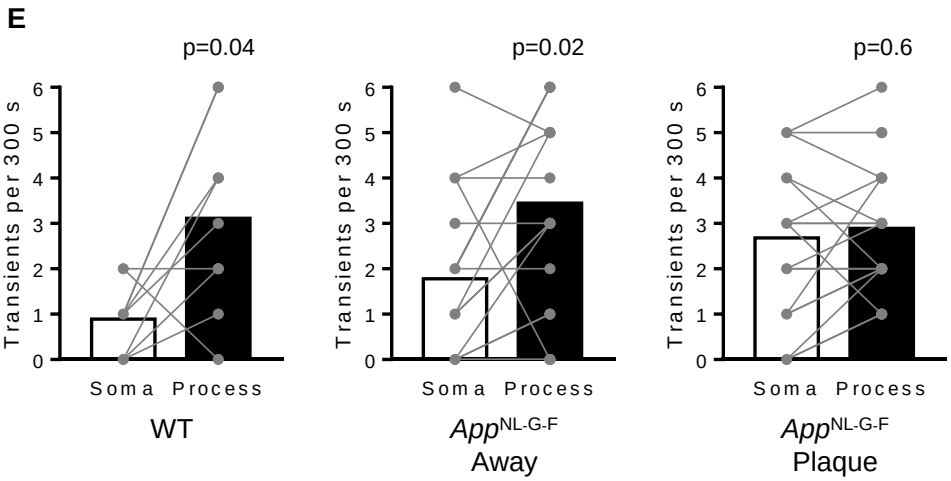
E
p=0.04
p=0.02
p=0.6
Transients per 300 s
0
1
2
3
4
5
6
Soma
Process
WT
AppNL-G-F
Away
AppNL-G-F
Plaque

Figure 6.6. Spontaneous Ca^{2+} activity in microglial somata was increased near Aβ plaques.

(A) Representative traces showing spontaneous Ca^{2+} transients (red arrowheads) in microglial somata from wildtype (WT) and *App*$^{NL-G-F}$ mice at, or >50µm away from, Aβ plaques. **(B)** Quantification of spontaneous Ca^{2+} transient frequency, showing an increase closer to Aβ plaques (WT: n=27 somata from 5 mice; *App*$^{NL-G-F}$ away from plaques: n=56 somata from 8 mice; *App*$^{NL-G-F}$ at plaques: n=43 somata from 8 mice). **(C)** As (A), but for processes. **(D)** As (B), but for processes, showing no effect of Aβ status (WT: n=11 processes from 3 mice; *App*$^{NL-G-F}$ away from plaques: n=42 processes from 6 mice; *App*$^{NL-G-F}$ at plaques: n=34 processes from 6 mice). **(E)** Pair-matched comparisons between process and somatic Ca^{2+} transient rate, showing that for a given microglial cell, spontaneous Ca^{2+} activity was higher in processes in WT (n=9 cells from 3 mice) and *App*$^{NL-G-F}$ microglia away from plaques (n=18 cells from 6 mice) but not in microglia at Aβ plaques (n=19 cells from 6 mice). Data shown as mean ± s.e.m. Statistical significance was tested with one-way ANOVA followed by Dunn's multiple comparison tests (B, D) or two-tailed Wilcoxon matched-pairs signed rank tests (E).

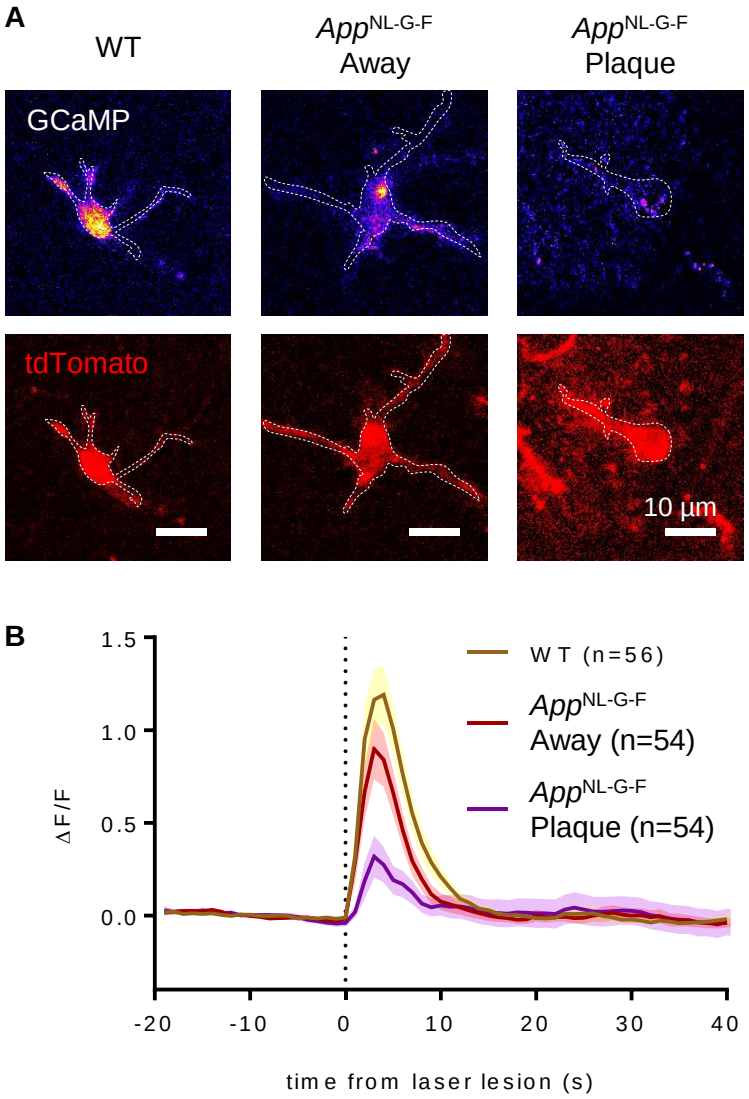

Figure 6.7. Lesion-induced microglial Ca^{2+} rises were reduced near Aβ plaques.

(A) Representative microglia (tdTomato, red) from wildtype (WT) and *App*$^{NL-G-F}$ mice at Aβ plaques or away (>50µm) from plaques. Laser lesion-evoked Ca^{2+} rises are measured by GCaMP fluorescence changes (ΔF/F shown at peak). **(B)** Quantification of somatic $[Ca^{2+}]_i$ levels over time (ΔF/F) showing their increase upon laser lesion (vertical dashed line). *App*$^{NL-G-F}$ microglia, both at (n=54 from 8 mice; p= 10^{-4}) and away from Aβ plaques (n=52 from 8 mice; p=0.03), showed a significantly reduced lesion-induced $[Ca^{2+}]_i$ rise compared to WT microglia (n=56 from 5 mice). Data shown as mean ± s.e.m. Statistical significance was tested with one-way ANOVA followed by Dunn's multiple comparison tests.

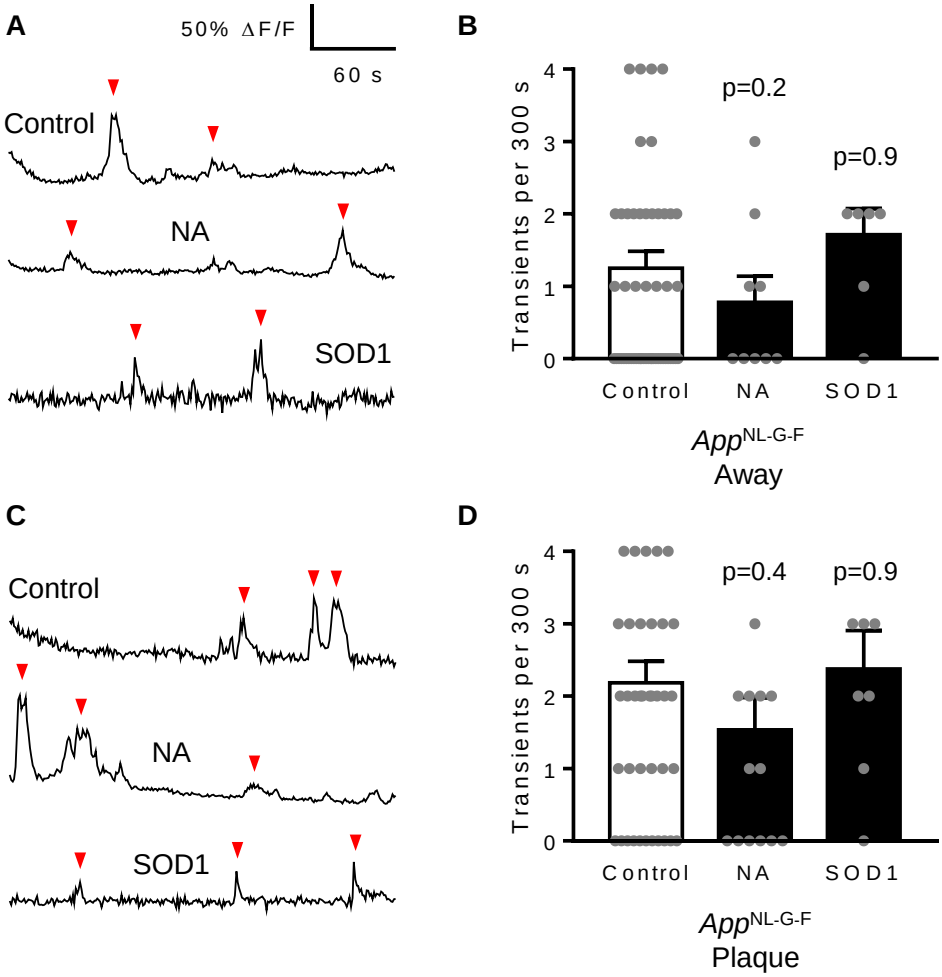

Figure 6.8. Spontaneous microglial Ca^{2+} activity in *App*$^{NL-G-F}$ microglia was not affected by noradrenaline or superoxide dismutase.

(A) Representative traces showing spontaneous Ca^{2+} transients (red arrowheads) in somata of *App*$^{NL-G-F}$ microglia >50µm away from Aβ plaques, as measured by GCaMP fluorescence changes (ΔF/F), in control aCSF (control) or in the presence of 15 µM noradrenaline (NA) or 150 U/ml superoxide dismutase (SOD1). **(B)** Quantification of spontaneous Ca^{2+} transient frequency, showing no effect of NA (n=15 from 5 mice) or SOD1 (n=8 from 3 mice) compared to control somata (n=43 from 8 mice). **(C)** As (A), but for microglia at Aβ plaques. **(D)** As (B), but for microglia at Aβ plaques, showing no effect of NA (n=9 from 5 mice) or SOD1 (n=7 from 3 mice) compared to control somata (n=56 from 8 mice). Data shown as mean ± s.e.m. Statistical significance was tested with one-way ANOVA followed by Dunn's multiple comparison tests.

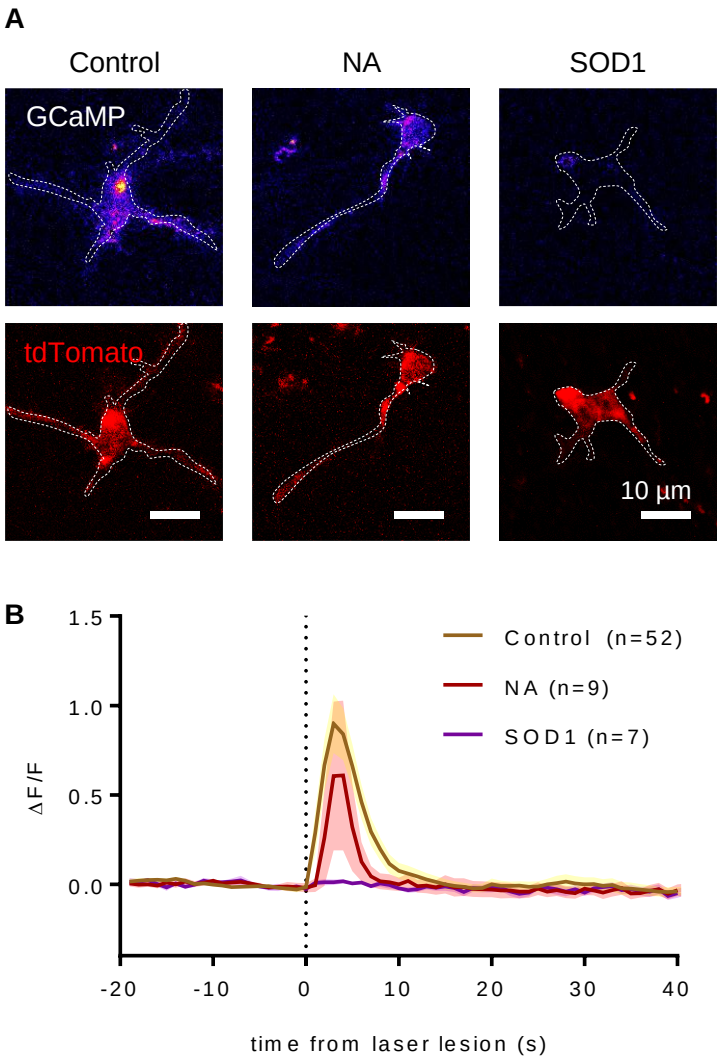

Figure 6.9. Lesion-induced Ca^{2+} rises in *App*$^{NL-G-F}$ microglia away from Aβ plaques were reduced by superoxide dismutase.

(A) Representative *App*$^{NL-G-F}$ microglia (tdTomato, red) >50µm away from Aβ plaques, in control aCSF (control) or in the presence of 15 µM noradrenaline (NA) or 150 U/ml superoxide dismutase (SOD1). Laser lesion-evoked Ca^{2+} rises are measured by GCaMP fluorescence changes (ΔF/F shown at peak). **(B)** Quantification of somatic $[Ca^{2+}]_i$ levels over time (ΔF/F) showing their increase upon laser lesion (vertical dashed line). SOD1 reduced the lesion-induced $[Ca^{2+}]_i$ rise (n=7 from 3 mice; p=0.03) compared to control cells (n=52 from 8 mice). NA did not have a significant effect (n=9 from 5 mice; p=0.1). Data shown as mean ± s.e.m. Statistical significance was tested with one-way ANOVA followed by Dunn's multiple comparison tests.

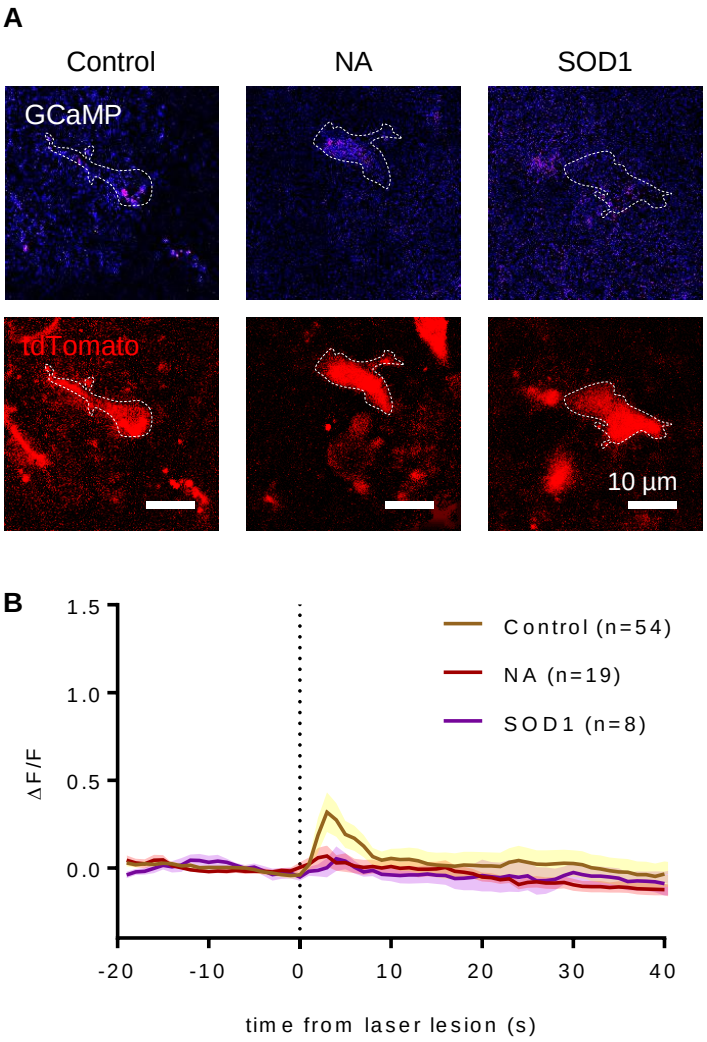

Figure 6.10. Lesion-induced Ca^{2+} rises in *App*$^{NL-G-F}$ microglia at Aβ plaques were not affected by noradrenaline or superoxide dismutase.

(A) Representative *App*$^{NL-G-F}$ microglia (tdTomato, red) at Aβ plaques, in control aCSF (control) or in the presence of 15 µM noradrenaline (NA) or 150 U/ml superoxide dismutase (SOD1). Laser lesion-evoked Ca^{2+} rises are measured by GCaMP fluorescence changes (ΔF/F shown at peak). **(B)** Quantification of somatic $[Ca^{2+}]_i$ levels over time (ΔF/F) showing their increase upon laser lesion (vertical dashed line). Neither NA (n=19 from 5 mice; p=0.3) nor SOD1 (n=8 from 3 mice; p=0.9) altered the lesion-induced $[Ca^{2+}]_i$ rise, compared to control cells (n=54 from 8 mice). Data shown as mean ± s.e.m. Statistical significance was tested with one-way ANOVA followed by Dunn's multiple comparison tests.

“Don't adventures ever have an end? I suppose not. Someone else always has to carry on the story. Well, it can’t be helped. I wonder if it’s any good trying to finish my book?”

J.R.R. Tolkien, *The Lord of the Rings* (1954)

7. Discussion and perspectives

7.1 Introduction

The work presented in this thesis contributes to advancing our knowledge of microglia and their interaction with their environment in physiological and pathological scenarios. The results presented in each chapter have been discussed in the respective chapter discussions. In this final chapter, I will put my PhD work in perspective and discuss how it relates to recent developments, emerging views and ongoing challenges in the field, while discussing further research that could extend the presented findings.

7.2 An updated view of synapse pruning

Seminal observations by Blinzinger and Kreutzberg (1968) implicated microglia in synaptic pruning, a process postulated as a global mechanism for circuit stabilisation and refinement (Changeux and Danchin, 1976). Most synapses in the neonatal mouse are glutamatergic and these are preferentially contacted and engulfed by microglia (Lee et al., 2021a; Wan et al., 2020). By contrast, regulation of inhibitory synapses by microglia is thought not to involve phagocytosis. Instead, microglial processes physically displace GABAergic inputs surrounding neuronal somata (Chen et al., 2014) and regulate the strength of glycinergic synapses in the spinal cord by altering synaptic trapping of glycine receptors as they diffuse in the plasma membrane (Cantaut-Belarif et al., 2017).

There is a fine balance between "eat-me" and "don't-eat-me" signals controlling microglial removal of synapses, but whether specific synapses are tagged for elimination by microglia remains unknown (Bartels et al., 2020). The data presented in Chapter 4 indicate that microglial removal of excitatory synapses is mainly by engulfing presynaptic material in the developing brain, while data in Chapter 5 imply that removal of postsynaptic structures could also occur in disease. Molecules involved in synaptic tagging during development, like

C1q or C3, may mediate the reactivation of microglial removal of synapses in disease (Dejanovic et al., 2018; Gratuze et al., 2020; Wu et al., 2019). As discussed in section 5.5, targeting and engulfment of postsynaptic material could be context-dependent and take place in disease even though they may not occur in development.

Despite microglia traditionally being thought to act by removing redundant synapses (e.g. Paolicelli et al., 2011), new evidence supports a more complex model where microglial effects on synapses are a combined result of partial phagocytosis of presynaptic terminals and remodelling of postsynaptic terminals (the latter will be discussed in detail in the next section). Using correlative light and electron microscopy of organotypic hippocampal cultures, most microglia-synapse contacts were found to comprise apposition rather than complete encapsulation (Weinhard et al., 2018). The process might be more passive than previously thought, whereby synaptic material is partially phagocytosed by sinking into microglial invaginations to be degraded in a process termed “trogocytosis” (“trogo-” for nibbling; Weinhard et al., 2018).

The results presented describe a role for THIK-1 K^+ channels in controlling microglial phagocytosis of synapses, such that the absence or pharmacological block of these channels leads to an increase in the numbers of synapses that remain in the rodent or human brain (see Chapter 4). However, phagocytosis does not occur in isolation from process motility, and it is possible that the observed regulation of phagocytosis by THIK-1 is a consequence, at least partly, of the increased process ramification and hence surveillance that it promotes (see Chapter 3).

Interestingly, $P2Y_{12}$ receptor signalling mediates recruitment of microglia to synapses, and synapse engulfment induced by sensory deprivation is prevented in $P2Y_{12}$ KO microglia (Sipe et al., 2016). This may reflect downstream activation of THIK-1 by $P2Y_{12}$ (Madry et al., 2018) being absent in the $P2Y_{12}$ KO, as my results indicate that THIK-1 controls microglial uptake of synaptic material. Future work could examine whether downstream activation of THIK-1 may underlie other effects attributed to $P2Y_{12}$, such as the

control of microglial interaction with neuronal somata in the cortex (Cserép et al., 2020b) or their engulfment of myelinated axons in the spinal cord (Maeda et al., 2010).

7.3 Microglial interaction with neurons

Microglia interact with neurons at different spatial scales. These include both direct membrane-membrane contact and interactions via intermediate cells and released soluble factors (Cserép et al., 2020a). As THIK-1 channels (like TREM2 receptors; Liu et al., 2020) regulate not only microglial process motility and phagocytosis (see Chapters 3 and 4) but also cytokine release (Madry et al., 2018), they are particularly suited to regulate microglial interactions with neurons.

Upon such interactions, microglia can promote not just removal (as discussed in the previous section) but also formation of synapses. The synapse remodelling rate depends on brain area, spine type (Pfeiffer et al., 2018; Trachtenberg et al., 2002) and preparation (Xu et al., 2007). In the mouse cortex, most spines have a very slow turnover and persist for months or years (Grutzendler et al., 2002). By contrast, spines of hippocampal neurons may turn over completely in a time window between a week and a month (Attardo et al., 2015; Pfeiffer et al., 2018). While the microglial role in synapse formation has not been directly addressed in this study, microglial contacts with neurons lead to formation of filopodia and dendritic spines in the hippocampus (Weinhard et al., 2018) and cortex (Miyamoto et al., 2016). Microglia-secreted paracrine factors such as the brain-derived neurotrophic factor (BDNF) may also help the formation of new spines (Parkhurst et al., 2013).

THIK-1 may be involved in both inducing and removing synapses. On the one hand, I have shown that THIK-1 promotes phagocytic removal of synapses by microglia. On the other hand, I have also observed (in agreement with previous work; Madry et al., 2018) that THIK-1 promotes brain surveillance by microglial processes, which could arguably increase synapse-inducing contacts with neurons. In addition to directly stimulating filopodial outgrowth by promoting such interactions, THIK-1 may also promote synapse formation by

enhancing phagocytic clearing of the extracellular matrix in which neurons are embedded (which creates space for new synapses; Nguyen et al., 2020). Given the key role of THIK-1 in controlling microglial process ramification and surveillance, further work would likely benefit from looking at direct interactions between microglial processes and synaptic elements. For instance, it would be interesting to assess contact of microglial processes with spines in the presence or absence of THIK-1, and to analyse spine number and morphology near and away from microglia. Of note, such interactions are rare and fast, and the cellular components at play are small, which makes them challenging to investigate, although new approaches to studying microglia-synapse interaction and remodelling are being developed (e.g. based on photodamage; Cangalaya et al., 2020).

Synapse formation and elimination occur throughout life, but are more pronounced in younger animals (e.g. spine turnover in mice is around 4-fold higher at 1 month than at 4-6 months of age; Zuo et al., 2005). In terms of synapse numbers, cortical spine density peaks at 1-4 years post birth in humans, and then declines gradually into adulthood (Huttenlocher and Dabholkar, 1997). A similar pattern is present in macaques (peak at 3.5 months post birth; Elston et al., 2009) and mice (where phagocytosis peaks around P20; Paolicelli et al., 2011; Weinhard et al., 2018). Thus, modulation of THIK-1 might be more effective in affecting synapse numbers in early life, which would coincide with my observed decrease in the effect of THIK-1 blockers on microglial surveillance with age. However, I have shown that drugs which block THIK-1 also affected microglia and synapses in adult human microglia (although more work is needed to confirm the specificity of these results). This may be important for clinical relevance, particularly as developmental microglial functions (including the removal of synapses) are thought to be re-engaged in the diseased brain.

Lastly, direct microglia-neuron contacts are functionally segregated and have been reported at various neuronal compartments, not just at synapses (Cserép et al., 2020a). In fact, contacts with neuronal somata are much more common and prolonged than those at synaptic sites (~25 minutes and ~7.5 min on average, respectively; Cserép et al., 2020b). These contacts may help microglia sense and regulate neuronal activity (Cserép et al.,

2020b). Microglia respond to rises of neuronal activity, anaesthetics or loss of sensory input (Liu et al., 2019; Stowell et al., 2019; Umpierre et al., 2020) and high-frequency stimulation prolongs microglial contacts with neurons (Pfeiffer et al., 2016). The aberrant activity of neurons in disease (including AD; Busche et al., 2012) could thus alter microglial motility and interactions. In turn, microglial contact may feed back to change neuronal activity (Akiyoshi et al., 2018; Wan et al., 2020). It would be interesting to examine interactions between microglial processes and neuronal somata, whether these are altered in the absence of THIK-1 (or TREM2), and the potential electrophysiological consequences of any such alteration.

7.4 Studying Alzheimer's Disease: limitations of the current study

The present work used knock-in mice to model amyloid accumulation and gain insight into microglial roles in AD, but all mouse models for AD have limitations. Transgenic strains (e.g. for *App* or *Psen1/2*) are extensively used in AD research, but drawbacks of these "first-generation" models include overexpression artifacts, variable transgene copy number and random genomic insertion. To overcome such issues, knock-in strains were subsequently developed where Aβ accumulates without *App* overexpression (Joel et al., 2018; Sasaguri et al., 2017). Of these, this work has used $App^{NL\text{-}G\text{-}F}$ mice, but an unresolved issue is the lack of appropriate controls; like most studies, here I used wildtype mice as controls rather than mice harbouring the unmutated human *App* gene (which are now available).

Research on behavioural changes in $App^{NL\text{-}G\text{-}F}$ mice has yielded conflicting results, with most reporting a largely unaltered cognition. Spatial memory and memory of contextual fear are normal (Latif-Hernandez et al., 2019; Sakakibara et al., 2018) and behavioural changes are predominantly associated with non-cognitive processes, such as attention, anxiety-related behaviours and pain sensitivity (Masuda et al., 2016; Sakakibara et al., 2018).

It is important to stress that the *App*$^{NL-G-F}$ strain remains a model for preclinical AD, where the multifactorial nature of human disease is not recapitulated and neither tauopathy nor neurodegeneration occur (Saito et al., 2014). While some amyloid-based models provide certain tau hyperphosphorylation, a full model of AD (i.e., where amyloidosis leads to tau tangle formation and neuronal loss) is still lacking (Sasaguri et al., 2017). The apparent lower susceptibility of mice to full AD developing may be partly due to the their tau protein being more resistant to toxic change than ours (Joel et al., 2018), or to them overexpressing protective genes (e.g. *Trem2*) in response to rising Aβ levels (Matarin et al., 2015). The role of TREM2 in different contexts will be discussed in section 7.8.

Furthermore, sex may play a role in microglial activation, which has not been analysed in the current work given the small number of animals used. In the context of AD, female *App* transgenics are more prone to pathology (King et al., 1999), and expression of the reduced function TREM2-R47H in tau-P301S mice exacerbated memory deficits only in females (Sayed et al., 2020). Female *App*$^{NL-G-F}$ mice also showed increased Aβ burden compared to males but no difference was detected in mice younger than 12 months of age (Masuda et al., 2016) so sex is likely to play a minor role, if any, in the 4-month-old animals used in the present study. However, it would still be interesting to consider sex effects in future work, particularly as there is no consensus about whether male (VanRyzin et al., 2019) or female (Nelson et al., 2017) microglia are more phagocytic, which could be age-, region- and context-dependent.

7.5 The role of microglia in Alzheimer's Disease

Removal of synapses by microglia actively contributes to forgetting in adult mice (Wang et al., 2020a), where microglial depletion or impairment prevents synapse loss in both healthy (Wang et al., 2020a) and AD model animals (Shi et al., 2017a; Spangenberg et al., 2016). Thus, preventing microglial phagocytosis of synapses may be beneficial in neurodegenerative contexts. In the current study, when blocking or deleting THIK-1, levels of

synaptic markers increased in healthy rodent and human tissue and hippocampal spine density increased in AD model mice (where Aβ plaque load remained unaltered). Thus, this may be a promising approach to protect against synapse loss in disease. However, it remains unclear: (i) to what extent a short-term pharmacological block of THIK-1 *in vivo* will affect synapse levels, (ii) how lasting the effects of any such block will be, and (iii) whether the preserved synapses remain functional or represent an accumulation of dysfunctional connections, which would be undesirable. Future work could examine these aspects.

On the other hand, microglial phagocytosis can help to remove synapses, but also Aβ (Paolicelli et al., 2017), raising questions as to whether its net effect is detrimental or beneficial in pathology. If microglia contribute to removing synapses first, but Aβ later (Sheng et al., 2019), inhibiting phagocytosis may be a double-edged sword. Thus, disease stage is a key factor to consider for therapy. It would be desirable to target microglial phagocytosis in the initial stages of the disease (for which early detection of patients is essential; Zetterberg and Blennow, 2020). While disease-modifying approaches have largely failed to date, trials are starting to include more prodromal/preclinical patients (Long and Holtzman, 2019). Approaches that seek to prevent synapse loss, as does blocking THIK-1, would be interesting for early treatment before damage is extensive. By contrast, preventing phagocytosis may be detrimental later with regard to amyloid.

However, there is growing evidence that, in fact, microglia do not contribute to the clearance of Aβ deposits. Reducing microglial activation (Roy et al., 2020) or depleting these cells once plaques were already present (Spangenberg et al., 2016) failed to affect plaque load. Indeed, when microglia were ablated prior to Aβ deposition, their depletion attenuated the formation of plaques, reducing their number and volume (Sosna et al., 2018; Spangenberg et al., 2019). This may be explained by the fact that microglia-released ASC specks promote Aβ aggregation (Venegas et al., 2017) because microglial repopulation in brains previously lacking these cells restored Aβ pathology (Spangenberg et al., 2019), suggesting that microglia contribute to plaque seeding.

In summary, microglia may not affect the amount of Aβ present, i.e., Aβ production or clearance (Olmos-Alonso et al., 2016; Spangenberg et al., 2019, 2016), but rather its distribution in the AD brain. Specifically, their role could be in compacting plaques (Huang et al., 2021). Microglial depletion in *App*$^{NL-G-F}$ mice did not alter plaque coverage but resulted in larger plaque cores (although discrepancies between results obtained using different antibodies remain an important consideration; Clayton et al., 2020). This would be consistent with the idea that microglia provide a physical barrier that prevents the spread of amyloidosis (Condello et al., 2015).

In addition to the above, the microglial contribution to the generation of ROS in response to Aβ oligomers (see Chapter 5) could play a major role in AD pathogenesis, as ROS induce pericyte-mediated constriction of capillaries and a subsequent reduction in cerebral blood flow (Nortley et al., 2019). A clear implication of this work is that Aβ-evoked generation of ROS may be targeted as a therapeutic approach in AD. Indeed, overexpression or application of the scavenger SOD1 in *App* transgenic mice reversed the deleterious effects of *App* overexpression (Carlson et al., 1997; Iadecola et al., 1999). As a proof of concept, combined block of ROS generation and of the downstream capillary constricting endothelin receptor ET_A in rat slices prevented vasoconstriction by Aβ oligomers (Nortley et al., 2019). Our results also raise the question of what fraction of the neuronal damage seen in AD is caused by the decrease of energy supply that Aβ produces by constricting capillaries, as opposed to by direct toxicity of Aβ and tau.

7.6 Is microglial phagocytosis impaired in Alzheimer's Disease?

The results presented in Chapter 5 suggest that phagocytosis is affected in our AD mouse model, as microglia in proximity to Aβ plaques show morphological changes and increased lysosomal coverage. Similarly, in AD patient microglia, expression of the lysosomal marker CD68 also increased at the RNA (Zhou et al., 2020) and protein level (Woollacott et al., 2020).

However, increased lysosome load may not reflect enhanced phagocytosis, but perhaps the opposite. In zebrafish, microglia expressing mutant RagA, a key lysosomal regulator, present expanded lysosomes but are less able to digest ingested materials (Shen et al., 2016). In AD, phagocytes might become unable to degrade Aβ. Damaged lysosomes and their cargos may not be degraded effectively when microglia become overwhelmed by amyloid pathology, which would contribute to cell toxicity (Hung et al., 2013). This would reconcile the facts that microglia accumulate more lysosomes in AD (El Hajj et al., 2019) but they are less able to phagocytose Aβ (Krabbe et al., 2013; Wendt et al., 2017). Indeed, impairments in autophagy have been linked to AD (Fujikake et al., 2018), and microglia from human AD brains show reduced levels of an autophagy protein required for efficient recycling of phagocytic receptors (Lucin et al., 2013).

In summary, it is possible that the increased lysosome burden in AD reflects impaired resolution of phagocytosis or defective recycling of lysosomes/phagosomes. Thus, it would be interesting to expand the current work by studying downstream function rather than merely relying on simple markers of phagocytosis (e.g. CD68). For instance, tools like $A\beta^{pH}$ may allow investigation of downstream mechanisms such as protein degradation. Bafilomycin A1 can be used to block acidification of endosomes and thus slow breakdown of inclusions (Hughes and Appel, 2020; Peri and Nüsslein-Volhard, 2008), which would also be helpful to assess digestion and degradation of cargos.

7.7 The toxic species of Aβ

As discussed in section 7.5, recent evidence suggests that microglia are involved in seeding and compaction of Aβ plaques. While this would suggest that microglia are initiators of plaque formation in the brain, it also raises the question as to how damaging plaques are in AD. Aβ plaques may act rather as a “reservoir” of oligomers, which form a halo around plaques and are thought to be the toxic species (Koffie et al., 2009).

Of note, plaque load alone does not correlate with dementia. Instead, the ratio of Aβ dimer equivalents to plaque area was found to distinguish better between people depositing Aβ with or without dementia (Esparza et al., 2013). In mice, cognitive improvement can be achieved without altering plaque load (Olmos-Alonso et al., 2016; Spangenberg et al., 2016) or indeed despite increasing it (Shi et al., 2017a). Further, changes in synaptic transmission (Cummings et al., 2015) and aberrant neuronal activation (Busche et al., 2012) precede plaque formation, while Aβ dimers (100 nM) instantly increased hyperactivity (Busche et al., 2012). Less dense plaques are associated with greater neuronal damage (Wang et al., 2016; Yuan et al., 2016), and Aβ oligomers are more neurotoxic than fibrils in culture (Giovanna et al., 2010). These data support the view that oligomers might be more damaging to synapses when they remain soluble. In line with this, soluble Aβ oligomers have emerged as a prominent therapeutic target in the past decade. Four drugs with completed phase 2 or 3 trials and conditional approval (aducanumab) or potential near-term approval (the injectable antibodies gantenerumab and lecanemab and the small molecule oral tablet ALZ-801) can all bind or neutralise soluble Aβ (Bohrmann et al., 2012; Sevigny et al., 2016; Tolar et al., 2020). In fact, ALZ-801 works by inhibiting oligomerisation and does not bind plaques (Gervais et al., 2007).

This study has shown that microglia can engulf Aβ particles (both synthetic $Aβ^{pH}$ and endogenously produced Aβ in *App*$^{NL-G-F}$ mice, see Chapter 5). Because Aβ oligomers impair phagocytosis while fibrils might trigger it (Pan et al., 2011), the Aβ species detected inside microglia are likely to be mainly aggregates rather than oligomers (although this may be affected by how the acidic pH environment of the lysosome affects aggregation). As the different forms of Aβ are not equivalent, and assuming that oligomers are the key driver of pathology, plaque levels and microglial engulfment of Aβ aggregates may provide little information about pathogenesis by itself. Therefore, future work would benefit from focusing on the levels and effects of Aβ oligomers. Specifically, it would be interesting to expand the current study by examining, in *App*$^{NL-G-F}$ mice, whether lack of THIK-1 affects either the levels of soluble Aβ in the parenchyma, or the clustering of microglia around plaques (as

decreased encirclement of plaques may result in more diffusion of toxic oligomers and perhaps greater neuronal damage).

7.8 Ageing and disease: the role of TREM2

There are similarities between the transformation of microglia in AD and in ageing. Microglial heterogeneity, which is progressively reduced during life, rises again in both contexts (Masuda et al., 2020b). Like AD (Keren-Shaul et al., 2017), ageing also causes the expansion of specific microglial subpopulations, although these only represent a small fraction of microglia (Hammond et al., 2019). As some microglial changes that occur in AD mirror those detected in old animals, Aβ and tau are thought to aggravate processes involved in ageing, such as cellular senescence, calcium dyshomeostasis and inflammation (Busche and Hyman, 2020). Altered process motility (Hefendehl et al., 2014; Del Moral et al., 2019), Ca^{2+} activity (Del Moral et al., 2019) and cargo digestion (Cantuti-Castelvetri et al., 2018) are all seen in aged microglia. Ageing also leads to a larger lysosome volume fraction (O'Neil et al., 2018) and slower phagocytosis in microglia (Damisah et al., 2020). Expression of a microglial metabolism protein module increases in both ageing and AD (Johnson et al., 2020). In fact, single-cell and bulk profiling of microglia from AD and non-AD old donors found no differences between them (Alsema et al., 2020).

While similar features are shared by both physiological ageing and AD, differences also exist. The results presented in Chapter 3 suggest an age-dependent function of AD-linked TREM2 receptors and raise the question of whether microglial responses in "healthy" ageing and disease are comparable. Although loss of function variants of TREM2 increase the risk of AD (Guerreiro et al., 2013; Jonsson et al., 2013), my results (indicating improved microglial surveillance in old mice lacking TREM2) add to emerging evidence that impaired TREM2 function may be protective in normal ageing in mice. Aged TREM2 KO mice show increased synapse levels, slightly enhanced plasticity and improved spatial memory (Qu and Li, 2020). These data are in line with the reduced synapse engulfment mediated by TREM2-

deficient microglia (Filipello et al., 2018) and with transcriptomic analyses revealing that ageing failed to trigger DAM genes in microglia from old TREM2 KO mice (Nugent et al., 2020).

It may be that, in normal ageing, the increased process ramification and motility caused by TREM2 deficiency stimulate formation of filopodia and spines, as a consequence of more interaction between neurons and microglial processes (see section 7.3). In addition, synapses may be protected from removal by the loss of microglial phagocytic capacity, thereby conferring resilience to subtle memory deficits in ageing and perhaps in the early stages of AD. However, impairment of Aβ handling by lack of functional TREM2 could be detrimental later. In agreement with this notion, knockdown of *Trem2* in APP/PSEN1 transgenic mice prevented loss of synapses in young animals but avoided removal of amyloid thus accelerating loss of synapses in older mice (Sheng et al., 2019).

As overexpression of TREM2 reduces amyloid pathology, some therapeutic strategies in AD seek to enhance TREM2 activation. Candidates predominantly target the receptor rather than its ligands (because our knowledge of them is limited; Deczkowska et al., 2020). An antibody directed to the stalk region of TREM2 (avoiding its proteolytic shedding and promoting its signalling) reduced levels of $A\beta_{1\text{-}42}$ in mice (Schlepckow et al., 2020), and the agonist AL002c attenuated neurite damage (Wang et al., 2020b).

In the context of tau pathology, however, TREM2 activation might be detrimental. TREM2-R47H expression (to reduce TREM2 function) in a mouse model of tauopathy increased levels of synaptic markers as a result of decreased microglial engulfment (Gratuze et al., 2020), and complete TREM2 deficiency reduced tau-mediated brain atrophy (Leyns et al., 2017). However, this is controversial, with TREM2 deficiency exacerbating tau phosphorylation in some studies (Jiang et al., 2015). Recent work suggests that TREM2 might restrict Aβ-induced spreading of tau (as TREM2 deletion exacerbated tau pathology only in the presence of Aβ; Lee et al., 2021b). Adding to this complexity, it is possible that effects on synaptic transmission are dose-dependent, whereby loss of function variants and full deficiency have opposite effects (Sayed et al., 2018).

In summary, the net effect of TREM2 activation with regards to different aspects of AD needs to be considered carefully when devising when and how to target it in therapy. Future work should examine how TREM2 deficiency alters microglial morphology and surveillance with age in a mouse depositing Aβ, and whether synapses and long-range connectivity are affected.

7.9 Ca^{2+} signalling as a proxy for microglial function

The experiments presented in Chapter 6 explore the dynamics and functional importance of $[Ca^{2+}]_i$ in microglia. While previous research has relied heavily on Ca^{2+}-sensitive dyes, we now have mice expressing a genetically encoded Ca^{2+} indicator in microglia (*Cx3cr1*^{CreER} x GCaMP5g-IRES-tdTomato), which I used to examine Ca^{2+} transients that arise both spontaneously and upon laser lesioning.

Microglial Ca^{2+} activity is very rare under basal conditions. Our understanding of Ca^{2+} signalling in microglia has greatly benefited from mechanistic and technical insight from astrocytic research (Semyanov et al., 2020). While basal activity is much lower in microglia, their Ca^{2+} responses to a damaged neuron are more rapid (latency of 0-5 s) than those in astrocytes (5-10 s) (Eichhoff et al., 2011). This suggests an inverse correlation between basal Ca^{2+} activity and the ability to mount robust, rapid stimulus-evoked responses — which would fit with my finding that activated, Aβ-exposed microglia show an increased basal Ca^{2+} activity but impaired lesion-evoked responses (see Chapter 6).

In AD model mice, neuronal Ca^{2+} signals are reportedly upregulated (Busche et al., 2012). However, Ca^{2+} dyshomeostasis in AD is not restricted to neurons, as was initially thought. In fact, astrocytes and microglia also present aberrant Ca^{2+} signalling in the disease (Brawek and Garaschuk, 2014). Astrocytes exhibit intercellular $[Ca^{2+}]_i$ waves that propagate across the astrocytic network, but their basal Ca^{2+} activity is independent of proximity to Aβ plaques. By contrast, I have shown that microglial Ca^{2+} responses depend on their proximity to plaques. In microglia isolated from AD brains, basal Ca^{2+} levels in microglia were higher

than in cells from non-demented controls, and their ATP-evoked responses were smaller (McLarnon et al., 2005). That research used microglia extracted from postmortem samples, cultured and loaded with a Ca^{2+} dye, but provided a first approximation to Ca^{2+} dyshomeostasis in human AD microglia and their results are consistent with the current study examining GECI-expressing microglia *in situ*.

It is interesting to assess how Ca^{2+} dyshomeostasis in AD compares to other scenarios. Indeed, various stimuli inducing microglial activation might converge by regulating Ca^{2+} levels as a core signalling element. For instance, ageing also leads to a progressive increase in the proportion of microglia showing spontaneous Ca^{2+} transients while reducing the size of UDP-evoked Ca^{2+} transients (Del Moral et al., 2019). Another example is inflammatory stimuli: LPS treatment of cultured microglia results in elevated basal Ca^{2+} but reduced agonist-induced Ca^{2+} signals (Hoffmann et al., 2003). Similarly, peripheral LPS administration to mice increased the percentage of cortical microglia that display spontaneous transients (Riester et al., 2020). Given that THIK-1 channels are required for LPS-mediated activation of microglial cytokine release (Madry et al., 2018) and for their Ca^{2+} responses (see Chapter 6), THIK-1 activation may contribute to LPS-evoked $[Ca^{2+}]_i$ changes. Therefore, it would be interesting to see whether Ca^{2+} activity in LPS-treated mice would be compromised when THIK-1 channels are blocked. Because Aβ and LPS both activate microglia and lead to the same pattern of alterations in Ca^{2+} activity (increased basal fluctuations but smaller evoked changes), it is conceivable that THIK-1 also contributes to Aβ-evoked changes in Ca^{2+} activity, which could be tested by blocking this channel in GCaMP-expressing *App*$^{NL\text{-}G\text{-}F}$ microglia.

Ca^{2+} signalling (and specifically, IP_3-mediated Ca^{2+} release from stores; Lee et al., 2012) contributes to activation of the NLRP3 inflammasome (Murakami et al., 2012). Thus, the frequent Ca^{2+} transients observed in microglia near plaques might mediate activation of inflammatory signalling by Aβ. In AD, both Aβ oligomers and fibrils (Lučiūnaitė et al., 2019) and tau aggregates (Stancu et al., 2019) activate NLRP3. In turn, NLRP3 activation feeds back to drive both Aβ- (Heneka et al., 2013) and tau-related pathology (Ising et al., 2019),

suggesting a harmful contribution of inflammasome activation to AD. Indeed, the oral NLRP3 inhibitor dapansutrile lowered microglial activation and Aβ plaque coverage in the cortex of adult APP/PSEN1 transgenic mice, where synaptic plasticity and cognitive deficits recovered to wildtype levels (Lonnemann et al., 2020). Therefore, THIK-1 activity could be deleterious in AD both through its contribution to synapse removal (as suggested by my Golgi-Cox staining of adult *App*$^{NL-G-F}$ mice: see Chapter 5) and by triggering inflammasome activation, both directly through K^+ flux (Madry et al., 2018) and possibly via regulating Ca^{2+} transients (which were abolished by two-pore domain channel blockers; see Chapter 6).

7.10 Microglial interaction with other cells

This work shows that microglia share certain functions with other cells, including ROS generation and phagocytosis. For instance, Aβ was internalised by both microglia and astrocytes in brain slices (see Chapter 5), cortex and retina (Prakash et al., 2021), as assessed with the Aβ^{pH} probe. Even pericytes can engulf Aβ in AD mouse and human tissue (Ma et al., 2018), so the Aβ^{pH} that was not located inside microglia nor astrocytes could be in pericytes.

Similarly, microglia are not the sole mediators of synapse removal, as astrocytes eliminate synaptic material in development (Chung et al., 2013) and adulthood (Lee et al., 2021a). Although astrocytes are much less dynamic than microglia, their processes are tightly associated with synapses (Ventura and Harris, 1999). Both cell types can sense neuronal activity, regulate synapse formation and pruning during development, and become more phagocytic in pathological states (Vainchtein and Molofsky, 2020). However, the signalling mediating phagocytosis varies across cell types. For instance, astrocytes can activate phagocytosis via Megf10 (Iram et al., 2016), Abca1 (Morizawa et al., 2017) or the LRP4 receptor (Zhang et al., 2020), the expression of which is negligible in microglia (Zhang et al., 2014).

Not only do microglia and astrocytes both phagocytose targets, but their crosstalk can also affect each other's performance. Factors present in microglia-conditioned media instruct astrocytic elimination of synapses (Jay et al., 2019), and astrocytes can contribute to microglial removal of synapses via factors like IL-33 (Vainchtein et al., 2018) and C3 (Lian et al., 2016). On the other hand, there is robust evidence that astrocytes can compensate for absence or impairment of microglia (Damisah et al., 2020; Jay et al., 2019; Konishi et al., 2020) and microglia may also compensate for impaired astrocytic phagocytosis (Chung et al., 2013). Of note, however, astrogliosis was not affected after 2 months of microglial depletion in *App*$^{NL-G-F}$ mice (Clayton 2020), suggesting that compensation mechanisms might be disrupted in AD. Taken together, these data encourage analysing whether astrocytic phagocytosis of synapses is affected by (and possibly, partly compensates for) the decline in microglial removal of synapses in the absence of THIK-1 in the healthy brain and in AD.

Additionally, blocking THIK-1 might have direct effects on oligodendrocytes, which also express this channel (Zhang et al., 2014). For example, blockers of THIK-1 affect oligodendrocyte maturation and myelination in neonates (Wu et al., 2020) and remyelination upon injury (Ronzano et al., 2020). Although the work on THIK-1 presented here has focused on microglial behaviours, indirect effects via global THIK-1 KO in oligodendrocytes cannot be excluded. In future work, effects of THIK-1 specifically in oligodendrocytes and microglia could be dissected using cell type-specific Cre-inducible THIK-1 KO lines, which are now available.

7.11 Conclusion

In this thesis I have investigated microglial features in health and disease, namely process ramification and surveillance, phagocytosis, production of ROS and Ca^{2+} signalling. In healthy animals, I identified membrane K^+ flux as a factor regulating microglial phagocytosis and showed that THIK-1 channels control microglial phagocytosis *in situ*. In addition to using fluorophore-labelled resin microbeads for initial screenings, I also examined

phagocytosis of physiologically meaningful substrates such as synapses and Aβ. THIK-1 promotes microglial uptake of presynaptic material in the developing hippocampus, and thus affects the number of functional glutamatergic synapses. Potentially importantly for clinical translation, block of THIK-1 channels in human microglia recapitulated its effects in rodents, reducing microglial ramification and increasing levels of a presynaptic marker. The role of THIK-1 in phagocytosis may be partly due to its function in regulating microglial ramification and surveillance, but blockade of THIK-1 channels also reduced Ca^{2+} transients, suggesting a potential mechanism linking these channels to phagocytosis since Ca^{2+} was found to be required for phagocytosis in microglia *in situ*.

This project also assessed microglial functions in AD-relevant models. Microglia phagocytosed Aβ aggregates and produced ROS in response to Aβ. In microglia from older animals, deletion of the AD-linked receptor TREM2 increased process motility. In Aβ-depositing mice, microglia near Aβ plaques exhibited proximity-dependent deramification and increased lysosomal burden. THIK-1 did not alter plaque levels but its deletion slightly increased hippocampal spine density. Ca^{2+} dysregulation was also observed in microglia near plaques, whereby their basal Ca^{2+} activity was increased but they were less able to respond to laser lesions. Together, my results suggest that targeting channels and receptors (such as THIK-1 and TREM2) modulating microglial responses that are affected by ageing and neurodegeneration may alter network function in the brain and provide therapeutic benefits.

Bibliography

Afroz, S., Parato, J., Shen, H., and Smith, S.S. (2016). Synaptic pruning in the female hippocampus is triggered at puberty by extrasynaptic $GABA_A$ receptors on dendritic spines. eLife *5*, 1–23.

Aikawa, T., Ren, Y., Yamazaki, Y., Tachibana, M., Johnson, M.R., Anderson, C.T., Martens, Y.A., Holm, M.L., Asmann, Y.W., Saito, T., et al. (2019). ABCA7 haplodeficiency disturbs microglial immune responses in the mouse brain. PNAS *116*, 23790–23796.

Akiyoshi, R., Wake, H., Kato, D., Horiuchi, H., Ono, R., Ikegami, A., Haruwaka, K., Omori, T., Tachibana, Y., Moorhouse, A.J., et al. (2018). Microglia enhance synapse activity to promote local network synchronization. eNeuro *5*, 1–13.

Albert, B.M.L., Pearce, S.F.A., Francisco, L.M., Sauter, B., Roy, P., Silverstein, R.L., and Bhardwaj, N. (1998). Immature dendritic cells phagocytose apoptotic cells via alpha-v-beta-5 and CD36, and cross-present antigens to cytotoxic T lymphocytes. J. Exp. Med. *188,* 1359–1368.

Albertini, G., Etienne, F., and Roumier, A. (2020). Regulation of microglia by neuromodulators: Modulations in major and minor modes. Neurosci. Lett. *733*, 135000.

Allen, N.J., and Lyons, D.A. (2018). Glia as architects of central nervous system formation and function. Science *362*, 181–185.

Alsema, A.M., Jiang, Q., Kracht, L., Gerrits, E., Dubbelaar, M.L., Miedema, A., Brouwer, N., Hol, E.M., Middeldorp, J., van Dijk, R., et al. (2020). Profiling microglia from Alzheimer's Disease donors and non-demented elderly in acute human postmortem cortical tissue. Front. Mol. Neurosci. *13*, 134.

Alzheimer's Association (2020). 2020 Alzheimer's Disease facts and figures. Alzheimer's Dement. *16*, 391–460.

Alzheimer, A. (1910). Beiträge zur Kenntnis der Pathologischen Neuroglia und ihrer Beziehungen zu den Abbauvorgängen im Nervengewebe. In Histologische Und

Histopathologische Arbeiten Über Die Grosshirnrinde Mit Besonderer Berücksichtigung Der Pathologischen Anatomie Der Geisteskrankheiten. 401–562.

El Amki, M., Glück, C., Binder, N., Middleham, W., Wyss, M.T., Weiss, T., Meister, H., Luft, A., Weller, M., Weber, B., et al. (2020). Neutrophils obstructing brain capillaries are a major cause of no-reflow in ischemic stroke. Cell Rep. *33*, 108260.

Anderson, R.M., Hadjichrysanthou, C., Evans, S., and Wong, M.M. (2017). Why do so many clinical trials of therapies for Alzheimer's disease fail? Lancet *390*, 2327–2329.

Anderson, S.R., Roberts, J.M., Zhang, J., Steele, M.R., Romero, C.O., Bosco, A., and Vetter, M.L. (2019). Developmental apoptosis promotes a disease-related gene signature and independence from CSF1R signaling in retinal microglia. Cell Rep. *27*, 2002–2013.

Aoyagi, A., Condello, C., Stöhr, J., Yue, W., Rivera, B.M., Lee, J.C., Woerman, A.L., Halliday, G., van Duinen, S., Ingelsson, M., et al. (2019). Aβ and tau prion-like activities decline with longevity in the Alzheimer's disease human brain. Sci. Transl. Med. *11*, eaat8462.

Askew, K., Li, K., Olmos-Alonso, A., Garcia-Moreno, F., Liang, Y., Richardson, P., Tipton, T., Chapman, M.A., Riecken, K., Beccari, S., et al. (2017). Coupled proliferation and apoptosis maintain the rapid turnover of microglia in the adult brain. Cell Rep. *18*, 391–405.

Attardo, A., Fitzgerald, J.E., and Schnitzer, M.J. (2015). Impermanence of dendritic spines in live adult CA1 hippocampus. Nature *523*, 592–596.

Avignone, E., Lepleux, M., Angibaud, J., and Nägerl, U.V. (2015). Altered morphological dynamics of activated microglia after induction of status epilepticus. J. Neuroinflammation *12*, 1–13.

Ayata, P., Badimon, A., Strasburger, H.J., Duff, M.K., Montgomery, S.E., Loh, Y.H.E., Ebert, A., Pimenova, A.A., Ramirez, B.R., Chan, A.T., et al. (2018). Epigenetic regulation of brain region-specific microglia clearance activity. Nat. Neurosci. *21*, 1049–1060.

Bacskai, B.J., Kajdasz, S.T., Christie, R.H., Carter, C., Games, D., Seubert, P., Schenk, D., and Hyman, B.T. (2001). Imaging of amyloid-β deposits in brains of living mice

permits direct observation of clearance of plaques with immunotherapy. Nat. Med. *7*, 369–372.

Badimon, A., Strasburger, H.J., Ayata, P., Chen, X., Nair, A., Ikegami, A., Hwang, P., Chan, A.T., Graves, S.M., Uweru, J.O., et al. (2020). Negative feedback control of neuronal activity by microglia. Nature *586*, 417–423.

Baird, G.S., Zacharias, D.A., and Tsien, R.Y. (1999). Circular permutation and receptor insertion within green fluorescent proteins. PNAS *96*, 11241–11246.

Bánsághi, S., Golenár, T., Madesh, M., Csordás, G., Ramachandrarao, S., Sharma, K., Yule, D.I., Joseph, S.K., and Hajnóczky, G. (2014). Isoform- and species-specific control of IP_3 receptors by reactive oxygen species. J. Biol. Chem. *289*, 8170–8181.

Bartels, T., De Schepper, S., and Hong, S. (2020). Microglia modulate neurodegeneration in Alzheimer's and Parkinson's diseases. Science *370*, 66–69.

Basak, J.M., Verghese, P.B., Yoon, H., Kim, J., and Holtzman, D.M. (2012). Low-density lipoprotein receptor represents an apolipoprotein E-independent pathway of Aβ uptake and degradation by astrocytes. J. Biol. Chem. *287*, 13959–13971.

Basilico, B., Pagani, F., Grimaldi, A., Cortese, B., Di Angelantonio, S., Weinhard, L., Gross, C., Limatola, C., Maggi, L., and Ragozzino, D. (2019). Microglia shape presynaptic properties at developing glutamatergic synapses. Glia *67*, 53–67.

Bellenguez, C., Küçükali, F., Jansen, I., Andrade, V., and Moreno-Grau, S. (2020). New insights on the genetic etiology of Alzheimer's and related dementia. MedRxiv. DOI: 10.1101/2020.10.01.20200659.

Bennett, F.C., Bennett, M.L., Yaqoob, F., Mulinyawe, S.B., Grant, G.A., Hayden Gephart, M., Plowey, E.D., and Barres, B.A. (2018). A combination of ontogeny and CNS environment establishes microglial identity. Neuron *98*, 1170–1183.

Benninger, R.K.P., and Piston, D.W. (2013). Two-photon excitation microscopy for the study of living cells and tissues. Curr. Protoc. Cell Biol. *Chapter 4*, Unit 4.11.1-24.

Bernier, L.P., Bohlen, C.J., York, E.M., Choi, H.B., Kamyabi, A., Dissing-Olesen, L., Hefendehl, J.K., Collins, H.Y., Stevens, B., Barres, B.A., et al. (2019). Nanoscale

surveillance of the brain by microglia via cAMP-regulated filopodia. Cell Rep. *27*, 2895-2908.

Bischofberger, J., Engel, D., Li, L., Geiger, J.R., and Jonas, P. (2006). Patch-clamp recording from mossy fiber terminals in hippocampal slices. Nat. Protoc. *1*, 2075–2081.

Blinzinger, K., and Kreutzberg, G. (1968). Displacement of synaptic terminals from regenerating motoneurons by microglial cells. Zeitschrift Für Zellforsch. Und Mikroskopische Anat. *85*, 145–157.

Blume, Z.I., Lambert, J.M., Lovel, A.G., and Mitchell, D.M. (2020). Microglia in the developing retina couple phagocytosis with the progression of apoptosis via $P2RY_{12}$ signaling. Dev. Dyn. *249*, 723–740.

Bohlen, C.J., Bennett, F.C., Tucker, A.F., Collins, H.Y., Mulinyawe, S.B., and Barres, B.A. (2017). Diverse requirements for microglial survival, specification, and function revealed by defined-medium cultures. Neuron *94*, 759-773.

Bohrmann, B., Baumann, K., Benz, J., Gerber, F., Huber, W., Knoflach, F., Messer, J., Oroszlan, K., Rauchenberger, R., Richter, W.F., et al. (2012). Gantenerumab: a novel human anti-Aβ antibody demonstrates sustained cerebral amyloid-β binding and elicits cell-mediated removal of human amyloid-β. J. Alzheimer's Dis. *28*, 49–69.

Brawek, B., and Garaschuk, O. (2013). Microglial calcium signaling in the adult, aged and diseased brain. Cell Calcium *53*, 159–169.

Brawek, B., and Garaschuk, O. (2014). Network-wide dysregulation of calcium homeostasis in Alzheimer's disease. Cell Tissue Res. *357*, 427–438.

Brawek, B., Schwendele, B., Riester, K., Kohsaka, S., Lerdkrai, C., Liang, Y., and Garaschuk, O. (2014). Impairment of *in vivo* calcium signaling in amyloid plaque-associated microglia. Acta Neuropathol. *127*, 495–505.

Brown, G.C., and Neher, J.J. (2014). Microglial phagocytosis of live neurons. Nat. Rev. Neurosci. *15*, 209–216.

Busche, M.A., and Hyman, B.T. (2020). Synergy between amyloid-β and tau in Alzheimer's disease. Nat. Neurosci. *23*, 1183–1193.

Busche, M.A., Chen, X., Henning, H.A., Reichwald, J., Staufenbiel, M., Sakmann, B., and Konnerth, A. (2012). Critical role of soluble amyloid-β for early hippocampal hyperactivity in a mouse model of Alzheimer's disease. PNAS *109*, 8740–8745.

Butler, C.A., Popescu, A., Kitchener, E., Allendorf, D.H., Puigdellivol, M., and Brown, G.C. (2021). Microglial phagocytosis of neurons in neurodegeneration, and its regulation. J. Neurochem 1– 19.

Butovsky, O., Jedrychowski, M.P., Moore, C.S., Cialic, R., Lanser, A.J., Gabriely, G., Koeglsperger, T., Dake, B., Wu, P.M., et al. (2014). Identification of a unique TGF-β-dependent molecular and functional signature in microglia. Nat. Neurosci. *17*, 131–143.

Cangalaya, C., Stoyanov, S., Fischer, K.D., and Dityatev, A. (2020). Light-induced engagement of microglia to focally remodel synapses in the adult brain. eLife *9*, 1–16.

Cantaut-Belarif, Y., Antri, M., Pizzarelli, R., Colasse, S., Vaccari, I., Soares, S., Renner, M., Dallel, R., Triller, A., and Bessis, A. (2017). Microglia control the glycinergic but not the GABAergic synapses via prostaglandin E2 in the spinal cord. J. Cell Biol. *216*, 2979–2989.

Canton, J. (2014). Phagosome maturation in polarized macrophages. J. Leukoc. Biol. *96*, 729–738.

Cantuti-Castelvetri, L., Fitzner, D., Bosch-Queralt, M., Weil, M., Su, M., Sen, P., Ruhwedel, T., Mitkovski, M., Trendelenburg, G., Lütjohann, D., et al. (2018). Defective cholesterol clearance limits remyelination in the aged central nervous system. Science *359*, 684–688.

Capetillo-Zarate, E., Gracia, L., Yu, F., Banfelder, J.R., Lin, M.T., Tampellini, D., and Gouras, G.K. (2011). High-resolution 3D reconstruction reveals intra-synaptic amyloid fibrils. Am. J. Pathol. *179*, 2551–2558.

Carlson, G.A., Borchelt, D.R., Dake, A., Turner, S., Danielson, V., Coffin, J.D., Eckman, C., Meiners, J., Nilsen, S.P., Younkin, S.G., et al. (1997). Genetic modification of the phenotypes produced by amyloid precursor protein overexpression in transgenic mice. Hum. Mol. Genet. *6*, 1951–1959.

Chang, P.K.Y., Khatchadourian, A., McKinney, A.A., and Maysinger, D. (2015). Docosahexaenoic acid (DHA): A modulator of microglia activity and dendritic spine morphology. J. Neuroinflammation *12*, 1–15.

Changeux, J.-P., and Danchin, A. (1976). Selective stabilisation of developing synapses as a mechanism for the specification of neuronal networks. Nature *264*, 705–712.

Chatelain, F.C., Bichet, D., Feliciangeli, S., Larroque, M.M., Braud, V.M., Douguet, D., and Lesage, F. (2013). Silencing of the tandem pore domain halothane-inhibited K^+ Channel 2 (THIK2) relies on combined intracellular retention and low intrinsic activity at the plasma membrane. J. Biol. Chem. *288*, 35081–35092.

Chaudhury, S., Brookes, K.J., Patel, T., Fallows, A., Guetta-Baranes, T., Turton, J.C., Guerreiro, R., Bras, J., Hardy, J., Francis, P.T., et al. (2019). Alzheimer's disease polygenic risk score as a predictor of conversion from mild-cognitive impairment. Transl. Psychiatry *9*.

Chavez, R.A., Gray, A.T., Zhao, B.B., Kindler, C.H., Mazurek, M.J., Mehta, Y., Forsayeth, J.R., and Yost, C.S. (1999). TWIK-2, a new weak inward rectifying member of the tandem pore domain potassium channel family. J. Biol. Chem. *274*, 7887–7892.

Chen, W.T., Lu, A., Craessaerts, K., Pavie, B., Sala Frigerio, C., Corthout, N., Qian, X., Laláková, J., Kühnemund, M., Voytyuk, I., et al. (2020). Spatial transcriptomics and *in situ* sequencing to study Alzheimer's Disease. Cell *182*, 976-991.

Chen, Z., Jalabi, W., Hu, W., Park, H.J., Gale, J.T., Kidd, G.J., Bernatowicz, R., Gossman, Z.C., Chen, J.T., Dutta, R., et al. (2014). Microglial displacement of inhibitory synapses provides neuroprotection in the adult brain. Nat. Commun. *33*, 108346.

Chidlow, G., Wood, J.P.M., Manavis, J., Finnie, J., and Casson, R.J. (2017). Investigations into Retinal Pathology in the Early Stages of a Mouse Model of Alzheimer's Disease. J. Alzheimer's Dis. *56*, 655–675.

Choi, H.B., Ryu, J.K., Kim, S.U., and McLarnon, J.G. (2007). Modulation of the purinergic $P2X_7$ receptor attenuates lipopolysaccharide-mediated microglial activation and neuronal damage in inflamed brain. J. Neurosci. *27*, 4957–4968.

Choudhury, M.E., Miyanishi, K., Takeda, H., Islam, A., Matsuoka, N., Kubo, M., Matsumoto, S., Kunieda, T., Nomoto, M., Yano, H., et al. (2020). Phagocytic elimination of synapses by microglia during sleep. Glia *68*, 44–59.

Chung, W.-S., Clarke, L.E., Wang, G.X., Stafford, B.K., Sher, A., Chakraborty, C., Joung, J., Foo, L.C., Thompson, A., Chen, C., et al. (2013). Astrocytes mediate synapse elimination through MEGF10 and MERTK pathways. Nature *504*, 394–400.

Ciudad, S., Puig, E., Botzanowski, T., Meigooni, M., Arango, A.S., Do, J., Mayzel, M., Bayoumi, M., Chaignepain, S., Maglia, G., et al. (2020). $A\beta_{1-42}$ tetramer and octamer structures reveal edge conductivity pores as a mechanism for membrane damage. Nat. Commun. *11*, 3014.

Clarke, D., Crombag, H.S., and Hall, C.N. (2021). An open-source pipeline for analyzing changes in microglial morphology. BioRxiv. DOI: 10.1101/2021.01.12.426422.

Clayton, K., Delpech, J.C., Herron, S., Iwahara, N., Ericsson, M., Saito, T., Saido, T.C., Ikezu, S., and Ikezu, T. (2021). Plaque associated microglia hyper-secrete extracellular vesicles and accelerate tau propagation in a humanized APP mouse model. Mol. Neurodegener. *16*, 1–16.

Combs, C.K., Johnson, D.E., Cannady, S.B., Lehman, T.M., and Landreth, G.E. (1999). Identification of microglial signal transduction pathways mediating a neurotoxic response to amyloidogenic fragments of β-amyloid and prion proteins. J. Neurosci. *19*, 928–939.

Condello, C., Yuan, P., Schain, A., and Grutzendler, J. (2015). Microglia constitute a barrier that prevents neurotoxic protofibrillar $A\beta_{42}$ hotspots around plaques. Nat. Commun. *6*, 6176.

Cruz, C.M., Rinna, A., Forman, H.J., Ventura, A.L.M., Persechini, P.M., and Ojcius, D.M. (2007). ATP activates a reactive oxygen species-dependent oxidative stress response and secretion of proinflammatory cytokines in macrophages. J. Biol. Chem. *282*, 2871–2879.

Császár, E., Lénárt, N., Cserép, C., Környei, Z., Fekete, R., Pósfai, B., Balázsfi, D., Hangya, B., Schwarcz, A.D., Szöllősi, D., et al. (2021). Microglia control cerebral blood flow

and neurovascular coupling via $P2Y_{12}R$-mediated actions. BioRxiv. DOI: 10.1101/2021.02.04.429741.

Cserép, C., Pósfai, B., and Dénes, Á. (2020a). Shaping neuronal fate: functional heterogeneity of direct microglia-neuron interactions. Neuron *109*, 222–240.

Cserép, C., Pósfai, B., Lénárt, N., Fekete, R., László, Z.I., Lele, Z., Orsolits, B., Molnár, G., Heindl, S., Schwarcz, A.D., et al. (2020b). Microglia monitor and protect neuronal function through specialized somatic purinergic junctions. Science *367*, 528–537.

Cummings, D.M., Liu, W., Portelius, E., Bayram, S., Yasvoina, M., Ho, S.H., Smits, H., Ali, S.S., Steinberg, R., Pegasiou, C.M., et al. (2015). First effects of rising amyloid-β in transgenic mouse brain: synaptic transmission and gene expression. Brain *138*, 1992–2004.

Cunningham, C.L., Martínez-Cerdeño, V., and Noctor, S.C. (2013). Microglia regulate the number of neural precursor cells in the developing cerebral cortex. J. Neurosci. *33*, 4216–4233.

Damani, M.R., Zhao, L., Fontainhas, A.M., Amaral, J., Fariss, R.N., and Wong, W.T. (2011). Age-related alterations in the dynamic behavior of microglia. Aging Cell *10*, 263–276.

Damisah, E.C., Hill, R.A., Rai, A., Chen, F., Rothlin, C. V., Ghosh, S., and Grutzendler, J. (2020). Astrocytes and microglia play orchestrated roles and respect phagocytic territories during neuronal corpse removal *in vivo*. Sci. Adv. *6*, eaba3239.

Davalos, D., Grutzendler, J., Yang, G., Kim, J. V, Zuo, Y., Jung, S., Littman, D.R., Dustin, M.L., and Gan, W.-B. (2005). ATP mediates rapid microglial response to local brain injury *in vivo*. Nat. Neurosci. *8*, 752–758.

Davis, B.M., Salinas-Navarro, M., Cordeiro, M.F., Moons, L., and Groef, L. De (2017). Characterizing microglia activation: a spatial statistics approach to maximize information extraction. Sci. Rep. *7*, 1–12.

De Biase, L.M., Schuebel, K.E., Fusfeld, Z.H., Jair, K., Hawes, I.A., Cimbro, R., Zhang, H.Y., Liu, Q.R., Shen, H., Xi, Z.X., et al. (2017). Local cues establish and maintain region-specific phenotypes of basal ganglia microglia. Neuron *95*, 341–356.

De Simoni, A., Allen, N.J., and Attwell, D. (2008). Charge compensation for NADPH oxidase activity in microglia in rat brain slices does not involve a proton current. Eur. J. Neurosci. *28*, 1146–1156.

De Strooper, B., and Karran, E. (2016). The cellular phase of Alzheimer's Disease. Cell *164*, 603–615.

DeCoursey, T.E., Morgan, D., and Cherny, V. V. (2003). The voltage dependence of NADPH oxidase reveals why phagocytes need proton channels. Nature *422*, 531–534.

Deczkowska, A., Weiner, A., and Amit, I. (2020). The Physiology, Pathology, and Potential Therapeutic Applications of the TREM2 Signaling Pathway. Cell *181*, 1207–1217.

Dejanovic, B., Huntley, M.A., De Mazière, A., Meilandt, W.J., Wu, T., Srinivasan, K., Jiang, Z., Gandham, V., et al. (2018). Changes in the synaptic proteome in tauopathy and rescue of tau-induced synapse loss by C1q antibodies. Neuron *100*, 1322–1336.

DeKosky, S.T., Scheff, S.W., and Styren, S.D. (1996). Structural correlates of cognition in dementia: Quantification and assessment of synapse change. Neurodegeneration *5*, 417–421.

Del Río-Hortega, P. (1919). El "Tercer Elemento" de los Centros Nerviosos. I. La microglía en estado normal. Boletín Soc. Española Biol. VIII *VIII*, 67–82 (in Spanish).

Della Bianca, V., Dusi, S., Bianchini, E., Dal Prà, I., and Rossi, F. (1999). β-amyloid activates the $O_2{\cdot}^-$ forming NADPH oxidase in microglia, monocytes, and neutrophils. A possible inflammatory mechanism of neuronal damage in Alzheimer's disease. J. Biol. Chem. *274*, 15493–15499.

Diaz-Aparicio, I., Paris, I., Sierra-Torre, V., Plaza-Zabala, A., Rodríguez-Iglesias, N., Márquez-Ropero, M., Beccari, S., Abiega, O., Alberdi, E., Matute, C., et al. (2020). Microglia actively remodels adult hippocampal neurogenesis through the phagocytosis secretome. J. Neurosci. *40*, 1453–1482.

Duan, L., Zhang, X. Di, Miao, W.Y., Sun, Y.J., Xiong, G., Wu, Q., Li, G., Yang, P., Yu, H., Li, H., et al. (2018). PDGFRβ cells rapidly relay inflammatory signal from the circulatory system to neurons via chemokine CCL2. Neuron *100*, 183–200.

Edwards, F.A. (2019). A unifying hypothesis for Alzheimer's Disease: from plaques to neurodegeneration. Trends Neurosci. *42*, 310–322.

Eguchi, K., Velicky, P., Hollergschwandtner, E., Itakura, M., Fukazawa, Y., Danzl, J.G., and Shigemoto, R. (2020). Advantages of acute brain slices prepared at physiological temperature in the characterization of synaptic functions. Front. Cell. Neurosci. *14*, 35–37.

Eichhoff, G., Busche, M.A., and Garaschuk, O. (2008). *In vivo* calcium imaging of the aging and diseased brain. Eur. J. Nucl. Med. Mol. Imaging *35*, 99–106.

Eichhoff, G., Brawek, B., and Garaschuk, O. (2011). Microglial calcium signal acts as a rapid sensor of single neuron damage *in vivo*. Biochim. Biophys. Acta *1813*, 1014–1024.

Elston, G.N., Oga, T., and Fujita, I. (2009). Spinogenesis and pruning scales across functional hierarchies. J. Neurosci. *29*, 3271–3275.

Escott-Price, V., Sims, R., Bannister, C., Harold, D., Vronskaya, M., Majounie, E., Badarinarayan, N., Morgan, K., Passmore, P., Holmes, C., et al. (2015). Common polygenic variation enhances risk prediction for Alzheimer's disease. Brain *138*, 3673–3684.

Esparza, T.J., Zhao, H., Cirrito, J.R., Cairns, N.J., Bateman, R.J., Holtzman, D.M., and Brody, D.L. (2013). Amyloid-beta oligomerization in Alzheimer dementia versus high-pathology controls. Ann. Neurol. *73*, 104–119.

Femling, J.K., Cherny, V. V., Morgan, D., Rada, B., Davis, A.P., Czirják, G., Enyedi, P., England, S.K., Moreland, J.G., Ligeti, E., et al. (2006). The antibacterial activity of human neutrophils and eosinophils requires proton channels but not BK channels. J. Gen. Physiol. *127*, 659–672.

Ferreras, S., Fernández, G., Danelon, V., Pisano, M. V., Masseroni, L., Chapleau, C.A., Krapacher, F.A., et al. (2017). Cdk5 is essential for amphetamine to increase dendritic spine density in hippocampal pyramidal neurons. Front. Cell. Neurosci. *11*, 1–14.

Fiala, J.C., Kirov, S.A., Feinberg, M.D., Petrak, L.J., George, P., Goddard, C.A., and Harris, K.M. (2003). Timing of neuronal and glial ultrastructure disruption during brain slice preparation and recovery *in vitro*. J. Comp. Neurol. *465*, 90–103.

Filipello, F., Morini, R., Corradini, I., Zerbi, V., Canzi, A., Michalski, B., Erreni, M., Markicevic, M., Starvaggi-Cucuzza, C., Otero, K., et al. (2018). The Microglial Innate Immune Receptor TREM2 Is Required for Synapse Elimination and Normal Brain Connectivity. Immunity *48*, 979–991.

Flagmeier, P., De, S., Michaels, T.C.T., Yang, X., Dear, A.J., Emanuelsson, C., Vendruscolo, M., Linse, S., Klenerman, D., Knowles, T.P.J., et al. (2020). Direct measurement of lipid membrane disruption connects kinetics and toxicity of $A\beta_{42}$ aggregation. Nat. Struct. Mol. Biol. *27*, 886–891.

Fourgeaud, L., Traves, P.G., Tufail, Y., Leal-Bailey, H., Lew, E.D., Burrola, P.G., Callaway, P., Zagorska, A., Rothlin, C. V., Nimmerjahn, A., et al. (2016). TAM receptors regulate multiple features of microglial physiology. Nature *532*, 240–244.

Franciosi, S., Ryu, J.K., Choi, H.B., Radov, L., Kim, S.U., and McLarnon, J.G. (2006). Broad-spectrum effects of 4-aminopyridine to modulate amyloid $\beta_{1\text{-}42}$-induced cell signaling and functional responses in human microglia. J. Neurosci. *26*, 11652–11664.

Fujikake, N., Shin, M., and Shimizu, S. (2018). Association between autophagy and neurodegenerative diseases. Front. Neurosci. *12*, 1–11.

Gage, G.J., Kipke, D.R., and Shain, W. (2012). Whole animal perfusion fixation for rodents. J. Vis. Exp. e3564.

Galatro, T.F., Holtman, I.R., Lerario, A.M., Vainchtein, I.D., Brouwer, N., Sola, P.R., Veras, M.M., Pereira, T.F., Leite, R.E.P., Möller, T., et al. (2017). Transcriptomic analysis of purified human cortical microglia reveals age-associated changes. Nat. Neurosci. *20*, 1162–1171.

Gee, J.M., Smith, N.A., Fernandez, F.R., Economo, M.N., Brunert, D., Rothermel, M., Morris, S.C., Talbot, A., Palumbos, S., Ichida, J.M., et al. (2014). Imaging activity in neurons and glia with a Polr2a-based and Cre-dependent GCaMP5G-IRES-tdTomato reporter mouse. Neuron *83*, 1058–1072.

Geirsdottir, L., David, E., Keren-Shaul, H., Weiner, A., Bohlen, S.C., Neuber, J., Balic, A., Giladi, A., Sheban, F., Dutertre, C.A., et al. (2019). Cross-species single-cell

analysis reveals divergence of the primate microglia program. Cell *179*, 1609–1622.

Gervais, F., Paquette, J., Morissette, C., Krzywkowski, P., Yu, M., Azzi, M., Lacombe, D., Kong, X., Aman, A., Laurin, J., et al. (2007). Targeting soluble Aβ peptide with Tramiprosate for the treatment of brain amyloidosis. Neurobiol. Aging *28*, 537–547.

Gierten, J., Ficker, E., Bloehs, R., Schlömer, K., Kathöfer, S., Scholz, E., Zitron, E., Kiesecker, C., Bauer, A., Becker, R., et al. (2008). Regulation of two-pore-domain (K_{2P}) potassium leak channels by the tyrosine kinase inhibitor genistein. Br. J. Pharmacol. *154*, 1680–1690.

Giovanna, C., Cecchi, C., Pensalfini, A., Bonini, S.A., Ferrari-Toninelli, G., Liguri, G., Memo, M., and Uberti, D. (2010). Generation of reactive oxygen species by β amyloid fibrils and oligomers involves different intra/extracellular pathways. Amino Acids *38*, 1101–1106.

Giulian, D., and Baker, T.J. (1986). Characterization of ameboid microglia isolated from developing mammalian brain. J. Neurosci. *6*, 2163–2178.

Görlach, A., Bertram, K., Hudecova, S., and Krizanova, O. (2015). Calcium and ROS: A mutual interplay. Redox Biol. *6*, 260–271.

Gosselin, D., Skola, D., Coufal, N.G., Holtman, I.R., Schlachetzki, J.C.M., Sajti, E., Jaeger, B.N., O'Connor, C., Fitzpatrick, C., Pasillas, M.P., et al. (2017). An environment-dependent transcriptional network specifies human microglia identity. Science *356,* 1–11.

Grathwohl, S.A., Kälin, R.E., Bolmont, T., Prokop, S., Winkelmann, G., Kaeser, S.A., Odenthal, J., Radde, R., Eldh, T., Gandy, S., et al. (2009). Formation and maintenance of Alzheimer's disease β-amyloid plaques in the absence of microglia. Nat. Neurosci. *12*, 1361–1363.

Gratuze, M., Leyns, C.E.G., Sauerbeck, A.D., St-Pierre, M.K., Xiong, M., Kim, N., Serrano, J.R., Tremblay, M.È., Kummer, T.T., Colonna, M., et al. (2020). Impact of $TREM2^{R47H}$ variant on tau pathology-induced gliosis and neurodegeneration. J. Clin. Invest. *130*, 4954–4968.

Griciuc, A., Patel, S., Federico, A.N., Choi, S.H., Innes, B.J., Oram, M.K., Cereghetti, G., McGinty, D., Anselmo, A., Sadreyev, R.I., et al. (2019). TREM2 acts downstream of

CD33 in modulating microglial pathology in Alzheimer's Disease. Neuron *103*, 820-835.

Gronski, M.A., Kinchen, J.M., Juncadella, I.J., Franc, N.C., and Ravichandran, K.S. (2009). An essential role for calcium flux in phagocytes for apoptotic cell engulfment and the anti-inflammatory response. Cell Death Differ. *16*, 1323–1331.

Groß, C.J., Mishra, R., Schneider, K.S., Médard, G., Wettmarshausen, J., Dittlein, D.C., Shi, H., Gorka, O., Koenig, P.A., Fromm, S., et al. (2016). K^+ efflux-independent NLRP3 inflammasome activation by small molecules targeting mitochondria. Immunity *45*, 761–773.

Grutzendler, J., Kasthuri, N., and Gan, W.B. (2002). Long-term dendritic spine stability in the adult cortex. Nature *420*, 812–816.

Guerreiro, R., Wojtas, A., Bras, J., Carrasquillo, M., Rogaeva, E., Majounie, E., Cruchaga, C., Kauwe, J.S.K., Younkin, S., Hazrati, L., et al. (2013). TREM2 variants in Alzheimer's Disease. N. Engl. J. Med. *368*, 117–127.

Guillot-Sestier, M.-V., Doty, K.R., Gate, D., Rodriguez, J., Leung, B.P., Rezai-Zadeh, K., Town, T., and Town, T. (2015). *Il10* deficiency rebalances innate immunity to mitigate Alzheimer-like pathology. Neuron *85*, 534–548.

Guneykaya, D., Ivanov, A., Hernandez, D.P., Haage, V., Wojtas, B., Meyer, N., Maricos, M., Jordan, P., Buonfiglioli, A., et al. (2018). Transcriptional and translational differences of microglia from male and female brains. Cell Rep. *24*, 2773-2783.

Gunner, G., Cheadle, L., Johnson, K.M., Ayata, P., Badimon, A., Mondo, E., Nagy, M.A., Liu, L., Bemiller, S.M., Kim, K.W., et al. (2019). Sensory lesioning induces microglial synapse elimination via ADAM10 and fractalkine signaling. Nat. Neurosci. *22*, 1075–1088.

Gustafsson, N., Culley, S., Ashdown, G., Owen, D.M., Pereira, P.M., and Henriques, R. (2016). Fast live-cell conventional fluorophore nanoscopy with ImageJ through super-resolution radial fluctuations. Nat. Commun. *7*, 12471.

Gutteridge, J.M.C. (1985). Superoxide dismutase inhibits the superoxide-driven Fenton reaction at two different levels. Implications for a wider protective role. FEBS Lett. *185*, 19–23.

Gyoneva, S., and Traynelis, S.F. (2013). Norepinephrine modulates the motility of resting and activated microglia via different adrenergic receptors. J. Biol. Chem. *288*, 15291–15302.

Györffy, B.A., Kun, J., Török, G., Bulyáki, É., Borhegyi, Z., Gulyássy, P., Kis, V., Szocsics, P., Micsonai, A., Matkó, J., et al. (2018). Local apoptotic-like mechanisms underlie complement-mediated synaptic pruning. PNAS *115*, 6303–6308.

Haass, C., Kaether, C., Thinakaran, G., and Sisodia, S. (2012). Trafficking and proteolytic processing of APP. Cold Spring Harb. Perspect. Med. *2*, 1–25.

El Hajj, H., Savage, J.C., Bisht, K., Parent, M., Vallières, L., Rivest, S., and Tremblay, M.È. (2019). Ultrastructural evidence of microglial heterogeneity in Alzheimer's disease amyloid pathology. J. Neuroinflammation *16*, 1–19.

Halle, A., Hornung, V., Petzold, G.C., Stewart, C.R., Monks, B.G., Reinheckel, T., Fitzgerald, K.A., Latz, E., Moore, K.J., and Golenbock, D.T. (2008). The NALP3 inflammasome is involved in the innate immune response to amyloid-β. Nat. Immunol. *9*, 857–865.

Hammond, T.R., Dufort, C., Dissing-Olesen, L., Giera, S., Young, A., Wysoker, A., Walker, A.J., Gergits, F., Segel, M., Nemesh, J., et al. (2019). Single-cell RNA sequencing of microglia throughout the mouse lifespan and in the injured brain reveals complex cell-state changes. Immunity *50*, 253–271.

Haney, M.S., Bohlen, C.J., Morgens, D.W., Ousey, J.A., Barkal, A.A., Tsui, C.K., Ego, B.K., Levin, R., Kamber, R.A., Collins, H., et al. (2018). Identification of phagocytosis regulators using magnetic genome-wide CRISPR screens. Nat. Genet. *50*, 1716–1727.

Hanseeuw, B.J., Betensky, R.A., Jacobs, H.I.L., Schultz, A.P., Sepulcre, J., Becker, J.A., Cosio, D.M.O., Farrell, M., Quiroz, Y.T., Mormino, E.C., et al. (2019). Association of amyloid and tau with cognition in preclinical Alzheimer Disease: A longitudinal study. JAMA Neurol. *76*, 915–924.

Harris, S.S., Wolf, F., De Strooper, B., and Busche, M.A. (2020). Tipping the scales: peptide-dependent dysregulation of neural circuit dynamics in AD. Neuron *107*, 417–435.

Haruwaka, K., Ikegami, A., Tachibana, Y., Ohno, N., Konishi, H., Hashimoto, A., Matsumoto, M., Kato, D., Ono, R., Kiyama, H., et al. (2019). Dual microglia effects on blood brain barrier permeability induced by systemic inflammation. Nat. Commun. *10*, 5816.

Haynes, S.E., Hollopeter, G., Yang, G., Kurpius, D., Dailey, M.E., Gan, W.-B.B., and Julius, D. (2006). The $P2Y_{12}$ receptor regulates microglial activation by extracellular nucleotides. Nat. Neurosci. *9*, 1512–1519.

He, Y., Taylor, N., Fourgeaud, L., and Bhattacharya, A. (2017). The role of microglial $P2X_7$: Modulation of cell death and cytokine release. J. Neuroinflammation *14*, 1–13.

Hefendehl, J.K., Neher, J.J., Sühs, R.B., Kohsaka, S., Skodras, A., and Jucker, M. (2014). Homeostatic and injury-induced microglia behavior in the aging brain. Aging Cell *13*, 60–69.

Heindl, S., Gesierich, B., Benakis, C., Llovera, G., Duering, M., and Liesz, A. (2018). Automated morphological analysis of microglia after stroke. Front. Cell. Neurosci. *12*, 1–11.

Heneka, M.T., Ramanathan, M., Jacobs, A.H., Dumitrescu-Ozimek, L., Bilkei-Gorzo, A., Debeir, T., Sastre, M., Galldiks, N., Zimmer, A., Hoehn, M., et al. (2006). Locus ceruleus degeneration promotes Alzheimer pathogenesis in amyloid precursor protein 23 transgenic mice. J. Neurosci. *26*, 1343–1354.

Heneka, M.T., Nadrigny, F., Regen, T., Martinez-Hernandez, A., Dumitrescu-Ozimek, L., Terwel, D., Jardanhazi-Kurutz, D., Walter, J., Kirchhoff, F., Hanisch, U.K., et al. (2010). Locus ceruleus controls Alzheimer's disease pathology by modulating microglial functions through norepinephrine. PNAS *107*, 6058–6063.

Heneka, M.T., Kummer, M.P., Stutz, A., Delekate, A., Schwartz, S., Vieira-Saecker, A., Griep, A., Axt, D., Remus, A., Tzeng, T.C., et al. (2013). NLRP3 is activated in Alzheimer's disease and contributes to pathology in APP/PS1 mice. Nature *493*, 674–678.

Heo, D.K., Lim, H.M., Nam, J.H., Lee, M.G., and Kim, J.Y. (2015). Regulation of phagocytosis and cytokine secretion by store-operated calcium entry in primary isolated murine microglia. Cell. Signal. *27*, 177–186.

Hernández, F., Gómez de Barreda, E., Fuster-Matanzo, A., Lucas, J.J., and Avila, J.

(2010). GSK3: A possible link between beta amyloid peptide and tau protein. Exp. Neurol. *223*, 322–325.

Hickman, S.E., Kingery, N.D., Ohsumi, T.K., Borowsky, M.L., Wang, L.C., Means, T.K., and El Khoury, J. (2013). The microglial sensome revealed by direct RNA sequencing. Nat. Neurosci. *16*, 1896–1905.

Hines, D.J., Hines, R.M., Mulligan, S.J., and Macvicar, B.A. (2009). Microglia processes block the spread of damage in the brain and require functional chloride channels. Glia *57*, 1610–1618.

Hirasawa, T., Ohsawa, K., Imai, Y., Ondo, Y., Akazawa, C., Uchino, S., and Kohsaka, S. (2005). Visualization of microglia in living tissues using Iba1-EGFP transgenic mice. J. Neurosci. Res. *81*, 357–362.

Hoffmann, A., Kann, O., Ohlemeyer, C., Hanisch, U.K., and Kettenmann, H. (2003). Elevation of basal intracellular calcium as a central element in the activation of brain macrophages (microglia): Suppression of receptor-evoked calcium signaling and control of release function. J. Neurosci. *23*, 4410–4419.

Holtman, I.R., Raj, D.D., Miller, J.A., Schaafsma, W., Yin, Z., Brouwer, N., Wes, P.D., Möller, T., Orre, M., Kamphuis, W., et al. (2015). Induction of a common microglia gene expression signature by aging and neurodegenerative conditions: a co-expression meta-analysis. Acta Neuropathol. Commun. *3*, 31.

Hong, S., Beja-Glasser, V.F., Nfonoyim, B.M., Frouin, A., Li, S., Ramakrishnan, S., Merry, K.M., Shi, Q., Rosenthal, A., Barres, B.A., et al. (2016a). Complement and microglia mediate early synapse loss in Alzheimer mouse models. Science *352*, 712–716.

Hong, S., Dissing-Olesen, L., and Stevens, B. (2016b). New insights on the role of microglia in synaptic pruning in health and disease. Curr. Opin. Neurobiol. *36*, 128–134.

Horikoshi, Y., Sakaguchi, G., Becker, A.G., Gray, A.J., Duff, K., Aisen, P.S., Yamaguchi, H., Maeda, M., Kinoshita, N., and Matsuoka, Y. (2004). Development of Aβ terminal end-specific antibodies and sensitive ELISA for Aβ variant. Biochem. Biophys. Res. Commun. *319*, 733–737.

Hovens, I.B., Nyakas, C., and Schoemaker, R. (2014). A novel method for evaluating microglial activation using ionized calcium-binding adaptor protein-1 staining: cell body to cell size ratio. Neuroimmunol. Neuroinflammation *1*, 82–88.

Hu, J., Liu, C.C., Chen, X.F., Zhang, Y.W., Xu, H., and Bu, G. (2015). Opposing effects of viral mediated brain expression of apolipoprotein E2 (apoE2) and apoE4 on apoE lipidation and Aβ metabolism in apoE4-targeted replacement mice. Mol. Neurodegener. *10*, 1–11.

Huang, Y., Happonen, K.E., Burrola, P.G., O'Connor, C., Hah, N., Huang, L., Nimmerjahn, A., and Lemke, G. (2021). Microglia use TAM receptors to detect and engulf amyloid β plaques. Nat. Immunol. *22*, 586–594.

Hughes, A.N., and Appel, B. (2020). Microglia phagocytose myelin sheaths to modify developmental myelination. Nat. Neurosci. *23*, 1055–1066.

Hung, Y.H., Chen, L.M.W., Yang, J.Y., and Yuan Yang, W. (2013). Spatiotemporally controlled induction of autophagy-mediated lysosome turnover. Nat. Commun. *4*, 2111.

Huttenlocher, P.R., and Dabholkar, A.S. (1997). Regional differences in synaptogenesis in human cerebral cortex. J. Comp. Neurol. *387*, 167–178.

Iadecola, C., Zhang, F., Niwa, K., Eckman, C., Turner, S.K., Fischer, E., Younkin, S., Borchelt, D.R., Hsiao, K.K., and Carlson, G.A. (1999). SOD1 rescues cerebral endothelial dysfunction in mice overexpressing amyloid precursor protein. Nat. Neurosci. *2*, 157–161.

Imbert, P.R.C., Saric, A., Pedram, K., Bertozzi, C.R., Grinstein, S., and Freeman, S.A. (2021). An acquired and endogenous glycocalyx forms a bidirectional "don't eat" and "don't eat me" barrier to phagocytosis. Curr. Biol. *31*, 77-89.

Iram, T., Ramirez-Ortiz, Z., Byrne, M.H., Coleman, U.A., Kingery, N.D., Means, T.K., Frenkel, D., and El Khoury, J. (2016). Megf10 Is a receptor for C1q that mediates clearance of apoptotic cells by astrocytes. J. Neurosci. *36*, 5185–5192.

Ising, C., Venegas, C., Zhang, S., Scheiblich, H., Schmidt, S. V., Vieira-Saecker, A., Schwartz, S., Albasset, S., McManus, R.M., Tejera, D., et al. (2019). NLRP3 inflammasome activation drives tau pathology. Nature *575*, 669–673.

Ito, D., Imai, Y., Ohsawa, K., Nakajima, K., Fukuuchi, Y., and Kohsaka, S. (1998). Microglia-specific localisation of a novel calcium binding protein, Iba1. Mol. Brain Res. *57*, 1–9.

Iturria-Medina, Y., Sotero, R.C., Toussaint, P.J., Mateos-Pérez, J.M., Evans, A.C., Weiner, M.W., Aisen, P., Petersen, R., Jack, C.R., et al. (2016). Early role of vascular dysregulation on late-onset Alzheimer's disease based on multifactorial data-driven analysis. Nat. Commun. *7,* 11934.

Izquierdo, P., Attwell, D., and Madry, C. (2019). Ion channels and receptors as determinants of microglial function. Trends Neurosci. *42*, 278–292.

Jamjoom, A.A.B., Rhodes, J., Andrews, P.J.D., and Grant, S.G.N. (2021). The synapse in traumatic brain injury. Brain *144*, 18–31.

Jay, T.R., von Saucken, V.E., Muñoz, B., Codocedo, J.F., Atwood, B.K., Lamb, B.T., and Landreth, G.E. (2019). TREM2 is required for microglial instruction of astrocytic synaptic engulfment in neurodevelopment. Glia *67*, 1873–1892.

Jiang, T., Tan, L., Zhu, X.C., Zhou, J.S., Cao, L., Tan, M.S., Wang, H.F., Chen, Q., Zhang, Y.D., and Yu, J.T. (2015). Silencing of TREM2 exacerbates tau pathology, neurodegenerative changes, and spatial learning deficits in P301S tau transgenic mice. Neurobiol. Aging *36*, 3176–3186.

Jiang, X., Newell, E.W., and Schlichter, L.C. (2003). Regulation of a TRPM7-like current in rat brain microglia. J. Biol. Chem. *278*, 42867–42876.

Jin, M., Shepardson, N., Yang, T., Chen, G., Walsh, D., and Selkoe, D.J. (2011). Soluble amyloid β-protein dimers isolated from Alzheimer cortex directly induce tau hyperphosphorylation and neuritic degeneration. PNAS *108*, 5819–5824.

Jinno, S., Fleischer, F., Eckel, S., Schmidt, V., and Kosaka, T. (2007). Spatial arrangement of microglia in the mouse hippocampus: A stereological study in comparison with astrocytes. Glia *55*, 1334–1347.

Joel, Z., Izquierdo, P., Salih, D.A., Richardson, J.C., Cummings, D.M., and Edwards, F.A. (2018). Improving mouse models for dementia. Are all the effects in tau mouse models

due to overexpression? Cold Spring Harb. Symp. Quant. Biol. *83*, 151–161.

Johnson, E.C.B., Dammer, E.B., Duong, D.M., Ping, L., Zhou, M., Yin, L., Higginbotham, L.A., Guajardo, A., White, B., et al. (2020). Large-scale proteomic analysis of Alzheimer's disease brain and cerebrospinal fluid reveals early changes in energy metabolism associated with microglia and astrocyte activation. Nat. Med. *26*, 769–780.

Jolly, S., Lang, V., Koelzer, V.H., Sala Frigerio, C., Magno, L., Salinas, P.C., Whiting, P., and Palomer, E. (2019). Single-cell quantification of mRNA expression in the human brain. Sci. Rep. *9*, 1–9.

Jones, R.S., Minogue, A.M., Connor, T.J., and Lynch, M.A. (2013). Amyloid-β-induced astrocytic phagocytosis is mediated by CD36, CD47 and RAGE. J. Neuroimmune Pharmacol. *8*, 301–311.

Jonsson, T., Stefansson, H., Steinberg, S., Jonsdottir, I., Jonsson, P. V., Snaedal, J., Bjornsson, S., Huttenlocher, J., Levey, A.I., Lah, J.J., et al. (2013). Variant of TREM2 associated with the risk of Alzheimer's Disease. N. Engl. J. Med. *368*, 107–116.

Jordà-Siquier, T., Petrel, M., Kouskoff, V., Cordelières, F., Frykman, S., Müller, U., Mulle, C., and Barthet, G. (2020). APP accumulates around dense-core amyloid plaques with presynaptic proteins in Alzheimer's disease brain. BioRxiv. DOI: 10.1101/2020.10.16.342196.

Jung, C.K.E., and Herms, J. (2014). Structural dynamics of dendritic spines are influenced by an environmental enrichment. Cereb. Cortex *24*, 377–384.

Kalla, R., Bohatschek, M., Kloss, C.U.A., Krol, J., Von Maltzan, X., and Raivich, G. (2003). Loss of microglial ramification in microglia-astrocyte cocultures: Involvement of adenylate cyclase, calcium, phosphatase, and G_i-protein systems. Glia *41*, 50–63.

Kang, S.S., Kurti, A., Baker, K.E., Liu, C.C., Colonna, M., Ulrich, J.D., Holtzman, D.M., Bu, G., and Fryer, J.D. (2018). Behavioral and transcriptomic analysis of Trem2-null mice: Not all knockout mice are created equal. Hum. Mol. Genet. *27*, 211–223.

Karperien, A., Ahammer, H., and Jelinek, H.F. (2013). Quantitating the subtleties of microglial morphology with fractal analysis. Front. Cell. Neurosci. *7*, 1–34.

Katsnelson, M.A., Rucker, L.G., Russo, H.M., and Dubyak, G.R. (2015). K^+ efflux agonists induce NLRP3 inflammasome activation independently of Ca^{2+} signaling. J. Immunol. *194*, 3937–3952.

Keren-Shaul, H., Spinrad, A., Weiner, A., Matcovitch-Natan, O., Dvir-Szternfeld, R., Ulland, T.K., David, E., Baruch, K., Lara-Astaiso, D., et al. (2017). A unique microglia type associated with restricting development of Alzheimer's Disease. Cell *169*, 1276–1290.

Khanna, R., Roy, L., Zhu, X., and Schlichter, L.C. (2001). K^+ channels and the microglial respiratory burst. Am. J. Physiol. - Cell Physiol. *280*, 796–806.

Kiianitsa, K., Kurtz, I., Beeman, N., Matsushita, M., Chien, W.M., Raskind, W.H., and Korvatska, O. (2021). Novel TREM2 splicing isoform that lacks the V-set immunoglobulin domain is abundant in the human brain. J Leukoc Biol. 1–9.

Kim, J.H., Na, H.J., Kim, C.K., Kim, J.Y., Ha, K.S., Lee, H., Chung, H.T., Kwon, H.J., Kwon, Y.G., and Kim, Y.M. (2008). The non-provitamin A carotenoid, lutein, inhibits NFκB-dependent gene expression through redox-based regulation of the phosphatidylinositol 3-kinase/PTEN/Akt and NFκB-inducing kinase pathways: Role of H_2O_2 in NFκB activation. Free Radic. Biol. Med. *45*, 885–896.

Kim, S.R., Kim, S.U., Oh, U., and Jin, B.K. (2006). Transient Receptor Potential Vanilloid subtype 1 mediates microglial cell death *in vivo* and *in vitro* via Ca^{2+}-mediated mitochondrial damage and cytochrome C release. J. Immunol. *177*, 4322–4329.

King, D.L., Arendash, G.W., Crawford, F., Sterk, T., Menendez, J., and Mullan, M.J. (1999). Progressive and gender-dependent cognitive impairment in the APP(SW) transgenic mouse model for Alzheimer's disease. Behav. Brain Res. *103*, 145–162.

Klein, W.L., Krafft, G.A., and Finch, C.E. (2001). Targeting small Aβ oligomers: The solution to an Alzheimer's disease conundrum? Trends Neurosci. *24*, 219–224.

Klunk, W.E., Bacskai, B.J., Mathis, C.A., Kajdasz, S.T., McLellan, M.E., Frosch, M.P., Debnath, M.L., Holt, D.P., Wang, Y., and Hyman, B.T. (2002). Imaging Aβ Plaques in living transgenic mice with multiphoton microscopy and methoxy-X04, a systemically administered congo red derivative. J. Neuropathol. Exp. Neurol. *61*, 797–805.

Kober, D.L., and Brett, T.J. (2017). TREM2-ligand interactions in health and disease. J. Mol. Biol. *429*, 1607–1629.

Kober, D.L., Alexander-Brett, J.M., Karch, C.M., Cruchaga, C., Colonna, M., Holtzman, M.J., and Brett, T.J. (2016). Neurodegenerative disease mutations in TREM2 reveal a functional surface and distinct loss-of-function mechanisms. eLife *5*, 1–24.

Koffie, R.M., Meyer-Luehmann, M., Hashimoto, T., Adams, K.W., Mielke, M.L., Garcia-Alloza, M., Micheva, K.D., Smith, S.J., Kim, M.L., Lee, V.M., et al. (2009). Oligomeric amyloid β associates with postsynaptic densities and correlates with excitatory synapse loss near senile plaques. PNAS *106*, 4012–4017.

Koffie, R.M., Hashimoto, T., Tai, H.C., Kay, K.R., Serrano-Pozo, A., Joyner, D., Hou, S., Kopeikina, K.J., Frosch, M.P., Lee, V.M., et al. (2012). Apolipoprotein E4 effects in Alzheimer's disease are mediated by synaptotoxic oligomeric amyloid β. Brain *135*, 2155–2168.

Koizumi, S., Shigemoto-Mogami, Y., Nasu-Tada, K., Shinozaki, Y., Ohsawa, K., Tsuda, M., Joshi, B. V., Jacobson, K.A., Kohsaka, S., and Inoue, K. (2007). UDP acting at $P2Y_6$ receptors is a mediator of microglial phagocytosis. Nature *446*, 1091–1095.

Kolodziejczak, M., Béchade, C., Gervasi, N., Irinopoulou, T., Banas, S.M., Cordier, C., Rebsam, A., Roumier, A., and Maroteaux, L. (2015). Serotonin modulates developmental microglia via $5\text{-}HT_{2B}$ receptors: Potential implication during synaptic refinement of retinogeniculate projections. ACS Chem. Neurosci. *6*, 1219–1230.

Konishi, H., Okamoto, T., Hara, Y., Komine, O., Tamada, H., Maeda, M., Osako, F., Kobayashi, M., Nishiyama, A., Kataoka, Y., et al. (2020). Astrocytic phagocytosis is a compensatory mechanism for microglial dysfunction. EMBO J. *39*, 1–18.

Korvers, L., de Andrade Costa, A., Mersch, M., Kettenmann, H., and Semtner, M. (2016). Spontaneous Ca^{2+} transients in mouse microglia. Cell Calcium *60*, 396–406.

Kouri, J., Noa, M., Diaz, B., and Niubo, E. (1980). Hyperpolarisation of rat peritoneal macrophages phagocytosing latex particles. Nature *283*, 868–869.

Krabbe, G., Matyash, V., Pannasch, U., Mamer, L., Boddeke, H.W.G.M., and Kettenmann, H. (2012). Activation of serotonin receptors promotes microglial injury-induced motility but attenuates phagocytic activity. Brain. Behav. Immun. *26*, 419–428.

Krabbe, G., Halle, A., Matyash, V., Rinnenthal, J.L., Eom, G.D., Bernhardt, U., Miller, K.R., Kettenmann, H., and Heppner, F.L. (2013). Functional impairment of microglia coincides with beta-amyloid deposition in mice with Alzheimer-like pathology. PLoS One *8*, e60921.

Krasemann, S., Madore, C., Cialic, R., Baufeld, C., Calcagno, N., El Fatimy, R., Beckers, L., O'Loughlin, E., Xu, Y., Fanek, Z., et al. (2017). The TREM2-APOE pathway drives the transcriptional phenotype of dysfunctional microglia in neurodegenerative diseases. Immunity *47*, 566–581.

Krasnow, A.M., Ford, M.C., Valdivia, L.E., Wilson, S.W., and Attwell, D. (2018). Regulation of developing myelin sheath elongation by oligodendrocyte calcium transients *in vivo*. Nat. Neurosci. *21*, 24–30.

Kunkle, B.W., Grenier-Boley, B., Sims, R., Bis, J.C., Damotte, V., Naj, A.C., Boland, A., Vronskaya, M., van der Lee, S.J., Amlie-Wolf, A., et al. (2019). Genetic meta-analysis of diagnosed Alzheimer's disease identifies new risk loci and implicates Aβ, tau, immunity and lipid processing. Nat. Genet. *51*, 414–430.

Kuroda, J., Ago, T., Nishimura, A., Nakamura, K., Matsuo, R., Wakisaka, Y., Kamouchi, M., and Kitazono, T. (2014). Nox4 is a major source of superoxide production in human brain pericytes. J. Vasc. Res. *51*, 429–438.

Kurpius, D., Wilson, N., Fuller, L., Hoffman, A., and Dailey, M.E. (2006). Early activation, motility, and homing of neonatal microglia to injured neurons does not require protein synthesis. Glia *54*, 58–70.

Laprell, L., Schulze, C., Brehme, M.L., and Oertner, T.G. (2021). The role of microglia membrane potential in chemotaxis. J. Neuroinflammation *18*, 1–10.

Latif-Hernandez, A., Shah, D., Craessaerts, K., Saido, T., Saito, T., De Strooper, B., Van der Linden, A., and D'Hooge, R. (2019). Subtle behavioral changes and increased

prefrontal-hippocampal network synchronicity in APP^{NL-G-F} mice before prominent plaque deposition. Behav. Brain Res. *364*, 431–441.

Lawson, L., Perry, V., Dri, P., and Gordon, S. (1990). Heterogeneity in the distribution and morphology of microglia in the normal adult mouse brain. Neuroscience *39*, 151–170.

Lee, C.Y.D., Daggett, A., Gu, X., Jiang, L.-L., Langfelder, P., Li, X., Wang, N., et al. (2018). Elevated TREM2 gene dosage reprograms microglia responsivity and ameliorates pathological phenotypes in Alzheimer's Disease models. Neuron *97*, 1032–1048.

Lee, G.S., Subramanian, N., Kim, A.I., Aksentijevich, I., Goldbach-Mansky, R., Sacks, D.B., Germain, R.N., Kastner, D.L., and Chae, J.J. (2012). The calcium-sensing receptor regulates the NLRP3 inflammasome through Ca^{2+} and cAMP. Nature *492*, 123–127.

Lee, J.-H., Kim, J., Noh, S., Lee, H., Lee, S.Y., Mun, J.Y., Park, H., and Chung, W. (2021a). Astrocytes phagocytose adult hippocampal synapses for circuit homeostasis. Nature *590*, 612–617.

Lee, S., Meilandt, W.J., Xie, L., Gandham, V.D., Ngu, H., Barck, K.H., Rezzonico, M., Imperio, J., Lalehzadeh, G., Huntley, M.A., et al. (2021b). TREM2 restrains the enhancement of tau accumulation and neurodegeneration by β-amyloid pathology. Neuron *109*, 1283–1301.

Lehrman, E.K., Wilton, D.K., Litvina, E.Y., Welsh, C.A., Chang, S.T., Frouin, A., Walker, A.J., Heller, M.D., Umemori, H., Chen, C., et al. (2018). CD47 protects synapses from excess microglia-mediated pruning during development. Neuron *100*, 120–134.

Leyns, C.E.G., Ulrich, J.D., Finn, M.B., Stewart, F.R., Koscal, L.J., Serrano, J.R., Robinson, G.O., Anderson, E., Colonna, M., and Holtzman, D.M. (2017). TREM2 deficiency attenuates neuroinflammation and protects against neurodegeneration in a mouse model of tauopathy. PNAS *114*, 11524–11529.

Lian, H., Litvinchuk, A., Chiang, A.C.A., Aithmitti, N., Jankowsky, J.L., and Zheng, H. (2016). Astrocyte-microglia cross talk through complement activation modulates amyloid pathology in mouse models of alzheimer's disease. J. Neurosci. *36*, 577–589.

Liebscher, S., Page, R.M., Käfer, K., Winkler, E., Quinn, K., Goldbach, E., Brigham, E.F., Quincy, D., Basi, G.S., Schenk, D.B., et al. (2014). Chronic γ-secretase inhibition reduces amyloid plaque-associated instability of pre- and postsynaptic structures. Mol. Psychiatry *19*, 937–946.

Linnartz-Gerlach, B., Bodea, L.G., Klaus, C., Ginolhac, A., Halder, R., Sinkkonen, L., Walter, J., Colonna, M., and Neumann, H. (2019). TREM2 triggers microglial density and age-related neuronal loss. Glia *67*, 539–550.

Liu, W., Taso, O., Wang, R., Bayram, S., Graham, A.C., Garcia-Reitboeck, P., Mallach, A., Andrews, W.D., Piers, T.M., Botia, J.A., et al. (2020). Trem2 promotes anti-inflammatory responses in microglia and is suppressed under pro-inflammatory conditions. Hum. Mol. Genet. *29*, 3224–3248.

Liu, Y.U., Ying, Y., Li, Y., Eyo, U.B., Chen, T., Zheng, J., Umpierre, A.D., Zhu, J., Bosco, D.B., Dong, H., et al. (2019). Neuronal network activity controls microglial process surveillance in awake mice via norepinephrine signaling. Nat. Neurosci. *22*, 1771–1781.

Long, J.M., and Holtzman, D.M. (2019). Alzheimer Disease: An update on pathobiology and treatment strategies. Cell *179*, 312–339.

Lonnemann, N., Hosseini, S., Marchetti, C., Skouras, D.B., Stefanoni, D., D'Alessandro, A., Dinarello, C.A., and Korte, M. (2020). The NLRP3 inflammasome inhibitor OLT1177 rescues cognitive impairment in a mouse model of Alzheimer's disease. PNAS *117*, 32145–32154.

Lööv, C., Mitchell, C.H., Simonsson, M., and Erlandsson, A. (2015). Slow degradation in phagocytic astrocytes can be enhanced by lysosomal acidification. Glia *63*, 1997–2009.

Lotshaw, D.P. (2007). Biophysical, pharmacological, and functional characteristics of cloned and native mammalian two-pore domain K^+ channels. Cell Biochem. Biophys. *47*, 209–256.

Di Lucente, J., Nguyen, H.M., Wulff, H., Jin, L.-W., and Maezawa, I. (2018). The voltage-gated potassium channel $K_v1.3$ is required for microglial pro-inflammatory activation

in vivo. Glia *66*, 1881–1895.

Lucin, K.M., O'Brien, C.E., Bieri, G., Czirr, E., Mosher, K.I., Abbey, R.J., Mastroeni, D.F., Rogers, J., Spencer, B., et al. (2013). Microglial Beclin 1 regulates retromer trafficking and phagocytosis and is impaired in Alzheimer's Disease. Neuron *79*, 873–886.

Lučiūnaitė, A., McManus, R.M., Jankunec, M., Rácz, I., Dansokho, C., Dalgėdienė, I., Schwartz, S., Brosseron, F., and Heneka, M.T. (2019). Soluble Aβ oligomers and protofibrils induce NLRP3 inflammasome activation in microglia. J. Neurochem. *155*, 650–661.

Ma, Q., Zhao, Z., Sagare, A.P., Wu, Y., Wang, M., Owens, N.C., Verghese, P.B., Herz, J., Holtzman, D.M., and Zlokovic, B. V. (2018). Blood-brain barrier-associated pericytes internalize and clear aggregated amyloid-β_{42} by LRP1-dependent apolipoprotein E isoform-specific mechanism. Mol. Neurodegener. *13*, 1–13.

Ma, X., Chen, K., Cui, Y., Huang, G., Nehme, A., Zhang, L., Li, H., Wei, J., Liong, K., Liu, Q., et al. (2020). Depletion of microglia in developing cortical circuits reveals its critical role in glutamatergic synapse development, functional connectivity, and critical period plasticity. J. Neurosci. Res. *98*, 1968–1986.

Madry, C., and Attwell, D. (2015). Receptors, ion channels, and signaling mechanisms underlying microglial dynamics. J. Biol. Chem. *290*, 12443–12450.

Madry, C., Kyrargyri, V., Arancibia-Cárcamo, I.L., Jolivet, R., Kohsaka, S., Bryan, R.M., and Attwell, D. (2018). Microglial ramification, surveillance, and interleukin-1β release are regulated by the two-pore domain K^+ channel THIK-1. Neuron *97*, 299–312.

Maeda, M., Tsuda, M., Tozaki-Saitoh, H., Inoue, K., and Kiyama, H. (2010). Nerve injury-activated microglia engulf myelinated axons in a $P2Y_{12}$ signaling-dependent manner in the dorsal horn. Glia *58*, 1838–1846.

Maezawa, I., Nguyen, H.M., Di Lucente, J., Jenkins, D.P., Singh, V., Hilt, S., Kim, K., Rangaraju, S., Levey, A.I., Wulff, H., et al. (2018). $K_v1.3$ inhibition as a potential microglia-targeted therapy for Alzheimer's disease: Preclinical proof of concept. Brain *141*, 596–612.

Magnus, T., Chan, A., Linker, R.A., Toyka, K. V., and Gold, R. (2002). Astrocytes are less efficient in the removal of apoptotic lymphocytes than microglia cells: Implications for

the role of glial cells in the inflamed CNS. J. Neuropathol. Exp. Neurol. *61*, 760–766.

Maguire, E., Menzies, G., Phillips, T., Sasner, M., Williams, H., Czubala, M., et al. (2020). The Alzheimer's disease protective P522R variant of PLCG2, consistently enhances stimulus-dependent PLCγ2 activation, depleting substrate and altering cell function. BioRxiv. DOI: 10.1101/2020.04.27.059600.

Majewska, A.K., Newton, J.R., and Sur, M. (2006). Remodeling of synaptic structure in sensory cortical areas *in vivo*. J. Neurosci. *26*, 3021–3029.

Man, S.M., and Kanneganti, T.D. (2015). Regulation of inflammasome activation. Immunol. Rev. *265*, 6–21.

Mander, P., and Brown, G.C. (2005). Activation of microglial NADPH oxidase is synergistic with glial iNOS expression in inducing neuronal death: A dual-key mechanism of inflammatory neurodegeneration. J. Neuroinflammation *2*, 1–15.

Mao, Y., and Finnemann, S.C. (2015). Regulation of phagocytosis by Rho GTPases. Small GTPases *6*, 89–99.

Marsh, S.E., Kamath, T., Walker, A.J., Dissing-Olesen, L., Hammond, T.R., Young, A.M.H., Abdulraouf, A., Nadaf, N., Dufort, C., Murphy, S., et al. (2020). Single cell sequencing reveals glial specific responses to tissue processing and enzymatic dissociation in mice and humans. BioRxiv. DOI: 10.1101/2020.12.03.408542.

Masters, C.L., Simms, G., Weinman, N.A., Multhaup, G., McDonald, B.L., and Beyreuther, K. (1985). Amyloid plaque core protein in Alzheimer disease and Down's syndrome. PNAS *82*, 4245–4249.

Masuda, A., Kobayashi, Y., Kogo, N., Saito, T., Saido, T.C., and Itohara, S. (2016). Cognitive deficits in single *App* knock-in mouse models. Neurobiol. Learn. Mem. *135*, 73–82.

Masuda, T., Amann, L., Sankowski, R., Staszewski, O., Lenz, M., d´Errico, P., Snaidero, N., Costa Jordão, M.J., Böttcher, C., Kierdorf, K., et al. (2020a). Novel Hexb-based tools for studying microglia in the CNS. Nat. Immunol. *21*, 802–815.

Masuda, T., Sankowski, R., Staszewski, O., and Prinz, M. (2020b). Microglia heterogeneity in the single-cell era. Cell Rep. *30*, 1271–1281.

Matarin, M., Salih, D.A., Yasvoina, M., Cummings, D.M., Guelfi, S., Liu, W., NahabooSolim, M.A., Moens, T.G., Paublete, R.M., Ali, S.S., et al. (2015). A genome-wide gene-expression analysis and database in transgenic mice during development of amyloid or tau pathology. Cell Rep. *10*, 633–644.

Mathys, H., Davila-Velderrain, J., Peng, Z., Gao, F., Mohammadi, S., Young, J.Z., Menon, M., He, L., Abdurrob, F., Jiang, X., et al. (2019). Single-cell transcriptomic analysis of Alzheimer's disease. Nature *570*, 332–337.

Mazaheri, F., Snaidero, N., Kleinberger, G., Madore, C., Daria, A., Werner, G., Krasemann, S., Capell, A., Trümbach, D., Wurst, W., et al. (2017). TREM2 deficiency impairs chemotaxis and microglial responses to neuronal injury. EMBO Rep. *18*, 1186–1198.

McKinsey, G.L., Lizama, C.O., Keown-Lang, A.E., Niu, A., Santander, N., Larpthaveesarp, A., Chee, E., Gonzalez, F.F., and Arnold, T.D. (2020). A new genetic strategy for targeting microglia in development and disease. eLife *9*, 1–34.

McLarnon, J.G., Choi, H.B., Lue, L.F., Walker, D.G., and Kim, S.U. (2005). Perturbations in calcium-mediated signal transduction in microglia from Alzheimer's disease patients. J. Neurosci. Res. *81*, 426–435.

McLeod, F., Marzo, A., Podpolny, M., Galli, S., and Salinas, P. (2017). Evaluation of synapse density in hippocampal rodent brain slices. J. Vis. Exp. *128*, 56153.

McMahon, S.M., and Jackson, M.B. (2018). An inconvenient truth: calcium sensors are calcium buffers. Trends Neurosci. *41*, 880–884.

Medawar, E., Benway, T.A., Liu, W., Hanan, T.A., Haslehurst, P., James, O.T., Yap, K., Muessig, L., Moroni, F., Nahaboo Solim, M.A., et al. (2019). Effects of rising amyloid β levels on hippocampal synaptic transmission, microglial response and cognition in APP Swe/PSEN1 M146V transgenic mice. EBioMedicine *39*, 422–435.

Melendez, A.J., and Tay, H.K. (2008). Phagocytosis: A repertoire of receptors and Ca2+ as a key second messenger. Biosci. Rep. *28*, 287–298.

Merlini, M., Rafalski, V.A., Rios Coronado, P.E., Gill, T.M., Ellisman, M., Muthukumar, G., et al. (2019). Fibrinogen induces microglia-mediated spine elimination and

cognitive impairment in an Alzheimer's Disease model. Neuron *101*, 1099–1108.

Merlini, M., Rafalski, V.A., Ma, K., Kim, K.Y., Bushong, E.A., Rios Coronado, P.E., Yan, Z., Mendiola, A.S., Sozmen, E.G., Ryu, J.K., et al. (2021). Microglial G_i-dependent dynamics regulate brain network hyperexcitability. Nat. Neurosci. *24*, 19–23.

Michaelis, M., Nieswandt, B., Stegner, D., Eilers, J., and Kraft, R. (2015). STIM1, STIM2, and Orai1 regulate store-operated calcium entry and purinergic activation of microglia. Glia *63*, 652–663.

Mishra, A., O'Farrell, F.M., Reynell, C., Hamilton, N.B., Hall, C.N., and Attwell, D. (2014). Imaging pericytes and capillary diameter in brain slices and isolated retinae. Nat. Protoc. *9*, 323–336.

Mitchell, C.H., Carré, D.A., Mcglinn, A.M., Stone, R.A., and Civan, M.M. (1998). A release mechanism for stored ATP in ocular ciliary epithelial cells. PNAS *95*, 7174–7178.

Miyamoto, A., Wake, H., Ishikawa, A.W., Eto, K., Shibata, K., Murakoshi, H., Koizumi, S., Moorhouse, A.J., Yoshimura, Y., and Nabekura, J. (2016). Microglia contact induces synapse formation in developing somatosensory cortex. Nat. Commun. *7*, 12540.

Del Moral, M.O., Asavapanumas, N., Uzcátegui, N.L., and Garaschuk, O. (2019). Healthy brain aging modifies microglial calcium signaling *in vivo*. Int. J. Mol. Sci. *20,* 589.

Morizawa, Y.M., Hirayama, Y., Ohno, N., Shibata, S., Shigetomi, E., Sui, Y., Nabekura, J., Sato, K., Okajima, F., et al. (2017). Reactive astrocytes function as phagocytes after brain ischemia via ABCA1-mediated pathway. Nat. Commun. *8*, 28.

Morrison, H., and Filosa, J. (2013). A quantitative spatiotemporal analysis of microglia morphology during ischemic stroke and reperfusion. J.Neuroinflammation *10*, 1-20.

Muñoz-Planillo, R., Kuffa, P., Martínez-Colón, G., Smith, B.L., Rajendiran, T.M., and Núñez, G. (2013). K+ efflux is the common trigger of NLRP3 inflammasome activation by bacterial toxins and particulate matter. Immunity *27*, 1142–1153.

Murakami, T., Ockinger, J., Yu, J., Byles, V., McColl, A., Hofer, A.M., and Horng, T. (2012). Critical role for calcium mobilization in activation of the NLRP3 inflammasome. PNAS *109*, 11282–11287.

Murana, E., Pagani, F., Basilico, B., Sundukova, M., Batti, L., Di Angelantonio, S., Cortese, B., Grimaldi, A., Francioso, A., Heppenstall, P., et al. (2017). ATP release during cell swelling activates a Ca^{2+}-dependent Cl^- current by autocrine mechanism in mouse hippocampal microglia. Sci. Rep. *7*, 1–16.

Muth, C., Hartmann, A., Sepulveda-Falla, D., Glatzel, M., and Krasemann, S. (2019). Phagocytosis of apoptotic cells is specifically upregulated in apoE4 expressing microglia *in vitro*. Front. Cell. Neurosci. *13*, 1–15.

Nayernia, Z., Jaquet, V., and Krause, K.H. (2014). New insights on NOX enzymes in the central nervous system. Antioxidants Redox Signal. *20*, 2815–2837.

Nebeling, F.C., Poll, S., Schmid, L.C., Mittag, M., Steffen, J., Keppler, K., and Fuhrmann, M. (2019). Microglia motility depends on neuronal activity and promotes structural plasticity in the hippocampus. BioRxiv. DOI: 10.1101/515759.

Neher, J.J., Neniskyte, U., Hornik, T., and Brown, G.C. (2014). Inhibition of UDP/$P2Y_6$ purinergic signaling prevents phagocytosis of viable neurons by activated microglia *in vitro* and *in vivo*. Glia *62*, 1463–1475.

Nelson, L.H., Warden, S., and Lenz, K.M. (2017). Sex differences in microglial phagocytosis in the neonatal hippocampus. Brain. Behav. Immun. *64*, 11–22.

Nelson, P.T., Alafuzoff, I., Bigio, E.H., Bouras, C., Braak, H., Cairns, N.J., Castellani, R.J., Crain, B.J., Davies, P., Tredici, K. Del, et al. (2012). Correlation of Alzheimer's disease neuropathologic changes with cognitive status: A review of the literature. J. Neuropathol. Exp. Neurol. *71*, 362–381.

Newell, E.W., and Schlichter, L.C. (2005). Integration of K^+ and Cl^- currents regulate steady-state and dynamic membrane potentials in cultured rat microglia. J. Physiol. *567*, 869–890.

Nguyen, P.T., Dorman, L.C., Pan, S., Vainchtein, I.D., Han, R.T., Nakao-Inoue, H., Taloma, S.E., Barron, J.J., Molofsky, A.B., Kheirbek, M.A., et al. (2020). Microglial remodeling of the extracellular matrix promotes synapse plasticity. Cell *182*, 1–16.

Nimmerjahn, A., Kirchhoff, F., and Helmchen, F. (2005). Resting microglial cells are highly dynamic surveillants of brain parenchyma *in vivo*. Science *308*, 1314–1318.

Nolte, C., Kirchhoff, F., and Kettenmann, H. (1997). Epidermal growth factor is a motility factor for microglial cells *in vitro*: Evidence for EGF receptor expression. Eur. J. Neurosci. *9*, 1690–1698.

Nortley, R., Korte, N., Izquierdo, P., Hirunpattarasilp, C., Mishra, A., Jaunmuktane, Z., Kyrargyri, V., Pfeiffer, T., Khennouf, L., et al. (2019). Amyloid beta oligomers constrict human capillaries in Alzheimer's disease via signaling to pericytes. Science *365*, eaav9518.

Nugent, A.A., Lin, K., van Lengerich, B., Lianoglou, S., Przybyla, L., Davis, S.S., Llapashtica, C., Wang, J., Kim, D.J., Xia, D., et al. (2020). TREM2 regulates microglial cholesterol metabolism upon chronic phagocytic challenge. Neuron *105*, 837–854.

Nunes, P., and Demaurex, N. (2010). The role of calcium signaling in phagocytosis. J. Leukoc. Biol. *88*, 57–68.

Nunes, P., Cornut, D., Bochet, V., Hasler, U., Oh-Hora, M., Waldburger, J.M., and Demaurex, N. (2012). STIM1 juxtaposes ER to phagosomes, generating Ca^{2+} hotspots that boost phagocytosis. Curr. Biol. *22*, 1990–1997.

O'Brien, R.J., and Wong, P.C. (2011). Amyloid precursor protein processing and Alzheimer's Disease. Annu. Rev. Neurosci. *34*, 185–204.

O'Neil, S.M., Witcher, K.G., McKim, D.B., and Godbout, J.P. (2018). Forced turnover of aged microglia induces an intermediate phenotype but does not rebalance CNS environmental cues driving priming to immune challenge. Acta Neuropathol. Commun.*6*,129.

Ohsawa, K., Irino, Y., Sanagi, T., Nakamura, Y., Suzuki, E., Inoue, K., and Kohsaka, S. (2010). $P2Y_{12}$ receptor-mediated integrin-β1 activation regulates microglial process extension induced by ATP. Glia *58*, 790–801.

Okochi, Y., Sasaki, M., Iwasaki, H., and Okamura, Y. (2009). Voltage-gated proton channel is expressed on phagosomes. Biochem. Biophys. Res. Commun. *382*, 274–279.

Olah, M., Patrick, E., Villani, A.C., Xu, J., White, C.C., Ryan, K.J., Piehowski, P., Kapasi, A., Nejad, P., Cimpean, M., et al. (2018). A transcriptomic atlas of aged human

microglia. Nat. Commun. *9*, 539.

Olmos-Alonso, A., Schetters, S.T.T., Sri, S., Askew, K., Mancuso, R., Vargas-Caballero, M., Holscher, C., Perry, V.H., and Gomez-Nicola, D. (2016). Pharmacological targeting of CSF1R inhibits microglial proliferation and prevents the progression of Alzheimer's-like pathology. Brain *139*, 891–907.

Ormel, P.R., Vieira de Sá, R., van Bodegraven, E.J., Karst, H., Harschnitz, O., Sneeboer, M.A.M., Johansen, L.E., van Dijk, R.E., Scheefhals, N., et al. (2018). Microglia innately develop within cerebral organoids. Nat. Commun. *9*, 4167.

Orr, A.G., Orr, A.L., Li, X.J., Gross, R.E., and Traynelis, S.F. (2009). Adenosine A_{2A} receptor mediates microglial process retraction. Nat. Neurosci. *12*, 872–878.

Pagani, F., Paolicelli, R.C., Murana, E., Cortese, B., Di Angelantonio, S., Zurolo, E., Guiducci, E., Ferreira, T.A., Garofalo, S., Catalano, M., et al. (2015). Defective microglial development in the hippocampus of Cx3cr1 deficient mice. Front. Cell. Neurosci. *9*, 1–14.

Paloneva, J., Manninen, T., Christman, G., Hovanes, K., Mandelin, J., Adolfsson, R., Bianchin, M., Bird, T., Miranda, R., Salmaggi, A., et al. (2002). Mutations in two genes encoding different subunits of a receptor signaling complex result in an identical disease phenotype. Am. J. Hum. Genet. *71*, 656–662.

Pan, J., Ma, N., Yu, B., Zhang, W., and Wan, J. (2020). Transcriptomic profiling of microglia and astrocytes throughout aging. J. Neuroinflammation *17*, 1–19.

Pan, X., Zhu, Y., Lin, N., Zhang, J., Ye, Q., Huang, H., and Chen, X. (2011). Microglial phagocytosis induced by fibrillar β-amyloid is attenuated by oligomeric β-amyloid: implications for Alzheimer's disease. Mol. Neurodegener. *6*, 45.

Paolicelli, R.C., Bolasco, G., Pagani, F., Maggi, L., Scianni, M., Panzanelli, P., Giustetto, M., Ferreira, T.A., Guiducci, E., Dumas, L., et al. (2011). Synaptic pruning by microglia is necessary for normal brain development. Science *333*, 1456–1458.

Paolicelli, R.C., Jawaid, A., Henstridge, C.M., Valeri, A., Merlini, M., Robinson, J.L., Lee, E.B., Rose, J., Appel, S., Lee, V.M.Y., et al. (2017). TDP-43 depletion in microglia promotes amyloid clearance but also induces synapse loss. Neuron *95*, 297–308.

Parhizkar, S., Arzberger, T., Brendel, M., Kleinberger, G., Deussing, M., Focke, C., Nuscher, B., Xiong, M., Ghasemigharagoz, A., et al. (2019). Loss of TREM2 function increases amyloid seeding but reduces plaque-associated ApoE. Nat. Neurosci. *22*,191-204.

Park, L., Uekawa, K., Garcia-Bonilla, L., Koizumi, K., Murphy, M., Pistik, R., Younkin, L., Younkin, S., Zhou, P., Carlson, G., et al. (2017). Brain perivascular macrophages initiate the neurovascular dysfunction of Alzheimer Aβ peptides. Circ. Res. *121*, 258–269.

Parkhurst, C.N.N., Yang, G., Ninan, I., Savas, J.N.N., Yates, J.R.R., Lafaille, J.J.J., Hempstead, B.L.L., Littman, D.R.R., and Gan, W.-B.B. (2013). Microglia promote learning-dependent synapse formation through brain-derived neurotrophic factor. Cell *155*, 1596–1609.

Parzych, K., Zetterqvist, A. V., Wright, W.R., Kirkby, N.S., Mitchell, J.A., and Paul-Clark, M.J. (2017). Differential role of pannexin-1/ATP/$P2X_7$ axis in IL-1β release by human monocytes. FASEB J. *31*, 2439–2445.

Pasciuto, E., Burton, O.T., Roca, C.P., Lagou, V., Rajan, W.D., Theys, T., Mancuso, R., Tito, R.Y., Kouser, L., Callaerts-Vegh, Z., et al. (2020). Microglia require CD4 T cells to complete the fetal-to-adult transition. Cell *182*, 625–640.

Peri, F., and Nüsslein-Volhard, C. (2008). Live imaging of neuronal degradation by microglia reveals a role for v0-ATPase a1 in phagosomal fusion *in vivo*. Cell *133*, 916–927.

Pfeiffer, T., Avignone, E., and Nägerl, U.V. (2016). Induction of hippocampal long-term potentiation increases the morphological dynamics of microglial processes and prolongs their contacts with dendritic spines. Sci. Rep. *6*, 1–9.

Pfeiffer, T., Poll, S., Bancelin, S., Angibaud, J., Inavalli, V.V.G.K., Keppler, K., Mittag, M., Fuhrmann, M., and Nägerl, U.V. (2018). Chronic 2P-STED imaging reveals high turnover of dendritic spines in the hippocampus *in vivo*. eLife *7*, 1–17.

Phillips, A.E.M., Villegas-Llerena, C., Piers, T.M., Cosker, K., Hardy, J., and Pocock, J.M. (2018). Loss of function of TREM2 results in cytoskeletal malfunction in microglia. J. Neurol. Neurobiol. *4*, 1–11.

Piechotta, P.L., Rapedius, M., Stansfeld, P.J., Bollepalli, M.K., Erhlich, G., Andres-Enguix, I., Fritzenschaft, H., Decher, N., Sansom, M.S.P., Tucker, S.J., et al. (2011). The pore structure and gating mechanism of K2P channels. EMBO J. *30*, 3607–3619.

Plescher, M., Seifert, G., Hansen, J.N., Bedner, P., Steinhäuser, C., and Halle, A. (2018). Plaque-dependent morphological and electrophysiological heterogeneity of microglia in an Alzheimer's disease mouse model. Glia 1464–1480.

Podleśny-Drabiniok, A., Marcora, E., and Goate, A.M. (2020). Microglial phagocytosis: A Disease-associated process emerging from Alzheimer's Disease genetics. Trends Neurosci. *43*, 965–979.

Poliani, P.L., Wang, Y., Fontana, E., Robinette, M.L., Yamanishi, Y., Gilfillan, S., and Colonna, M. (2015). TREM2 sustains microglial expansion during aging and response to demyelination. J. Clin. Invest. *125*, 2161–2170.

Polydoro, M., Acker, C.M., Duff, K., Castillo, P.E., and Davies, P. (2009). Age-dependent impairment of cognitive and synaptic function in the hTau mouse model of Tau pathology. J. Neurosci. *29*, 10741–10749.

Pozner, A., Xu, B., Palumbos, S., Gee, J.M.J.M., Tvrdik, P., and Capecchi, M.R. (2015). Intracellular calcium dynamics in cortical microglia responding to focal laser injury in the PC::G5-tdT reporter mouse. Front. Mol. Neurosci. *8*, 12.

Prakash, P., Jethava, K.P., Korte, N., Izquierdo, P., Favuzzi, E., Rose, I., Guttenplan, K., Dutta, S., Rochet, J.C., Fishell, G., et al. (2021). Monitoring phagocytic uptake of amyloid beta into glial cell lysosomes in real time. Chem. Sci. DOI: 10.1039/D1SC03486C.

Prakriya, M., Feske, S., Gwack, Y., Srikanth, S., Rao, A., and Hogan, P.G. (2006). Orai1 is an essential pore subunit of the CRAC channel. Nature *443*, 230–233.

Praticò, D., and Sung, S. (2004). Lipid peroxidation and oxidative imbalance: Early functional events in Alzheimer's disease. J. Alzheimer's Dis. *6*, 171–175.

Prinz, M., Jung, S., and Priller, J. (2019). Microglia biology: One century of evolving concepts. Cell *179*, 292–311.

Puigdellívol, M., Allendorf, D.H., and Brown, G.C. (2020). Sialylation and galectin-3 in microglia-mediated neuroinflammation and neurodegeneration. Front. Cell. Neurosci. *14*, 1–11.

Purro, S.A., Dickins, E.M., and Salinas, P.C. (2012). The secreted Wnt antagonist dickkopf-1 is required for amyloid β-mediated synaptic loss. J. Neurosci. *32*, 3492–3498.

Qiu, L., Ng, G., Tan, E.K., Liao, P., Kandiah, N., and Zeng, L. (2016). Chronic cerebral hypoperfusion enhances Tau hyperphosphorylation and reduces autophagy in Alzheimer's disease mice. Sci. Rep. *6*, 1–9.

Qu, W., and Li, L. (2020). Loss of TREM2 confers resilience to synaptic and cognitive impairment in aged mice. J. Neurosci. *40*, 9552–9563.

Raiders, S., Han, T., Scott-Hewitt, N., Kucenas, S., Lew, D., Logan, M.A., and Singhvi, A. (2021). Engulfed by glia: Glial pruning in development, function, and injury across species. J. Neurosci. *41*, 823–833.

Rajendran, L., and Paolicelli, R.C. (2018). Microglia-mediated synapse loss in Alzheimer's disease. J. Neurosci. *38*, 2911–2919.

Ramsey, I.S., Ruchti, E., Kaczmarek, J.S., and Clapham, D.E. (2009). H_v1 proton channels are required for high-level NADPH oxidase-dependent superoxide production during the phagocyte respiratory burst. PNAS *106*, 7642–7647.

Rangaraju, S., Raza, S.A., Pennati, A., Deng, Q., Dammer, E.B., Duong, D., Pennington, M.W., Tansey, M.G., Lah, J.J., Betarbet, R., et al. (2017). A systems pharmacology-based approach to identify novel $K_v1.3$ channel-dependent mechanisms in microglial activation. J. Neuroinflammation *14*, 1–20.

Ransohoff, R.M. (2016). A polarizing question: Do M1 and M2 microglia exist? Nat. Neurosci. *19*, 987–991.

Rasmussen, M.K., Mestre, H., and Nedergaard, M. (2018). The glymphatic pathway in neurological disorders. Lancet Neurol. *17*, 1016–1024.

Reeves, A.M.B., Shigetomi, E., and Khakh, B.S. (2011). Bulk loading of calcium indicator dyes to study astrocyte physiology: Key limitations and improvements using

morphological maps. J. Neurosci. *31*, 9353–9358.

Renigunta, V., Zou, X., Kling, S., Schlichthörl, G., and Daut, J. (2014). Breaking the silence: Functional expression of the two-pore-domain potassium channel THIK-2. Pflugers Arch. *466*, 1735–1745.

Riester, K., Brawek, B., Savitska, D., Fröhlich, N., Zirdum, E., Mojtahedi, N., Heneka, M.T., and Garaschuk, O. (2020). *In vivo* characterization of functional states of cortical microglia during peripheral inflammation. Brain. Behav. Immun. *87*, 243–255.

Risher, W.C., Ustunkaya, T., Alvarado, J.S., and Eroglu, C. (2014). Rapid Golgi analysis method for efficient and unbiased classification of dendritic spines. PLoS One *9*, e107591.

Roberts, B.R., Lind, M., Wagen, A.Z., Rembach, A., Frugier, T., Li, Q.X., Ryan, T.M., McLean, C.A., Doecke, J.D., Rowe, C.C., et al. (2017). Biochemically-defined pools of amyloid-β in sporadic Alzheimer's disease: Correlation with amyloid PET. Brain *140*, 1486–1498.

Rojo, A.I., McBean, G., Cindric, M., Egea, J., López, M.G., Rada, P., Zarkovic, N., and Cuadrado, A. (2014). Redox control of microglial function: Molecular mechanisms and functional significance. Antioxidants Redox Signal. *21*, 1766–1801.

Ronzano, R., Roux, T., Thetiot, M., Aigrot, M.S., Richard, L., Lejeune, F.X., and Mazuir, E. (2020). Microglia-neuron communication at nodes of Ranvier depends on neuronal activity through potassium release and contributes to myelin repair. BioRxiv. DOI: 10.1101/2020.09.02.279562.

Roy, E.R., Wang, B., Wan, Y.W., Chiu, G., Cole, A., Yin, Z., Propson, N.E., Xu, Y., Jankowsky, J.L., Liu, Z., et al. (2020). Type I interferon response drives neuroinflammation and synapse loss in Alzheimer disease. J. Clin. Invest. *130*, 1912–1930.

Ruan, C., Sun, L., Kroshilina, A., Beckers, L., De Jager, P., Bradshaw, E.M., Hasson, S.A., Yang, G., and Elyaman, W. (2020). A novel Tmem119-tdTomato reporter mouse model for studying microglia in the central nervous system. Brain. Behav. Immun. *83*, 180–191.

Sadleir, K.R., Kandalepas, P.C., Buggia-Prévot, V., Nicholson, D.A., Thinakaran, G., and Vassar, R. (2016). Presynaptic dystrophic neurites surrounding amyloid plaques are sites of microtubule disruption, BACE1 elevation, and increased Aβ generation in Alzheimer's disease. Acta Neuropathol. *132*, 235–256.

Saito, T., Matsuba, Y., Mihira, N., Takano, J., Nilsson, P., Itohara, S., Iwata, N., and Saido, T.C. (2014). Single App knock-in mouse models of Alzheimer's disease. Nat. Neurosci. *17*, 661–663.

Sakakibara, Y., Sekiya, M., Saito, T., Saido, T.C., and Iijima, K.M. (2018). Cognitive and emotional alterations in App knock-in mouse models of Aβ amyloidosis. BMC Neurosci. *19*, 1–17.

Salter, M.W., and Stevens, B. (2017). Microglia emerge as central players in brain disease. Nat. Med. *23*, 1018–1027.

Sasaguri, H., Nilsson, P., Hashimoto, S., Nagata, K., Saito, T., De Strooper, B., Hardy, J., Vassar, R., Winblad, B., and Saido, T.C. (2017). APP mouse models for Alzheimer's disease preclinical studies. EMBO J. *36*, 2473–2487.

Sayed, F.A., Telpoukhovskaia, M., Kodama, L., Li, Y., Zhou, Y., Le, D., Hauduc, A., Ludwig, C., Gao, F., Clelland, C., et al. (2018). Differential effects of partial and complete loss of TREM2 on microglial injury response and tauopathy. PNAS *115*, 10172–10177.

Sayed, F.A., Kodama, L., Udeochu, J.C., Fan, L., Carling, G.K., Le, D., Li, Q., Zhou, L., Mathys, H., Wang, M., et al. (2020). AD-linked R47H-TREM2 mutation induces disease-enhancing proinflammatory microglial states in mice and humans. BioRxiv. DOI: 10.1101/2020.07.24.218719.

Schafer, D.P., Lehrman, E.K., Kautzman, A.G., Koyama, R., Mardinly, A.R., Yamasaki, R., Ransohoff, R.M., Greenberg, M.E., Barres, B.A., and Stevens, B. (2012). Microglia sculpt postnatal neural circuits in an activity and complement-dependent manner. Neuron *74*, 691–705.

Schafer, D.P., Lehrman, E.K., and Stevens, B. (2013). The "quad-partite" synapse: Microglia-synapse interactions in the developing and mature CNS. Glia *61*, 24–36.

Schilling, T., and Eder, C. (2009). Importance of the non-selective cation channel TRPV1 for microglial reactive oxygen species generation. J. Neuroimmunol. *216*, 118–121.

Schilling, T., and Eder, C. (2011). Amyloid-β-induced reactive oxygen species production and priming are differentially regulated by ion channels in microglia. J. Cell. Physiol. *226*, 3295–3302.

Schilling, T., and Eder, C. (2015). Microglial K^+ channel expression in young adult and aged mice. Glia *63*, 664–672.

Schlepckow, K., Monroe, K.M., Kleinberger, G., Cantuti-Castelvetri, L., Parhizkar, S., Xia, D., Willem, M., Werner, G., Pettkus, N., Brunner, B., et al. (2020). Enhancing protective microglial activities with a dual function TREM2 antibody to the stalk region . EMBO Mol. Med. *12*, 1–22.

Schmidt, E., and Oheim, M. (2020). Infrared excitation induces heating and calcium microdomain hyperactivity in cortical astrocytes. Biophys. J. *119*, 2153–2165.

Scott-Hewitt, N., Perrucci, F., Morini, R., Erreni, M., Mahoney, M., Witkowska, A., Carey, A., Faggiani, E., et al. (2020). Local externalization of phosphatidylserine mediates developmental synaptic pruning by microglia. EMBO J. *39*, 1–20.

Semyanov, A., Henneberger, C., and Agarwal, A. (2020). Making sense of astrocytic calcium signals — from acquisition to interpretation. Nat. Rev. Neurosci. *21*, 551–564.

Sevigny, J., Chiao, P., Bussière, T., Weinreb, P.H., Williams, L., Maier, M., Dunstan, R., Salloway, S., Chen, T., Ling, Y., et al. (2016). The antibody aducanumab reduces Aβ plaques in Alzheimer's disease. Nature *537*, 50–56.

Shen, K., Sidik, H., and Talbot, W.S. (2016). The Rag-Ragulator complex regulates lysosome function and phagocytic flux in microglia. Cell Rep. *14*, 547–559.

Sheng, L., Chen, M., Cai, K., Song, Y., Yu, D., Zhang, H., and Xu, G. (2019). Microglial Trem2 induces synaptic impairment at early stage and prevents amyloidosis at late stage in APP/PS1 mice. FASEB J. *33*, 10425–10442.

Shi, Q., Chowdhury, S., Ma, R., Le, K.X., Hong, S., Caldarone, B.J., Stevens, B., and Lemere, C.A. (2017a). Complement C3 deficiency protects against neurodegeneration in

aged plaque-rich APP/PS1 mice. Sci. Transl. Med. *9*, eaaf6295.

Shi, Y., Yamada, K., Liddelow, S.A., Smith, S.T., Zhao, L., Luo, W., Tsai, R.M., Spina, S., Grinberg, L.T., Rojas, J.C., et al. (2017b). ApoE4 markedly exacerbates tau-mediated neurodegeneration in a mouse model of tauopathy. Nature *549*, 523–527.

Shimohama, S., Tanino, H., Kawakami, N., Okamura, N., Kodama, H., Yamaguchi, T., Hayakawa, T., Nunomura, A., Chiba, S., Perry, G., et al. (2000). Activation of NADPH oxidase in Alzheimer's disease brains. Biochem. Biophys. Res. Commun. *273*, 5–9.

Sholl, D.A. (1953). Dendritic organization in the neurons of the visual and motor cortices of the cat. J. Anat. *87*, 387–406.

Siddiqui, T.A., Lively, S., Vincent, C., and Schlichter, L.C. (2012). Regulation of podosome formation, microglial migration and invasion by Ca^{2+}-signaling molecules expressed in podosomes. J. Neuroinflammation *9*, 250.

Sierksma, A., Escott-Price, V., and De Strooper, B. (2020). Translating genetic risk of Alzheimer's disease into mechanistic insight and drug targets. Science *370*, 61–66.

Sierra, A., Paolicelli, R.C., and Kettenmann, H. (2019). Cien años de microglía: milestones in a century of microglial research. Trends Neurosci. *42*, 778–792.

Simpson, D.S., and Oliver, P.L. (2020). ROS generation in microglia: Understanding oxidative stress and inflammation in neurodegenerative disease. Antioxidants *9*, 1–27.

Sipe, G.O., Lowery, R.L., Tremblay, M., Kelly, E.A., Lamantia, C.E., and Majewska, A.K. (2016). Microglial $P2Y_{12}$ is necessary for synaptic plasticity in mouse visual cortex. Nat. Commun. *7,* 10905.

Smith, N.A., Kress, B.T., Lu, Y., Chandler-Militello, D., Benraiss, A., and Nedergaard, M. (2018). Fluorescent Ca^{2+} indicators directly inhibit the Na,K-ATPase and disrupt cellular functions. Sci. Signal. *11*, eaal2039.

Socodato, R., Portugal, C.C., Canedo, T., Rodrigues, A., Almeida, T.O., Henriques, J.F., Vaz, S.H., Magalhães, J., Silva, C.M., Baptista, F.I., et al. (2020). Microglia dysfunction caused by the loss of rhoa disrupts neuronal physiology and leads to neurodegeneration. Cell Rep. *31*, 107796.

Sosna, J., Philipp, S., Albay, R.I., Reyes-Ruiz, J.M., Baglietto-Vargas, D., LaFerla, F.M., and Glabe, C.G. (2018). Early long-term administration of the CSF1R inhibitor PLX3397 ablates microglia and reduces accumulation of intraneuronal amyloid, neuritic plaque deposition and pre-fibrillar oligomers in 5XFAD mouse model of Alzheimer's disease. Mol. Neurodegener. *13*, 1–11.

Spangenberg, E., Severson, P.L., Hohsfield, L.A., Crapser, J., Zhang, J., Burton, E.A., Zhang, Y., Spevak, W., Lin, J., Phan, N.Y., et al. (2019). Sustained microglial depletion with CSF1R inhibitor impairs parenchymal plaque development in an Alzheimer's disease model. Nat. Commun. *10*, 3758.

Spangenberg, E.E., Lee, R.J., Najafi, A.R., Rice, R.A., Elmore, M.R.P., Blurton-Jones, M., West, B.L., and Green, K.N. (2016). Eliminating microglia in Alzheimer's mice prevents neuronal loss without modulating amyloid-β pathology. Brain *139*, 1265–1281.

Srinivasan, K., Friedman, B.A., Etxeberria, A., Huntley, M.A., van der Brug, M.P., Foreman, O., Paw, J.S., Modrusan, Z., Beach, T.G., Serrano, G.E., et al. (2020). Alzheimer's patient microglia exhibit enhanced aging and unique transcriptional activation. Cell Rep. *31*, 107843.

Srinivasan, R., Huang, B.S., Venugopal, S., Johnston, A.D., Chai, H., Zeng, H., Golshani, P., and Khakh, B.S. (2015). Ca^{2+} signaling in astrocytes from $Ip3r2^{-/-}$ mice in brain slices and during startle responses *in vivo*. Nat. Neurosci. *18*, 708–717.

Stancu, I.C., Cremers, N., Vanrusselt, H., Couturier, J., Vanoosthuyse, A., Kessels, S., Lodder, C., Brône, B., Huaux, F., Octave, J.N., et al. (2019). Aggregated tau activates NLRP3–ASC inflammasome exacerbating exogenously seeded and non-exogenously seeded tau pathology *in vivo*. Acta Neuropathol. *137*, 599–617.

Stevens, B., Allen, N.J., Vazquez, L.E., Howell, G.R., Christopherson, K.S., Nouri, N., Micheva, K.D., Mehalow, A.K., Huberman, A.D., Stafford, B., et al. (2007). The classical complement cascade mediates CNS synapse elimination. Cell *131*, 1164–1178.

Stifter, S.A., and Greter, M. (2020). STOP floxing around: Specificity and leakiness of inducible Cre/loxP systems. Eur. J. Immunol. *50*, 338–341.

Stowell, R.D., Wong, E.L., Batchelor, H.N., Mendes, M.S., Lamantia, C.E., Whitelaw, B.S., and Majewska, A.K. (2018). Cerebellar microglia are dynamically unique and survey Purkinje neurons *in vivo*. Dev. Neurobiol. *78*, 627–644.

Stowell, R.D., Sipe, G.O., Dawes, R.P., Batchelor, H.N., Lordy, K.A., Whitelaw, B.S., et al. (2019). Noradrenergic signaling in the wakeful state inhibits microglial surveillance and synaptic plasticity in the mouse visual cortex. Nat. Neurosci. *22*, 1782–1792.

Suo, Z., Humphrey, J., Kundtz, A., Sethi, F., Placzek, A., Crawford, F., and Mullan, M. (1998). Soluble Alzheimers β-amyloid constricts the cerebral vasculature *in vivo*. Neurosci. Lett. *257*, 77–80.

Takahashi, K., Rochford, C.D.P., and Neumann, H. (2005). Clearance of apoptotic neurons without inflammation by microglial triggering receptor expressed on myeloid cells-2. J. Exp. Med. *201*, 647–657.

Takalo, M., Wittrahm, R., Wefers, B., Parhizkar, S., Jokivarsi, K., Kuulasmaa, T., Mäkinen, P., Martiskainen, H., Wurst, W., et al. (2020). The Alzheimer's disease-associated protective Plcγ2-P522R variant promotes immune functions. Mol. Neurodegener. *15*, 1–14.

Tamada, H., Blanc, J., Korogod, N., Petersen, C.C.H., and Knott, G.W. (2020). Ultrastructural comparison of dendritic spine morphology preserved with cryo and chemical fixation. eLife *9*, 1–15.

Tauer, U. (2002). Advantages and risks of multiphoton microscopy in physiology. Exp. Physiol. *87*, 709–714.

Tejera, D., and Heneka, M.T. (2019). *In vivo* phagocytosis analysis of amyloid beta, in "Microglia: Methods in molecular biology" (Humana, New York, NY).

Terry, R.D., Masliah, E., Salmon, D.P., Butters, N., DeTeresa, R., Hill, R., Hansen, L.A., and Katzman, R. (1991). Physical basis of cognitive alterations in Alzheimer's disease: Synapse loss is the major correlate of cognitive impairment. Ann. Neurol. *30*, 572–580.

Thion, M.S., and Garel, S. (2017). On place and time: microglia in embryonic and perinatal brain development. Curr. Opin. Neurobiol. *47*, 121–130.

Thomas, D.C. (2017). The phagocyte respiratory burst: Historical perspectives and recent advances. Immunol. Lett. *192*, 88–96.

Tolar, M., Abushakra, S., Hey, J.A., Porsteinsson, A., and Sabbagh, M. (2020). Aducanumab, gantenerumab, BAN2401, and ALZ-801: the first wave of amyloid-targeting drugs for AD with potential for near term approval. Alzheimers. Res. Ther. *12*, 1–10.

Tönnies, E., and Trushina, E. (2017). Oxidative stress, synaptic dysfunction, and Alzheimer's Disease. J. Alzheimer's Dis. *57*, 1105–1121.

Trachtenberg, J.T., Chen, B.E., Knott, G.W., Feng, G., Sanes, J.R., Welker, E., and Svoboda, K. (2002). Long-term *in vivo* imaging of experience-dependent synaptic plasticity in adult cortex. Nature *420*, 788–794.

Tsien, J.Z., Chen, D.F., Gerber, D., Tom, C., Mercer, E.H., Anderson, D.J., Mayford, M., Kandel, E.R., and Tonegawa, S. (1996). Subregion- and cell type-restricted gene knockout in mouse brain. Cell *87*, 1317–1326.

Turnbull, I.R., Gilfillan, S., Cella, M., Aoshi, T., Miller, M., Piccio, L., Hernandez, M., and Colonna, M. (2006). Cutting edge: TREM2 attenuates macrophage activation. J. Immunol. *177*, 3520–3524.

Tzioras, M., Daniels, M.J.D., King, D., Popovic, K., Holloway, R.K., Stevenson, A.J., Tulloch, J., Kandasamy, J., Sokol, D., Latta, C., et al. (2019). Altered synaptic ingestion by human microglia in Alzheimer's disease. BioRxiv. DOI: 10.1101/795930.

Ulland, T.K., Song, W.M., Huang, S.C.C., Ulrich, J.D., Sergushichev, A., Beatty, W.L., Loboda, A.A., Zhou, Y., Cairns, N.J., Kambal, A., et al. (2017). TREM2 Maintains Microglial Metabolic Fitness in Alzheimer's Disease. Cell *170*, 649–663.

Umpierre, A.D., and Wu, L.J. (2020). How microglia sense and regulate neuronal activity. Glia 1–17.

Umpierre, A.D., Bystrom, L.L., Ying, Y., Liu, Y.U., Worrell, G., and Wu, L.-J. (2020). Microglial calcium signaling is attuned to neuronal activity in awake mice. eLife *9,* e56502.

Vainchtein, I.D., and Molofsky, A. V. (2020). Astrocytes and microglia: In sickness and in health. Trends Neurosci. *43*, 144–154.

Vainchtein, I.D., Chin, G., Cho, F.S., Kelley, K.W., Miller, J.G., Chien, E.C., Liddelow, S.A., Nguyen, P.T., Nakao-Inoue, H., Dorman, L.C., et al. (2018). Astrocyte-derived interleukin-33 promotes microglial synapse engulfment and neural circuit development. Science *359*, 1269–1273.

Van Hove, H., Antunes, A.R.P., De Vlaminck, K., Scheyltjens, I., Van Ginderachter, J.A., and Movahedi, K. (2020). Identifying the variables that drive tamoxifen-independent CreERT2 recombination: Implications for microglial fate mapping and gene deletions. Eur. J. Immunol. *50*, 459–463.

VanRyzin, J.W., Marquardt, A.E., Argue, K.J., Vecchiarelli, H.A., Ashton, S.E., Arambula, S.E., Hill, M.N., and McCarthy, M.M. (2019). Microglial phagocytosis of newborn cells is induced by endocannabinoids and sculpts sex differences in juvenile rat social play. Neuron *102*, 435-449.

Vasek, M.J., Garber, C., Dorsey, D., Durrant, D.M., Bollman, B., Soung, A., Yu, J., Perez-Torres, C., Frouin, A., Wilton, D.K., et al. (2016). A complement-microglial axis drives synapse loss during virus-induced memory impairment. Nature *534*, 538–543.

Venegas, C., Kumar, S., Franklin, B.S., Dierkes, T., Brinkschulte, R., Tejera, D., Vieira-Saecker, A., Schwartz, S., Santarelli, F., Kummer, M.P., et al. (2017). Microglia-derived ASC specks crossseed amyloid-β in Alzheimer's disease. Nature *552*, 355–361.

Ventura, R., and Harris, K.M. (1999). Three-dimensional relationships between hippocampal synapses and astrocytes. J. Neurosci. *19*, 6897–6906.

Villani, A., Benjaminsen, J., Moritz, C., Henke, K., Hartmann, J., Norlin, N., Richter, K., Schieber, N.L., Franke, T., Schwab, Y., et al. (2019). Clearance by microglia depends on packaging of phagosomes into a unique cellular compartment. Dev. Cell *49*, 77–88.

Wallace, J., Lord, J., Dissing-Olesen, L., Stevens, B., and Murthy, V.N. (2020). Microglial depletion disrupts normal functional development of adult-born neurons in the olfactory bulb. eLife *9*, 1–30.

Wallen, W.J., Belanger, M.P., and Wittnich, C. (2001). Sex hormones and the selective estrogen receptor modulator tamoxifen modulate weekly body weights and food

intakes in adolescent and adult rats. J. Nutr. *131*, 2351–2357.

Wan, Y., Feng, B., You, Y., Yu, J., Xu, C., Dai, H., Trapp, B.D., Shi, P., Chen, Z., and Hu, W. (2020). Microglial displacement of GABAergic synapses is a protective event during complex febrile seizures. Cell Rep. *33*, 108346.

Wang, C., Yue, H., Hu, Z., Shen, Y., Ma, J., Li, J., Wang, X., et al. (2020a). Microglia mediate forgetting via complement-dependent synaptic elimination. Science *367*, 688–694.

Wang, S., Mustafa, M., Yuede, C.M., Salazar, S.V., Kong, P., Long, H., Ward, M., Siddiqui, O., Paul, R., Gilfillan, S., et al. (2020b). Anti-human TREM2 induces microglia proliferation and reduces pathology in an Alzheimer's disease model. J. Exp. Med. *217*, e20200785.

Wang, Y., Cella, M., Mallinson, K., Ulrich, J.D., Young, K.L., Robinette, M.L., Gilfillan, S., Krishnan, G.M., Sudhakar, S., Zinselmeyer, B.H., et al. (2015). TREM2 lipid sensing sustains the microglial response in an Alzheimer's disease model. Cell *160*, 1061–1071.

Wang, Y., Ulland, T.K., Ulrich, J.D., Song, W., Tzaferis, J.A., Hole, J.T., Yuan, P., Mahan, T.E., Shi, Y., Gilfillan, S., et al. (2016). TREM2-mediated early microglial response limits diffusion and toxicity of amyloid plaques. J. Exp. Med. *213*, 667–675.

Weinhard, L., Di Bartolomei, G., Bolasco, G., Machado, P., Schieber, N.L., Neniskyte, U., Exiga, M., Vadisiute, A., et al. (2018). Microglia remodel synapses by presynaptic trogocytosis and spine head filopodia induction. Nat. Commun. *9*, 1228.

Welsh, C.A., Stephany, C.-É.É., Sapp, R.W., and Stevens, B. (2020). Ocular dominance plasticity in binocular primary visual cortex does not require C1q. J. Neurosci. *40*, 769–783.

Wen, R.X., Shen, H., Huang, S.X., Wang, L.P., Li, Z.W., Peng, P., Mamtilahun, M., Tang, Y.H., Shen, F.X., Tian, H.L., et al. (2020). $P2Y_6$ receptor inhibition aggravates ischemic brain injury by reducing microglial phagocytosis. CNS Neurosci. Ther. *26*, 416–429.

Wendt, S., Maricos, M., Vana, N., Meyer, N., Guneykaya, D., Semtner, M., and Kettenmann, H. (2017). Changes in phagocytosis and potassium channel activity in microglia of 5xFAD mice indicate alterations in purinergic signaling in a mouse model of

Alzheimer's disease. Neurobiol. Aging *58*, 41–53.

Werneburg, S., Jung, J., Kunjamma, R.B., Ha, S.K., Luciano, N.J., Willis, C.M., Gao, G., Biscola, N.P., Havton, L.A., Crocker, S.J., et al. (2020). Targeted complement inhibition at synapses prevents microglial synaptic engulfment and synapse loss in demyelinating disease. Immunity *52*, 167–182.

Wightman, D.P., Jansen, I.E., Savage, J.E., and Shadrin, A.A. (2020). Largest GWAS (N=1,126,563) of Alzheimer's Disease implicates microglia and immune cells. MedRxiv. DOI: 10.1101/2020.11.20.20235275.

Wilton, D.K., Dissing-Olesen, L., and Stevens, B. (2019). Neuron-glia signaling in synapse elimination. Annu. Rev. Neurosci. *42*, 107–127.

Won, S.J., Kim, J.E., Cittolin-Santos, G.F., and Swanson, R.A. (2015). Assessment at the single-cell level identifies neuronal glutathione depletion as both a cause and effect of ischemia-reperfusion oxidative stress. J. Neurosci. *35*, 7143–7152.

Woollacott, I.O.C., Toomey, C.E., Strand, C., Courtney, R., Benson, B.C., Rohrer, J.D., and Lashley, T. (2020). Microglial burden, activation and dystrophy patterns in frontotemporal lobar degeneration. J. Neuroinflammation *17*, 1–27.

Wu, L.-J.J., Wu, G., Sharif, M.R.A., Baker, A., Jia, Y., Fahey, F.H., Luo, H.R., Feener, E.P., and Clapham, D.E. (2012). The voltage-gated proton channel H_v1 enhances brain damage from ischemic stroke. Nat. Neurosci. *15*, 565–573.

Wu, T., Dejanovic, B., Gandham, V.D., Gogineni, A., Edmonds, R., Schauer, S., Srinivasan, K., Huntley, M.A., Wang, Y., Wang, T.M., et al. (2019). Complement C3 is activated in human AD brain and is required for neurodegeneration in mouse models of amyloidosis and tauopathy. Cell Rep. *28*, 2111–2123.

Wu, Z., Xue, H., Gao, Q., and Zhao, P. (2020). Effects of early postnatal sevoflurane exposure on oligodendrocyte maturation and myelination in cerebral white matter of the rat. Biomed. Pharmacother. *131*, 110733.

Xu, H.-T.T., Pan, F., Yang, G., and Gan, W. (2007). Choice of cranial window type for *in vivo* imaging affects dendritic spine turnover in the cortex. Nat. Neurosci. *10*, 549–551.

Yan, Y., Wei, C.L., Zhang, W.R., Cheng, H.P., and Liu, J. (2006). Cross-talk between calcium and reactive oxygen species signaling. Acta Pharmacol. Sin. *27*, 821–826.

Ye, Z., Cudmore, R.H., and Linden, D.J. (2019). Estrogen-dependent functional spine dynamics in neocortical pyramidal neurons of the mouse. J. Neurosci. *39*, 4874–4888.

Yin, Z., Raj, D., Saiepour, N., Van Dam, D., Brouwer, N., Holtman, I.R., Eggen, B.J.L., Möller, T., Tamm, J.A., Abdourahman, A., et al. (2017). Immune hyperreactivity of Aβ plaque-associated microglia in Alzheimer's disease. Neurobiol. Aging *55*, 115–122.

Yona, S., Kim, K.W., Wolf, Y., Mildner, A., Varol, D., Breker, M., Strauss-Ayali, D., Viukov, S., Guilliams, M., Misharin, A., et al. (2013). Fate mapping reveals origins and dynamics of monocytes and tissue macrophages under homeostasis. Immunity *38*, 79–91.

Yuan, P., and Grutzendler, J. (2016). Attenuation of β-amyloid deposition and neurotoxicity by chemogenetic modulation of neural activity. J. Neurosci. *36*, 632–641.

Yuan, P., Condello, C., Keene, C.D., Wang, Y., Bird, T.D., Paul, S.M., Luo, W., Colonna, M., Baddeley, D., and Grutzendler, J. (2016). TREM2 haplodeficiency in mice and humans impairs the microglia barrier function leading to decreased amyloid compaction and severe axonal dystrophy. Neuron *90*, 724–739.

Yup, J., Oana, L., and Anthony, C.M. (2021). Defective lysosomal lipid catabolism as a common pathogenic mechanism for dementia. Neuromolecular Med *1*, 1–24.

Zanier, E.R., Fumagalli, S., Perego, C., Pischiutta, F., and De Simoni, M.-G. (2015). Shape descriptors of the "never resting" microglia in three different acute brain injury models in mice. Intensive Care Med. Exp. *3*, 1–18.

Zaqout, S., and Kaindl, A.M. (2016). Golgi-Cox staining step by step. Front. Neuroanat. *10*, 38.

Zetterberg, H., and Blennow, K. (2020). Blood Biomarkers: Democratizing Alzheimer's Diagnostics. Neuron *106*, 881–883.

Zhan, Y., Paolicelli, R.C., Sforazzini, F., Weinhard, L., Bolasco, G., Pagani, F., Vyssotski, A.L., Bifone, A., et al. (2014). Deficient neuron-microglia signaling results in impaired functional brain connectivity and social behavior. Nat. Neurosci. *17*, 400–406.

Zhang, B., Gaiteri, C., Bodea, L.G., Wang, Z., McElwee, J., Podtelezhnikov, A.A., Zhang, C., Xie, T., Tran, L., Dobrin, R., et al. (2013). Integrated systems approach identifies genetic nodes and networks in late-onset Alzheimer's disease. Cell *153*, 707–720.

Zhang, H., Chen, W., Tan, Z., Zhang, L., Dong, Z., Cui, W., Zhao, K., Wang, H., Jing, H., Cao, R., et al. (2020). A role of low-density lipoprotein receptor-related protein 4 (LRP4) in astrocytic Aβ clearance. J. Neurosci. *40*, 5347–5361

Zhang, Y., Chen, K., Sloan, S.A., Bennett, M.L., Scholze, A.R., O'Keeffe, S., Phatnani, H.P., Guarnieri, P., Caneda, C., Ruderisch, N., et al. (2014). An RNA-sequencing transcriptome and splicing database of glia, neurons, and vascular cells of the cerebral cortex. J. Neurosci. *34*, 11929–11947.

Zhang, Y., Sloan, S.A., Clarke, L.E., Caneda, C., Plaza, C.A., Blumenthal, P.D., Vogel, H., Steinberg, G.K., Edwards, M.S.B., Li, G., et al. (2016). Purification and characterization of progenitor and mature human astrocytes reveals transcriptional and functional differences with mouse. Neuron *89*, 37–53.

Zhao, Y., Wu, X., Li, X., Jiang, L.-L., Gui, X., Liu, Y., Sun, Y., Zhu, B., Piña-Crespo, J.C., Zhang, M., et al. (2018). TREM2 is a receptor for β-amyloid that mediates microglial function. Neuron *97*, 1023–1031.

Zhong, F., Liu, L., Wei, J.-L., and Dai, R.-P. (2019). Step by step Golgi-Cox staining for cryosection. Front. Neuroanat. *13*, 62.

Zhong, L., Chen, X.F., Wang, T., Wang, Z., Liao, C., Wang, Z., Huang, R., Wang, D., Li, X., Wu, L., et al. (2017). Soluble TREM2 induces inflammatory responses and enhances microglial survival. J. Exp. Med. *214*, 597–607.

Zhou, Y., Song, W.M., Andhey, P.S., Swain, A., Levy, T., Miller, K.R., Poliani, P.L., Cominelli, M., Grover, S., Gilfillan, S., et al. (2020). Human and mouse single-nucleus transcriptomics reveal TREM2-dependent and TREM2-independent cellular responses in Alzheimer's disease. Nat. Med. *26*, 131–142.

Ziegler-Waldkirch, S., d'Errico, P., Sauer, J., Erny, D., Savanthrapadian, S., Loreth, D., Katzmarski, N., Blank, T., Bartos, M., Prinz, M., et al. (2018). Seed-induced Aβ

deposition is modulated by microglia under environmental enrichment in a mouse model of Alzheimer's disease. EMBO J. *37*, 167–182.

Zott, B., Simon, M.M., Hong, W., Unger, F., Chen-Engerer, H.-J., Frosch, M.P., Sakmann, B., Walsh, D.M., and Konnerth, A. (2019). A vicious cycle of β amyloid–dependent neuronal hyperactivation. Science *365*, 559–565.

Zou, X., Conrad, L.J., Koschinsky, K., Schlichthörl, G., Preisig-Müller, R., Netz, E., Krüger, J., Daut, J., and Renigunta, V. (2020). The phosphodiesterase inhibitor IBMX blocks the potassium channel THIK-1 from the extracellular side. Mol. Pharmacol. *98*, 143–155.

Zuo, Y., Lin, A., Chang, P., and Gan, W.B. (2005). Development of long-term dendritic spine stability in diverse regions of cerebral cortex. Neuron *46*, 181–189.